

Imperial College of Science, Technology and Medicine
Department of Bioengineering
Neural Coding Laboratory

**Low-dimensional representations of neural
time-series data**

with applications to peripheral nerve decoding

Carl Henning Thore Lubba

Submitted in part fulfilment of the requirements for the degree of
Doctor of Philosophy in Bioengineering of the University of London and
the Diploma of Imperial College, March 2020

Declaration of Originality

I herewith certify that all the material in this thesis is my own work, except for quotations from published and unpublished sources which are clearly indicated and acknowledged as such. The source of any picture, diagram or other figure that is not my own work is also indicated. The copyright of this thesis rests with the author and is made available under a Creative Commons Attribution Non-Commercial No Derivatives licence. Researchers are free to copy, distribute or transmit the thesis on the condition that they attribute it, that they do not use it for commercial purposes and that they do not alter, transform or build upon it. For any reuse or redistribution, researchers must make clear to others the licence terms of this work.

Carl Henning Lubba

January 2020

Acknowledgements

None of this work would have been possible without the extensive input I received from my supervisors Simon and Nick. Simon, thanks for the positive, trusting supervision style that allowed me to freely explore different aspects of my topic while at the same time providing valuable advice when needed. Nick, thanks for the inspiring conceptual discussions and for taking every little topic seriously.

In addition, I am very grateful for the support I received from Ben Fulcher. Not only has his *hctsa*-toolbox been a major source of advancement in my PhD, but also did I learn many things through working with him both in terms of technical skills and importantly in terms of science communication and effective writing. Thanks Ben!

As another important collaboration I would like to thank Simon Cork. By attending his experiments, I understood a lot of the properties of the data I was analysing, as well as many biological details. Without his data, I could not have validated my simulator.

Special thanks to Peter Quicke, Subhojit Chakraborty, and June Kyu Hwang for the two-photon microscopy images and Thomas Knöpfel for the ChAT-Cre FLEX-VSFP 2.3 mice they were acquired from. Based on these images I could implement my placing algorithm for virtual tortuous axons.

I am further grateful for the data we received from Warren Grill at Duke and the more detailed recordings acquired by Tim Bruns and Aileen Ouyang at Michigan University. Both datasets enabled me to conduct decoding studies of the same study object (bladder) at different recording resolutions. Tim and Aileen also provided valuable input to the resulting publication.

I would also like to thank my examiners Konstantin Nikolic and David Halliday for the time they invested in preparing the viva and the input they gave me for improving the thesis text.

Abstract

Bioelectronic medicines, implanted devices that influence physiological states by peripheral neuro-modulation, have promise as a new way of treating diverse conditions from rheumatism to diabetes. We here explore ways of creating nerve-based feedback for the implanted systems to act in a dynamically adapting closed loop.

In a first empirical component, we carried out decoding studies on *in vivo* recordings of cat and rat bladder afferents. In a low-resolution data-set, we selected informative frequency bands of the neural activity using information theory to then relate to bladder pressure. In a second high-resolution dataset, we analysed the population code for bladder pressure, again using information theory, and proposed an informed decoding approach that promises enhanced robustness and automatic re-calibration by creating a low-dimensional population vector.

Coming from a different direction of more general time-series analysis, we embedded a set of peripheral nerve recordings in a space of main firing characteristics by dimensionality reduction in a high-dimensional feature-space and automatically proposed single efficiently implementable estimators for each identified characteristic. For bioelectronic medicines, this feature-based pre-processing method enables an online signal characterisation of low-resolution data where spike sorting is impossible but simple power-measures discard informative structure. Analyses were based on surrogate data from a self-developed and flexibly adaptable computer model that we made publicly available.

The wider utility of two feature-based analysis methods developed in this work was demonstrated on a variety of datasets from across science and industry. (1) Our feature-based generation of interpretable low-dimensional embeddings for unknown time-series datasets answers a need for simplifying and harvesting the growing body of sequential data that characterises modern science. (2) We propose an additional, supervised pipeline to tailor feature subsets to collections of classification problems. On a literature standard library of time-series classification tasks, we distilled 22 generically useful estimators and made them easily accessible.

Contents

Acknowledgements	5
Abstract	7
1 Introduction	1
1.1 Motivation	2
1.2 Objectives	3
1.3 Contributions	4
1.4 Publications	5
1.5 Organisation of this thesis	7
2 Background	8
2.1 The peripheral nervous system	8
2.1.1 Organisation	8
2.1.2 Peripheral nerves	11
2.1.3 Axons	12
2.2 Engineering principles of peripheral nerves	15
2.3 Physiological information transmission on peripheral nerves	16
2.4 Recording techniques	18
2.5 Decoding	21
2.5.1 Decoding from the central nervous system	22
2.5.2 Decoding from the peripheral nervous system	24
2.6 Feature-based time-series characterisation and analysis	29
2.7 Simulation of peripheral nerves	31
2.7.1 Conclusion on background	33
3 Simulation – PyPNS	35
3.1 Introduction	35
3.2 Methodology	38
3.2.1 Experiments	38
3.2.1.1 Validation of simulated recordings	38
3.2.1.2 Imaging of peripheral nerve tortuosity	39
3.2.2 PyPNS overview	40
3.2.3 Assumptions and simplifications	40
3.2.4 Axon models	42
3.2.5 Generation of axonal geometry	43
3.2.6 Extracellular potentials	43
3.2.7 Homogeneous media	46
3.2.8 Radially inhomogeneous media	47
3.2.9 Longitudinally inhomogeneous media	48
3.3 Results	50
3.3.1 Axon models	50

3.3.2	Profiles of extracellular media	51
3.3.3	Extracellular single fibre action potentials	53
3.3.4	Effects of varying the cuff length	55
3.3.5	Compound action potentials	56
3.3.6	Fitting axon tortuosity to experimental data	59
3.3.7	Recording from tortuous axons	60
3.3.8	Stimulation of tortuous axons	63
3.4	Discussion on our simulator PyPNS	63
3.5	Appendices	66
3.5.A	Axon model equations	66
3.5.A.1	Unmyelinated fibres: Hodgkin-Huxley-model	67
3.5.A.2	Myelinated fibres: McIntyre (MRG) model	67
3.5.B	Calculation of the random component of the axon placing algorithm	69
3.5.C	Generation of simulated c -distributions	69
3.5.D	Fitted cuff transmission function	70
4	Encoding and decoding of bladder pressure	72
4.1	Decoding of bladder pressure from hook electrode recordings of the rat pelvic nerve	74
4.1.1	Methods	75
4.1.1.1	Experiments	75
4.1.1.2	Frequency band selection	75
4.1.1.3	Piecewise Linear Fit	76
4.1.1.4	Optimal Linear Filter	77
4.1.1.5	Piecewise Linear Fit followed by Optimal Linear Filter	77
4.1.1.6	Cross-validation	77
4.1.2	Results	78
4.1.2.1	A broad spectrum is informative of bladder pressure	78
4.1.2.2	Relation between nerve activity and bladder pressure is nonlinear	79
4.1.2.3	Accurate bladder pressure estimation from pelvic nerve activity	79
4.1.2.4	PGE2 administration leads to bladder pressure underestimation	81
4.1.3	Discussion low-resolution decoder	81
4.2	Bladder pressure encoding by groups of stereotypical fibres	82
4.2.1	Methods	83
4.2.1.1	Experiments	83
4.2.1.2	Fibre selection and characterization	84
4.2.1.3	Surrogate data	87
4.2.1.4	Information theoretic analysis	88
4.2.1.5	Decoding	89
4.2.2	Results	91
4.2.2.1	Groups of stereotypical bladder neuron types exist	91
4.2.2.2	Encoding by groups of stereotypical bladder neurons is efficient and robust	93
4.2.2.3	A robust decoder based on stereotypical bladder neuron clusters	97
4.2.3	Discussion encoding and informed high-resolution decoder	99
4.2.4	Appendices	101
4.2.4.A	Detailed analysis of the relation between activity clusters and cell types	101
4.2.4.B	Tables of mutual information and redundancy	103
4.2.4.C	Redundancy towards fast pressure components	103
4.3	Conclusion on decoding work	104

5	Feature-based time-series analyses	106
5.1	Inferring low-dimensional variation in time-series datasets	107
5.1.1	Methods	109
5.1.1.1	Theory	109
5.1.1.2	Constructing a feature space	111
5.1.1.3	Normalisation and dimensionality reduction	112
5.1.1.4	Dimensionality estimation	113
5.1.1.5	Evaluating the embedding	114
5.1.1.6	Selecting efficiently implementable features	114
5.1.1.7	Datasets	114
5.1.2	Results	116
5.1.2.1	Feature library assessment	117
5.1.3	Case study 1: The Van der Pol Oscillator	119
5.1.4	Low-dimensional projections	121
5.1.5	Case study 2: Simulated peripheral nerve recordings	124
5.1.6	Performance across diverse synthetic time-series models	127
5.1.6.1	Dimensionality estimation	127
5.1.6.2	Parameter reconstruction	128
5.1.7	What characteristics of data are suitable	130
5.1.8	Case Study 3: Empirical fly data	131
5.1.9	Robustness and Sensitivity	132
5.1.9.1	Number of features required	133
5.1.9.2	Number of time series required	134
5.1.9.3	Influence of number of samples, sampling rate, and signal-to-noise ratio	136
5.1.10	Discussion	137
5.1.11	Appendix	139
5.1.11.A	Feature library	139
5.1.11.B	Time-series Datasets	139
5.2	Condensed feature-spaces – <i>catch22</i>	144
5.2.1	Methods	146
5.2.1.1	Data	146
5.2.1.2	Time-series features	147
5.2.1.3	Performance-based selection	148
5.2.1.4	Quantifying feature performance	148
5.2.1.5	Statistical prefiltering	150
5.2.1.6	Selecting a canonical set of features	151
5.2.1.7	Overall classification performance	151
5.2.1.8	Execution times and scaling	152
5.2.1.9	Selecting the two most informative features from a small subset	152
5.2.2	Results	152
5.2.2.1	Performance diversity across classification tasks	153
5.2.2.2	Features with performance consistent with chance	153
5.2.2.3	Top-performing features	154
5.2.2.4	A canonical feature set, <i>catch22</i>	155
5.2.2.5	Computation time and complexity	160
5.2.2.6	Performance comparison	161
5.2.2.7	Case studies: feature- vs shape-based representations	163
5.2.2.8	Informative features provide understanding	165
5.2.3	Discussion	166

5.2.4	Appendix	170
5.2.4.A	Time series for computation time evaluation	170
5.2.4.B	Manually replaced features	171
5.3	Conclusion on feature-based time-series analyses	171
6	Conclusion	173
6.1	Summary of thesis achievements	173
6.2	Future Work	175
	Bibliography	179

List of Tables

2.1	Axon types and where they are found in the PNS	14
3.1	Conductivities of different tissues contained in the simulated peripheral nerve . . .	48
3.2	Rat vagus nerve axon parameters (count, diameter distribution)	56
3.3	Quantitative comparison between experimental and simulated CAPs	57
3.S1	Parameters of the potential transfer function for cuff media	71
4.1	Decoder Performance in RMSE \pm cross validation standard deviation (cm H ₂ O) .	80
4.2	Surrogate bladder neurons	87
4.3	Identified bladder units across trials	92
4.4	Activity clusters vs fibre types	92
4.5	Decoding errors with and without cell loss	98
4.S1	Detailed compairson of activity clusters and fibre types	102
4.S2	Fractional redundancy between types	103
4.S3	Joint mutual information of fibre type average firing rates	103
4.S4	Joint mutual information single fibres	103
5.2.1	Diversity of <i>catch22</i> feature performances	157
5.2.2	The 16 features of <code>tsfeatures</code> used for classification.	158
5.2.S1	40 empirical time series selected for evaluating the computation times of features.	170
5.2.S2	Manually exchanged features	171

List of Figures

2.1	Overview of the peripheral nervous system	10
2.2	Visceral afferent nerves	11
2.3	A peripheral nerve and its fascicles	12
2.4	Types of recording electrodes	19
2.5	Examples of peripheral nerve recordings	20
2.6	Different pre-processing methods depending on SNR	28
3.1	Experimental recording setup in rat for simulation validation	39
3.2	Flowchart of PyPNS's internal information flow	41
3.3	Parameter-extrapolation of McIntyre's myelinated axon model	42
3.4	Axon segments can be interpreted as current point sources	44
3.5	The impact of the longitudinal profile $\phi_{\text{SFAP}}(z)$ on SFAPs	46
3.6	A circularly symmetric geometry makes potential field import possible	49
3.7	Unmyelinated axon membrane current is smoother than myelinated	52
3.8	Comparison of the longitudinal potential profile of different media	52
3.9	Influence of the extracellular space on unmyelinated and myelinated SFAPs	54
3.10	Unmyelinated and myelinated axons have different ideal cuff lengths	55
3.11	Comparison between experimental and simulated CAP: time domain	58
3.12	Comparison between experimental and simulated CAP: frequency domain	59
3.13	Fluorescence microscopy images of the mouse sciatic and vagus nerve	60
3.14	The axon placing algorithm result	60
3.15	Susceptibility of SFAPs towards tortuosity	62
3.16	Extracellular activation of tortuous axons	64
3.S1	Relation between angle- and direction-change-distributions	70
3.S2	Analytic transfer function between current and extracellular potential	70
4.1	Cystometrogram and information spectrum	76
4.2	Piecewise linear fit between bladder pressure and pelvic nerve activity	78
4.3	Nonlinear relation between nerve activity and bladder pressure	79
4.4	Optimal Linear Filter coefficients	80
4.5	PGE2 causes underestimation of bladder pressure	81
4.6	Types of bladder neurons	85
4.7	Finite sampling bias in MI calculation vs #samples	89
4.8	Activity cluster example	91
4.9	Information theoretic analysis of <i>in vivo</i> data	93
4.10	Information theoretic analysis of surrogate data	95
4.11	Bar diagram of decoding errors	98
4.S1	Redundancy with respect to pressure derivative, <i>in vivo</i> data	104
4.S2	Redundancy with respect to high-pass filtered pressure, surrogate data	104
5.1.1	Principle of unsupervised detection of main characteristics	109
5.1.2	High- and low-dimensional parameter spaces	111
5.1.3	Non-linear dimensionality reduction can disentangle complex point clouds	113

5.1.4	Example signals with different firing characteristics	115
5.1.5	Measurement space examples	117
5.1.6	Feature-parameter correlations	118
5.1.7	Case study 1: Van der Pol oscillator	120
5.1.8	Example projections in 1D, 2D, and 3D	122
5.1.9	Case study 2: peripheral nerve	125
5.1.10	Robustness against noise and feature-removal	126
5.1.11	Estimated dimensionality	128
5.1.12	Parameter reconstruction across all synthetic systems	129
5.1.13	Case study 3: fly movements	131
5.1.14	Methodological comparisons	134
5.1.15	Number of required features and time series	135
5.1.16	Performance in dependence of SNR, signal length, sampling rate	137
5.1.S1	Number of highly correlated features vs parameter reconstruction performance . .	139
5.2.1	Selection pipeline for generating condensed feature sets	149
5.2.2	Combining normalised feature-accuracies across tasks	153
5.2.3	Selecting single features from a few clusters	154
5.2.4	Performance comparison full feature set vs <i>catch22</i>	155
5.2.5	Performance comparison to <i>tsfeatures</i>	159
5.2.6	<i>catch22</i> feature performance across all tasks	160
5.2.7	Comparison to benchmark classification methods	162
5.2.8	Case studies: <i>catch22</i> vs benchmark methods	164
5.2.9	Two dimensional feature-spaces provide an understanding	166

Chapter 1

Introduction

Much of today's medicine can be classified as 'molecular': chemicals are administered to the patient that target certain receptors, influence organ function, kill intruding bacteria, etc. This dominant mode of treatment is powerful and proven, but is also known to generate side effects due to poor effect localisation, does not adapt dynamically to changing physiological conditions and is often unsuitable for chronic diseases (Stöllberger et al., 2009; Barber et al., 2004; Martel et al., 2015). Continued medication increases tolerances and aggravates side effects and patients often do not adhere to the prescribed intake (Barber et al., 2004; McCracken et al., 2006; Al Qasem et al., 2011).

In recent years, an alternative route to treating especially chronic diseases has attracted interest and capital: so called bioelectronic medicines (Birmingham et al., 2014; Waltz, 2016) attempt to harness the existing control loops of the peripheral nervous system (PNS) and treat diseases by means of peripheral electrical neuromodulation. Such implanted devices that interact with nerves are very closely related to well-known active implants such as pacemakers for the heart or deep brain stimulation in the central nervous system against the symptoms of Parkinson's disease (Benabid et al., 2009), but tackle the much larger class of non-neurological conditions (Luan et al., 2014). Like these known devices, they constitute a potentially permanent, localised treatment and might form a complement or even a replacement for classical molecular medicines in numerous conditions ranging from hypertension to rheumatism.

Already today, commercial bioelectronic medicines devices exist that predominantly target the vagus nerve (e.g., by SetPoint, LivaNova). Vagus nerve stimulation has proven useful in the treatment of

diverse conditions such as rheumatoid arthritis (Andersson and Tracey, 2012; Koopman et al., 2016) and sepsis (Cohen et al., 2015), refractory epilepsy (Milby et al., 2010), Alzheimer’s disease (Sjogren et al., 1997), anxiety (George et al., 2008), obesity (Krzysztof et al., 2011; Gautron et al., 2015; Apovian et al., 2017), chronic heart failure (Rousselet et al., 2014), hypertension (Sevcencu et al., 2018; Sevcencu and Struijk, 2018; Carnevale et al., 2016; Plachta et al., 2014) and to evoke anti-inflammatory effects (Meregnani et al., 2011; Borovikova et al., 2000). Other locations of intervention such as the hypoglossal nerve against sleep apnea (Malhotra, 2014; Strollo et al., 2014; Woodson et al., 2018), the pelvic, pudendal, and spinal nerves for incontinence (Kent and Grill, 2013; Mendez and Sawan, 2014; Chew et al., 2013), sympathetic pathways against hypertension (Gassler and Bisognano, 2014; Lohmeier and Hall, 2019) (commercialised by CVRx), or carotid sinus nerve for diabetes type 2 (Sacramento et al., 2018; Cracchiolo et al., 2019; Yin et al., 2019) are being actively explored.

1.1 Motivation

Even though the field is blossoming, most current bioelectronic medicines devices still operate in a simple open-loop fashion that is independent of changes in the physiological processes they try to influence and simply overwrite any existing activity on the nerve by stimulation or block rather than finely modulating it. In the future, peripheral neuromodulation devices are expected to become more advanced and include real-time feedback about current organ and nerve states (Bouton, 2015, 2017). By only blocking or stimulating when necessary, closed-loop devices can be much more efficient and effective (as shown in the central nervous system (Rosin et al., 2011)), and even capable of dynamically managing conditions, e.g., detecting parasympathetic bronchoconstriction in asthma and suppressing it (Lewis et al., 2006).

To close the loop and implement feedback control, physiological quantities of interest may be measured by chemical, mechanical, or other sensors that are implanted in addition to the nerve interface (Majerus et al., 2017; Karam et al., 2016; Cao et al., 2013; Schwartz et al., 2001; LaFleur and Yager, 2013; Mehrotra, 2016; Peh et al., 2018). While this approach seems straightforward from an engineering point of view, surgery becomes more difficult and the probability of complications (e.g., device movement, tissue damage, loss of signal (Majerus et al., 2017; Mendez and Sawan, 2014)) post surgery rises. An alternative approach is to harness, where possible, the body’s own sensors for

monitoring and control of organs. Thousands of afferent fibres continuously transmit signals about organ physiological state. These existing biological sensors are sensitive and may offer a stable source of organ state information as an elegant alternative to implanted artificial sensors. It was thus one of the main motivating ideas behind the work presented in this thesis to exploit the body's own monitoring system for the creation of nerve-based feedback about organ states to bioelectronic medicines.

1.2 Objectives

To enable neural feedback for closed-loop neuromodulation, we explored different aspects of the highly interdisciplinary research area at the interface of electrical device engineering, signal processing, software engineering, biology, translational medicine and certainly other disciplines that is neurotechnology.

- In order to support our work and in general research in the field, we want to propose easy-to-use simulation tools from which we can quickly generate accurate surrogate data. We want to validate these models and use them for our algorithm development.
- We envisage to propose decoding algorithms for experimentally obtained data that can estimate organ function based solely on recorded nerve activity. Ideally, these algorithms should be adapted to different recording resolutions available today – and perhaps tomorrow – and find new ways of exploiting the recorded signals. We aim at developing decoders that are real-time suitable, robust against noise and changing recording conditions and energy-efficient. Where possible, we would like to propose informed decoders that build on an understanding of the encoding principles used by the body. Through this work, we hope to inspire next generation decoders for bioelectronic medicines.
- Having a particularly rich library of global time series features at our disposition, we aim at exploring ways of analysing peripheral nerve activity from a new perspective: namely by characterising the continuous waveform of the recorded nerve activity without trying to identify single units or recurring events by the waveform shape (spike sorting). We hope that feature-based representations of peripheral nerve recordings will be useful in characterising low-resolution recordings.

1.3 Contributions

The main individual contributions of the presented thesis to the field of bioelectronic medicines can be divided into the three areas (1) decoding on *in vivo* data, (2) simulation, and (3) feature-based firing characterisation.

In the first, empirical component, *in vivo* peripheral nerve recordings of bladder afferents were analysed in terms of decoding possibilities and physiological encoding strategies. We based this research on two datasets in which afferent peripheral nerve activity was recorded from bladder neurons alongside bladder pressure. In a first low-resolution dataset acquired from the rat pelvic nerve using a hook electrode, we selected informative frequency bands and constructed a decoder based on a linearisation of the nonlinear relationship between the pre-filtered nerve activity and pressure. We could faithfully decode bladder pressure in a way suitable for real-time implementation in a bioelectronics medicine device equipped with a common low-resolution interface. Linearisation is key to avoid more complex decoders, a principle readily transferable to decoding from other sensory populations. In a second dataset, recordings were obtained at a much higher degree of detail using microelectrode arrays in the dorsal root ganglion of cats. This enhanced resolution did not only allow a *decoding* of bladder pressure, but let us investigate the *encoding* of this quantity by the population of sensory neurons. We identified stereotypical fibre response types, quantified their interaction using information theory, and drew parallels to other sensory populations in the periphery. Based on the encoding analysis, we proposed an informed decoding method that summarises the population activity in a low-dimensional population vector and is accurate, robust against cell-loss, and offers means of automatic re-calibration. We therefore make a first step towards peripheral nerve decoding methods tailored to the physiological encoding principles and demonstrate the advantages of this approach.

As a tool to test signal processing algorithms without *in vivo* data, we developed a Python-based simulation module, PyPNS, in which a peripheral nerve with arbitrary number of myelinated and unmyelinated fibres can be stimulated and recorded *in silico*. The simulator is innovative in its incorporation of voltage distributions from finite element models (FEM) that enable a both efficient and accurate computation of extracellular potentials from current sources in inhomogeneous media. It further contains the functionality to automatically generate tortuous axons with geometrical properties fit to imaged data to represent single fibres more realistically. In the present work, PyPNS was

used to generate surrogate data for signal processing algorithms but it is of wider use for the bioelectronic medicines community in investigating stimulation efficiency of different electrode geometries and currents and to aid the design of recording electrodes.

In a third contribution to the field, we developed feature-based signal processing methods to summarise peripheral nerve activity (and other time series) in a low-dimensional vector of key dynamical properties. For two separate methods, we leveraged decades of multidisciplinary time-series analysis condensed in the Highly Comparative Time-Series Analysis (*hctsa*) toolbox, a comprehensive collection of over 7 500 global time-series features. As a first contribution, we constructed a feature selection pipeline for the generation of informative, low-dimensional property-spaces tailored to collections of classification problems and demonstrated its utility on diverse real-world datasets. As a second method, we applied dimensionality reduction in the high-dimensional feature space to (1) automatically infer the low-dimensional dynamical variation across time series of a given dataset and to (2) select single efficiently implementable estimators for these main varying dynamics. For peripheral nerves, these captured dynamics are firing characteristics that change during long recordings as acquired by e.g., a chronic implant. Quantifying these relevant signatures in a low-dimensional feature vector can form a key step to pre-process peripheral nerve activity on-line in an implanted bioelectronic medicines device – as a basis for decoding, to detect unusual activity, etc. Looking beyond the scope of bioelectronic medicines, inference of low-dimensional structure in time-series datasets by the time series' dynamics has a much wider application and is a highly relevant task given the ever growing body of sequential data acquired across science and industry. We tackle this task here for the first time thanks to the availability of a sufficiently large feature set and demonstrate the utility of our approach on diverse synthetic systems, a real-world dataset, and on simulated peripheral nerve recordings obtained from PyPNS.

1.4 Publications

Journal papers

Lubba, CH, Le Guen, Y, Jarvis, S, Jones, N S, Cork, S C, Eftekhari, A, Schultz, SR (2018). PyPNS: Multiscale simulation of a peripheral nerve in Python. *Neuroinformatics*, 17(1), pp. 63-81.

Contributions: software development (starting from previous work by YLG but rewriting and extending substantially), model validation, simulation studies, manuscript writing

Lubba, CH, Sethi, SS, Knaute, P, Schultz, SR, Fulcher, BD, Jones, NS (2019). *catch22: CAnonical Time-series CHaracteristics*. *Data Mining and Knowledge Discovery*, 33(6), pp. 1821-1852.

Contributions: part of the selection pipeline development (based on previous works by SSS and PK), performance evaluation, feature implementation in C and wrapping, manuscript writing together with BDF

Fulcher, BD, Lubba, CH, Sethi, SS, Jones, NS. *CompEngine*: a self-organizing, living library of time-series data. (*submitted*)

Contributions: *catch22* feature-space, clustering analysis, manuscript editing

Lubba, CH, Ouyang, Z, Jones, NS, Bruns, TM, Schultz, SR. Bladder pressure encoding by near-independent fibre subpopulations - implications for decoding. (*submitted*)

Contributions: data analysis of spike-sorted data, literature research, surrogate data generation, decoding study, manuscript writing

Fulcher, BD*, Lubba, CH*, Gilestro, G, Schultz, SR, Jones, NS. Inferring low-dimensional parametric variation underlying time-series datasets. (*to be submitted*)

Contributions: data generation, analysis including exploration of various methodological optimisations, in-depth analysis of the method's performance, figure generation, part of manuscript writing

Conference papers

Lubba, CH*, Mitrani, E*, Hokanson, J, Grill, WM, Schultz, SR. (2017) Real-time decoding of bladder pressure from pelvic nerve activity, *2017 8th International IEEE/EMBS Conference on Neural Engineering (NER)*, pp. 617–620.

Contributions: part of the decoding analysis (correcting the groundwork of EM), manuscript writing

together with SRS

Lubba, CH, Fulcher, BD, Schultz, SR, Jones, NS. (2019) Efficient peripheral nerve firing characterisation through massive feature extraction. *2019 9th International IEEE/EMBS Conference on Neural Engineering (NER)*, pp. 179–182.

Contributions: data generation, data analysis, manuscript writing

1.5 Organisation of this thesis

In the Background chapter (Ch. 2) following this introduction, we give an overview of the anatomy of the peripheral nervous system, review encoding hypotheses, recording techniques, and decoding methods, and provide a historical and technical context for peripheral nerve simulations. We then move on to our simulation software PyPNS in the Simulation chapter (Ch. 3) that forms an engineering contribution to the field and helped us generate surrogate data to test algorithms. Chapter 4 on decoding presents the two studies of *in vivo* data acquired from the rat and cat bladder afferents. We present two different decoding methods tailored to the recording resolutions of the respective datasets and a study of the encoding of bladder pressure by a population of afferent fibres. Finally, in chapter 5, we describe our feature-based time-series analyses: an unsupervised method to infer low-dimensional variation of time-series dynamics and a supervised selection pipeline to generate feature subsets. Chapter 6 summarises the thesis achievements and provides an outlook.

Chapter 2

Background

I here provide the context of my work in terms of the anatomy of the peripheral nervous system (Sec. 2.1), its design constraints (Sec. 2.2), encoding hypotheses (Sec. 2.3), recording interfaces (Sec. 2.4), and decoding methods (Sec. 2.5), and simulation techniques (Sec. 2.7). We spot gaps in the current state-of-the-art knowledge and technology and position our presented contributions within their respective area.

2.1 The peripheral nervous system

The following gives a brief primer on the biological background of this work – the anatomy of the peripheral nervous system (PNS). Much of this section is established ‘textbook knowledge’ and can be re-read in standard literature such as ‘Essentials of Medical Physiology’ by Sembulingam (2012) or ‘The Integrative Action of the Autonomic Nervous System - Neurobiology of Homeostasis’ by Jänig (2006) for a more in-depth collection of observations.

2.1.1 Organisation

The PNS can be understood as the interface between the central nervous system (CNS; brain and spinal cord) and the organs. Its main parts are displayed in an organogram in Fig. 2.1. We can distinguish the somatic and the autonomic nervous system (ANS). The somatic nervous system transports

motor commands in its efferent (CNS → organs) part and sensory feedback in its afferent (organs → CNS) part that can be consciously controlled and perceived. It passes via the spinal and cranial nerves. The ANS, on the other hand, is composed of the efferent and afferent pathways that enable the unconscious and involuntary regulation of body functions like blood pressure and digestion, often through reflex centers in the spine. Literature usually distinguishes two efferent divisions of the ANS: the sympathetic and the parasympathetic system that are thought to have opposing effects on the body and promote either an active or a resting state (Langley, 1921). Parasympathetic innervation mainly passes via the cranial nerves (III, VII, IX, and X). Most prominently the vagus nerve (X) contains approximately 75% (McCorry, 1964) to 80% (Berthoud and Neuhuber, 2000) of all parasympathetic fibres. Other than that, some parasympathetic fibres projecting to the colon, bladder and genitals exit the sacral spinal cord (Feher, 2012). All parasympathetic neurons synapse once in localized ganglia close to the target organ. Sympathetic neurons exit the spinal cord from T1 to L2 to synapse in either the paravertebral ganglia to both sides of the spinal cord, one of the three prevertebral ganglia in the abdomen (celiac, superior mesenteric or inferior mesenteric ganglion) or the adrenal medulla. They group into so called splanchnic nerves on their way to the organs. The synapsing of both efferent autonomic divisions, before reaching their target, has several advantages. It enables divergence (few → many fibres) to different degrees (1:1 – 1:200) (Wang et al., 1995) with a varying ‘neural unit size’ (Johnson and Purves, 1981; Purves et al., 1986) that amplifies the influence of a single preganglionic fibre¹. Also, short reflex arcs might close in the ganglia for certain subsystems and be gated by central inputs (Clerc and Niel, 1993) and pattern generators might exist in the ganglia (Gola et al., 1992). As cells outside the central nervous system are exposed to endocrine messengers (no blood-brain-barrier), the synapsing cell pools outside the CNS might be able to integrate these inputs (Browning and Travagli, 2014). Afferent autonomic nerves are called ‘visceral sensory’. Their pathways are displayed in Fig. 2.2 and are usually paired with the mainly sympathetic (efferent) splanchnic nerves with cell bodies in the dorsal root ganglion next to the spine. Some pass through cranial nerves (e.g., vagus nerve). One additional division of the PNS exists that is sometimes referred to as part of the ANS: the enteric nervous system. It controls the gastrointestinal tract and is the only part of the peripheral nervous system that contains a considerable amount of neural circuits (Furness, 2007; Wood, 2008).

¹The opposite mechanism of a convergence and integration of inputs is unlikely as usually very few preganglionic fibres dominate (Jänig, 2006; Lichtman, 1977).

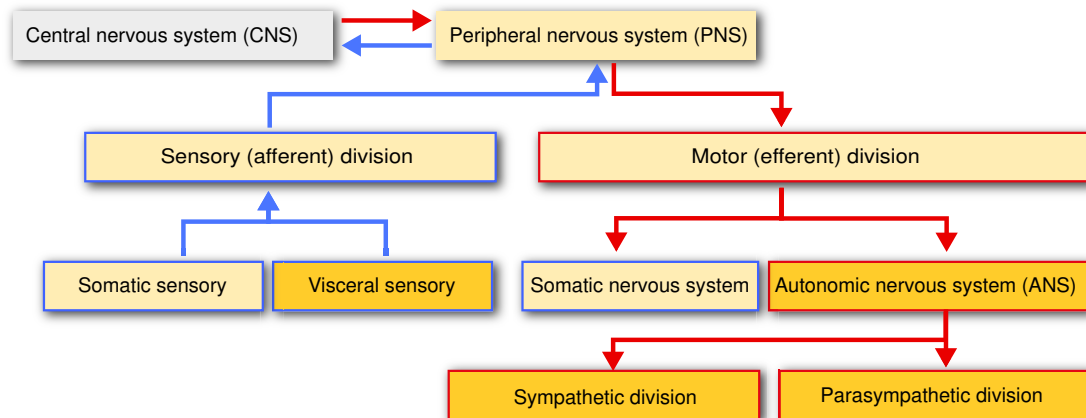


Figure 2.1: The main divisions of the peripheral nervous system. Autonomic parts are highlighted.

Among these different divisions, some parts of the PNS present especially promising intervention sites for bioelectronic medicines. For the neuromodulation step (stimulation or block), the efferent autonomic division (and the enteric nervous system) is an appropriate target. As the ANS is involved in the control of diverse physiological states by a complex network of pathways (e.g., heart rate, inflammatory responses, blood pressure, gland secretion, etc), a corresponding wealth of effects can be achieved by intervening at the right site. As some of the important resting and healing functionalities (Tracey et al., 2009; Sundman and Olofsson, 2015) are mediated by a large cranial nerve, the vagus nerve, this particular stimulation site has received major attention in the past years. As about 90% of the axons contained in the vagus nerve are afferent (Cramer and Darby, 2013), afferent pathways might form an important target as well and single very effective afferent neurons to trigger reflex arcs have been identified for e.g., the lung (Chang et al., 2015). Due to a higher variability of the pathways of smaller nerves and a higher difficulty to build interfaces, current bioelectronic medicines are limited to larger nerves. Future systems are expected to build on next generation electrode techniques and a more detailed knowledge of the peripheral pathways (through mapping studies like the ones conducted by Hammer et al. (2018) and Saylam et al. (2009)), including the identification of regions of low inter-subject variability. Only then, interfaces with smaller nerves that carry signals to a single organ can be reliably formed to enable a more finely controlled and more localised neuromodulation. This important area of research will not be touched by the work presented in this thesis.

For the purpose of implementing nerve-based feedback and creating closed-loop bioelectronic medicines

without additional sensors, organ states need to be estimated on-line from nervous activity.² Here, the sensory populations that innervate organs provide an obvious target. Both the visceral sensory and somatic sensory fibres transport rich information about the current physiological state and can, once recorded and interpreted appropriately, from a very precise, sensitive feedback. See Fig. 2.2 for an overview of the afferent pathways.

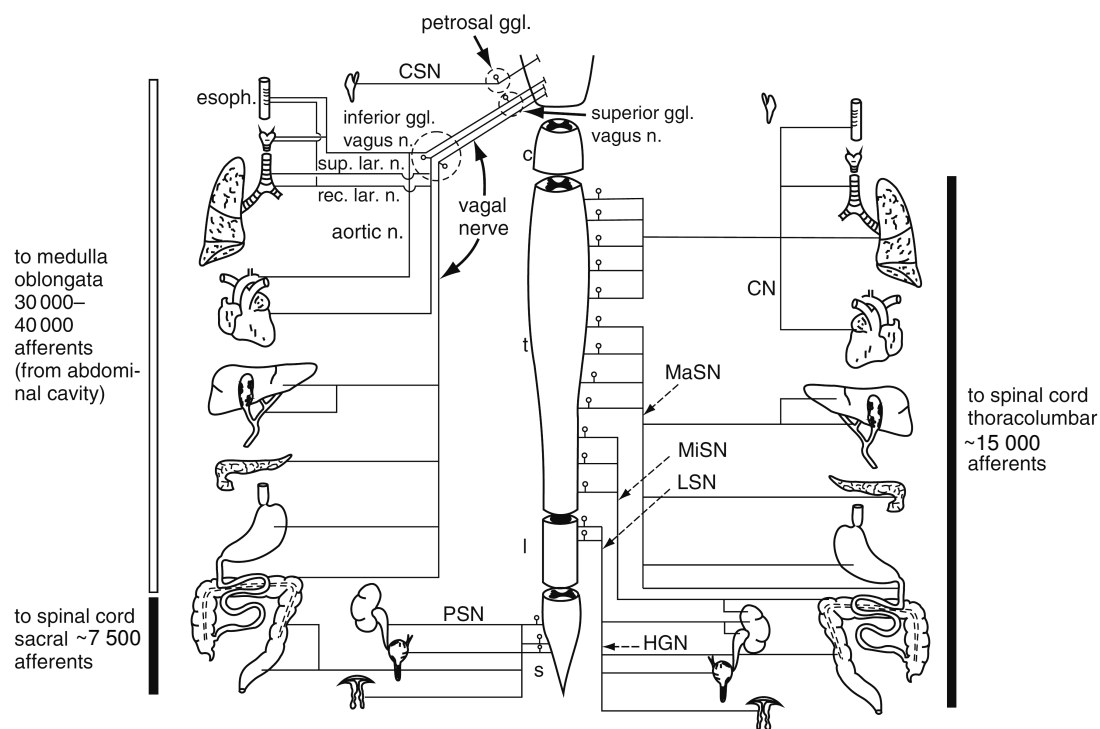


Figure 2.2: Pathways of the afferent visceral nerves. Adapted from (Jänig, 2006, p.40). NTS: nucleus tractus solitarius, PNS: pelvic splanchnic nerve, CNS: carotid sinus nerve, CN: cardiac nerves, HGN: hypogastric nerve, LSN: lumbar splanchnic nerve, MaSN: major splanchnic nerve, MiSN: minor splanchnic nerve, sup./rec. lar. n., superior/recurrent laryngeal nerve; ggl., ganglion; c, cervical; t, thoracic; l, lumbar; s, sacral

2.1.2 Peripheral nerves

Peripheral nerves bundle and protect the long peripheral axons and form routes between the CNS and the organs. See Fig. 2.3 for an overview of their components. Larger nerves that supply multiple targets are subdivided into so called fascicles, separate subpopulations of axons. Three distinct sheaths support the nerve. The endoneurium fills the space between axons in one fascicles, the perineurium surrounds the fascicle, and the epineurium embraces the whole nerve.

²The alternative methods to estimate organ states using additional sensors mentioned in the introduction (Ch. 1) will not be a topic in this thesis.

To form interfaces with peripheral nerves, their organisation poses some challenges for bioelectronic medicines. The thick protective layers both attenuate stimulation pulses into the nerve and silence extracellular potential changes caused by axonal firing. Moreover, the combination of many fascicles and many more axons ($>10\,000$) to a single nerve complicates selective recording and stimulation without an invasive interface (Navarro et al., 2005; Spearman et al., 2018).

Important peripheral nerves that have received a lot of attention in neuromodulation research are the somatic sciatic nerve innervating the leg for limb movements (Citi et al., 2008; Raspopovic et al., 2011) (27 000 fibres in rat (Schmalbruch, 1986)), the vagus nerve as one of the main pathways of the parasympathetic system for a variety of effects (Gayet and Guillaumie, 1933; Tracey et al., 2009; Guiraud et al., 2016) ($\sim 80\,000$ fibres in humans (Shimizu et al., 2011), $\sim 20\,000$ in rat (Prechtl and Powley, 1990)), and the pelvic and pudendal nerves for bladder control (Chancellor and Chartier-Kastler, 2000).

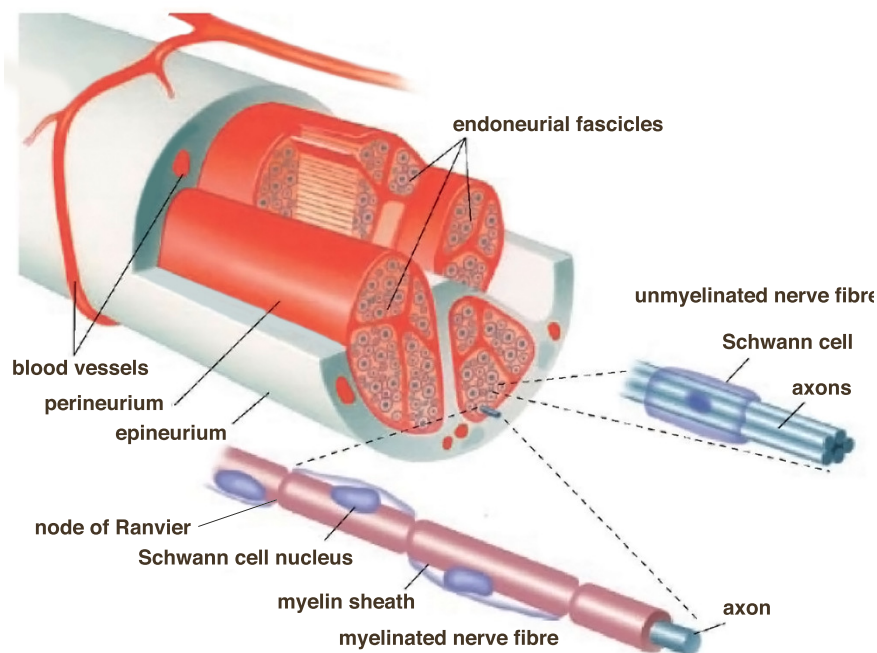


Figure 2.3: A peripheral nerve and its fascicles. Adapted from (what-when-how.com).

2.1.3 Axons

Reaching down to the single cell level, neurons (e.g., afferent sensors) transport information by single action potentials (APs), localized increases of the membrane voltage (depolarisations), that propagate along the terminal extension of the neurons: axons. Since the axon's cytoplasm (called axoplasm)

has a resistance which, combined with the membrane capacitance, is too high for a purely passive conduction over long distances (as would be possible e.g. in a metal cable), the APs are amplified and renewed along the way by voltage gated ion channels: when the membrane voltage is increased above a threshold, specialised sodium-channels open in order to let positive charge enter the cell and further increase the potential difference between inside and outside, afterwards opening potassium channels lead to a re- and hyperpolarisation. Two main axon types and respective ion channel distributions exist. ‘Unmyelinated’ axons express the relevant channels in an approximately uniform manner over their entire cell membrane. Thereby, passive conduction is reduced to a minimum. This mode of conduction is simple but comparably slow and consumes much energy (Neishabouri and Faisal, 2011). As an alternative, ‘myelinated’ axons enable a piecewise passive conduction by the use of an insulating layer on the membrane that reduces membrane capacitance. Schwann cells produce a myelin sheath around the axon (equivalent to oligodendrocytes in the central nervous system). Channels can then be omitted in the myelinated sections of the axon and concentrated at the nodes of Ranvier where the cell membrane is exposed to the intercellular space. See Fig. 2.3. Depolarisation ‘jumps’ (‘saltatory conduction’) from node to node and as an effect, both conduction velocity and transmission efficiency rise dramatically. In addition to the higher conduction velocity at a given diameter, the scaling of conduction velocity with axon diameter is more favourable in myelinated axons (linearly) compared to unmyelinated axons (proportional to the square root of the diameter) (Waxman, 1980). Thicker axons ($>1\ \mu\text{m}$) are therefore exclusively myelinated (Snaidero and Simons, 2014). Thick ($10\ \mu\text{m}$) myelinated fibres reach conduction velocities of about $100\ \text{m/s}$ (Waxman, 1980), unmyelinated thin fibres stay below $1\ \text{m/s}$ (e.g., $0.4\ \mu\text{m} \rightarrow 0.28\ \text{m/s}$ (Sundt et al., 2015)).

In Tab. 2.1, typical diameters found for different pathways are shown. The thickest, and therefore fastest axons are used for the transmission of motor commands to skeletal muscle and sensory feedback from muscle spindles. Postganglionic efferent autonomic nerve fibers are not myelinated and transmission is slow. Many peripheral fibres fire at very low rates, as expected from their small diameter (Perge et al., 2012). Typical single efferent sympathetic fibres stay below $3\ \text{s}^{-1}$. To give a few examples: sudomotor (to sweat glands) $0.2\ \text{s}^{-1}$ (Jänig and Kümmel, 1977); pilomotor (to hair) $0.6\ \text{s}^{-1}$ (Macefield et al., 1994, 1999); preganglionic skeletal muscle vasoconstrictor (MVC) fibres stay at higher resting rates of $1.8 \pm 1.3\ \text{s}^{-1}$, postganglionic $0.5 - 3\ \text{s}^{-1}$ (Jänig, 1988); renal nerves (rabbit) 2 -

2.5 s^{-1} depending on anaesthetics (Dorward et al., 1987); renal and splenic nerves (cat) $1.2 \pm 0.2 \text{ s}^{-1}$ (Meckler and Weaver, 1988).

Fiber Types	Name	Subtype	Diameter (μm)	Conduction Velocity (m s ⁻¹)
Myelinated				
Somatic Afferent				
Cutaneous	A	β	8–12	40–75
		γ	4–8	15–40
		δ	1–4	5–15
Muscle	A	α	12–21	75–120
		β	8–12	40–75
Somatic Efferent				
Muscle	A	α	12–21	75–120
		γ	4–8	15–40
Autonomic Efferent				
Preganglionic efferent	B		1–3	3–14
Unmyelinated				
Somatic Afferent				
to dorsal root ganglion (pain)	C		0.1–1	0.2–2
Autonomic Efferent				
Postganglionic efferent	C		0.1–1	0.2–2
Sensory Receptor				
Hair follicle	Aβ			
Skin follicle	Aβ			
Muscle spindle	Aα			
Joint receptor	Aβ			
Pain, Temperature	Aδ, C			

Table 2.1: Axon types and where they are found in the PNS (Smith, 2006; Mann, 2019)

Forming interfaces with the very thin unmyelinated fibres that are responsible for the autonomic peripheral signalling is one of the challenges in bioelectronic medicines. These fibres only provoke rare (see above) and small extracellular potentials (in the order of μV (Spearman et al., 2018)) and are therefore difficult to separate from background noise and artefacts caused by other electrical sources, complicating any recording. C-fibre activation thresholds are furthermore high (Sdrulla et al., 2015), making stimulation more energy-intensive compared to myelinated fibres. This core challenge of the interface development for bioelectronic medicines will not be touched by the contributions of this thesis. It will, however, surface again as a limiting factor for signal processing algorithms (see Sec. 2.4 and 2.5.2) that generally have no access to detailed information about the population activity.

2.2 Engineering principles of peripheral nerves

Before going on to the observed encoding on peripheral nerves (Sec. 2.3) and artificial interfaces with the peripheral nervous system in Sec. 2.4, we want to take a more abstract perspective of the PNS as an engineered communication system here to understand its design better. In any nervous system, there is an undeniable interplay between the information processing functionality (including an encoding strategy) and the physical implementation of this function – axon diameters used, locations of major neuron pools, etc. In the CNS, the evolution of this design could purely be guided by the energy efficiency of information processing (Sterling and Laughlin, 2015). Taking this perspective, a fundamental trade-off has been identified between energy-consumption and information transmission capacity for different axon dimensions (diameters, length) (Sterling and Laughlin, 2015; Perge et al., 2009, 2012). The higher the diameter, the higher the maximum firing rate and therefore information rate (French et al., 2001). As energy consumption rises quadratically with diameter and information rate only rises sublinearly (Sterling, 2014, p.53), a law of diminishing returns constrains axon dimensions and thin, short axons will be used wherever affordable. This concept can explain many design choices in the CNS such as the thick axons of the quick and precise vestibular system that fire at high rates and the thin olfactory axons where low firing and information rates are acceptable (Sterling, 2014, p.75) as well as minimizing ‘wire’ by grouping related areas close to each other.

In the PNS, axon length cannot be freely re-configured because pre-defined distances to organs have to be covered. Delay, in addition to information rate, becomes a crucial indicator for transmission performance of a nerve that improves with rising diameter. Nakahira et al. (2015) investigated the relation between delay, information rate and energy consumption for somatosensory control in the quantised and delayed channel that is a nerve and showed that at a given nerve diameter, different axon diameters suit different organ control requirements (speed vs accuracy trade-off). It is tempting to speculate that the modest control requirements of slow organs (high accepted lag, low required information rate) combined with energy constraints can explain the observed high number of slow, low diameter fibres that dominate the autonomic periphery which are low in their energy consumption and cause high delays. A stark contrast becomes visible when comparing to the thick and fast-conducting fibres used for the quick somatic control of muscles.

2.3 Physiological information transmission on peripheral nerves

We have briefly covered the organisation of the peripheral nervous system and the anatomy of peripheral nerves and axons and speculated what constraints may have guided its development. But what is the current knowledge about the communication principles on the nerves that we record from? How does the peripheral nervous system encode the information that it relays across the whole body? Answering this scientifically interesting question will be vital for bioelectronic medicines – to build informed decoders and to tailor neuromodulation interventions to the physiological communication on nerves.

We will almost exclusively cover sensory (afferent) encoding here. It is much easier to study than efferent pathways because the input can be measured and manipulated. Understanding the encoding of sensory information by afferent fibre populations can further enable informed decoders for bioelectronic medicines. A dominant encoding hypothesis in afferent encoding are so called ‘labeled lines’ (Donaldson, 1885). In this simple concept, each fibre conveys the scalar intensity of one quantity of interest (e.g., temperature at a specific skin area), independent of the activity of other fibres. Evidence for this encoding principle was demonstrated for the sensations of pain (Basbaum, 1991), taste (Barretto et al., 2015; Frank, 1973; Scott, 2004), touch (Jones and Smith, 2014), temperature (Donaldson, 1885; Gallio et al., 2011)) and others. It is therefore an established concept in peripheral sensory encoding. Still, the labeled line code is, to an extent, an oversimplification and more complex patterns across fibres were demonstrated that challenge the clean idea of ‘one-fibre-one-message’. Evidence suggests there exists ‘crosstalk’ between labelled lines (Ma, 2010): messages about a stimulus are not transported by each fibre independently, but as a group activity pattern resulting from the interactions between fibres. Similarly, relative codes were proposed early (Pfaffmann, 1959): single fibre activities might only transmit their respective meaning in relation to other fibre activities. Sensory receptors’ individual characteristics might combine in synergistic ways even without direct interaction as ‘diversity sweet spots’ to achieve high accuracy by a set of noisy sensors (Nakahira et al., 2019; Nakahira, 2019). Differently behaving cells as slow and fast reacting sensors have been reported for various sensory populations such as the colon (Blumberg et al., 1983; Jänig and Koltzenburg, 2017; Sengupta and Gebhart, 1994a), gall bladder (Foreman et al., 1986), the lung (slowly- and rapidly-adapting sensors) (Yu et al., 2017; Schelegle and Green, 2001; Coleridge and Coleridge, 2010; Kubin

et al., 2006), muscle spindles (Brown et al., 1965; Koeze, 1973) which may hint towards a separate encoding of stimulus time and intensity of the same quantity by distinct fibres within a population.

Another debated aspect of the coding across fibres (be it labeled lines or a more complex population code), is how single fibres encode intensity. Most often, a simple rate-code is assumed where firing rate equals encoded intensity (Adrian and Zotterman, 1926). Temporal coding by spike timing has, however, been demonstrated in taste (synchrony of fibres, onset- and tonic-fibres) (Hallock and Di Lorenzo, 2006), touch (gaps between bursts instead of rate code for frequency) (Saal et al., 2016; Birznieks and Vickery, 2017), and proprioception (50 ms precision of spikes) (DiCaprio et al., 2007). In touch, an ensemble of first activated sensors transmits complex information much faster than a rate code could (Johansson and Birznieks, 2004). In efferent branches, spike timing dependent coding for motor control was demonstrated as well (Srivastava et al., 2017). In the sympathetic nervous system, rhythms of different frequencies have been an established observation of much debate for a long time³ (Janssen et al., 1997; McAllen and Malpas, 1997) and might form part of an encoding strategy. These rhythms have been related to timing-dependent encoding hypotheses (Gilbey, 2001, 2007; Macefield et al., 1999) (timing relative to rhythm phase), but also control theory (Julien, 2006; Ringwood and Malpas, 2001). The higher efficiency of synchronised, grouped activation in bursts in releasing neurotransmitters (Birks, 1978; Hardebo, 1992) and reduce delay (Wallin et al., 1994) might explain their existence as well, or synchronisation might provide a means of binding different neuron pools across the body (Conway et al., 1995).

The exact intensity coding by single fibres in the periphery and the role of spike timing remains, just as the significance of rhythms and the employed population code, uncertain (Jänig, 2006) for both afferent and efferent pathways. Given the simplicity and the explanatory power for many sensory systems, we judge that an encoding by rate coded labelled lines is a reasonable first assumption and a hypothesis to challenge by observations. We also base our encoding study in section 4.2 on this encoding assumption.

Overall, there exists a mosaic of descriptive information on many peripheral subsystems that has been collected in biological studies which often put an emphasis on single cell responses and non-

³Different frequencies were observed: 0.1 – 0.4 Hz (Mayer-waves) (Janssen et al., 1997; Brown et al., 1994; Julien, 2006), the T-rhythm around 1 Hz (Chang et al., 1999), another ‘cardiac’ one in the range 2 - 6 Hz (Malpas, 1998; Janssen et al., 1997; Adrian et al., 1932), then a respiratory modulation of activity and a 10 Hz rhythm (Deuchars, 2015; Ootsuka et al., 1995; Chang et al., 1999) (or rather 6 - 20 Hz (Ninomiya et al., 1990)).

functional anatomy. Meanwhile, neuroscience of the CNS has for over 60 years focused on the function (information processing) of populations of neurons and has developed into a discipline empowered by numerous analysis tools. One of the most commonly used techniques is information theory, a useful model-free framework to uncover nonlinear interactions (Shannon, 1948; Cover and Thomas, 2005) and to capture the information content of spike trains, reducing dimensions (Kraskov et al., 2005), etc. Information theory is an especially promising tool for the investigation of sensory systems because of the known non-linearities including hysteretic behaviour (Ross et al., 2016) between the sensed quantity and the output of neurons. Methodologically grounded investigations of peripheral fibre populations using these tools might benefit our understanding of the peripheral nervous system if combined with carefully repeated, analysis-friendly experimental procedures. We might then not only challenge the simplifying dominant models of a labeled line code by rate-coded fibres with single contradictory observations, but propose alternative mechanistic encoding models that can then be exploited by informed decoding algorithms and stimulation protocols.

As a step towards principled investigations of the encoding strategies on peripheral nerves, we studied a model population of sensory fibres that monitor bladder pressure, see Sec. 4.2. We identified different fibre types and explained their individual and combined significance for information transmission using information theory. As a relevant result for bioelectronic medicines, we proposed an informed decoding scheme as mentioned again in Sec. 2.5.2 and covered in detail in Sec. 4.2.2.3.

Investigating the encoding is interesting as a scientific exercise and requires a high recording resolution that allows to differentiate single cells. But is this level of detail necessary for a decoder to work well? What resolution *can* be attained by today's interfaces and are there drawbacks in pursuing maximum recording detail? The next section will cover current recording techniques followed by decoding approaches at different resolutions.

2.4 Recording techniques

We are interested in artificial systems that interact with the peripheral nervous system, by both recording from it and modulating its activity. In the following section we give an overview of the existing interface technologies for recording, as relevant for decoders, in terms of their advantages and disad-

vantages including the aspects recording resolution and long-term stability.

Nervous activity can be monitored in various ways, e.g., by functional imaging of the neurovascular response (Engel et al., 1994), optogenetic methods (Nagel et al., 2002) (shown for the PNS (Fontaine et al., 2017; Anderson et al., 2018)), and electrical recording. For today's implementations of bio-electronic medicines, electrodes in close proximity to nerves are commonly used. These electrical probes record changes in extracellular potentials caused by action potentials of the nerve's axons. See Fig. 2.5 for two example recordings. The main difficulty in interfacing with the PNS lies in the fact that the axons are densely packed and protected by sheaths. At the same time, interfaces cannot afford to damage the nerve and are expected to keep a good signal quality over long time scales (years). With higher invasiveness, inflammatory response, foreign body reactions, and fibrous encapsulation of the implanted devices are a danger (Ward, 2008; Sheikh et al., 2015). Consequently, compromises on spatial resolution and signal-to-noise ratio are accepted in favor of mildly invasive interfaces. In the quest for a long-term stable interface with a good selectivity and signal-to-noise ratio, a large variety of electrode designs have been developed. Good reviews can be found in Navarro et al. (2005) and Spearman et al. (2018) and we provide an overview in the following.

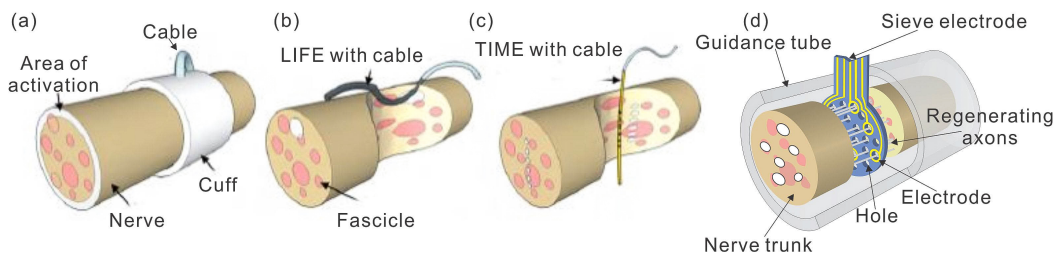


Figure 2.4: Different electrode types for PNS recording. Adapted from Rijnbeek et al. (2018).

The first, very important and widely used electrode design is the cuff electrode (Stein et al., 1975). It embraces a nerve in a circular manner by a non-conducting material, creating an insulation that amplifies the recorded voltage. Further advantages are the low invasiveness and therefore increased long-term stability (Romero et al., 2001; Struijk et al., 1999; Stein et al., 1977). Cuff electrodes possess qualities for stimulation as well, such as current steering (Tarler and Mortimer, 2004), field confinement (Navarro et al., 2005), and long-term stability (Christie et al., 2017). As the recorded activity must pass through all surrounding sheaths, especially the epineurium, and a multitude of enclosed axons contribute to the recording, signal-to-noise ratio remains low and differentiating fibres

is close to impossible (Navarro et al., 2005). Still, some structure such as short phases of high activity ('bursts', see encoding in Sec. 2.3) and low-activity phases can be distinguished in the processed signal, see Fig. 2.5.

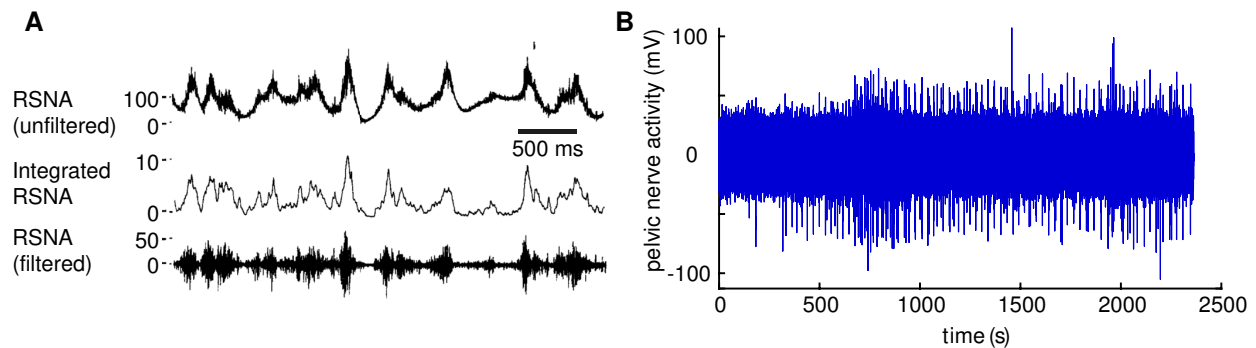


Figure 2.5: **PNS recordings are often noisy but still contain distinguishable activity phases.** **A** Microneedle recording from renal sympathetic nerves (renal sympathetic nerve activity, RSNA) in cats (McAllen and Malpas, 1997). **B** Hook in oil recording from the pelvic nerve in rats (Danziger and Grill, 2015).

As an alternative electrode design with a higher degree of invasiveness, intrafascicular electrodes can be inserted into the nerve fascicle (see Fig. 2.3 in Sec. 2.1.2 for fascicles). They enable a higher signal-to-noise ratio and selectiveness (Navarro et al., 2005) that makes it possible to differentiate single fibres. There exist transversal (TIME) (Boretius et al., 2010) and longitudinal intrafascicular electrodes (LIFEs) (Bowman and Erickson, 1985; Lawrence et al., 2004). In the scenario of a disrupted nerve, the very selective 'regenerative electrodes' are applicable. The growing nerves pass through holes in the electrode which can lead to a resolution at the single axon-level. An overview of these four classical electrode types is shown in Fig. 2.4. More exotic solutions like microchannel electrodes into which the teased nerve is fitted allow a similar resolution as regenerative electrodes from intact nerves (Chew et al., 2013). As an alternative to recording from axons, the cell bodies of sensory fibres in the dorsal root ganglion (DRG) can be targeted by microelectrode arrays. This approach allows for a high spatial resolution at increased signal strength from the cell bodies' activity (Bruns et al., 2011b) similar to the recordings in CNS at the cost of a lower, but still acceptable long-term stability (Khurram et al., 2017) despite tissue responses like inflammations and scar tissue provoked by penetrating interfaces (Christensen et al., 2016; Wurth et al., 2017).

A wealth of new interface technologies is being developed that explore different materials like carbon nanotubes (Gillis et al., 2018; McCallum et al., 2017; Yan et al., 2019a; Kostick, 2018; Patel et al., 2016) and graphene in general (Kostarelos et al., 2017), flexible and polymer (Stieglitz et al., 1997;

Rodríguez et al., 2000; Lee et al., 2017b,a; Sperry et al., 2018; Xue et al., 2015; Caravaca et al., 2017), and organic materials (Löffler et al., 2017; Lanzani, 2014). Adapted geometries like small diameter cuffs (Ordonez et al., 2014; Lissandrello et al., 2017), small needle interfaces (Yan et al., 2019b), and surface electrodes (Sperry et al., 2018) were proposed. Similarly, innovative recording techniques such as conduction velocity selective recording (VSR) (Metcalf et al., 2014; Taylor et al., 2015), battery-free ‘neural dust’ powered by ultrasound (Seo et al., 2016), bioimpedance tomography to selectively monitor fascicles (Aristovich et al., 2018) or even sensing of pH rather than electrical potentials (Cork et al., 2018) were proposed.

As can be seen, a diversity of peripheral nerve interfaces exists and novel ones are invented ‘by the minute’. Each of them will produce a different signal in terms of signal-to-noise ratio, spatial resolution, and dimensionality of the resulting signal. It is difficult to guess what electrode technology is the most promising and might dominate the area in the future. Surely, different interfaces will be applied to different nerves. Small nerves innervating a single target do not require a selective recording. For them we might still use rather simple cuff electrodes in the far future. For thicker nerves in which a recording has to differentiate the activity of fascicles or single axons, no optimal interface exists today. As a personal opinion, organic and soft materials that can penetrate the nerve without causing strong tissue reactions are probably the holy grail that neurotechnology is waiting for and that will significantly catalyse progress of the field. The next section will take a look at what decoding and pre-processing algorithms have been applied to each of the different recorded signals.

2.5 Decoding

By ‘decoding’, we mean the process of estimating a variable of interest from an observed process in which information is somehow *encoded*. For bioelectronic medicines, the observed process is a recorded population of axons that encode information in their firing patterns, and the quantity of interest is an organ parameter such as bladder fullness or level of bronchoconstriction.

In a scenario with a perfect measurement (no noise, infinite temporal and spatial resolution) and knowledge of the encoding principle of e.g., response to temperature changes of a population of sensory fibres innervating the skin (forward model), a decoding can easily be accomplished by building

the inverse relation. For peripheral nerve decoding, however, the reality is quite far away from this ideal case. The exact code of the spiking patterns by which the fibres transport their information is largely unknown (Sec. 2.3) and as detailed in section 2.4, differentiated recordings of every axon are furthermore impossible with current electrode technology. A decoder for our object of study will therefore need to interpret the imprecise signal obtained from the recording technique used in which many subtleties of the population activity are obscured.

2.5.1 Decoding from the central nervous system

Let us first take a look at the more established field of decoding limb movements from the motorcortex in the central nervous system (CNS) as a case study to draw parallels from, before covering the related work in the peripheral nervous system (PNS). In 1986, Georgopoulos et al. described the direction-encoding in the primary motor cortex M1 by a population of neurons that each represent a certain movement direction. Some 15 years later, in 2000, a brain machine interface (BMI) to move a virtual cursor ‘by thoughts’ has been demonstrated for the CNS (Kennedy et al., 2000) based on this groundwork using invasive electrodes. Decoding from the CNS typically involves the following steps. (1) Spike sorting (Rey et al., 2015): due to the high density of neurons in the cortex, electrodes record signals from multiple cells. Spike sorting associates each recorded spike to a certain neuron. See (Lewicki, 1998) for a review of early techniques. (2) Binning: for each neuron, its spikes are counted over a certain time interval. (3) Training: building the relationship between pre-processed recording (binned firing rates of the spike-sorted units) and observed movement by the decoder.

Based on the binned firing rates per spike-sorted unit, different choices can be made for the decoder that is often a multipurpose, off-the-shelf algorithm. The first decoding (as a demonstration for the encoding model), done by Georgopoulos et al. (1986), used the so called population vector (PV) approach where each neuron was assumed to encode one direction and was weighted by its firing rate for decoding. The weighted sum over all recorded neurons gives the ‘population vector’ as a decoded direction. Following work then proposed the optimal linear filter (OLE) method (Salinas and Abbott, 1994). While the PV-method assumes a uniform distribution of preferred directions, OLE can incorporate the correlation of neurons (Brockwell et al., 2004). OLE showed similar decoding performance to more complex decoders such as artificial neural networks (ANNs) (Wessberg et al.,

2000). In general, linear estimators were very successful in cortical decoding (Serruya et al., 2002, 2003; Hochberg et al., 2006; Collinger et al., 2013).

All described decoders so far base their state estimate on the current measurement only. This relationship between measurement and decoded state is normally called an ‘observation model’. The resulting estimates usually contain a few implausible outliers that can be removed afterwards by a smoothing in time (e.g., by a moving average filter). What these estimators lack, is a measure of plausibility of the next state given the current state. Every possible next estimate is assumed to have equal probability. More advanced, probabilistic estimators can integrate prior knowledge of the state evolution in their estimation process through the use of a ‘state model’. They are often called ‘Bayesian’ (Bayes, 1763; Barker et al., 1995; Brockwell et al., 2004; Thrun, 2002; Chen, 2013) due to their basic working principle, and substantial increases in decoding performance can be achieved in this way. In cortical decoding, Bayesian filters were realized as Kalman Filters (KF) (Wu et al., 2005; Li et al., 2009; O’Doherty et al., 2011; Yu and Yu, 2017) in different variants (Extended KF, Unscented KF (Thrun, 2002)) and Particle Filters (Brockwell et al., 2004) and achieved considerable increases in decoding performance. The sequential, recursive nature of these filtering techniques enables fitting to the highly nonlinear behaviour of neural systems in time (Brockwell et al., 2004). In fact it was found that tuning of the observation model only has a minor impact on decoding performance (Koyama et al., 2010); a good state model substantially improves it (Koyama et al., 2010; Wu et al., 2005; Yu and Yu, 2017). Moreover, the probabilistic nature of these estimators provides confidence intervals for estimated states. Still, there exist caveats to the Bayesian approach. The most commonly used Kalman filter requires system properties not necessarily fulfilled (Gaussian probability densities, linear models) and comes with a substantial computational complexity that remains a problem for closed-loop application (Li et al., 2009). This computational load mainly comes from the necessity to calculate multiple matrix multiplications per time step for state and observation model and correction. Particle filters overcome (Brockwell et al., 2004) the system requirements of Kalman filters, but only at the price of an even higher computational cost. New, even more advanced and consequentially more computational burdensome decoders, such as long short term memory (LSTM) neural networks, have shown promising results for movement decoding in CNS as well (Yousefi et al., 2019; Hosman et al., 2019).

Comparing the different decoding algorithms employed in the CNS, those decoders that incorporate

a state model (Kalman, particle) have clear benefits for the decoding accuracy but come at the cost of an increased computational burden. Even more complex decoders such as deep neural networks only achieve minor improvements and are much more expensive to run. If computing resources are a limiting factor (as in the case of implanted devices), the simple optimal linear estimator remains a good baseline approach that has proven successful for decades.

Most decoders for the CNS are trained on the firing rates of spike-sorted units recorded by micro-electrode arrays (MEA). As MEAs in the brain do not possess a high long-term stability (Biran et al., 2005), electrocorticography (ECoG) – electrodes placed on the surface of the brain – was proposed as a less invasive recording method with lower spatial resolution that only captures the continuous local field potential (LFP), no spikes. Decoders from this low-resolution signal were demonstrated (Zhuang et al., 2010; Flint et al., 2012; Stavisky et al., 2015). Using e.g., Kalman-filters or recurrent neural networks, such as LSTMs, decoding performance from ECoG recordings can be almost as accurate as decoders trained on sorted spikes (Ahmadi et al., 2019). As noted above, these complex decoders are computationally expensive, however. Observing activity at a reduced level of detail can have advantages for the long-term stability of the recorded signal, in addition to the reduced tissue response of less invasive electrodes. It has been demonstrated that coarser wavelet features, rather than spike-sorted units, have promise to monitor cortical activity over long time scales (3 years) (Zhang et al., 2018). Similarly, threshold crossing per electrode, rather than spike-sorted units were shown to yield higher decoder stability (Chestek et al., 2011; Christie et al., 2015).

We thus conclude that for decoding from the CNS, a simple linear decoding algorithm usually works well and marginal performance gains can be attained by using more complex ones (Kalman, Particle, LSTM). The preprocessing of the recorded signals, if electrode activity, spike sorting, or other features is a second important decision that can have big effects on both decoding accuracy and long term stability.

2.5.2 Decoding from the peripheral nervous system

Neural activity in the cortex happens largely in parallel and in spatially distinct sites that can be recorded simultaneously by microelectrode arrays or by electrocorticography. Recordings from the peripheral nervous system (PNS) are different. To prevent tissue-damage and ensure long-term stabil-

ity, minimally invasive interfaces that do not penetrate the nerve are commonly used. Artifacts from movements and from other sources of electricity such as muscles pollute the signal. The resulting noisy recording, acquired by a few electrodes outside the protective sheaths, generally does not allow for single fibres to be differentiated. A decoder therefore often needs to extract information from the shape of a single continuous time series per electrode.

This is especially true for the most commonly used interface, the cuff electrode. It captures neural activity at one site with few electrodes that all receive signals from many densely packed axons that superpose to a compound action potential (CAP). A differentiation of axons or groups of axons would increase the number of observations input to the decoder considerably. But, even though adapted spike sorting techniques were developed early (Wheeler and Heetderks, 1982; McNaughton and Horch, 1994), the limited recording resolution generally prevents such signal processing and the undifferentiated superposition of the spikes of all fibers has to be analysed directly. Common processing steps comprise a bandpass-filter (e.g., 700 Hz and 2 kHz (Diedrich et al., 2003)) to remove noise and slow local field potentials (LFP), an artifact removal by e.g., a linear minimum mean square error (LMMSE) filter (Gharibans et al., 2018), and a rectification followed by an average filtering (Micera et al., 2001; Diedrich et al., 2003; Cavallaro et al., 2003). The decoder receives a simple amplitude measure of the recording at different nerve locations as an input without trying to identify distinct events or units. Micera et al. (2001) successfully applied this technique to recordings from cuff electrodes using a neuro-fuzzy estimator (e.g., Jang and Sun (1995) for further reference). The decoding of the angular leg position from the activity of the tibial and the peroneal nerve was possible (Micera et al., 2001). Further refinement of the decoder could be achieved with a genetically optimized fuzzy logic (Cavallaro et al., 2003). In these examples, the low recording resolution and dimensionality of the signal was compensated by complex estimators.

Within the area of low-resolution recordings, we provide a first decoding contribution in this work that maps and linearises the response characteristic of a sensory population recorded by a hook electrode in oil to maximise decoding performance. See Ch. 4.1 for more details.

As dominant as the cuff electrode is in today's implementations of bioelectronic medicines, the ongoing research on new materials and alternative designs will lead to a higher signal resolution in the future and will allow adapted, more sophisticated pre-processing techniques to generate a more in-

formative input to the decoder. One good example of this paired progress (recording and processing) is the combination of intrafascicular electrodes and wavelet denoising. Intrafascicular electrodes provide a higher spatial resolution and signal-to-noise ratio than cuff electrodes (Boretius et al., 2010; Lawrence et al., 2004; Citi et al., 2008). Wavelet denoising (Donoho, 1995) applies a threshold in the wavelet-domain and therefore only keeps signal components that well fit the wavelet basis function. This basis function shape can be matched to the spike shapes and wavelet denoising is applicable as soon as spikes can be clearly distinguished from noise. Diedrich et al. (2003) first applied wavelet thresholding techniques for denoising PNS recordings acquired through microneurography, a method where a needle-electrode is inserted into a nerve. They were then able to classify spikes in the denoised recording by pattern matching and therefore largely enhanced the signal dimensionality from a univariate continuous waveform to firing rates of multiple single units (or groups of units). On the basis of this research, Micera et al. (Citi et al., 2008; Micera et al., 2010) successfully applied Diedrich's techniques in a discrete decoding of mechanoreceptor signals using intrafascicular electrodes (which in fact have similarities with microneurography needles). Hardware for the implementation of these techniques has been developed as well (Carta, 2013).

Intrafascicular electrodes allow the observation of single units but require intense pre-processing including an expensive online wavelet denoising and pattern matching that is a substantial burden for the limited battery capacity of any implanted device. An alternative route to a higher-dimensional decoder input is to further increase the raw recording quality by an even more invasive interface. In this way, a high resolution, potentially at the single action potential (AP) level, can be attained with less computationally expensive signal pre-processing – at the cost of a reduced long-term stability. Single AP recording resolution of peripheral nerve activity has been obtained from stripped nerves in microchannels (Chew et al., 2013) and by inserting microelectrode arrays near cell bodies, e.g., soma of sensory fibres in the dorsal root ganglion (Bruns et al., 2011a). Using the latter method of a micro electrode array (MEA), the acquired signal resembles the recordings in CNS. These more invasive interfaces provide a higher dimensional raw signal (number of electrodes) and open up ways towards reliably spike sorting single units. Successful decoders were demonstrated, even on unsorted data (Ross et al., 2018; Ouyang et al., 2019) with better results for more sophisticated decoders (neural net > Kalman \geq optimal linear estimator (Ross et al., 2018)).

The more detail the interface provides, the higher-dimensional and potentially informative the input

to a decoder will be. The decoder can then, in a data-driven way, select informative aspects of the recording automatically by e.g., least absolute shrinkage and selection operator (LASSO) (Tibshirani, 1996) and build the relationship to the quantity of interest. A high recording resolution can, however, also be used to implement an informed decoder that exploits an understanding of the physiological encoding as opposed to a purely data-driven machine-learning approach. Following this idea, we analysed the encoding principle of bladder pressure by a population of sensory afferent fibres monitoring the bladder wall using information theory in a first step and then designed an adapted decoder. Based on a quantitative understanding of the population code, this decoder makes use of groups of stereotypical bladder units to create a low-dimensional population vector and is accurate, robust, and offers means of automatic re-calibration. See Ch. 4.2 for details.

As we have seen for the three interfaces cuff electrode, intrafascicular electrode, and microelectrode array, there exists an intimately intertwined and evolving interplay between the interface that trades recording resolution against long-term stability, and the adapted pre-processing that extract as much information as possible from the available raw recording. While the choice of the decoding algorithm receiving the pre-processed data, be it a optimal linear filter/ estimator (Salinas and Abbott, 1994), a Kalman filter (Kalman and Bucy, 1961) involving a state model or a neural network (Yousefi et al., 2019; Hosman et al., 2019; Ross et al., 2018), has an impact on decoding performance (Ross et al., 2018), the generation of the input to the decoder by both recording technique and the adapted pre-processing is the most important task in technological development for bioelectronic medicines.

Such pre-processing is already quite evolved for high-resolution electrodes, as we have seen in the shape of wavelet denoising and pattern-matching for intrafascicular electrodes, spike sorting for microelectrode arrays. If we take a look at the lower end of signal-to-noise ratio and spatial resolution generated by e.g., a cuff electrode, however, the raw recording was usually simply summarised by its amplitude or power in the past, sometimes preceded by a denoising step (Donoho, 1995; Diedrich et al., 2003; Citi et al., 2008). Computing an amplitude measure is, however, a very coarse measure of activity that only quantifies intensity but discards any subtle waveform shapes that potentially contain additional information about the quality of activity such as active fibre diameters, active fascicles, and different rhythms. It should be asked whether such imprecise measures are really the best we can do as soon as spike sorting or pattern matching becomes impossible. It seems, there exists a gap between the two signal pre-processing paradigms ‘unit identification’ and ‘population power’ – ex-

actly for a regime of low signal-to-noise ratio and spatial resolution that is very common in peripheral nerve recordings. See a simplifying cartoon of this concept of a missing signal processing option in Fig. 2.6. Especially for cuff electrodes but also for intrafascicular electrodes with low signal to noise ratio, information might be lost by coarse summary measures of the activity.

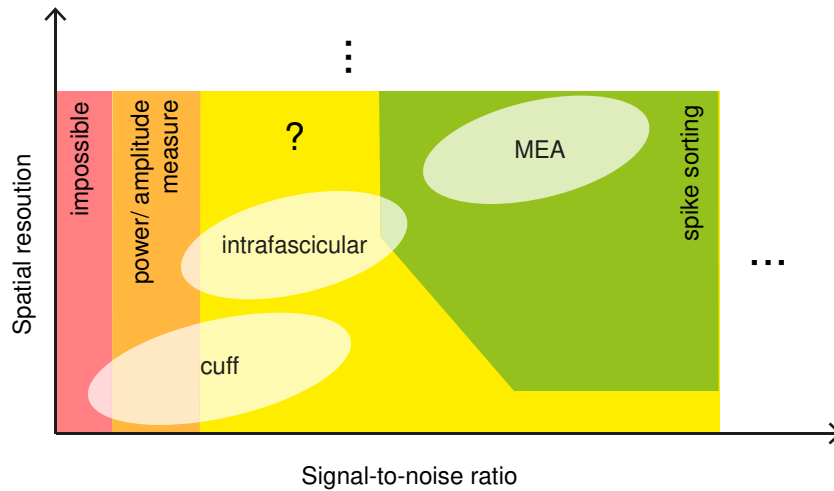


Figure 2.6: **There exists a regime of signal-to-noise ratio where more than a signal intensity could be extracted but is not currently.** A simplified view on pre-processing steps depending on the recorded signal quality (signal-to-noise ratio (SNR) and spatial resolution). At very low SNR, no decoding is possible (red). As soon as some spiking activity is visible (orange), intensity can be detected, but not quality of the activity. At intermediate SNRs, more than an intensity could be quantified but this information is usually discarded. Only in the high-SNR regime, single fibre waveforms can be distinguished and sorted. The combinations of spatial resolution and signal to noise ratio are shown for three common electrode designs: the cuff electrode, the intrafascicular electrode and the microelectrode array (MEA).

We attempt to address this unmet need for a pre-processing and characterisation of low-SNR raw neural recordings in a third contribution towards peripheral nerve decoding, in addition to our low-resolution decoder (Sec. 4.1) and the informed one for high-resolution interfaces (Sec. 4.2). Based on general purpose time-series features, we developed a pre-processing method that detects and summarises firing characteristics in a low-dimensional feature vector in a regime of signal-to-noise ratio where no spike sorting or waveform pattern matching is possible.

It has to be noted that the classic pattern-matching techniques including spike sorting (at least for differentiating fibre subgroup signatures), will most likely become possible even for commercial mildly invasive electrodes with advances in interface technologies. Some progress for e.g., the vagus nerve has been demonstrated in combination with wavelet denoising (Zanos et al., 2018). The reduced signal reliability and stability in peripheral interfaces (e.g., changing electrode positions due to movement causing recorded waveforms to change) compared to the CNS might, however, favour less sophis-

ticated measures of the continuous waveform that are more robust and long-term stable (like in the CNS (Zhang et al., 2018)). Characterising the waveform may in addition be more energy-efficient than the computationally expensive spike sorting.

2.6 Feature-based time-series characterisation and analysis

The reader might ask why time-series features are relevant for the analysis of peripheral nerve recordings? As detailed before, common interfaces often generate low-resolution recordings that do not allow the identification of single fibres or subpopulations. The resulting compound action potentials (CAP) have to be treated as a continuous waveform. Currently, these recordings have been summarised in coarse statistics like power (e.g., root mean square (RMS) power) or amplitude that discard any subtle dynamics captured in the waveform. If we can identify any additional informative properties of the unprocessed peripheral nerve recordings that go beyond power, this would enable us to describe the continuous low-resolution recording – shaped by the particular nerve, the interface, and the fibre population activity – efficiently in a few key figures without any energetically expensive high-maintenance processing steps such as wavelet denoising or on-line spike sorting. Such a set of relevant features, for instance implemented as hardware for efficiency, might form a core component of a closed-loop neuromodulation device one day. The interpretable feature-vector can inform a clinician about the nerve’s health, form the input to a decoder, or can be used to classify unusual states based on a density estimation in feature-space.

To better understand the feature-based analysis of time-series – in our particular case peripheral nerve recordings – let us first define global time-series features for univariate sequences. By ‘feature’, we mean any quantity that can be calculated from the time series’ set of values. Each such feature quantifies one particular dynamical property of the sequential data $\mathbf{x} = \{x_t\} \ t = 1, \dots, T$ of a potentially high length T in a single number f . Global time-series features can be simple e.g., the mean or standard deviation, or complex, for instance measures of entropy, local predictability, measures from nonlinear time series analysis, etc. Given a set of F such features $\{f_i\} \ i = 1, \dots, F$, a time series \mathbf{x} can be transformed to a feature vector $\mathbf{f} = \{f_i\}$ that describes the sequence’s dynamical properties: $\mathbf{x} \rightarrow \mathbf{f} \in \mathbb{R}^F$ on the time window T .

Representing a time series as a feature vector that captures its key dynamics has obvious benefits. If we find the right feature set, a recording can be summarised by a compact array of interpretable measures that provide a clear insight into its dynamical nature. A few features (say, frequency, phase, amplitude, and duration for a sinusoid) can fully describe the time series and lead to a potentially drastic dimensionality reduction from countless samples to a few numbers. The advantages of a feature-based representation become even more obvious when conducting analyses of multiple recordings. Standard automated grouping analyses, supervised (classification) or unsupervised (clustering), are difficult (Berndt and Clifford, 1994; Vlachos et al., 2002; Moon et al., 2001; Faloutsos et al., 1994; Ye and Keogh, 2009) and expensive (Bagnall et al., 2017a) if time-series are to be compared one-by-one on the basis of their raw ordered measurements. Once transformed to a point in feature-space, the similarity of two objects is readily established by their proximity and can even be assessed straightforwardly for sequences of different lengths and sampling rates. As all dimensions in feature space correspond to interpretable dynamical properties, the locations of different recordings might inform the investigator about key differences and guide further research towards a deeper understanding.

In this work, we use a particularly rich collection of over 7 500 time-series features united in the Highly Comparative Time-Series Analysis toolbox *hctsa* (Fulcher et al., 2013; Fulcher and Jones, 2017) to connect the extensive body of general purpose time-series features to our domain of peripheral nerve recordings. Features included in *hctsa* are derived from a wide conceptual range of algorithms, including measurements of the basic statistics of time-series values (e.g., location, spread, Gaussianity, outlier properties), linear correlations (e.g., autocorrelation, power spectral features), stationarity (e.g., StatAv, sliding window measures, prediction errors), entropy (e.g., auto-mutual information, Approximate Entropy, Lempel-Ziv complexity), methods from the physical nonlinear time-series analysis literature (e.g., correlation dimension, Lyapunov exponent estimates, surrogate data analysis), linear and nonlinear model parameters, fits, and predictive power (e.g., from autoregressive moving average (ARMA), Gaussian Process, and generalized autoregressive conditional heteroskedasticity (GARCH) models), and others (e.g., wavelet methods, properties of networks derived from time series, etc.) (Fulcher et al., 2013; Fulcher and Jones, 2017).

Based on this comprehensive feature library, we present two analysis methods that both lead to a selection of informative features which can be used to generate low-dimensional summaries of time series for subsequent analyses such as classification, clustering, forecasting, etc (Fulcher, 2018). A

supervised (Ch. 5.2) selection pipeline generates condensed feature subsets with high classification performance while an unsupervised (Ch. 5.1) method uncovers the low-dimensional parametric variation in a time-series dataset by unsupervised dimensionality reduction in the high-dimensional feature space and identifies single estimators for each dynamical property. In a proof-of-concept, we applied the second, unsupervised method to simulated peripheral nerve recordings generated in our simulator (see next section 2.7). We could retrieve the firing characteristics firing rate, myelination ratio, and burstiness in an unsupervised way and proposed single efficiently implementable estimators for each. See chapter 5.1 for more details.

Both these data-driven analysis methods for low-dimensional feature set selection have an application far beyond the domain of peripheral nerve recordings. We demonstrate the utility of our unsupervised method (Ch. 5.1) on a variety of simulated dynamical systems and a real-world example in addition to peripheral nerve recordings. The supervised feature-selection method was applied to a literature standard of time-series classification tasks (Ch. 5.2) to distill a generally useful set of time-series features that we implemented efficiently in C for the use in all major computing environments. Instead of attempting to curate feature sets manually to our limited problem domain, we therefore propose time-series feature selection and analysis methodologies with much wider potential application than our original scope of study.

2.7 Simulation of peripheral nerves

Much of the described decoding in section 2.5 has been developed in a data-driven way based on simultaneous recordings of neural activity on the one hand and a physiological quantity of interest on the other. The generation of such data is, however, tied to laborious and expensive experiments that importantly each time cost the life of a laboratory animal. To reduce, supplement, and make the best use of this indispensable experimental data-generation, modelling approaches are an important aid in biomedical research. Computer simulations of biological systems can incorporate knowledge won through numerous experiments on different aspects at different sites and different temporal and spatial scales and make these insights reusable and available to many investigators. Often, simulations offer a higher level of detail across a variety of phenomena than any single experiment can offer – from heat exchanges between large body regions over fluid motions in large and small cavities (e.g., each

of thousands of glomeruli) down to ion exchanges through microscopic channels on cell walls. They further allow the quick adaption of various parameters and pave the way to a much wider coverage of expected variability in the patient population including pathologies, ages, sexes, etc., than any number of experiments could (Gosselin et al., 2014).

Just as in other biomedical engineering disciplines, the progress of bioelectronic medicines will thus in part hinge on the availability of accurate, flexible, and efficient computational models (Evans and Nikolic, 2016). Using these tools will speed up the development of interfaces (optimising electrode positions, stimulation pulses, etc.) (e.g., Raspopovic et al. (2011); Perra et al. (2018); Rapeaux et al. (2015)), enable the prediction of organ reactions to planned interventions, and generate realistic artificial recordings for the development of signal processing methods.

Simulations of electrical phenomena such as nervous activity in biological tissues are, however, complicated for different reasons. Even the electrically passive tissues in the body (fat, organs, etc) have inhomogeneous and anisotropic conductances (Aström et al., 2012) that are furthermore dependent on the frequency of the propagated signal (Gabriel et al., 1996). This complicates the computation of extracellular potentials and currents. Axons pose additional difficulties as their behaviour is guided by the quick nonlinear action of various ion channels. These two scales (axons and extracellular medium) are usually implemented as separate simulations with different computational approaches that together form a hybrid model: a compartmental one-dimensional model for neurons (Hines and Carnevale, 1997; Hines et al., 2009) and an finite element model (FEM) for extracellular conduction. The latter usually applies a resistive, electro-quasistatic approximation (no capacitances, immediate potential-propagation). Full FEM models including axons for a higher degree of detail were developed as well (Agudelo-Toro and Neef, 2013; Tveito et al., 2017; Tarotin et al., 2019) but are slow. Many other approaches for simplified axon models (McNeal, 1976; Veltink et al., 1989; Plachta et al., 2012; Goodall et al., 1995), simplified (Holt and Koch, 1999; Lindén et al., 2014) and more detailed (Haines et al., 2016; Pods et al., 2013; Pods, 2017) extracellular spaces were proposed, but the hybrid model remains today's standard.

Even though the research community converged towards the hybrid model as a default method for peripheral nerve simulation in the study of both stimulation and recording, simulations are usually set up from scratch (e.g., Grinberg et al. (2008); Raspopovic et al. (2011)), developed for one particular

purpose without any reusability in mind. This laborious process gives the highest freedom to the investigator in fitting the model to the studied object. On the other hand, the set-up process comes with a lot of time-consuming work, especially for a researcher inexperienced at simulations. The result is not necessarily easily adjustable to new settings and the coordination of two separate simulations (axons and extracellular fields) is error-prone. In recent times, a large simulation platform, Sim4Life (Gosselin et al., 2014), incorporated peripheral nerves into their portfolio and now offers a unified modelling framework. This model is, however, a closed proprietary system (no open source), very expensive, and not easily accessible to researchers.

Against this background, the need for a flexible, freely accessible, and easily usable peripheral nerve simulator becomes apparent that ideally finds a compromise between accuracy, flexibility, and execution speed. In chapter 3, we describe a model we developed to address this need. Some of its features are innovative such as automatically generated tortuous axons fit to *in vivo* images and an efficient computation of extracellular potentials from pre-computed voltage distributions. The package is built as a Python module for enhanced usability and easy post-processing. We use it to test our feature-based signal processing algorithms.

2.7.1 Conclusion on background

This chapter reviewed the most important topics relevant to the work presented. I first summarised the organisation of the anatomy of the peripheral nervous system and discussed what fundamental constraints on energy and control may have guided its evolution. In a literature review of the encoding on peripheral nerves, I identified a need for quantitative analyses of the encoding of peripheral populations. Sec. 4.2 will describe contributions to this topic. It followed a discussion of the recording techniques and decoding methods, both for the CNS and the PNS. Here, I explained the dominance of the cuff electrode in today's bioelectronic medicines by its benefits of long-term stability. Because of its wide spread we tried to make the most of this data type in our first decoding study in Sec. 4.1. As an alternative, I hinted on the potential merits of a more selective interface including informed decoding approaches. Sec. 4.2 explores these ideas on a model system. In the context of decoding, the importance of pre-processing methods for peripheral nerve recordings was highlighted. By tailoring the pre-processing to the recording technique used, informative summaries can be generated

for subsequent decoding algorithms without discarding much information. We introduced feature-based time-series analysis for this purpose and finally gave a short introduction on an important tool for biomedical research: computer simulations. Our contributions to this domain are covered in the following chapter 3.

Chapter 3

Simulation – PyPNS

3.1 Introduction

This thesis investigates methods to analyse the activity on peripheral nerves. As a first step in such an analysis it is often helpful to precisely model the object of interest – in our case the peripheral nerve. The process of setting up a simulation can be a very insightful learning process and the final model allows for a much quicker and more detailed investigation of the nerve’s electrical properties than an experiment would. This includes action potential propagation on single axons, extracellular potential generation by the population of neurons and stimulation effects. For the purpose of this work, the ability to generate surrogate peripheral nerve recordings at diverse parameters (e.g., fibre composition, firing rate and synchrony of fibres, extracellular medium) is of particular interest to test decoding methods as we do in Ch. 5.1. This synthetic data complements the studies on *in vivo* recordings we conduct in Ch. 4.

Of course the model developed in this thesis was not the first attempt to set up a computer simulation of a peripheral nerve. Already in 1997, Struijk (1997) proposed a 2D model for the extracellular potentials from a myelinated fibre. Other presented models for stimulation of peripheral fibres at the same time (Veltink et al., 1989; Goodall et al., 1995). In these early approaches, the main difficulty in simulating peripheral axons compared to central neurons in the CNS was the dominant focus in model development: the inhomogeneity of the surrounding medium and the resulting difficulties in computing extracellular potentials from current, be it current from membrane channels or current

from stimulation electrodes. Even the recording method, e.g., a cuff or an oil bath, can cause dramatic changes in the extracellular conductivity profiles and therefore in the electrical current propagation and potential formation. It was therefore reasonable to concentrate limited computational resources on extracellular space modelling and axon models were often simplified to e.g., the Fitz-Hugh-Nagumo formulation (Plachta et al., 2012) or the McNeal model (McNeal, 1976; Veltink et al., 1989). Only in the last 10 years, increasing computational power has enabled the combination of more precise, biologically accurate axon models and equally detailed extracellular space models (Grinberg et al., 2008; Raspopovic et al., 2011).

Important choices have to be made when it comes to the level of abstraction in the models of both the axon and the extracellular medium. The axon can, as described above, be approximated by models that do not explicitly incorporate ion channels. Alternatively, a simulated fibre can be made up by zero-dimensional compartments for which scalar membrane currents, voltages and the associated channel mechanisms are defined. Channel dynamics can be modeled deterministically such as by the common simulator NEURON (Hines and Carnevale, 1997) or explicitly capture their stochastic nature (Neishabouri, 2014; Faisal et al., 2002). The feed-back of variations in the extracellular potential caused by the neuron itself or its neighbours into the neuron's membrane dynamics, so called ephaptic coupling, signifies a further step in simulation detail that can be non-negligible (Tveito et al., 2017; Bokil et al., 2001). At the highest degree of detail/ lowest degree of abstraction, the axon *and* its surrounding medium can both be modeled as a three-dimensional structure, potentially defined in a finite element model (FEM) to capture detailed electrodynamical and -diffusive effects (Agudelo-Toro and Neef, 2013; Tveito et al., 2017; Tarotin et al., 2019) both inside and outside the axon. In search for a trade-off between computational effort and level of detail, we here settled for the standard compartmentalised, deterministic NEURON model for axons that is independent of its environment. This approach is detailed enough to investigate different ion-currents, but computationally feasible for a few hundred fibres.

Equally numerous choices exist for the extracellular medium model. In its most simple formulation, the medium can be assumed to be homogeneous, resistive and isotropic (Holt and Koch, 1999; Lindén et al., 2014). As a result, potentials from both line and point current sources can be expressed analytically as a function of medium resistivity, current strength and geometrical relation between source and recording position. While signifying an appropriate approximation for the extra-

cellular medium in the CNS, the medium surrounding a peripheral nerve is both inhomogeneous and anisotropic and can therefore not be modeled this way. Finite element models (FEM) with simplifying assumptions such as resistivity and the electro-quasistatic approximation of the Maxwell-equations can accommodate for both inhomogeneous and anisotropic media. Model detail can of course be increased by e.g., incorporating dielectric dispersion (polarisation at different microscopic levels) that is observed in almost all biological tissues (Gabriel et al., 1996) and shown to have effects on recordings (Bédard and Destexhe, 2009; Martinsen et al., 2002). The effects of charge-ion diffusion can be incorporated in Poisson-Nernst-Planck solvers, e.g., Pods et al. (2013); Halnes et al. (2016) and simplified formulations (Pods, 2017). We again, as for the axon-model, search for a compromise that maintains computational feasibility at sufficient degree of detail and decided for a resistive, electro-quasistatic extracellular space model that is implemented in an FEM solver from which we import pre-computed potential distributions into our self-contained simulation module.

The resulting simulator constitutes a Python module called PyPNS and offers several advantages over existing approaches. By exploiting symmetries in the medium-geometry and the resistive electro-quasistatic approximation of the Maxwell equations to separate space and time, it can reuse pre-computed potential fields at different source positions inside the nerve for arbitrary axon geometries without the need to re-run the expensive FEM simulations. In this way, the accuracy of hybrid FEM-based solutions was approached at the computational cost of the simple volume conductor method. The choice for creating this lookup-table and using it in combination with compartmentalised deterministic axon models was mainly guided by the efforts towards a low computational complexity and execution time. In addition, FEM-simulation and the NEURON-simulation of the axons thus need to be coordinated once in terms of units and geometry, from then on no further import/ export and alignment is necessary. As a Python module, PyPNS integrates nicely into a common data analysis framework. It further enables the simulation of tortuous axons as observed in the PNS with trajectory properties fit to imaged data and axons of very low diameter typical for the PNS. Its modular nature facilitates extensions by additional axon types, stimulation mechanism or extracellular media. Similar functionality can be achieved by commercially available simulators such as Sim4Life (Zurich MedTech AG), but our simulator is open source and commercial solutions are typically very expensive.

The latest version of our toolbox PyPNS for Python 3 can be accessed over GitHub: github.com/

chlubba/PyPNS.

Scripts for the figures are as well maintained on GitHub: github.com/chlubba/PyPNS-PaperFigures.

3.2 Methodology

3.2.1 Experiments

3.2.1.1 Validation of simulated recordings

To validate the simulation, Simon Cork obtained recordings from the rat vagus nerve. All experiments were carried out in accordance with the Animals (Scientific Procedures) Act 1986 (United Kingdom) and Home Office (United Kingdom) approved project and personal licenses, and experiments were approved by the Imperial College Animal Welfare Ethical Review Board under project license PPL 70/7365. A male Wistar rat (body weight 350-400 g) was initially anaesthetised with isoflurane and ventilated. Urethane was then slowly administered through a tail vein (20 mg kg^{-1}). The left cervical vagus nerve was exposed and contacted with a stainless steel pseudo-tripolar hook electrode of pole distance 1 - 2 mm for stimulation. The nerve was stimulated 10 times by a biphasic rectangular current pulse of amplitude 20 mA for 1 ms at a frequency of 1 kHz (one period). To record from the nerve, a bipolar platinum hook electrode (pole distance 2 - 3 mm) was then wrapped around the anterior branch of the subdiaphragmatic vagus nerve with an Ag/AgCl ground electrode placed in the abdominal cavity. Distance between recording and stimulating electrodes was 8 - 10 cm. See Fig. 3.1. Mineral oil heated to 37°C was applied to each site to insulate the electrodes from environmental and proximal noise sources. Stimulation of the cervical vagus nerve was performed using a Keithley 6221 current source, controlled by Standard Commands for Programmable Instruments (SCPI) via a custom built Matlab interface. Bipolar cuff recordings were achieved with an Intan Technology RHD2000 system, using a 16-channel bipolar ended amplifier (RHD221). The obtained recordings were averaged over 10 repeated stimulations in the same animal.

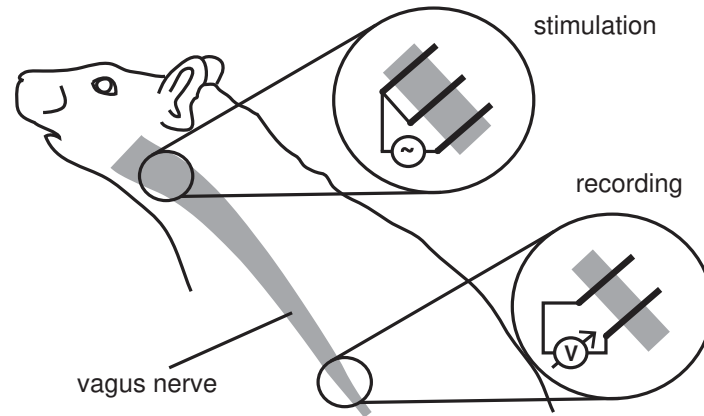


Figure 3.1: **The validation data were obtained through stimulation of a rat vagus nerve.** A pseudo-tetrapolar electrode excited axons at the cervical vagus nerve, signals were picked up at the subdiaphragmatic vagus nerve with a bipolar electrode.

3.2.1.2 Imaging of peripheral nerve tortuosity

All procedures were carried out in accordance with the Animals (Scientific Procedures) Act 1986 (United Kingdom) and Home Office (United Kingdom) approved project and personal licenses, and experiments were approved by the Imperial College Animal Welfare Ethical Review Board under project license PPL 70/7355. To match the morphology of our simulated axons to real ones, we used images of the vagus and sciatic nerves in mice acquired by Peter Quicke, Subhojit Chakraborty, and June Kyu Hwang using two photon fluorescence imaging. In the experiment, ChAT-Cre FLEX-VSFP 2.3 mice were euthanised by intraperitoneal overdose of pentobarbital (150 mg kg^{-1}). The pre-thoracic left and right vagus nerves were surgically exposed and 0.5 cm sections were removed and placed in phosphate buffered saline (155.1 mmol NaCl, 2.96 mmol Na_2HPO_4 , 1.05 mmol KH_2PO_4) adjusted to 8.0 pH with 1 mol NaOH. Sections of the left and right sciatic nerves of between 1 and 2 cm from above the knee were also removed. To prepare for microscopy, the nerves were placed on microscope slides, stretched until straight, and the nerve ends were fixed with super glue. The preparation was covered with PBS. Distortions potentially caused by the stretching of the nerves were assumed to lie within the physiological range of movement-induced deformations the nerve undergoes in the living organism. A commercial 2P microscope was used for imaging (Scientifica, emission blue channel: 475/50 nm, yellow channel 545/55 nm, 511 nm dichroic, Semrock) while exciting at 950 nm using a Ti-Sapphire laser (Mai Tai HP, Spectra-Physics).

3.2.2 PyPNS overview

A PyPNS simulation consists of one nerve bundle that contains myelinated and/ or unmyelinated axons that can be stimulated by different electrical means and that can be recorded both intra- and extracellularly.

The module is organised in an object oriented manner in which different classes map to the physiological entities encountered in a peripheral nerve. The main class is `Bundle`. At the time of creation of a `PyPNS-Bundle`, its dimensions and axons need to be specified. Stimulation and recording mechanisms are added later using specific methods of `Bundle`. Axons contained in `Bundle` derive from the `Axon`-class and define properties needed by the NEURON simulations. `Unmyelinated` and `Myelinated Axon`-children exist and each is characterised by its diameter and trajectory. To activate axons, `ExcitationMechanisms` are added to the `Bundle`. Those can be either synaptic input (`UpstreamSpiking`), intracellular stimulation (`StimIntra`) or extracellular stimulation (`StimField`). Similarly for recording, electrodes can be added to the whole nerve as a `RecordingMechanism`. For all interactions with the extracellular space, i.e. extracellular stimulation or recording, a model of the extracellular medium defined in a `Extracellular`-class has to be set. This can be either homogeneous (`homogeneous`), an FEM result (`precomputedFEM`) or an analytically defined potential distribution (`analytic`).

When the `Bundle.simulate`-routine is called, each axon is sequentially simulated in NEURON via the Python-NEURON-interface (Hines et al., 2009) taking care of the associated `ExcitationMechanisms`. From the membrane currents of each `Axon-segment` computed in NEURON, PyPNS calculates the extracellular single fibre action potential (SFAP) for each of the associated `RecordingMechanisms` (multiple, even different media, possible). The contributions of all `Axons` contained in the `Bundle` are added up to the overall compound action potential (CAP).

3.2.3 Assumptions and simplifications

Several assumptions ensured the computational feasibility and efficiency of PyPNS. Axons were assumed to be independent from each other in their activity (no ephaptic coupling). Properties such as diameter, myelination, and channel densities stayed exactly constant along the axon length. The

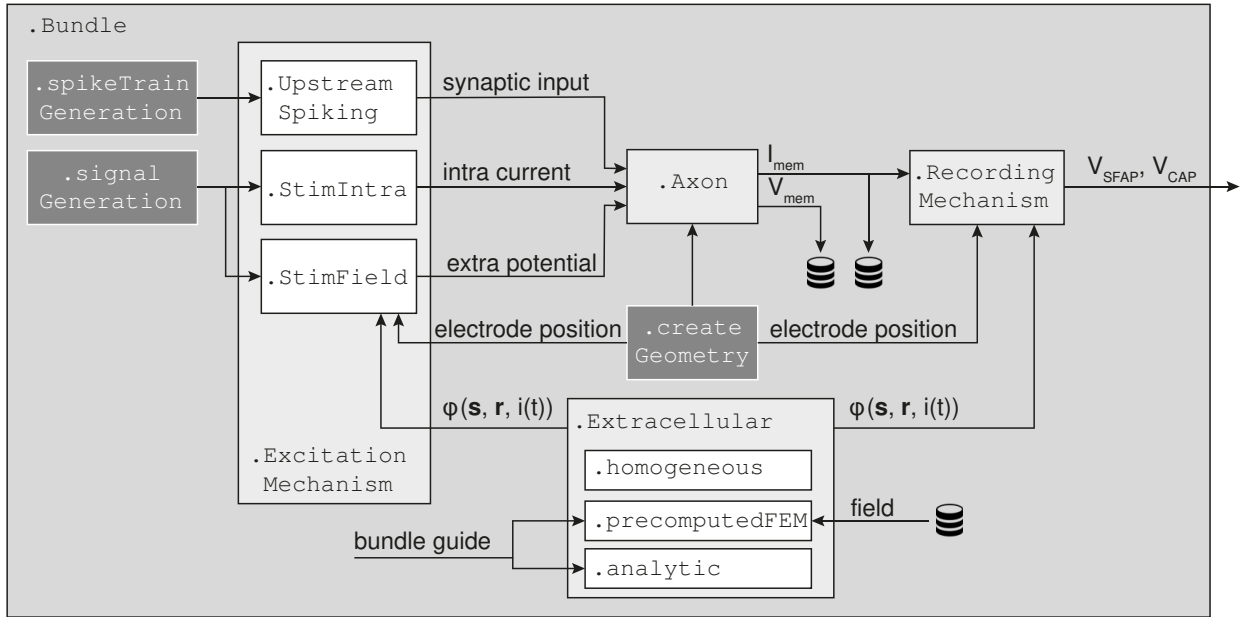


Figure 3.2: **Flowchart of PyPNS's internal information flow.** The Axon-class is the central object of PyPNS's internal information flow and all Axon-instances are managed by Bundle. Together with its ExcitationMechanisms, all associated to each Axon, it defines the NEURON simulation. Extracellular-objects allow the calculation of extracellular potentials given current $i(t)$, source position s and receiver position r . They are used by both StimField for extracellular stimulation (transmitted to NEURON) and by RecordingMechanism for recording (PyPNS post-processing of NEURON-generated currents). The Bundle-class manages all axons and is the main object of the PyPNS-API. It is supported by helper modules spikeTrainGeneration, signalGeneration and createGeometry.

extracellular space was modeled using the electro-quasistatic approximation of Maxwell's equations, neglecting magnetic induction:

$$\nabla \times E = -\frac{\partial B}{\partial t} \simeq 0. \quad (3.1)$$

Further and importantly, all media were assumed to be purely resistive. Thereby all changes in current affected the potentials of the entire space immediately, allowing us to separate time and space and further increasing simulation efficiency. In Maxwell's equations this results in neglecting displacement currents:

$$\nabla \times H = J + \frac{\partial D}{\partial t} \simeq J \quad (3.2)$$

For the brain and in the considered frequency range, the electro-quasistatic approximation is assumed to be valid (Hämäläinen et al., 1993; Bossetti et al., 2008); previous peripheral nerve simulation studies have built on both quasistatic and purely resistive approximations (Raspopovic et al., 2012; Struijk, 1997; Veltink et al., 1989; Goodall et al., 1995). We further only modeled one fascicle surrounded by circularly symmetric layers of tissue. Extracellular recordings and stimulation neglected the electrode-electrolyte interface. While this interface certainly has an impact on stimulation effi-

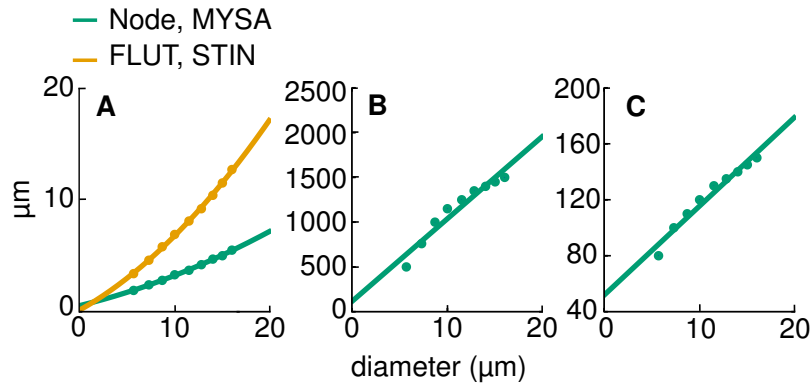


Figure 3.3: **Linear and quadratic fits were used to extrapolate the parameters of myelinated axons to smaller diameters.** **A** Diameters of all segments – nodes, MYSA (myelin attachment segments), and paranodal elements FLUT (paranode main segment) and STIN (internode segment, see McIntyre et al. (2002) for more information on the model) – were fit quadratically to prevent negative values. Node distance **B** and number of myelin sheaths **C** were extrapolated linearly.

ciency and consequently stimulation dosage in bioelectronic medicines (Cantrell et al., 2008), PyPNS is currently mainly designed for creating surrogate recordings. As there is no standard model for electrode-electrolyte interfaces today, we chose to keep our model as simple as possible without integrating more degrees of freedoms and assumptions than necessary.

3.2.4 Axon models

Unmyelinated axons were modeled based on the original Hodgkin-Huxley parameters (Hodgkin and Huxley, 1952), with temperature set to 37°C. For myelinated ones we used the model of McIntyre et al. (McIntyre et al., 2002) that has originally been developed for peripheral motor fibres with thicker diameters (5.7 - 16.0 μm). To match the thinner axons found in the PNS (0.2 - 3 μm), all diameter dependent parameters were extrapolated to smaller diameters as shown in Fig. 3.3: (1) the diameters of the different segments – nodes, MYSA (myelin attachment segment), FLUT (paranode main segment), STIN (internode segment), (2) node distance and (3) the number of myelin sheaths. Neither axon-model is claimed to exactly match the properties of single neurons found in the PNS. We aimed to implement a generalised framework in which parameters can be fine-tuned to match specific datasets.

3.2.5 Generation of axonal geometry

Axons in peripheral nerves do not assume a perfectly straight trajectory, but instead show a certain degree of tortuosity while following the nerve. This morphology is like to influence both stimulation efficiency and extracellular recordings. To model axon tortuosity in our simulation without manually describing the exact shape of each fibre we iteratively placed straight axon segments (length $15\text{ }\mu\text{m}$) along a previously defined bundle guide, itself composed of longer straight segments ($100\text{ }\mu\text{m}$). In each step, the axon segment direction \mathbf{a}_i was calculated as

$$\mathbf{a}_i = \frac{\mathbf{a}_{i-1} + (1.1 - \alpha) \cdot \mathbf{b}_k + \alpha \cdot \mathbf{w}_i}{\|\mathbf{a}_{i-1} + (1.1 - \alpha) \cdot \mathbf{b}_k + \alpha \cdot \mathbf{w}_i\|}, \quad (3.3)$$

based on the corresponding bundle guide segment direction \mathbf{b}_k ($k \leq i$, as bundle guide segments were longer than axon segments), the previous axon segment direction \mathbf{a}_{i-1} and a random component perpendicular to the bundle guide segment direction \mathbf{w}_i . All vectors have unit length. The parameter $\alpha \in [0, 1]$ regulates the tortuosity of the axon and can, together with the distribution of $\|\mathbf{w}\|$, be fit to geometries measured by microscopy. The factor $(1.1 - \alpha)$, rather than $(1 - \alpha)$, was chosen to maintain forward axon growth. See appendix 3.5.B for the exact implementation of \mathbf{w}_i which insures that axons stay within the nerve.

To fit the trajectory of our automatically generated axon trajectories to realistic fibre shapes, we manually traced axons in microscopy images and segmented into straight sections of the same length as our straight simulated segments ($15\text{ }\mu\text{m}$). For all traced axons of one nerve, the normalised difference in direction between consecutive segments $c = \|\mathbf{a}_i - \mathbf{a}_{i+1}\|$ was calculated. We then fit the distribution over the c -values of our artificial axons to the one of imaged fibres by adapting the tortuosity coefficients α and $\|\mathbf{w}\|$ -distribution. For details see appendix 3.5.C.

3.2.6 Extracellular potentials

One of the main purposes of PyPNS is the generation of surrogate recordings from peripheral nerves to then use for testing decoding algorithms. Such recordings from peripheral nerves capture changes in the potential of the extracellular medium at the electrode caused by membrane currents. To calculate

these changes in PyPNS, axon segments were interpreted as point current sources, each causing a potential change in the entire medium.¹ See Fig. 3.4. Potentials generated by all current sources (all segments of all axons) were superposed. From the electro-quasistatic approximation of the Maxwell equations, combined with pure resistivity, time and space can be separated in the compound action potential (CAP) calculation:

$$\phi_{\text{CAP}}(\mathbf{r}, t) = \sum_{s_i} \frac{\phi_{\text{static}}(\mathbf{s}_i, \mathbf{r}, I_{\text{ref}})}{I_{\text{ref}}} \cdot i(\mathbf{s}_i, t). \quad (3.4)$$

The extracellular potential over time at receiver position \mathbf{r} , $\phi_{\text{CAP}}(\mathbf{r}, t)$, was calculated as the sum over single axon segment contributions. The contribution of one segment at position \mathbf{s}_i to the potential recorded at position \mathbf{r} was obtained from a known static potential $\phi_{\text{static}}(\mathbf{s}_i, \mathbf{r}, I_{\text{ref}})$ at reference current I_{ref} that was then scaled by the temporally varying membrane current of the segment $i(\mathbf{s}_i, t)$.

Extracellular stimulation was realised following exactly the same principle. Here, stimulation electrodes were modeled as assemblies of point current sources and axon segments are extracellular potential receivers.

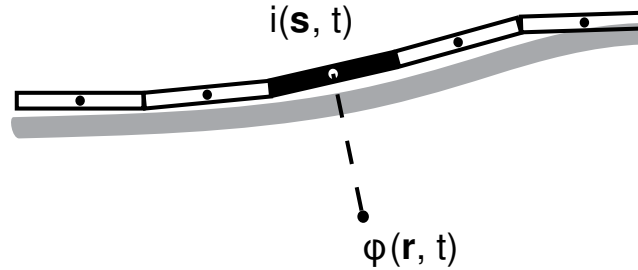


Figure 3.4: **Axon segments can be interpreted as current point sources.** The extracellular potential $\phi(\mathbf{r}, t)$ at position \mathbf{r} caused by a current $i(\mathbf{s}, t)$ at position \mathbf{s} is determined by current time course scaled with a static potential depending on the extracellular space and the spatial relation between source and receiver position.

The profile of the static potential along the nerve, ϕ_{CAP} in Eq. (3.4), shapes the recorded extracellular potential. A few interesting effects on extracellular recordings can be illustrated on the basis of a simplified example. Consider a single straight axon on the z -axis, so that $\phi_{\text{static}}(\mathbf{s}, \mathbf{r}, I_{\text{ref}})$ becomes $\phi_{\text{static}}(z, I_{\text{ref}})$ with $z = (\mathbf{s} - \mathbf{r}) \cdot \mathbf{e}_z$. In this case, the translation of membrane current to recorded single fibre action potential (SFAP) in the extracellular medium is solely determined by the profile of the static potential over longitudinal distance:

¹Even though the line-approximation is commonly used for homogeneous extracellular media, its use is impossible for our efficient method of precomputing voltage fields once to then reuse.

$$\phi_{\text{SFAP}}(t) = \sum_{z_i} \frac{\phi_{\text{static}}(z_i, I_{\text{ref}})}{I_{\text{ref}}} \cdot i(z_i, t). \quad (3.5)$$

Fig. 3.5 further illustrates how a lagged version of the membrane current of each axon segment contributes to the extracellular potential according to its distance z_i from the electrode and the conduction velocity CV (Fig. 3.5A):

$$i(z_i, t) = i\left(t - \frac{z_i}{CV} \mid z = 0\right) := i\left(t - \frac{z_i}{CV}\right). \quad (3.6)$$

For one $t = t'$, the instantaneous currents $i(z_i \mid t = t') = i(t' - z_i/CV)$ of all segments shown in Fig. 3.5B are multiplied by the static potential corresponding to their spatial displacement (Fig. 3.5C) and added up.

Let us consider two extreme cases of a static potential profile. In the first, $\phi_{\text{SFAP}}(z)$ is a the Kronecker delta ($\phi(z) = \delta(z)$). Here, the SFAP would have exactly the same time course as the membrane current. On the other hand a constant profile $\phi(z) = c$ will make the resulting SFAP vanish because of charge conservation ($\int i(t)dt = 0 \Rightarrow \int i(z/CV)dz/CV = 0$). Positive and negative components of the current cancel each other out. The real profile will always lie between those extreme cases and the recorded action potential is expected to be maximal if positive and negative peaks of membrane current add up constructively. To quantify when this happens, an active length l_a of an axon can be defined as

$$l_a = t_a \cdot CV, \quad (3.7)$$

with t_a denoting the time during which an axon segment emits current of constant sign and CV the conduction velocity. Membrane current is of the same sign over length l_a . The match between this length and the range of the profile ($\Delta z = z_2 - z_1$ with $\phi(z) > 0$ for z in $[z_1, z_2]$) will determine the amplitude of the SFAP – in addition to a scaling factor depending on the absolute values of $\phi(z)$ in (3.4).

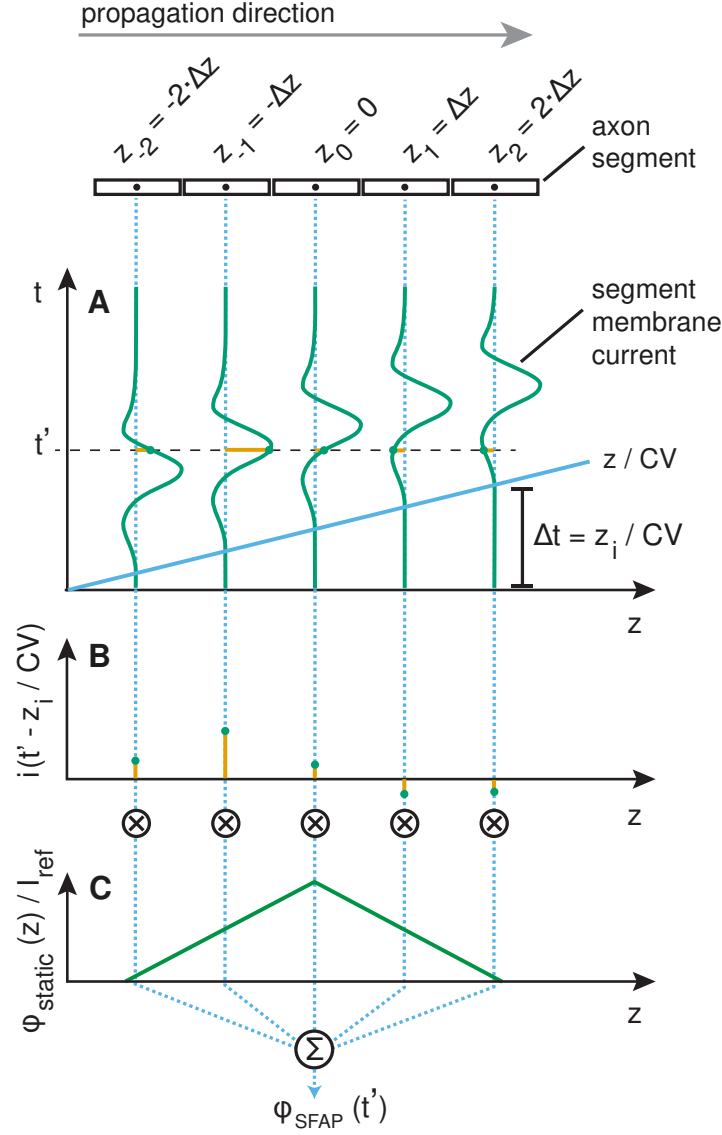


Figure 3.5: **The impact of the longitudinal profile $\phi_{\text{SFAP}}(z)$ on SFAPs.** It can be understood by studying the potential caused by a perfectly straight axon recorded at $z_0 = 0$ for $t = t'$. Axon segments of length Δz exhibit the exact same current time course except for a delay $\Delta t = z_i / CV$ **A**. The potential ϕ_{SFAP} at $t = t'$ is then obtained as the sum over membrane currents $i(z_i | t = t')$ shown in **B**, multiplied by the static potential $\phi_{\text{static}}(z_i, I_{\text{ref}}) / I_{\text{ref}}$ **C**.

3.2.7 Homogeneous media

The easiest case of an extracellular space is a homogeneous medium of constant conductivity σ . In this simple case, the potential $\phi(\mathbf{r}, t)$ at \mathbf{r} caused by a point source of current $i(\mathbf{s}, t)$ at \mathbf{s} can be computed analytically (see Malmivuo and Plonsey (1995) or Lindén et al. (2014) for reference) as

$$\phi(\mathbf{r}, t) = \frac{1}{4\pi\sigma} \frac{i(\mathbf{s}, t)}{|\mathbf{s} - \mathbf{r}|}. \quad (3.8)$$

Compared to the formulation in (3.4), the static potential term that translates current to voltage here became

$$\frac{\phi_{\text{static}}(\mathbf{s}, \mathbf{r}, I_{\text{ref}})}{I_{\text{ref}}} = \frac{1}{4\pi\sigma|\mathbf{s} - \mathbf{r}|}. \quad (3.9)$$

Even though no peripheral nerve will be surrounded by a homogeneous medium, PyPNS implements the homogeneous case for completeness and to compare it to other media as `PyPNS.Extracellular.homogeneous`.

3.2.8 Radially inhomogeneous media

The medium surrounding the axons in peripheral nerves is known to be anisotropic and inhomogeneous (Capogrosso et al., 2013; Struijk, 1997). PyPNS thus needs to implement an extracellular space model that goes beyond the homogeneous assumption. As no exact analytical solution for the potential caused by a point current source exists under these conditions (inhomogeneous, anisotropic), numerical methods become necessary.² In previous peripheral nerve models, simulation of either extracellular recording or stimulation in such media was realised in two different simulators between which data (either currents from axons to an FEM solver or extracellular potentials from an FEM solver to compartmental axons-simulators) had to be transferred for every simulation. One of the achievements of PyPNS is to offer a more efficient and less laborious way to coordinate compartmental axon models and FEM solvers. We precomputed potential fields once for a limited number of current point source positions in a finite element model (FEM) and then imported and reused them in PyPNS while making use of geometrical symmetries of the nerves and separation of time and space. This means that the computationally expensive field calculation only had to be carried out once per extracellular medium geometry. To ensure the feasibility of this approach, the extracellular space was modeled using the simplified geometry shown in Fig. 3.6A, with conductivities set to the values given in Tab. 3.1. With the conductivity as a function of radius only (i.e. conductivity boundaries were circularly symmetric), a very limited number of unique point source positions exists, each for a different radius (dots in Fig. 3.6A). We sample the space of unique point source positions and run an FEM simulation for each. This extracellular medium geometry will be referred to as a ‘radially inhomogeneous medium’ in the following.

²A homogeneous but anisotropic medium can in fact be modeled analytically using a conductivity tensor (Nicholson and Freeman, 1975; Goto et al., 2010). A combination of inhomogeneities and anisotropy is not feasible, however.

We used the FEM solver COMSOL 4.3, in which the nerve had a length of 10 cm and was placed in a cubic volume of equal edge length. The inner nerve radius was set to $190\text{ }\mu\text{m}$, the endoneurium thickness to $50\text{ }\mu\text{m}$. All inner boundaries had von Neumann boundary conditions, the potential of the outer border of the cubic volume was set to zero (Dirichlet boundary condition). The current entered the mesh at a single point.

As outlined above, potential fields $\phi(x, y, z, r)$ for different radial point source displacements r were computed. Due to our assumptions concerning the medium, steady state simulations were sufficient (separation of time and space). The static voltage fields were then exported on a grid of $x \in [-1.5, 1.5]\text{ mm}$ with a step of 0.015 mm , $y \in [0, 1.5]\text{ mm}$ with a step of 0.015 mm , $z \in [0, 30]\text{ mm}$ with a step size of 0.03 mm where z is the longitudinal nerve axis and source positions are placed along x . The potential fields were imported in PyPNS where a 4D spline interpolator was used to cover source and receiver positions between the exactly set values in COMSOL. PyPNS afterwards scales the static potentials with current time courses as given in (3.4) with I_{ref} set to 1 nA in COMSOL. The corresponding mechanism in PyPNS is `PyPNS.Extracellular.precomputedFEM`. When running the simulation using an imported potential field, it is vital to assure that the source radii used in the FEM precomputation step cover the requested radii in the PyPNS-simulation. The radius (for either axons segments or stimulation electrodes) selected in PyPNS needs to lie within the precomputed range. E.g., for stimulation, radii are typically larger than the nerve radius whereas for recording the precomputed source radii have to lie within the nerve. Of course, different precomputed fields can be used for recording and stimulation respectively.

Tissue	Conductivity S m^{-1}
Axons (light blue)	0.5 longitudinal, 0.8 transversal
Epineurium (darker blue)	0.1 isotropic
Saline (white)	2.0 isotropic

Table 3.1: Conductivity of different tissues contained in the simulated peripheral nerve; colors correspond to Fig. 3.6 (Capogrosso et al., 2013; Struijk, 1997)

3.2.9 Longitudinally inhomogeneous media

So far we covered extracellular media that have a homogeneous and isotropic conductivity and media that vary in conductivity perpendicularly to the nerve-direction. The latter covers a nerve in a saline

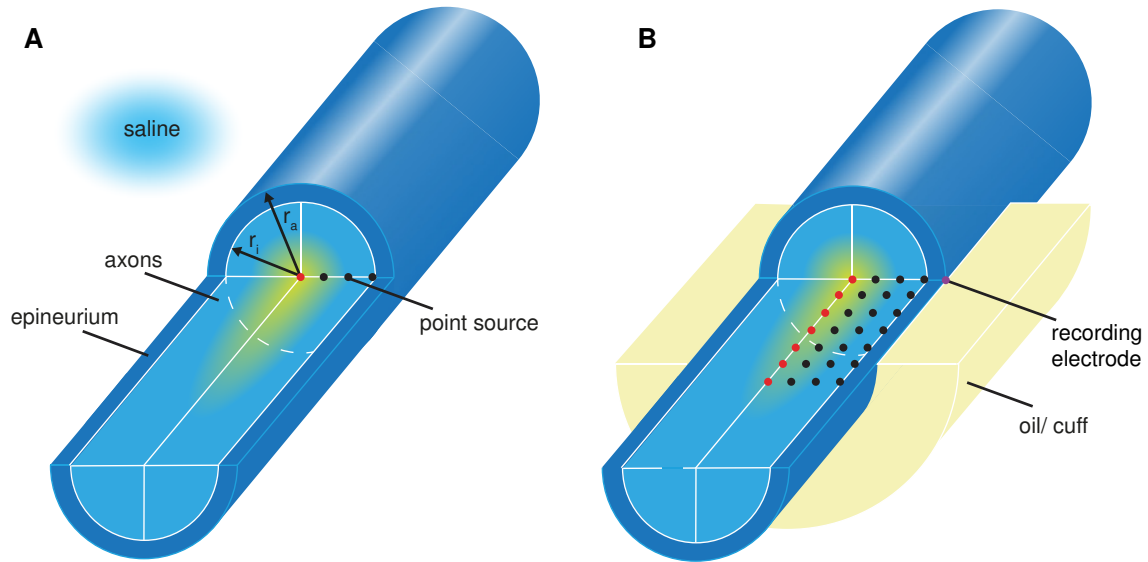


Figure 3.6: **A circularly symmetric geometry makes it possible to import precomputed potential fields.** The nerve is modeled as axons (white matter) surrounded by the epineurium. The positions of exemplary current point sources, each generating one potential field, are shown. **A** For radially inhomogeneous media, a line of sources does characterise all unique fields. **B** For longitudinal inhomogeneities, potential fields for a two-dimensional array of point current sources need to be precomputed.

bath which is a good approximation for a nerve in its natural surrounding. In electrophysiological experiments, however, the nerve does not usually stay in its surrounding tissue. Instead, to increase stimulation efficiency and recording amplitudes, a cuff or a mineral oil bath isolates the nerve and therefore increases the extracellular resistivity. The medium is in this case no longer longitudinally homogeneous, and any longitudinal shift in current source position will result in a different potential field. For stimulation, where the current source (stimulation electrode) position can be fixed in the FEM simulation and the precomputation of very few potential fields, each for one electrode radius, characterises the effect of the electrode completely. For stimulation, potential fields can thus, even for a longitudinally inhomogeneous nerve, be imported in the same way as for radially inhomogeneous media described above when fixing the longitudinal position. For recordings, however, the longitudinal source position necessarily varies, as the axon segments extend through the nerve. Therefore, to cover all unique axon segment potential fields, a 2D-array of source positions distributed along both radial and longitudinal direction must be precomputed, as shown in Fig. 3.6B.

Without circular symmetry, a volume of source positions would need to be sampled and simulated, rendering the precomputation infeasible³. In this case, one needed to abandon our efficient precom-

³For a nerve of radius 200 μm , a longitudinal length coverage of 20.000 μm and a source position grid step of 20 μm this would mean approximately 300,000 simulations, each taking at least 30 minutes on a single core of a state of the art workstation, totaling to a computation time of over 17 years. The result would occupy 12 TB of RAM.

putation and would be forced to fix the axon geometries for one particular case. An FEM simulation would need to be performed for each axon segment position to then either export the potential fields for the whole space or fix the electrode positions as well and export the potentials only at the electrodes. This described method, however, is less universal as axon geometry changes would require a full re-run of the FEM-simulations, is much more computationally expensive, and involves a lot more coordination between FEM simulation and compartmental axon model. Still, if the (axon and extracellular space) geometry stays the same, recordings and stimulation could still be simulated with different firing characteristics and stimulation pulses using the same FEM-result.

We came to the conclusion that for recording, a reasonable number of current source positions (~20, each using about 40MB of memory) still lead to interpolation errors between fields from longitudinally adjacent source positions causing artifacts in the extracellular action potentials. For the recording from longitudinally inhomogeneous media, we thus fit a smoothed transfer function to FEM model results that translates point current source position to the potential in the cuff. Details are given in appendix 3.5.D. This transfer function served in PyPNS as a variant of `PyPNS.Extracellular.analytic`.

3.3 Results

3.3.1 Axon models

As described in Methods Sec. 3.2.4, we extended the myelinated axon model of McIntyre et al. (2002) to smaller diameters by parameter-extrapolation. For very low diameters ($< 1 \mu\text{m}$), this extrapolation yielded bursting behavior as soon as the fibres became activated through either synaptic input or stimulation. Bursting is not surprising as the node size does not scale with diameter in McIntyre's model. Therefore the relationship between ion influx axon segment capacity rises with shrinking axons. In PyPNS, we prevented bursting by increasing the nodal potassium channel density by 50%. Alternatively, node size reduction with diameter achieved the same effect but is not observed in physiology (Tuisku and Hildebrand, 1992; Berthold and Rydmark, 1983). Potassium channels in the paranodal regions (not included in the original model) have been observed physiologically (Poliak and Peles, 2003; Röper and Schwarz, 1989) but their integration in the model did not abolish bursting in tests.

The myelinated conduction velocity (CV) of our extrapolated axons fit experimental data well (CV [m s^{-1}] $\sim 5 \cdot d$ with diameter d in μm).

Unmyelinated axons based on Hodgkin-Huxley channels had very low conduction velocities, CV $\sim 0.4 \cdot \sqrt{d}$, in comparison with expected values of around $2 \cdot \sqrt{d}$ (Waxman, 1980). This is an inherent property of the Hodgkin-Huxley axon model. Realistic unmyelinated axon models for mammalian nerves are still to be developed.

Membrane current directly shapes extracellular potential recordings as outlined in Sec. 3.2.6. There it is informative to take a look at the raw current output of both axon types shown in Fig. 3.7. Fig. 3.7A displays membrane current in time for one unmyelinated axon segment, Fig. 3.7B plots the current of one node of Ranvier. Fig. 3.7C provides an overview of the relation between diameter and integrated absolute current output. It is important to note that unmyelinated axons emitted more current per distance. Myelinated axons are more efficient in their use of ion channels thanks to their saltatory conduction principle. As a second observation, the signal shapes differed considerably. While the unmyelinated current time course was smooth in time, the myelinated current showed a more complex time course with a sharp peak and a long lasting recovery. The different segments (node, myelin attachment segment (MYSA), paranodal main segments (FLUT)) in a myelinated axon all contribute to the overall current output causing the visibly higher complexity in membrane current shape. See the model of McIntyre et al. (2002) for more details on section types.

3.3.2 Profiles of extracellular media

In section 3.2.6 we highlighted the impact of the longitudinal profile $\phi_{\text{static}}(z)$ on the single fibre action potentials (SFAPs). Building on these considerations, the normalised $\phi(z)$ -profiles of our media can be compared and their impact on extracellular recordings predicted. Fig. 3.8 shows the normalised static potentials over distance for all three media (homogeneous, nerve in saline, nerve in cuff). The strong impact of the cuff insulation on the extracellular potential profile immediately catches the eye. It became smooth, stretched out in space and strikingly triangular. The thin nerve surrounded by an insulation acted as two parallel resistors, causing a linear characteristic. For radial displacements of the current source towards the electrode, a sharp peak emerged (see also Fig. 3.S2). For such a wide profile we would expect fast conducting axons with long active length l_a to be best suited and

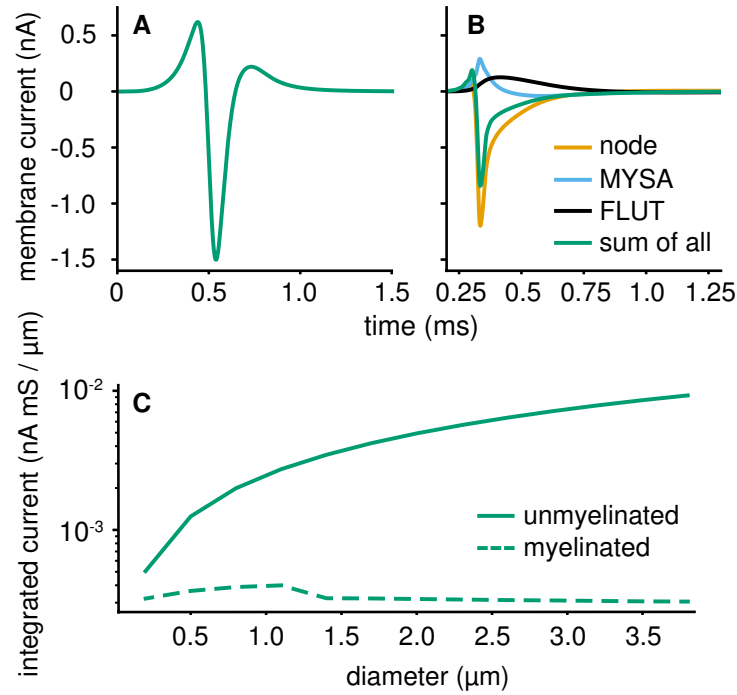


Figure 3.7: **Unmyelinated axons (A) produce a smoother membrane time course than myelinated (B) ones.** Both axons had a diameter of $3\mu\text{m}$. **C** Unmyelinated axons produce a higher current output per distance. The integrated absolute current during a single action potential over axon length is shown. Simulated data.

result in high recording amplitudes. The other two media resulted in a very different, much narrower potential characteristic. Radial inhomogeneities lead to a slightly smoother profile compared to the homogeneous case but differences remained very small. The steep decay in potential for both these media were expected to better suit slower conducting axons with a shorter l_a .

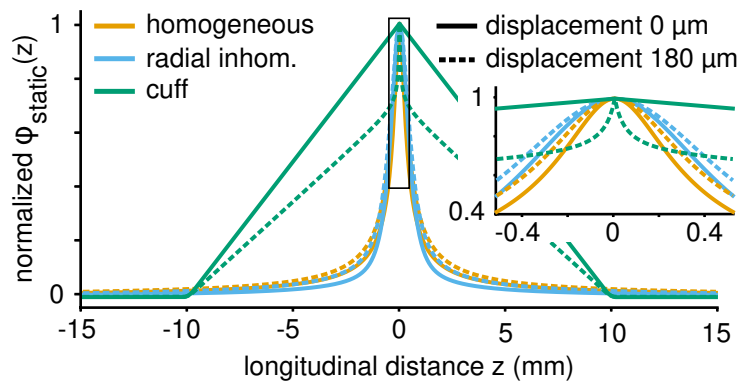


Figure 3.8: **Longitudinal potential profile of different media.** Compared to the homogeneous and radially inhomogeneous extracellular media the cuff insulation caused a much softer and strikingly linear characteristic. Electrode radius was $235\mu\text{m}$. The profiles are shown for two radial axon displacements in solid and dashed lines respectively. Simulated data.

3.3.3 Extracellular single fibre action potentials

So far we have seen the membrane currents and extracellular potential profiles that both together shape the extracellular recordings from axons. In Fig. 3.9, the resulting SFAPs can be compared for all three media and the two axon types. Axons were activated intracellularly by current injection and recorded by a monopolar circular electrode at radius $235\text{ }\mu\text{m}^4$. In the cuff medium, where the electrode position has to be fixed, it was placed centrally as shown for one point electrode in Fig. 3.6B. Fig. 3.9A displays a recording from a single unmyelinated fibre. When comparing the recordings from the three different media, mainly the amplitude varied but shape stayed relatively stable. When insulating the nerve using a cuff, the potential rose by a factor of about ten and caused a narrower signal shape. In addition, an entrance and an exit peak caused by the resistivity drop at the sides of the cuff emerged which were not present for the two longitudinally homogeneous media. The radially inhomogeneous medium (nerve in saline) slightly stretched the action potential in time compared to the homogeneous case which can be explained by the preference of current to flow along the nerve rather than transversally (compare to profile in Fig. 3.8).

The SFAP of myelinated axons in Fig. 3.9B showed a much higher susceptibility towards extracellular medium properties than unmyelinated fibres. While the difference between homogeneous and radially inhomogeneous medium remained small in shape (still amplitude more than doubled), the amplitude and shape changed radically in the cuff. Amplitude rose by a factor of about 20 and the recorded signal lasted longer with (as for unmyelinated axons) a negative main and two positive entrance and exit peaks.

Fig. 3.9C provides an overview of SFAP amplitudes for unmyelinated and myelinated axons against diameters for different media. In homogeneous and radially inhomogeneous media SFAP amplitudes of unmyelinated axons were similar and even higher than myelinated SFAPs for diameter above $1\text{ }\mu\text{m}$. In the cuff however, myelinated fibres achieved much stronger amplitudes following – even though their membrane current output is substantially smaller compared to unmyelinated fibres (see Fig. 3.7). This difference in the effect to the cuff isolation between fibre types can be traced back to the two different mechanisms through which cuff insulation changed SFAP amplitude. The first one is the increase in extracellular resistance the cuff causes. Current cannot dissipate freely into the

⁴Electrode radius was chosen to be slightly smaller than nerve radius to maintain a small distance to the non-conducting insulation layer surrounding the nerve.

surrounding tissue but is confined to the thin nerve. As membrane current was modeled to be independent of the medium, an increase in extracellular resistance equaled an increase in extracellular potentials. This mechanism takes the same effect on SFAP amplitudes of both fibre types. The second mechanism can explain the difference in amplitude gain between fibre types. It is the match between active length (as defined in (3.7)) and cuff dimension (equal to range of the profile; 20 mm in this case) as detailed in section 3.2.6. For a myelinated axon of diameter $3\ \mu\text{m}$ the active length evaluated to approximately $0.5\ \text{ms} \cdot 15\ \text{m s}^{-1} = 7.5\ \text{mm}$, an unmyelinated axon of this diameter only had an active length of about $0.5\ \text{ms} \cdot 1\ \text{m s}^{-1} = 0.5\ \text{mm}$. SFAPs from myelinated fibres are thus amplified by constructive superposition of contributions from many axon segments. Fig. 3.9C demonstrates this matching effect between myelinated axons and the cuff over all diameters.

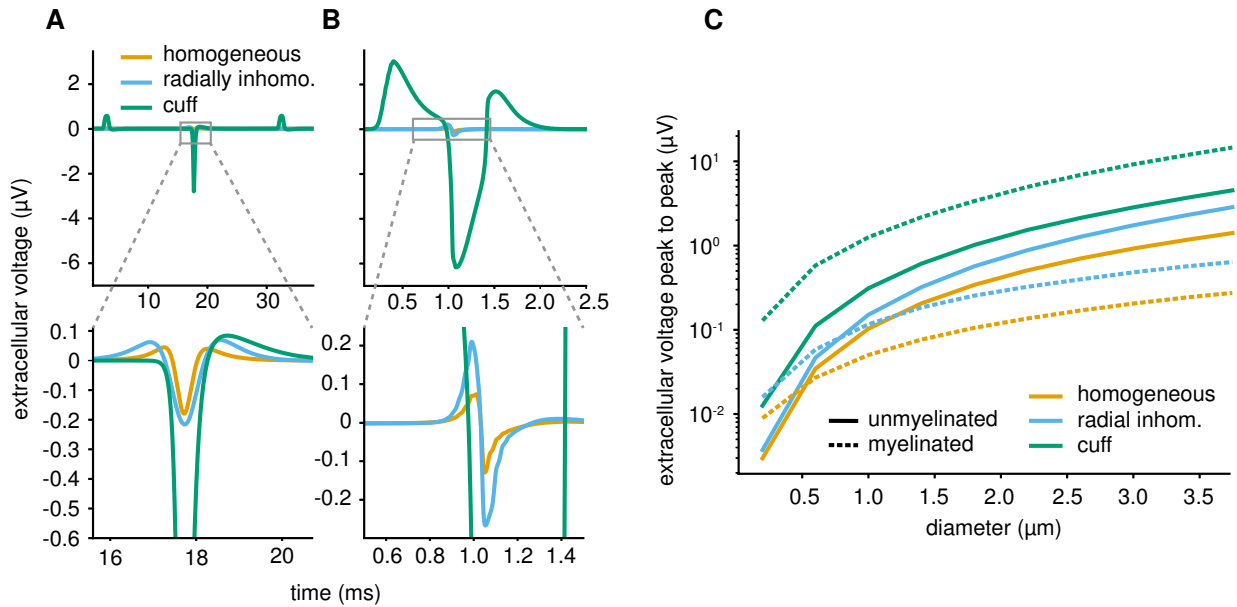


Figure 3.9: Unmyelinated and myelinated SFAPs showed different sensitivities towards the extracellular space. In the upper plots (A,B), diameters were set to $3\ \mu\text{m}$. **A** The main peak of unmyelinated fibres mostly varied in amplitude over media, not in shape. In cuff insulated nerves, additional side peaks emerged. **B** Myelinated fibres produced much higher and longer lasting SFAPs in the cuff insulated medium. Both axons had diameter $3\ \mu\text{m}$, were placed centrally within the nerve and recorded by a circular monopolar electrode with radius $235\ \mu\text{m}$. Conductivity of the homogeneous medium was set to $1\ \text{S m}^{-1}$. Lower row shows zoomed-in plots. **C** The amplitude boost achieved by cuff insulation was stronger for myelinated than for unmyelinated axons over the whole diameter range. For the other two media, unmyelinated SFAPs produced stronger SFAP amplitudes at diameters above 0.5 and $1\ \mu\text{m}$ respectively. Simulated data.

3.3.4 Effects of varying the cuff length

As a tool for bioelectronic medicines, PyPNS should, next to generating surrogate data, help the design of peripheral nerve interfaces. To demonstrate its utility for this cause, we take a look at the impact of cuff length on the recorded signal amplitude for both myelinated and unmyelinated axons of different diameters. Fig. 3.10 shows how unmyelinated and myelinated fibres require different cuff lengths for a maximal SFAP amplitude which is expected from their different active lengths (see above). Unmyelinated fibers with their lower conduction velocity and therefore shorter active length produce the strongest signals for (theoretic) cuff lengths of about 1 mm. While such short cuffs are most likely not implementable as they would need to be very thin as well, medium lengths of about 1 cm seem reasonable according to our simulation. The amplitude of myelinated axons keeps increasing until very high cuff lengths of 10 cm but are observed to saturate at intermediate lengths of about 1 cm. PyPNS therefore predicts an ideal cuff length for peripheral nerve interfaces in this order. Results will vary for a more accurate unmyelinated axon model, as higher conduction velocities will increase their active length and therefore ideal cuff length.

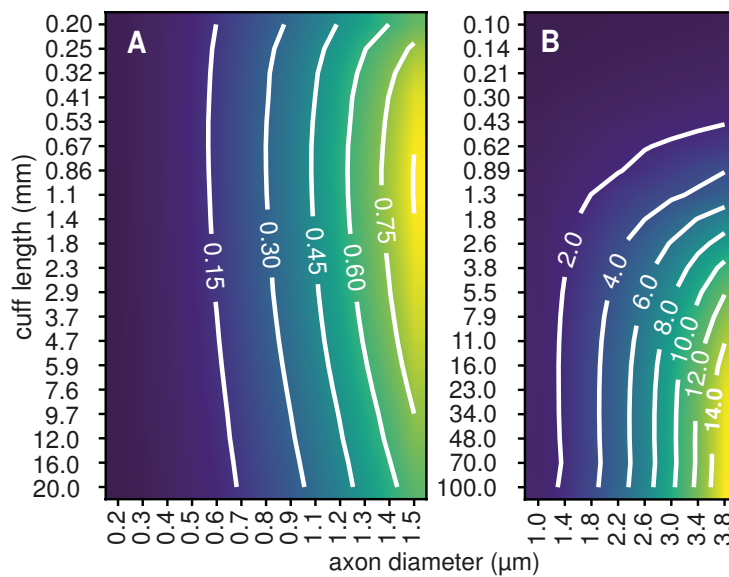


Figure 3.10: **Unmyelinated and myelinated axons have different ideal cuff lengths.** For unmyelinated fibres **A**, very short ranges around 1 mm produce the maximal amplitude. For myelinated ones **B**, the amplitude only rises with length. Contour lines show the peak-to-peak amplitude in μV . Simulated data.

3.3.5 Compound action potentials

To validate the extracellular recording generated by PyPNS, we attempted to reproduce experimental recordings from the stimulated rat vagus nerve. Physiological parameters such as diameter distributions and fibre counts were obtained from literature (microscopy analysis) (Precht and Powley, 1990) as summarised in Tab. 3.2. The nerve geometry and the recording electrode configuration was further set to match the experimental set-up. Outer and inner nerve radius were set to $240\text{ }\mu\text{m}$ and $190\text{ }\mu\text{m}$ respectively; a circular bipolar electrode of radius $235\text{ }\mu\text{m}$ and pole distance 3 mm (20 recording positions per pole) surrounded the nerve. Axons were placed centrally and were activated intracellularly; due to the difference in stimulation threshold between fibres types, the entire population of myelinated and only a small fraction of unmyelinated axons ($\sim 20\%$ of 10,000) was triggered. As unmyelinated fibres based on Hodgkin-Huxley channels conduct action potentials very slowly, we corrected their SFAP timings. In the experiment we seek to match, the nerve was bathed in mineral oil. Therefore only the cuff medium could be expected to reproduce the extracellular recording in the simulation. Results from homogeneous and radially inhomogeneous media are presented as well in the following for comparison.

Type	#	diameter (μm)
Unmyelinated	2000	$\in (0.2, 1.52)$ distribution from Precht and Powley (1990)
Myelinated	200	$\sim \mathcal{N}(1.7, 0.4)$ (Precht and Powley, 1990)

Table 3.2: Axon number and properties set in the simulation for comparing model results with experimental recordings

The simulation result with all parameters matched to the experiment, we obtain the compound action potential (CAP) shown in Fig. 3.11 along with the experimental data. As can be seen, a reasonable agreement between simulation and experiment was reached in the time domain. This match naturally only held for the cuff insulated medium – homogeneous and radially inhomogeneous media produced only very weak extracellular potential amplitudes as expected from their lower tissue resistances. The signal segment between A- and C-fibres from 25 to 40 ms corresponds to B-fibres which are not implemented in PyPNS.

Especially the signal portion caused by myelinated fibres (Fig. 3.11B) shows as satisfying match to the experiment – in peak amplitudes, area, zero crossings and overall duration. See Tab. 3.3 for a

Myelinated axons		
Feature	Experiment	Simulation
Area ($\mu\text{V ms}$)	115	83.2
Peak-to-peak voltage (μV)	57.5	50.3
Zero crossings	50	45
Unmyelinated axons		
Feature	Experiment	Simulation
Area ($\mu\text{V ms}$)	147	93.9
Peak-to-peak voltage (μV)	25.2	14.0
Zero crossings	271	133

Table 3.3: Quantitative comparison between compound action potentials from experiment and simulation (cuff medium).

quantitative comparison on these parameters. Unmyelinated axons (Fig. 3.11C) also produced a CAP comparable to the experiment in both amplitude and timing although comparison becomes more difficult as the signal to noise ratio in the experimental data is lower due to their overall lower amplitudes. Table 3.3 summarises how area and amplitude of the experimental recording are larger than in the simulation as well as the considerably higher number of zero crossings in the experiment. The noise in the experiment will be accountable for a share of the crossings. Differences in the extracellular recordings of unmyelinated axons were expected of course, as the Hodgkin-Huxley model used for unmyelinated axons did not to exactly match the properties of rat vagus nerve C-fibres.

In the time domain, a reasonable match between experiment and simulation has been shown above. Fig. 3.12 shows how this match holds reasonably well in the frequency domain for both fibre types. The spectrum of the unmyelinated signal proportion in our experimental data (black lines in Fig. 3.12A) had an overall flat profile with a main peak (lower plot) at around 500 Hz. PyPNS approaches this characteristic to a certain extent. While spectra from all three media have slightly earlier peaks below 500 Hz, homogeneous and cuff medium followed the characteristic of the experiment well between 0 to 2 kHz before decaying further below -20 dB from there. We surmise that the high frequency content of the experimental data may be caused by high frequency noise from the recording process. Meaningful, spike-event related signal components from experimental recordings usually stay below 2 kHz (Diedrich et al., 2003).

The experimental spectrum of myelinated fibres (Fig. 3.12B) was dominated by low frequency power below 2 kHz with a peak at about 500 Hz. It has to be noted that the frequency resolution at ~ 0.5 KHz

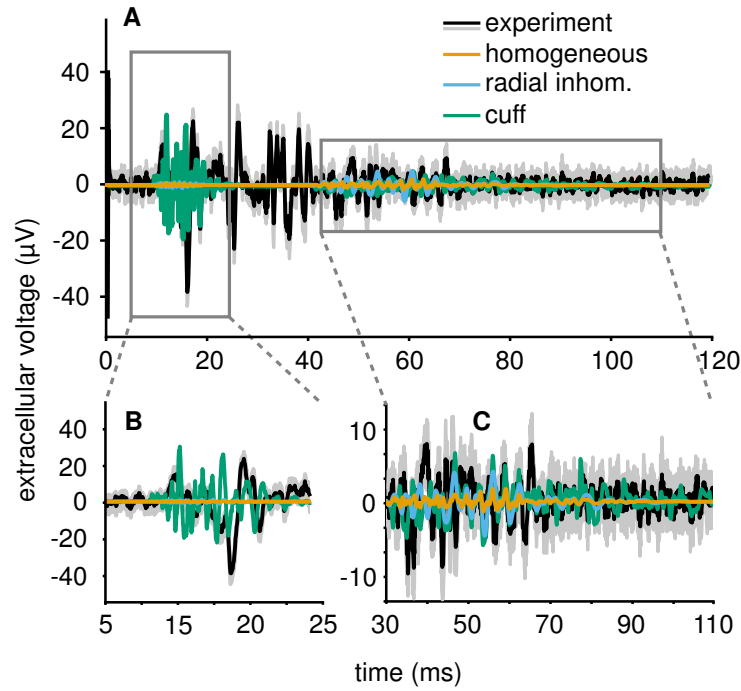


Figure 3.11: **Comparison between experimental and simulated CAP: time domain.** **A** The simulated compound action potential in the cuff medium approaches the experimental recording well in the relevant signal segments. As expected, homogeneous and radially inhomogeneous media lead to much weaker signal amplitudes. For the experimental recording, the gray underlying area indicates the standard deviation over the 10 stimulation repetitions. See Tab. 3.2 for axon properties. Distance between stimulation site and bipolar electrode (3 mm pole distance, 235 µm radius) was 8 cm. All axons were activated by intracellular stimulation. The timing of unmyelinated SFAPs was adapted to regular conduction velocity values assumed in mammalian peripheral nerves ($CV = 1.4 \cdot \sqrt{d}$, CV in m s^{-1} , d in µm). **B** The signal from myelinated fibres, which arrive first, appears similar to the experiment. **C** The unmyelinated signal segment (C-fibres) matches the amplitude and duration of the experimental recording as well. The signal-to-noise ratio of the recordings is much worse for unmyelinated fibres, however, as the amplitude of their SFAPs is low.

was rather coarse. We reproduce this characteristic well in our simulation for the cuff medium over the whole frequency range, at a slightly later peak around 1 kHz. The other two media led to a flat characteristic with a larger amount of high frequency power and less low frequency power. This was expected from the SFAP shapes in Fig. 3.9 with myelinated SFAPs much wider in the cuff than in the other media.

In conclusion, we could match the the experimentally obtained frequency characteristic of both axon types reasonably well by our simulation for the cuff medium.

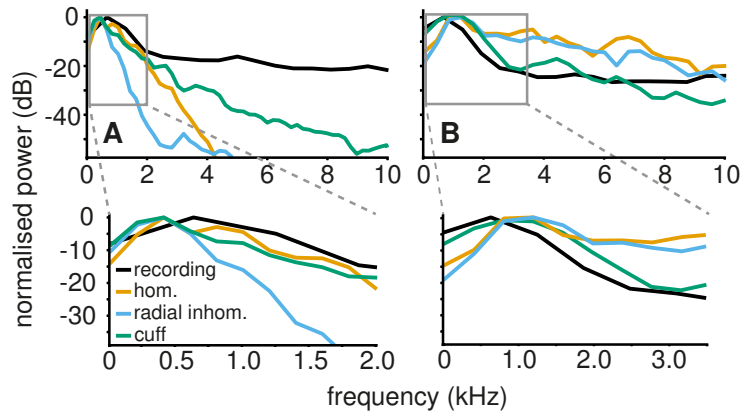


Figure 3.12: **In the frequency domain, simulation and experiment did not match equally well for both fibre types.** **A** For unmyelinated axons, the simulation did not perfectly approach the experimental spectrum in any medium with best results for the cuff. **B** The simulated frequency characteristic of myelinated axons in the cuff insulated medium was close to reality. Simulated data.

3.3.6 Fitting axon tortuosity to experimental data

In order to obtain axon shapes close to reality, we fit the distributions of axon segment direction changes c in simulation to imaged nerves as detailed in methods section 3.2.1.2. Fluorescence microscopy images were available for the mouse sciatic and vagus nerve as shown in Fig. 3.13.

In Fig. 3.14 we compare the direction change distributions from microscopy (Fig. 3.14A) to the ones of simulated axons (Fig. 3.14B) alongside a few example axons in space (Fig. 3.14C). The vagus nerve's axons are more tortuous than those of the sciatic nerve as Fig. 3.14A demonstrates in the wider distribution of segment direction changes (c -values). Fig. 3.14B shows simulated direction change distribution obtained at different parameters ($\|\mathbf{w}\|$ -distribution and α) in PyPNS. When comparing these to Fig. 3.14A, a Gaussian $\|\mathbf{w}\|$ -distribution clearly better reproduced imaged c -distributions. The sciatic nerve then corresponded to an α -value of about 0.6, the vagus nerve had a wider c -distribution as its axons were curvier, corresponding to a higher α . When inspecting the resulting trajectories in Fig. 3.14C from uniform (upper plot) and Gaussian (lower plot) c -distributions, the effect of a normal distribution of random vector length $\|\mathbf{w}\|$ is visible. It leads to both a slightly smoother trajectory and rare strong direction changes, especially for high α -values.

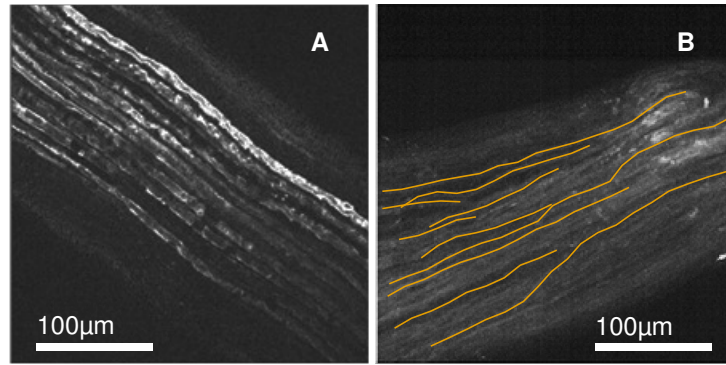


Figure 3.13: **Fluorescence microscopy images of the mouse sciatic and vagus nerve.** Both show slight tortuosity in their axon trajectories. **A** The thick myelinated fibres in the sciatic nerve appear very parallel. **B** The thinner axons in the vagus take a more curvy trajectory. Several manually traced fibres used to fit the model are highlighted in orange.

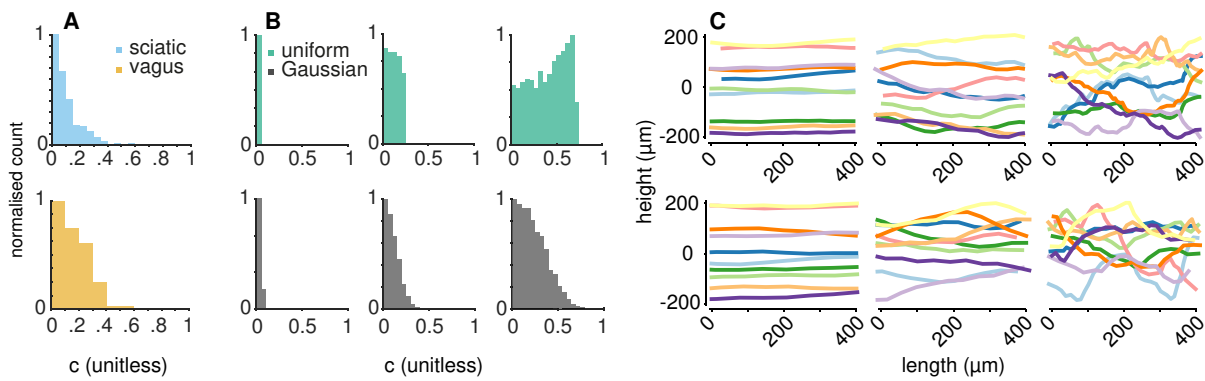


Figure 3.14: **The axon placing algorithm result (B, C) was fit to tortuosity of microscopy imaged fibres (A).** **A** Direction change distributions (c -distributions) for vagus and sciatic nerve. **B** c -distributions in the simulation for both normally and uniformly distributed amplitude of the random component $\|\mathbf{w}\|$ in (3.3) for α s of 0.2, 0.6, and 1.0. **C** Example axon trajectories in space for uniform (upper) and Gaussian (lower) $\|\mathbf{w}\|$ -distributions at α -values of 0.2, 0.6, and 1.0. Simulated data.

3.3.7 Recording from tortuous axons

Now that we can generate realistic axons shapes with different degrees of curviness we are equipped to investigate the impact of tortuosity on the recorded extracellular potentials. As Fig. 3.15 demonstrates, a more complex axon trajectory caused more complex SFAPs – but not to the same degree in both axon types.

Unmyelinated SFAPs (Fig. 3.15A) were especially sensitive to tortuosity. They developed complex, long lasting signals, especially in homogeneous and radially inhomogeneous media. When insulating the nerve by a cuff, the amplitude of the main SFAP peak became very weak at high tortuosity while many small side peaks arose, giving the signal a noisy appearance. Myelinated fibres (Fig. 3.15B) showed a higher robustness towards tortuosity – their SFAP shape remained invariant at low and

medium α -values. Only high degrees of tortuosity could change signal timing and shape; as for unmyelinated axons, the cuff isolated medium let the signal become noisy.

Why do SFAPs get more complex with rising tortuosity? This effect can be understood from looking at Eq. (3.10) (same as Eq. (3.5)) and changing it as in Eq. (3.11) where s is the distance along the axon. In a tortuous axon, the longitudinal distance $z(s)$ along the nerve becomes a function of s . For the sake of simplicity, differences in the potential ϕ depending on the radial displacement of the axon were neglected here. For a tortuous axons, the potential profiles of the extracellular media (see Fig. 3.8) are then both stretched ($z(s) \leq s$) and distorted in a degree dependent on tortuosity. Different axons show different susceptibilities to these distortions depending on their active length. If the active length is large compared to the spatial frequency of the tortuosity-induced profile distortion, variabilities in $\phi(z(s))$ are smoothed away. Axons with shorter active length can follow those variabilities in detail and produce a response to them in their SFAPs, giving it a 'noisy' appearance in which each bump corresponds to a longitudinal distortion the the potential profile caused by tortuosity. This explains the difference in susceptibility between axon types.

$$\phi_{\text{SFAP}} = \sum_{z_i} \phi(z_i) \cdot i \left(t - \frac{z_i}{CV} \right) \quad (3.10)$$

$$\Rightarrow \phi_{\text{SFAP}} = \sum_{s_i} \phi(z(s_i)) \cdot i \left(t - \frac{s_i}{CV} \right) \quad (3.11)$$

To quantify the influence of α on the heterogeneity of SFAP shape, we calculated the pairwise cross-correlation

$$(f \star g)(\tau) = \int_{-\infty}^{\infty} f(t) \cdot g(t + \tau) dt \quad (3.12)$$

between normalised SFAP waveforms $s_{\alpha,i}$ from repeated simulation runs while keeping α , fibre type, and medium unchanged. We then used the mean maximum cross-correlation over all waveform pairs to describe shape homogeneity:

$$c_\alpha = \frac{2}{n \cdot (n-1)} \sum_{k=0}^{n-1} \sum_{l=k+1}^{n-1} \max(s_{\alpha,k} \star s_{\alpha,l}). \quad (3.13)$$

The resulting Fig. 3.15 confirms that a higher tortuosity degrees α caused higher differences in shape (lower c_α). While myelinated SFAPs remained similar even for large α s, unmyelinated ones lost their similarity comparably quickly. Note that this measure does not take into account differences in timing or amplitude.

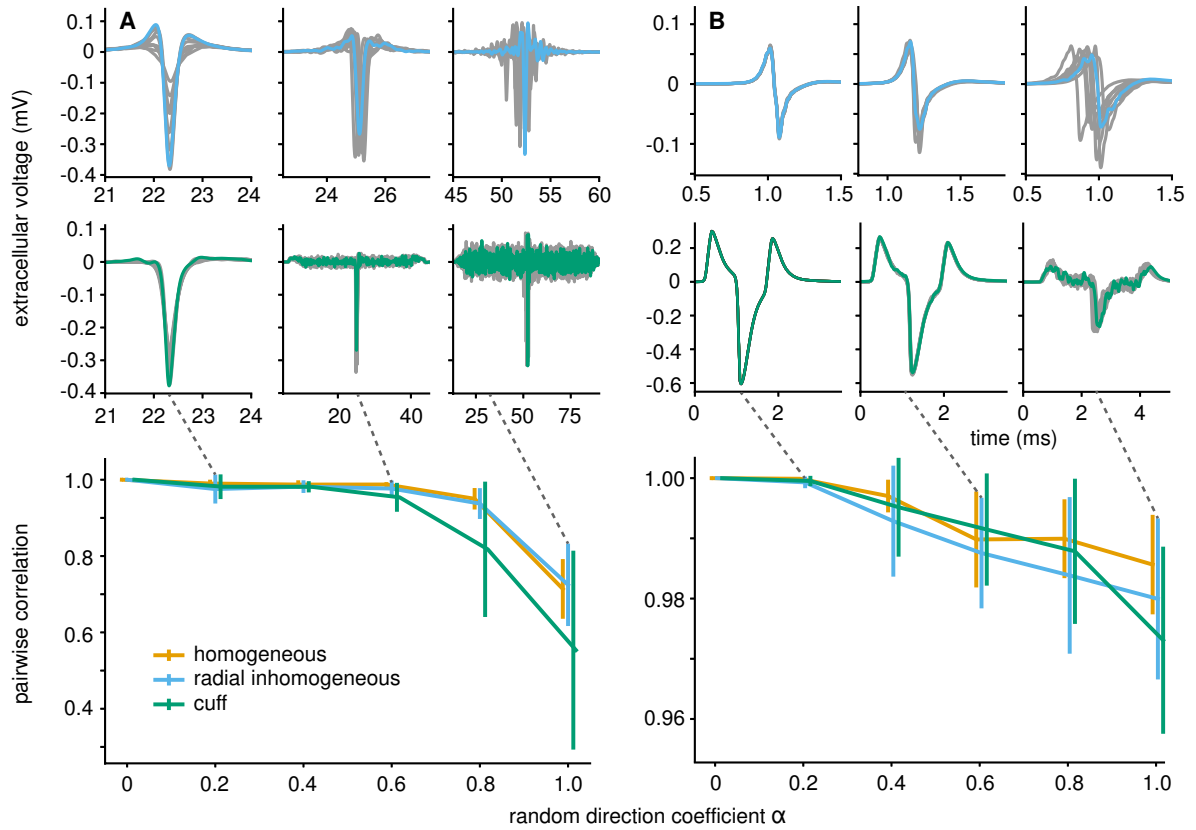


Figure 3.15: Unmyelinated axons were more sensitive to tortuosity in their SFAP shapes than myelinated ones. Tortuosity parameter α was set to 0.2, 0.6, and 1.0 for the signals shown in the first two rows. Gray lines correspond to SFAPs of different trials (axon geometries) at the same parameters. **A** Unmyelinated axons produced SFAPs differing both in timing and shape for the non-insulated nerve (radially inhomogeneous medium), even for small α -values of 0.2. In the cuff-insulated nerve (middle row) their signals became noisy at low α -values and the main SFAP peak almost disappeared for $\alpha = 1.0$. **B** Myelinated axons mostly differed in timing in the radially inhomogeneous extracellular space, and not as much in shape. In the cuff, noisiness only arose at high tortuosity values. In the lower plots, the mean maximum pairwise cross-correlation gives a quantitative confirmation of the higher susceptibility of unmyelinated axons to change their SFAP shape in the presence of tortuosity. Note the different ordinate scales. Simulated data.

3.3.8 Stimulation of tortuous axons

Not only the recording from but also the stimulation of axons is expected to be influenced by their trajectory. We therefore investigated the effect of tortuosity on extracellular stimulation efficiency for both fibre types. Fig. 3.16 shows the result as the activation ratio of unmyelinated and myelinated fibres for different degrees of tortuosity and different stimulation amplitudes. Again, as for recording, strong differences between both axon types exist.

One observation to make first, regardless of tortuosity, is the higher stimulation threshold of unmyelinated axons. Then, when taking a look at the influence of axon curviness, unmyelinated fibres showed an optimal stimulation current of about 3 mA with a smooth decrease in stimulation efficiency for higher and lower current amplitudes. In the low amplitude range (< 3 mA), perfectly straight axons are activated best. In higher current regimes, tortuous unmyelinated axons had better chances of becoming stimulated. Myelinated axons on the other hand were successfully stimulated from low amplitudes of about 150 nA and at almost any higher current at all degrees of tortuosity. A necessary closer look at a fine-grained increase in stimulation current in Fig. 3.16C reveals a minor increase in stimulation threshold with tortuosity. Therefore, tortuosity affected the activation ratio of unmyelinated axons substantially stronger than it did for myelinated ones. We only carried out this study at a fixed diameter of $3\text{ }\mu\text{m}$ as the focus here was to investigate the effect of tortuosity on stimulation thresholds. It would be interesting to compare the results for different diameters. Overall, stimulation thresholds are expected to fall with rising diameter but maybe the susceptibility of the fibres towards stimulation will change as well.

3.4 Discussion on our simulator PyPNS

The open-source simulation framework that we have proposed here for the first time integrates compartmental axon models and numerically solved extracellular space models into a single environment. To make the import of precomputed voltage fields feasible and efficient, the modeled media needed to fulfill certain constraints. One was the geometry that had to be circularly symmetric. While presenting a strong simplification of the extracellular medium, this implementation can be seen as a generic peripheral nerve in which axons can still cluster to fascicles. Another constraint concerned

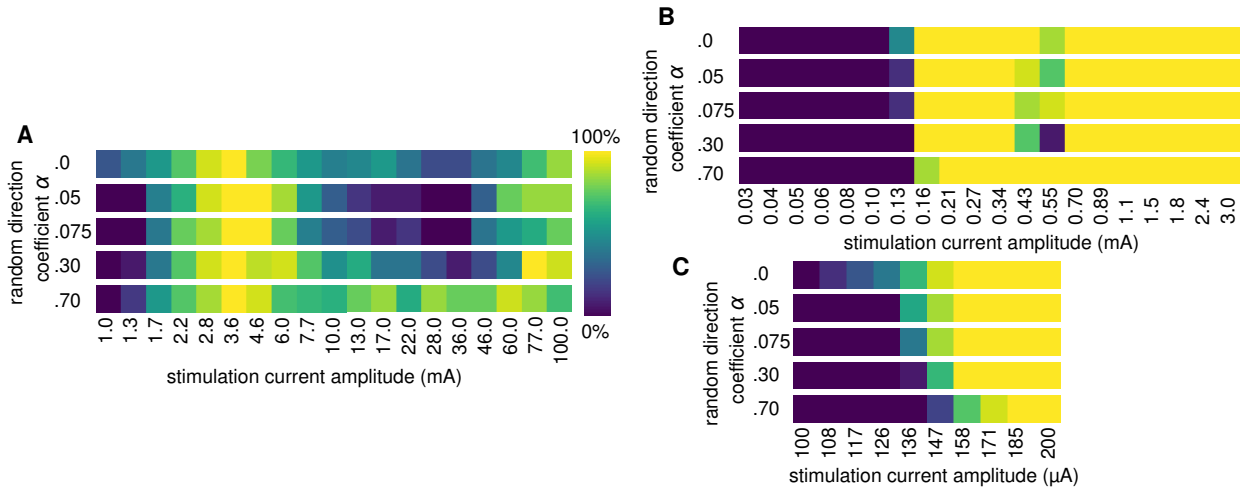


Figure 3.16: **Unmyelinated axons have higher stimulation thresholds and are activated less reliably than myelinated ones.** Both bundles consisted of 15 axons with diameter $3\text{ }\mu\text{m}$ and were stimulated with a bipolar electrode of radius $235\text{ }\mu\text{m}$ and pole distance 1 mm using a biphasic pulse of frequency 1 kHz , duration 1 ms and duty cycle 0.5 . The extracellular medium was a nerve of diameter $240\text{ }\mu\text{m}$ bathed in oil. **A** Unmyelinated axons started to be activated at 1 mA and showed a peak in activation ratio at about 3 mA . **B** Myelinated fibres had a sharp activation threshold at a much lower current of about 0.15 mA and stayed activated for higher currents. Only when incrementing the stimulation current in very small steps of about 10 nA **C** a slight tortuosity-induced increase in stimulation threshold became visible for them as well. Simulated data.

material properties. Displacement currents and therefore frequency dependence of the tissues was not accounted for. Such frequency dependence certainly exists to a certain extent. It can arise from macroscopic structures at constant material properties (dielectric constant ϵ and conductivity σ) – the epineurium can for instance act as a capacitor. In addition, polarisation at different microscopic levels (Bédard and Destexhe, 2009; Martinsen et al., 2002) can render the material properties ϵ and σ themselves frequency dependent. Such dielectric dispersion is observed in most biological tissues (Gabriel et al., 1996). Ephaptic coupling and neurodiffusive effects were neglected as well.

In terms of axon geometry, we implemented a simple iterative placement mechanism that was fit to microscopy data. To our knowledge this is the first implementation of such automated shape generation for peripheral nerve models. It enabled us to investigate the influence of tortuosity on recordings and stimulation efficiency and indicated that perfectly straight axons are an oversimplification. Our simulation predicted that SFAPs become more complex with increasing tortuosity – an effect that is exploited by spike sorting algorithms which differentiate single units from their SFAP shape. For now, axons were positioned independently from another. As a next step, fibre trajectories could be correlated as observed in microscopy images.

The modular nature of our model allows for an easy comparison of different extracellular media. Building on this functionality, we identified an ideal cuff length for peripheral nerve interfaces. We also showed how the long temporal extent of SFAPs in cuff-insulated media – especially for myelinated axons – makes differentiation of single fibre contributions difficult as overlaps are probable. Overall a cuff therefore increased amplitude but reduced recording precision.

One limitation of the current NEURON simulation is the unmyelinated axon model. Its conduction velocity was too low compared to that reported for mammalian axons. For the overall CAP, the velocity needed to be corrected. Still, the Hodgkin-Huxley parameters are the accepted standard model for unmyelinated axons and more detailed C-fibre models (e.g., Sundt et al. (2015)) do not achieve significantly higher conduction velocities either. Parameters of the current model such as membrane capacitance or intracellular resistivity could be adapted to reach the expected conduction velocity but we chose to leave them at their physiological values. If more accurate axon models become available, they can be integrated into PyPNS.

Several steps to improve the model beyond the mentioned limitations are imaginable. First, axons are currently simulated sequentially. For the simulation of closed loop systems interacting with peripheral nerves, the simultaneous simulation of all nerves would be preferable. Second, axon membrane sections only need to be simulated if they are either stimulated or recorded from extracellularly, otherwise the calculation of their highly uniform membrane processes is unnecessary and time consuming. In order to eliminate computational overhead, one could introduce an abstract layer into the simulation in which the position change of spikes along axons is computed based on a known conduction velocity profile. Only for axon segments relevant to stimulation or recording, would the full membrane process be simulated.

In conclusion, a unified computer model of a generic peripheral nerve was developed. It combined an efficient calculation of extracellular potentials in inhomogeneous media from precomputed potential fields with compartmental axon models in a convenient Python module. The model was validated against experimental data and used to investigate the effects of conductivity inhomogeneities on amplitude and frequency content as well as the influence of axon tortuosity on both recording and stimulation. We hope that the simulation framework presented here, PyPNS, becomes a useful tool for researchers working on peripheral nerves, nerve stimulation, and its medical applications, and

envision that the toolbox could be augmented by multiple branches, organ models, and a variety of specific axon models matched to fibre types found in different parts of the peripheral nervous system, to facilitate this. We use PyPNS in Chapter 5.1 as a source for surrogate data.

3.5 Appendices

3.5.A Axon model equations

The following two sections give the equations used for the simulation of each axon compartment in NEURON.

Each ionic current of both the myelinated and the unmyelinated model is governed by the following equation where g_{ion} is the maximum conductance, ω is a gating variable, V_m is the membrane voltage and E_{ion} is the potential of the respective ion es given by the concentration difference between inside and outside of the cell.

$$I_{ion} = g_{ion}\omega(V_m - E_{ion}) \quad (3.14)$$

The conductance g_{ion} is modulated by gating variables ω that vary between 0 and 1. Multiple gating variables can be combined by multiplication. Each can be described by the following equation with varying α_ω and β_ω .

$$\tau_\omega = 1/(\alpha_\omega + \beta_\omega) \quad (3.15)$$

$$d\omega/dt = \alpha(1 - \omega) - \beta_\omega\omega \quad (3.16)$$

3.5.A.1 Unmyelinated fibres: Hodgkin-Huxley-model

There are three currents in the Hodgkin-Huxley model (Hodgkin and Huxley, 1952), sodium I_{Na} , potassium I_K , and leakage I_L current. Gating variables m and h for the sodium current and n for the potassium current control their dynamics.

Sodium current

$$I_{Na} = g_{Na} \cdot m^3 \cdot h \cdot (V_m - E_{Na}) \quad (3.17)$$

$$\alpha_m = (0.1 \cdot (V_m + 25)) / e^{(V_m + 25)/10 - 1} \quad (3.18)$$

$$\beta_m = 4 \cdot e^{V_m/18} \quad (3.19)$$

$$\alpha_h = 0.07 \cdot e^{V_m/20} \quad (3.20)$$

$$\beta_h = 1 / e^{(V_m + 30)/10 + 1} \quad (3.21)$$

Potassium current

$$I_K = g_K \cdot n^4 \cdot (V_m - E_K) \quad (3.22)$$

$$\alpha_n = 0.01 \cdot (V_m + 10) / e^{(V_m + 10)/10 - 1} \quad (3.23)$$

$$\beta_n = 0.125 e^{V_m/80} \quad (3.24)$$

Leakage current

$$I_L = g_L (V_m - E_L) \quad (3.25)$$

3.5.A.2 Myelinated fibres: McIntyre (MRG) model

All parameters were taken from McIntyre et al. (2002), except for the potassium channel conductance g_{Ks} that we changed from 0.08 S/cm² to 0.16 S/cm². The equations in McIntyre et al. (2002) are the following.

The gating variables differ for all channels and their parameters are given in the following:

Fast sodium current

$$I_{Na_f} = g_{Na_f} \cdot m^3 \cdot h \cdot (V_m - E_{Na}) \quad (3.26)$$

$$\alpha_m = (6.57 \cdot (V_m + 20.4)) / (1 - e^{-(V_m + 20.4)/10.3}) \quad (3.27)$$

$$\beta_m = (0.304 \cdot (-(V_m + 25.7))) / (1 - e^{-(V_m + 25.7)/9.16}) \quad (3.28)$$

$$\alpha_h = (0.34 \cdot (-(V_m + 114))) / (1 - e^{-(V_m + 114)/11}) \beta_h = 12.6 / (1 + e^{-(V_m + 31.8)/13.4}) \quad (3.29)$$

$$(3.30)$$

Persistent sodium current

$$I_{Na_p} = g_{Na_p} \cdot p^3 \cdot (V_m - E_{Na}) \quad (3.31)$$

$$\alpha_p = (0.0353 \cdot (V_m + 27)) / (1 - e^{-(V_m + 27)/10.2}) \quad (3.32)$$

$$\beta_p = (0.000883 \cdot (-(V_m + 34))) / (1 - e^{(V_m + 34)/10}) \quad (3.33)$$

Slow potassium current

$$I_{K_s} = g_{K_s} \cdot s \cdot (V_m - E_K) \quad (3.34)$$

$$\alpha_s = 0.3 / (1 + e^{(V_m + 53)/-5}) \quad (3.35)$$

$$\beta_s = 0.03 / (1 - e^{(V_m + 90)/-1}) \quad (3.36)$$

Juxtaparanodal fast potassium current

$$I_{K_f} = g_{K_f} \cdot n^4 \cdot (V_m - E_K) \quad (3.37)$$

$$\alpha_n = (0.0462 \cdot (V_m + 83.2)) / (1 - e^{-(V_m + 83.2)/1.1}) \quad (3.38)$$

$$\beta_n = (0.0824 \cdot (-(V_m + 66))) / (1 - e^{(V_m + 66)/10.5}) \quad (3.39)$$

Leakage current

$$I_{Lk} = g_{Lk} (V_m - E_{Lk}) \quad (3.40)$$

3.5.B Calculation of the random component of the axon placing algorithm

The random vector \mathbf{w}_i in (3.3) is split into an inward pointing radial \mathbf{w}_{rad} and a tangential component \mathbf{w}_{tan} (3.41), both weighted independently with a weight drawn from a distribution \mathcal{P} (3.42, 3.43). \mathcal{P} can be either a uniform distribution $\mathcal{U}(-1, 1)$ between -1 and 1 or a normal distribution $\mathcal{N}(\mu, \sigma)$ with $\mu = 0$ and $\sigma = 0.33$ (sigma chosen to have 99.7% of all values in the range $[-1, 1]$). When the radial distance between axon segment and bundle guide d approaches the bundle radius r_{bundle} , the radial component \mathbf{w}_{rad} becomes more inward directed (3.43) and thereby ensures that the axon stays inside the nerve. One linear implementation of the correction factor e is shown in (3.44). The parameter r_{corr} defined the relative radius from which on the correction should begin, set to 0.7 in our simulation; e_{max} , set to 2 by default in PyPNS, limits the correction.

$$\mathbf{w}_i = \frac{\beta_{\text{rad}} \cdot \mathbf{w}_{\text{rad}} + \beta_{\text{tan}} \cdot \mathbf{w}_{\text{tan}}}{\|\beta_{\text{rad}} \cdot \mathbf{w}_{\text{rad}} + \beta_{\text{tan}} \cdot \mathbf{w}_{\text{tan}}\|} \quad (3.41)$$

$$\beta_{\text{tan}} \sim \mathcal{P} \quad (3.42)$$

$$\beta_{\text{rad}} \sim \mathcal{P} - e \quad (3.43)$$

$$e = \min(1, \max(0, \frac{d/r_{\text{bundle}} - r_{\text{corr}}}{1 - r_{\text{corr}}})) \cdot e_{\text{max}} \quad (3.44)$$

3.5.C Generation of simulated c -distributions

To directly translate $\|\mathbf{w}\|$ -distributions (\mathcal{P}) to distributions of the normed difference in direction of consecutive axon segments $c = \|\mathbf{a}_i - \mathbf{a}_{i+1}\|$ projected onto a 2D-plane, we made the simplifying assumption that \mathbf{b}_k and \mathbf{a}_i are aligned. By doing so $\|\mathbf{a}_i + (1.1 - \alpha) \cdot \mathbf{b}_k\|$ (see Eq. (3.3)) becomes $(2.1 - \alpha) \cdot \|\mathbf{a}_i\|$. Following Fig. 3.S1, it is easily shown that then $\|\mathbf{w}\|$ relates to c as

$$c = 2 \cdot \|\mathbf{a}\| \cdot \sin\left(\frac{1}{2} \cdot \arctan\left(\frac{\|\mathbf{w}\|}{\|\mathbf{a}\|} \frac{\alpha}{2.1 - \alpha}\right)\right). \quad (3.45)$$

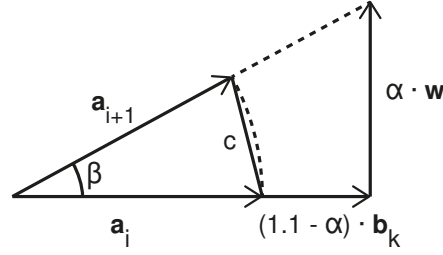


Figure 3.S1: If bundle \mathbf{b}_k and current axon segment \mathbf{a}_i have a fixed relation, e.g., parallel, the expected distribution of segment direction differences $c = \|\mathbf{a}_i - \mathbf{a}_{i+1}\|$ can be easily obtained from the distribution of $\|\mathbf{w}\|$ (\mathcal{P}) by their geometrical relation.

3.5.D Fitted cuff transmission function

For extracellular recording in a cuff, a transfer function between current point source position and the potential at an electrode longitudinally centrally placed in the cuff was fit. Input variables describe the spatial relation between source and receiver position. As apparent from Fig. 3.S2, the relation is strongly linear with an additional peak for low distances between current source and potential receiver – facilitating the fit of a transfer function.

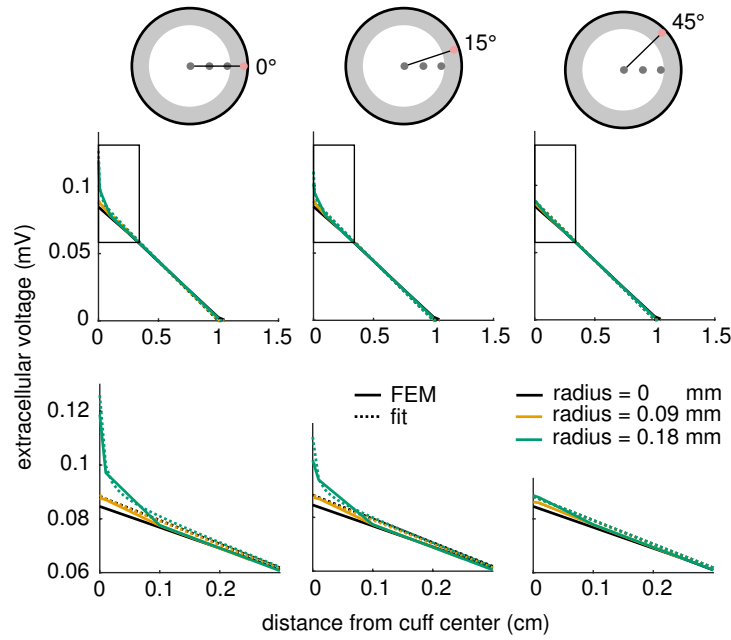


Figure 3.S2: **An analytic transmission function implements the relation between current source position and potential for recording in a cuff electrode.** In the shown case, a nerve of diameter $480\ \mu\text{m}$ in a cuff of 2 cm length was simulated in the FEM model. Functions are displayed for three different angles between the perpendiculars of source and electrode position onto the bundle guide respectively.

The static potential was therefore described as a linear component $f_{\text{lin}}(z)$ plus a nonlinear peak $f_{\text{peak}}(z)$. Equations (3.48) - (3.50) implement this characteristic for ϕ in mV with variables r_{ax} radial axon displacement in m, α angle between axon displacement direction and electrode perpendicular on the

nerve center in rad and z longitudinal distance between electrode and axon in m. The transfer function is parametrised with r_1 for the inner radius of the nerve in m, a and b for maximum peak amplitude and steepness, c for maximum of triangular component and d half the cuff length in m. The left and right borders of the $f_{\text{lin}}(z)$ -function were smoothed with a moving average of width $c/20$.

$$f_{\text{lin}}(z) = \max(0, c \cdot (1 - |z/d|)) \quad (3.46)$$

$$f_{\text{peak}}(z) = \frac{a}{|z| + b} \quad (3.47)$$

$$f_{\text{peak},r}(r_{\text{ax}}) = \min(1, (r_{\text{ax}}/r_1)^5) \quad (3.48)$$

$$f_{\text{peak},\alpha}(\alpha) = \max(0, (1 - |\text{mod}(\alpha + \pi, 2\pi) - \pi|)/\pi \cdot 5) \quad (3.49)$$

$$\phi(z, \alpha, r_{\text{ax}}) = tr(z) + p(z) \cdot pf_r(r_{\text{ax}}) \cdot pf_\alpha(\alpha) \quad (3.50)$$

parameter	value
r_1	$1.9 \cdot 10^{-4}$
a	$2.5 \cdot 10^{-9}$
b	$5 \cdot 10^{-5}$
c	$8.83 \cdot 10^{-4}$
d	0.01

Table 3.S1: Parameters of the fitted transmission function for cuff recordings. Spatial input variables in m, angle in rad, output in mV.

Chapter 4

Encoding and decoding of bladder pressure

While other parts of the thesis consist in more indirect contributions towards peripheral nerve decoding algorithms, such as simulation tools for algorithm development (Ch. 3) and feature-based time-series analyses to generate low-dimensional summaries of peripheral nerve activity (Ch. 5), this chapter covers decoding studies on *in vivo* data from the rat and cat bladder. We thus present decoders tailored to specific datasets that are shaped by today's recording technologies and the system in question rather than providing more general tools to support bioelectronic medicines research as done in the other chapters.

The bladder provides an ideal testbed for the development of closed-loop bioelectronic medicines. It has a single main parameter of interest – its fullness, characterised by both volume and resulting pressure – which can easily be manipulated and recorded. The bladder wall is further covered by numerous stretch sensors that monitor this central quantity. It is thus a good candidate for investigating the encoding and decoding of an organ parameter monitored by a multitude of cells. Developing closed-loop bioelectronic medicines for the bladder is furthermore clinically important, as bladder dysfunction is a common condition both in the elderly population (Diokno et al., 1986), and after spinal cord injury (Wyndaele, 2016; Cameron et al., 2010) and is a topic of much current interest (Wheeler et al., 2018). The resulting incontinence has devastating effects on a patient's quality of life (Milsom et al., 2014; Nitti, 2001). In addition, other malfunctions such as detrusor-sphincter dyssynergia and hyper-reflexia can occur in specific patient groups and cause renal damage, repeated urinary tract inflammations and kidney infections (Watanabe et al., 1996; Shingleton and Bodner,

1993). Sacral neuromodulation has been received well by patients (Damon et al., 2013; Van Wunnik et al., 2011).

The lower urinary tract (LUT), consisting of the bladder, urethra and sphincter, is innervated by the pelvic, the pudendal, and the hypogastric nerves (de Groat et al., 2015). The pelvic nerve projects to the internal pelvic organs including bladder, urethra, bowel, and vagina (de Groat, 2006; Vodušek, 2004). The pudendal nerve goes to the pelvic floor including urethra, sphincter, anal sphincter, perineal region, genitalia (Bahns et al., 1987; Todd, 1964; Cueva-Rolón et al., 1994). The hypogastric nerve forms a plexus with the pelvic nerve, innervating similar regions, including the bladder neck/proximal urethra. We are therefore mainly interested in pelvic nerve fibres that originate in the sacral-level dorsal root ganglion (DRG) (Nascimento et al., 2018) to innervate the bladder wall.

Most cell bodies giving rise to the afferent fibres projecting through the pelvic nerve to the bladder can be found in sacral-level S1 and S2 DRG (Downie et al., 1984; Applebaum et al., 1980). In cat, of the approximately 40 000 cell bodies in the sacral DRG S1 and S2 (Chung and Coggeshall, 1984), about 1000 innervate the bladder (Jänig and Morrison, 1986; Applebaum et al., 1980; Uemura et al., 1975; de Groat, 1986). This population is composed of both small myelinated A δ and unmyelinated C-fibres, of which the former are generally accepted to transport the mechanoreceptor impulses and trigger the normal micturition reflex (de Groat et al., 2015, 1981; Häbler et al., 1993; Evans, 1936). C-fibres are associated with nociception but have been reported to sense bladder pressure in addition to A δ fibres (Sengupta and Gebhart, 1994b). The bladder neuron responses were characterised as tonic (A δ) and phasic (C-fibres) (de Groat and Yoshimura, 2010), sometimes described as pressure (A δ) and volume (C) receptors (Morrison, 1997) and are usually found to have a diversity of activation thresholds within each diameter range (Bruns et al., 2011a; Iggo, 1955; Bahns et al., 1986; Sengupta and Gebhart, 1994b). Some exhibit hysteresis (Ross et al., 2016). While the large body of physiological studies draws a detailed descriptive picture of bladder afferents, elucidating the physiological significance of the different cell types for pressure encoding has not been attempted. The question of why the diverse bladder neuron responses exist is one we seek to answer in the encoding part of this work (Ch. 4.2).

For our studies, we could analyse two datasets of electrically recorded bladder afferents with different degrees of recording detail. First, a recording from the rat pelvic nerve by a hook electrode in oil with

simultaneous bladder pressure manipulation and recording. Second, microelectrode array (MEA) recordings from the dorsal root ganglion (DRG) in cats, again with simultaneously manipulated and recorded bladder pressure. The different data required us to implement different summary statistics of the recorded signal for decoding, adapted to the respective signal-to-noise ratio and spatial resolution. In the high-resolution recordings, we first quantitatively analysed the response characteristics of bladder units using information theory and established an encoding-model. Exploiting this understanding of the encoding, we implemented an informed bladder pressure decoding method from a low-dimensional population activity vector. In the dataset of lower recording resolution, we captured the characteristic of the population response in a nonlinear transfer function between nerve power and pressure.

4.1 Decoding of bladder pressure from hook electrode recordings of the rat pelvic nerve

In this first low-resolution dataset, we focussed on the development of a decoder capable of reading out bladder pressure in real-time from electroneurograms, or compound action potentials (CAPs), recorded from the pelvic nerve of the rat. The pelvic nerve is a parasympathetic nerve that monitors and controls bladder function (Danziger and Grill, 2015; de Groat et al., 2015), and is thus a suitable recording site to evaluate PNS decoding algorithms. We show that by extracting a spectral signature optimised for mutual information conveyed about the pressure signal, linearising to remove the effect of a static nonlinearity, and applying an optimal linear filter, it is possible to decode robustly and effectively bladder pressure from the pelvic nerve in both the Wistar and the Spontaneously Hypertensive Rat (SHR) model. We examined the effect on our decoder of delivery of PGE₂, which generates acute symptoms of overactive bladder, and found that PGE₂ resulted in systematic underestimation of bladder pressure by the decoder, which can be corrected by incorporating PGE₂ data into the training set.

4.1.1 Methods

4.1.1.1 Experiments

The animal experiments were done by the group of Warren Grill at Duke University for previous studies. All animal care and procedures were reviewed and approved by the Institutional Animal Care and Use Committee at Duke University. Experimental data collection was similar to that described in detail in (Danziger and Grill, 2015). Briefly, adult Wistar ($n=3$) or Spontaneously Hypertensive Rats ($n=3$) were initially anaesthetised with isoflurane gas, followed by two subcutaneous injections of urethane totalling 1.2 g kg^{-1} . One hour after injections the animal's reflexes were tested via foot pinch, and supplemental 0.1 g kg^{-1} doses of urethane were given as needed until the foot withdrawal reflex abated. A cystometrogram comprising two to six bladder contractions was obtained by inserting a catheter into the bladder, and using a syringe pump connected to the catheter in series with a pressure transducer to pass room temperature 0.9% NaCl into the bladder at controlled flow rates. Recordings were made from the pelvic and hypogastric nerves, using nerve hook electrodes in mineral oil with 0.1% collagenase, and recorded with an ADInstruments Powerlab 8/35 system. Nerve signals were sampled at 10 kHz, and bladder pressure at 1 kHz. See Fig. 2.5B for an example.

4.1.1.2 Frequency band selection

We extracted continuous signals in 50 Hz frequency bins from 1 Hz to 1 kHz without overlap, by using a Short Time Fourier Transform, with a window length of 0.5 s. The resulting signals were smoothed with a moving average window length of 10 s (for this analysis only), which was optimised to maximise mutual information while preserving temporal fidelity. To establish quantitatively the most informative frequency bands, we used the Kraskov estimator for the Shannon Mutual Information (MI) (Kraskov et al., 2004; Schultz et al., 2015) between the power spectral density for each band, and the bladder pressure time course. We selected the frequency range with MI above the mean for subsequent analysis, using the same range for all recordings.

It has to be noted here that the two signals pressure and nerve activity vary at entirely different time scales. We quantified the nerve signal power in windows (0.5 s) during which pressure did not change much, but many single action potentials could occur. We were thereby able to show that quick com-

ponents of the nerve activity (caused by a higher firing rate) are informative of the bladder pressure even if a direct spectral coherence measure (Halliday and Rosenberg, 2000) was not applicable for the two signals.

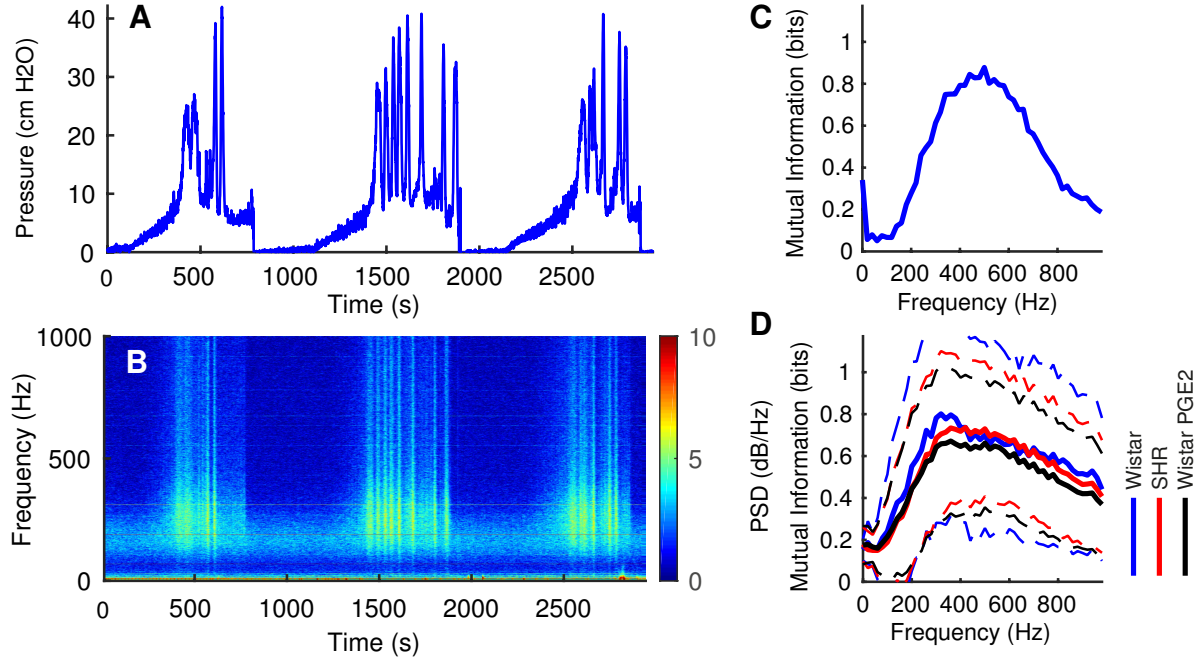


Figure 4.1: **Cystometrograms and information spectra.** **A** An example pressure recording from a Wistar rat, showing three bladder contraction cycles. **B** Power spectral density (PSD) fluctuations throughout the contraction cycle. **C** Information spectrogram for the example shown in Fig. 4.1. **D** Information spectrogram for the dataset of 3 Wistar and 3 SHR rats, as well as post delivery of PGE2 for two of the Wistar rats. Solid line: mean mutual information for the relevant frequency band; dashed lines indicate standard deviation.

4.1.1.3 Piecewise Linear Fit

The simplest decoder we examined involved performing a piece-wise linear (PWL) fit of the instantaneous relationship between the measured pressure (see Fig. 4.1A for an example) and the nerve power (PNA) (see Fig. 4.1B) integrated across the spectral band from 200 Hz to 1 kHz (selected from the MI analysis). For this purpose, the bladder pressure was divided into a fixed number of intervals in which a segment of the piece-wise linear curve would take a linear shape of constant slope. Neighboring segments could differ in slope but had to connect. The slopes of all segments were chosen to minimize the squared error between the piece-wise linear curve and the actual nerve power. As a compromise between overfitting and accuracy of the PWL, we selected 5 intervals. See Fig. 4.2A for an example fit. This PWL function was then used to look up the estimated pressure, instant by instant, for a given nerve power.

4.1.1.4 Optimal Linear Filter

An optimal linear filter (OLF) can build the time-dependent linear relationship between a series of measurements x_i and a quantity of interest y_i by convolving the last n measurement samples with a filter β and adding a constant offset. See Eq. (4.1). The coefficients $\hat{\beta}$ are optimized to minimize the error between estimated quantity of interest \hat{y} and the true values y for all time steps i . In our case, we used an OLF to derive an estimated bladder pressure (\hat{y}) from the last n samples of nerve recording power in the selected frequency band (x).

$$\hat{y}_i = f_{\beta,i}(x) = \hat{\beta}_0 + \hat{\beta}_1 x_i + \dots + \hat{\beta}_n x_{i-n+1} \quad (4.1)$$

$$\text{with } \hat{\beta} = \operatorname{argmin}_{\beta} \sum_i (y_i - f_{\beta,i}(x))^2 \quad (4.2)$$

4.1.1.5 Piecewise Linear Fit followed by Optimal Linear Filter

The OLF described in the last section can incorporate the history of measured nerve activities (PNA), but assumes a linear relationship between bladder pressure and PNA. On the other hand, the decoder based on the piece-wise linear fit mapped the stationary non-linearities between PNA and pressure but only used one single PNA measurement at a time to estimate pressure without considering the history of PNA values. To combine the two strengths of the respective decoders, we here first linearised the relation between PNA and pressure by subtracting the PWL curve from the PNA datapoints to obtain a PNALFit. We then combined this linearised nerve power with an optimal linear filter. Instead of training the OLF with the original PNA values, we used the linearised PNALfit values (see Fig. 4.2B).

4.1.1.6 Cross-validation

Five-fold cross-validation (Witten et al., 2002) was used throughout the analyses described here. The data of each dataset was divided into 5 measurement subsets and the fitting of our estimators was done 5 times with 4/5 of the data for training and 1/5 for testing. Training data only was used for (i) the PWL fit, and (ii) recovery of optimal linear filter parameters. The MI analysis was instead used here to set generically the frequency band, identically, across all recordings. Performance was

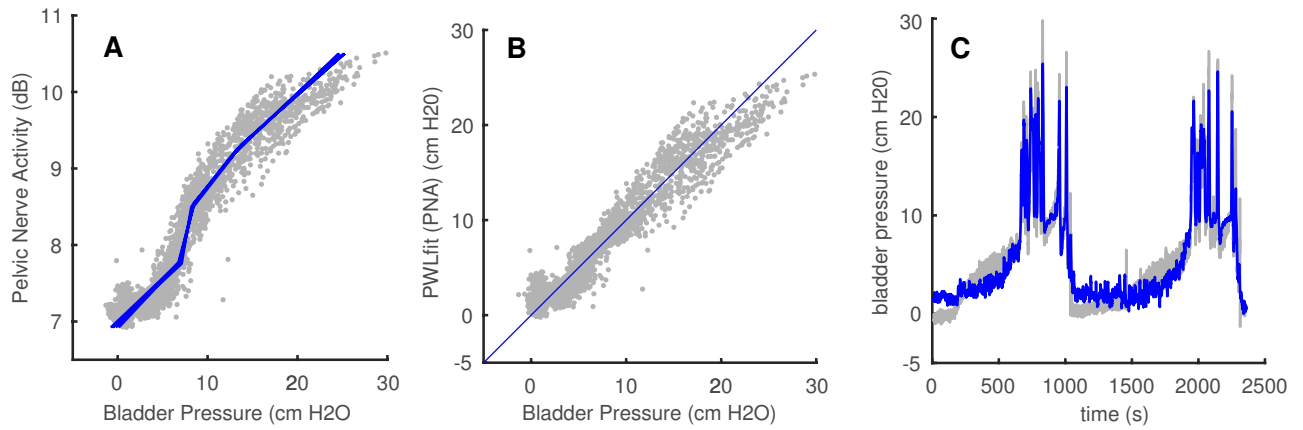


Figure 4.2: **The relationship between bladder pressure and pelvic nerve activity can be fitted well as with a piecewise linear function.** (A) Piecewise linear fit. (B) In our decoding approach, we use this fit to linearise the pressure-nerve activity characteristic. (C) The result of the optimal linear filter on the linearised data over time follows the pressure reasonably well.

then measured on test data. For the training of the PWL model only, data was divided by an entirely randomised sample selection from the whole recording. For the OLF and combined models, the dataset was divided equally into sequential periods.

4.1.2 Results

4.1.2.1 Information about bladder pressure is contained in a broad spectrum of pelvic nerve activity

We examined the frequency content of the pelvic nerve signal throughout the bladder contraction cycle, (Fig. 4.1), finding little power at low (< 200 Hz) frequencies, a band at moderate (200-400 Hz) frequencies that was present at low bladder pressures, but increased in power with bladder pressure, and rapid fluctuations in high frequency (400 Hz-1 kHz) power near the peak of the contraction cycle. To establish the best signal for decoding, we examined the MI conveyed about bladder pressure, by a narrowband signal scanned in frequency (Fig. 4.1). For the example shown in Fig. 4.1, MI about bladder pressure peaked at approximately 500 Hz (Fig. 4.1C). Across a population of 6 nerves, the spectral characteristics of the MI were broadly consistent, although typically peaking at a slightly lower frequency (< 400 Hz). The information spectrum did not differ between Wistar or SHR rats, nor did the delivery of PGE₂ affect information content (Fig. 4.1D).

4.1.2.2 Broad spectrum pelvic nerve activity provides a reliable but nonlinear representation of bladder pressure

A simple way to appreciate the relationship between bladder pressure and nerve activity is to plot the instantaneous time series values against each other (i.e. ignoring dynamics). This is shown in Fig. 4.3. Several things are immediately apparent: firstly, there is relatively little spread around the mean response to each bladder pressure value, indicating that the assumption of a lack of time-dependence is, at first order, reasonable. The residual noise may be accounted for by either noise or time dependence; some time-dependent effects may be addressed by the use of the linear filter approach below. A second observation is that the relationship follows a relatively stereotyped nonlinear form, differing however in detail for each nerve recorded (with respect to threshold, slope, etc). We take this to indicate that an instantaneous decoding approach should be relatively effective, with some small advantage potentially to be gained by the addition of a linear filter kernel.

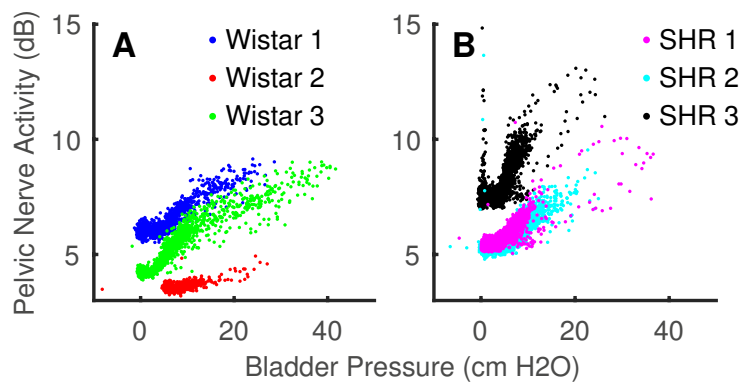


Figure 4.3: **Nonlinear relation between nerve activity and bladder pressure.** While nerve activity varies between individuals (different colours) and type of rat (**A**: Wistar, **B**: SHR), all relationships between bladder pressure and pelvic nerve activity show a similar nonlinear characteristic.

4.1.2.3 Bladder pressure can be accurately decoded from pelvic nerve activity

We found that while reasonably good performance could be obtained by simply estimating the nonlinear relationship between nerve spectral power and bladder pressure, or by instead assuming linearity but incorporating time-dependence through an optimal linear filter, the best decoding performance was achieved by linearising to remove the nonlinearity, then applying an optimal linear filter (see Table 4.1). This approach assumes that there is a static nonlinearity, which is separable from the filter time-course. The PWL+OLF decoder was significantly better, in root mean squared error (RMSE)

terms, than a PWL decoder alone ($p=9.60e-4$, one-sided Student's t-test, $n=6$), and appeared to be slightly (but not significantly) improved over the OLF alone.

Rat	PWL	OLF	PWL + OLF
Wistar 1	2.26 ± 0.10	1.66 ± 0.13	1.62 ± 0.19
Wistar 2	2.76 ± 0.11	2.31 ± 0.40	1.70 ± 0.26
Wistar 3	2.49 ± 0.23	1.90 ± 0.31	1.96 ± 0.29
Wistar (all)	2.52 ± 0.33	1.96 ± 0.28	1.76 ± 0.25
SHR 1	2.27 ± 0.15	2.06 ± 0.45	2.01 ± 0.32
SHR 2	2.11 ± 0.24	1.65 ± 0.18	1.61 ± 0.16
SHR 3	1.96 ± 0.14	1.27 ± 0.48	1.35 ± 0.54
SHR (all)	2.12 ± 0.21	1.66 ± 0.37	1.66 ± 0.34
Wistar and SHR (all)	2.32 ± 0.20	1.81 ± 0.32	1.71 ± 0.29

Table 4.1: Decoder Performance in RMSE \pm cross validation standard deviation (cm H₂O)

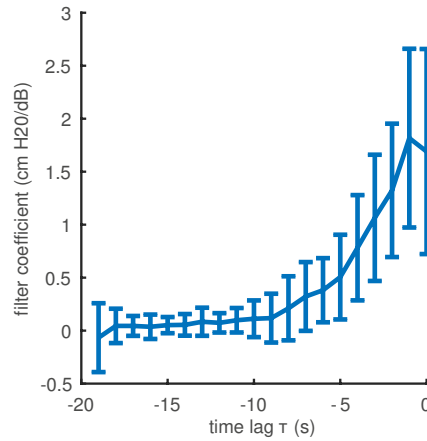


Figure 4.4: **Filter coefficients recovered for the Optimal Linear Filter.** Mean values over $n=6$ Wistar and SHR rats, error bars indicate standard deviation.

In the current version of the decoder, we used a simple PWL function to approximate the nonlinearity (Fig. 4.2A). The residuals from this model fit (Fig. 4.2B) suggest that the model can be improved, particularly at low bladder pressures. This leads to the decoder faithfully tracking the bladder pressure near the peak of the contraction cycle, but some systematic errors in the earlier phase of the contraction cycle (Fig. 4.2C), which should be addressable by incorporation of an improved, smooth, low order model function. The optimal linear filter function recovered (Fig. 4.4) includes structure extending 5-10 s back in time, which can be taken as an indication of the temporal fidelity of this system.

4.1.2.4 PGE2 administration leads to underestimation of bladder pressure by the pelvic nerve

Following recording of bladder pressure and nerve activity throughout the contraction cycle, in two experiments on Wistar rats, prostaglandin E2 (PGE2) was delivered into the bladder (100 μ mol). This offered the opportunity to evaluate how the decoder would behave (i.e. what can be read out from the nerve) under a condition in which the system is pharmacologically perturbed from the conditions under which the decoder was trained. In both examples, the bladder pressure signal decoded from the nerve after PGE2 injection under-estimated the true bladder pressure (Fig. 4.5A). Training in the presence of PGE2 eliminates this bias (Fig. 4.5B).

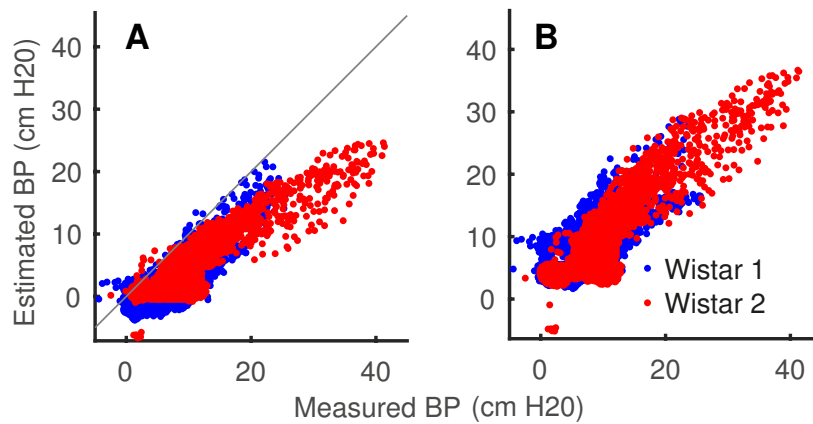


Figure 4.5: **The administration of PGE2 causes the decoder to underestimate bladder pressure.** **A** Mis-estimation due to training on pre- and testing on post-PGE2 administration data. **B** Performance achieved when training with PGE2 data (5-fold cross validation, same test data as A). Negative values are due to the measurement process.

4.1.3 Discussion low-resolution decoder

We have shown that a relatively simple approach to bladder decoding consisting of a piecewise linear fit of the steady-state transfer function and an optimal linear filter can lead to a bladder pressure estimation of satisfactory precision at an RMSE of less than 3 cmH2O. When normalising by the pressure amplitude, this equals a relative error of less than 10%. The frequency-band selection method allowed us to demonstrate how a surprisingly broad spectrum of the pelvic nerve activity is informative of bladder pressure. The linearisation of the transfer function between nerve power and bladder pressure circumvented more complex, nonlinear decoding approaches. This simple decoder is well suited for recordings of low signal to noise ratio that are commonly generated by cuff electrodes in current bioelectronic medicines devices.

4.2 Bladder pressure encoding by groups of stereotypical fibres

In the low-resolution data of our first dataset, we had to relate an imprecise recording of the superposed activity of many fibres to the quantity of interest – bladder pressure. There was no way of monitoring and exploiting the single-unit behaviour and the best we could do was to select an informative frequency band and map the non-linear transfer function between population activity power and bladder pressure. In similar engineering approaches, various ways to decode bladder pressure, volume and contractions from peripheral nerve activity have been explored in the past – usually in a data-driven way without trying to make use of the biological observations. Decoders using pelvic (Mendez et al., 2013; Mendez and Sawan, 2014) (as we did in Sec. 4.1 (Lubba et al., 2017)), pudendal (Wenzel et al., 2006, 2004) or spinal nerves (Chew et al., 2013; Jezernik et al., 2001) have been proposed.

As an alternative, one can interface with sacral-level dorsal root ganglion (DRG) where cell bodies of both pelvic and pudendal nerve fibres reside, see Fig. 4.6A. Recording cell bodies with penetrating microelectrode arrays (MEA) leads to a good signal-to-noise ratio at high spatial resolution. Moreover, the activation of efferent pathways can be accomplished at the same site through reflex circuits (Bruns et al., 2015; Khurram et al., 2017). Decoding from microelectrode arrays implanted in the DRG has been demonstrated (Bruns et al., 2011a; Ross et al., 2018; Ouyang et al., 2019), with a stable interface over weeks (Khurram et al., 2017). While many of the above decoding approaches, be it from a peripheral nerve or from the DRG, estimate bladder pressure quite accurately, none of them directly draw on insights from physiological studies of the encoding. If recording resolution allows, most proposed solutions rely on exact single cell responses (if spatial resolution and SNR allow) that are assumed to be stable over time. If a change in the recording setup occurs, however, e.g., due to electrode migration, cell death, etc, the decoder has no means of detecting this change, and can quickly lose its prediction quality without retraining.

We here want to take advantage of the higher degree of spatial resolution and signal-to-noise ratio that a microelectrode array recording in the dorsal root ganglion offers, to understand the communication principles employed by the sensory population of stretch sensors in the bladder wall as a first step before doing any decoding. A better understanding of the encoding on peripheral nerves will be crucial for next generation bioelectronic medicines for both the precise and robust read-out of physiological

quantities and for adapted ways to stimulate that mimic the existing firing characteristics. While physiologists have led a rich variety of studies on the afferent innervation of the bladder and counted fibres, characterised single fibres, etc. (see introduction of this chapter), principled, quantitative studies of the population codes are missing.

We conducted this research based on microelectrode array recordings from the sacral dorsal root ganglion levels S1 and S2 in cats (see Fig. 4.6A for the experimental apparatus) during a slow filling at a physiological rate. We identified three distinct stereotypical response types that recur across all experiments: slow tonic, phasic, and derivative. For each type, we used information theory to quantify the information it individually carries about bladder pressure, and further estimated the benefits of combining different bladder neuron types – on both real and simulated data. Taking advantage of the insights gained from this information theoretic encoding analysis, we propose an informed decoding strategy from stereotypical groups of fibres that proves to be robust and accurate.

4.2.1 Methods

4.2.1.1 Experiments

We analyse here data previously collected for a study of single-unit hysteresis (Ross et al., 2016) (experiments 1-5) and a comparison of bladder pressure decoding algorithms for the DRG (Ross et al., 2018) (experiments 6-8). The animal experiments were done by Aileen Ouyang, Shani Ross and their colleagues under the supervision of Tim Bruns at Michigan University. Full details of experimental procedures can be found in those respective publications. In short, 8 adult male cats of approximately 1 year of age were used. All procedures were approved by the University of Michigan Institutional Animal Care and Use Committee, in accordance with the National Institute of Health guidelines for the care and use of laboratory animals. For experiments 1 and 5 a 5×10 microelectrode array (Blackrock Microsystems, Salt Lake City, Utah, USA) was inserted in the left S1 DRG and a 4×10 microelectrode array into the left S2 DRG. For experiments 2, 3 and 4, 5×10 arrays were inserted bilaterally in S1 and 4×10 arrays were inserted bilaterally in S2. Experiments 6 to 8 had 4×8 electrode arrays in left and right S1. Microelectrode shank lengths were either 0.5 or 1.0 mm with 0.4 mm inter-shank spacing. Neural signals were recorded at 30 kHz with a Neural Interface Processor

(Ripple LLC, Salt Lake City, Utah). Bladder pressure was recorded simultaneously with a catheter either inserted through the urethra or inserted into the bladder dome, at a sampling rate of 1 kHz and low-pass filtered for further analysis at 4 Hz.

The experimental apparatus is shown in Fig. 4.6A. The bladder was emptied using the bladder catheter before filling it with saline at a near-physiological rate of 2 ml/min (Klevmark, 2002). Inflow was stopped when dripping from the external meatus or, if present, around the urethral catheter was observed. The saline had room-temperature (22°C) in experiments 1-4 and 6-8 and body-temperature (41°C) in experiment 5. Two infusion trials per experiment with only non-voiding bladder contractions form the basis of the following analysis (without the final voiding phase). Trials took 17 min on average (minimum 5 min, maximum 30 min).

After data collection, voltage signals on each microelectrode channel had an amplitude threshold between 20 and 35 μV applied (3–5.5 times the root-mean-square of the signal) to identify spike snippets of neuron action potential firings. Spike snippets were sorted in Offline Sorter v3.3.5 (Plexon, Dallas, TX), using principal component analysis, followed by manual review to identify unique spike clusters. In MATLAB (Mathworks, Natick, MA), instantaneous firing rates for each cell were then calculated by smoothing with a non-causal triangular kernel (Weber et al., 2007) of width 3 s.

4.2.1.2 Fibre selection and characterization

We first inspected fibre responses manually. In this process we observed three distinct response types: (1) ‘slow tonic’: a monotonic rise in firing rate with mean pressure across long time scales without coverage of the quick non-voiding contractions, (2) adapting ‘phasic’ fibres which respond to quick changes in bladder pressure during contractions but, because they adapt over time, do not report the mean pressure with the same fidelity as ‘slow tonic’ ones, and (3) ‘derivative’ fibres which only respond to phases of rising pressure and are, similar to phasic fibres, weakly indicative of the mean pressure.

To select relevant fibres and systematically associate them with the types we found through manual inspection, we computed the Pearson correlation coefficients between firing rates and (1) low-pass filtered pressure below 0.01 Hz, (2) high-pass filtered pressure above 0.005 Hz, and (3) derivative

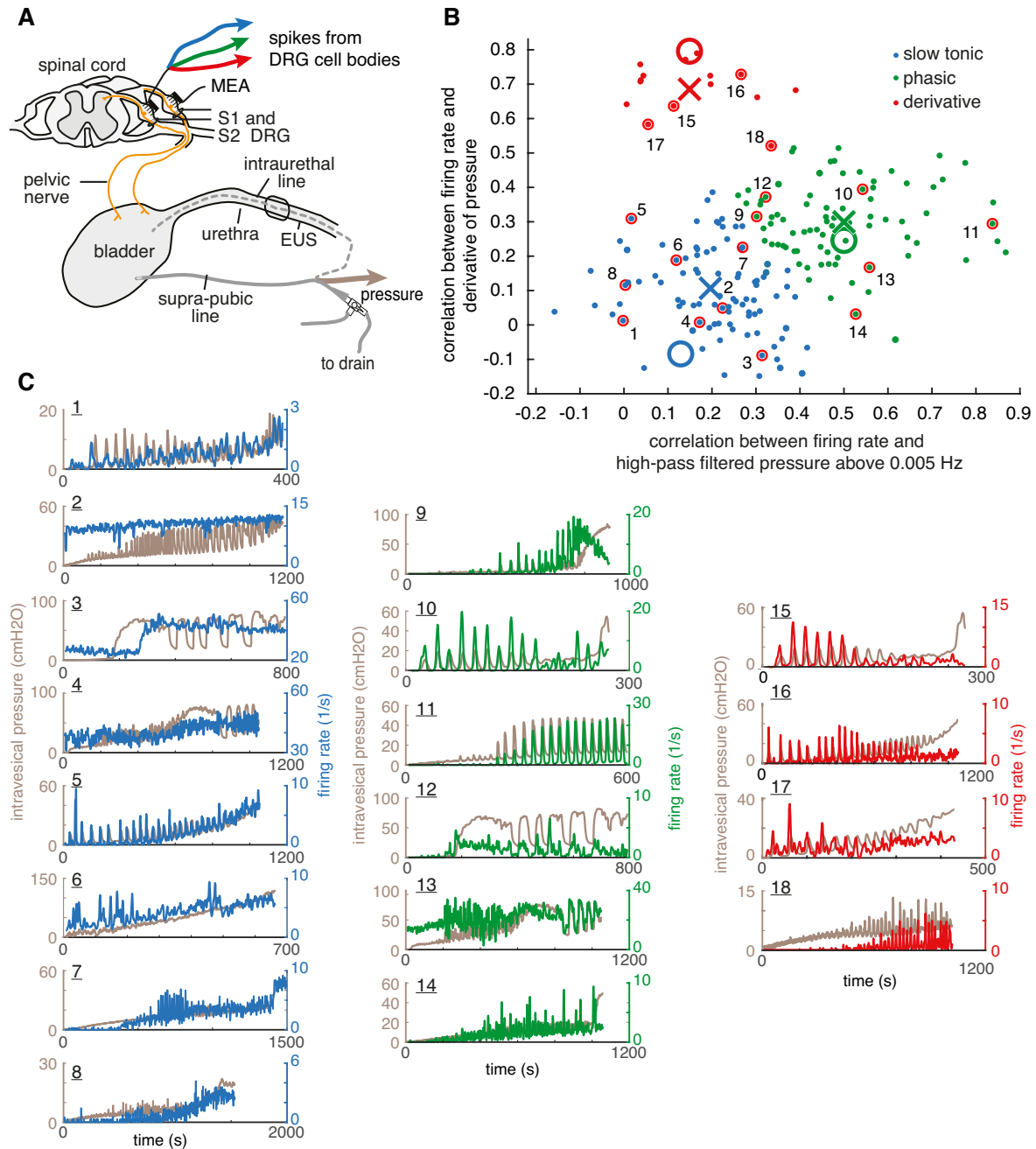


Figure 4.6: Bladder pressure is encoded by distinct groups of stereotypical cells. **A** Microelectrode array (MEA) recording of cells from the first and second sacral dorsal root ganglion (DRG S1/S2) along with the intravesical pressure. The bladder was filled through a catheter in the bladder dome (solid line) or urethra (dotted line). Graphic adapted from Ross et al. (2016). **B** When plotting all fibres of all trials in the 2D-plane of the correlations of firing rates with high-pass filtered pressure (x-axis) and derivative of pressure (y-axis), we can associate regions of this correlation-feature plane with the different bladder neuron types shown in (B). Crosses indicate the cluster centers obtained through *k*-means clustering and large circles show the manually selected initial centers. **C** Example firing rates of bladder neurons along with the corresponding intravesical pressure are shown for different trials. By the indices the plots can be related to the scatter in panel B. The cells stem from the following experiments and trials (E: Experiment, T: trial, C: cell index). 1: E1 T57 C1, 2: E3 T100 C15, 3: E4 T28 C22, 4: E4 T29 C23, 5: E5 T57 C5, 6: E6 T24 C1, 7: E7 T19 C2, 8: E8 T68 C7, 9: E2 T9 C1, 10: E2 T11 C7, 11: E3 T74 C10, 12: E4 T28 C12, 13: E4 T29 C3, 14: E7 T18 C1, 15: E2 T11 C2, 16: E5 T57 C1, 17: E5 T58 C7, 18: E8 T67 C1.

of pressure¹ for every fibre of every trial. A first assumption is underlying this selecting is thus an encoding by rate-coded labelled lines, cf. Sec. 2.3. The high- and low-pass filter cutoff frequencies were chosen to separate the pressure signal into a slow mean component without contractions and the contractions only. We only considered neurons as bladder units that had a raw correlation ρ above 0.4 to at least one of these filtered bladder pressure variants. As our experiments contained many candidate cells (~ 1000) to choose from, we could afford an increased selectivity and be sure to only consider unambiguously relevant neurons.

In the two-dimensional plane of the correlation measures between firing rate and high-pass filtered pressure (x-axis) and derivative of pressure (y-axis), shown in Fig. 4.6B, different fibre types occupy different regions.² We could therefore cluster bladder neurons globally across all trials by their responsiveness to different frequency components of the pressure signal using k-means clustering in this ‘correlation-feature’ plane (converged and initial centers shown in Fig. 4.6B). This approach will be referred to as ‘feature clustering’ and forms the basis of associating each cell to one of the three bladder neuron types slow tonic, phasic, and derivative. We note that no finer frequency analysis was possible, as the pressure signals did not contain spectral power above approximately 0.05 Hz.

Clustering by correlation-features relies on the availability of the pressure signal and its differently filtered variants. As an unsupervised alternative that could, for instance, be carried out on-line in an implanted device, we also clustered fibres hierarchically in each trial based on the pairwise Pearson correlation coefficients between their firing rates (number of clusters fixed to the number of fibre types in each trial). This step allowed us to identify clusters of similarly evolving firing rates – and therefore fibres of similar bladder neuron characteristics – without relying on the bladder pressure. We will denote this approach ‘activity clustering’. Clustering by activity was only possible within each trial, not across trials, as pressure dynamics differed in each trial.

¹The pressure was first low-pass filtered at a high frequency of 0.25 Hz to remove noisy transients. The derivative was computed as the step-wise difference between samples of this filtered pressure.

²As we first assured that all cells had at least 0.4 correlation to any filtered signal variant, cells with low correlations to both derivative and high-pass filtered pressure signals were implicitly identified as only highly correlated to the slow component.

4.2.1.3 Surrogate data

The dataset had three inconvenient properties which affected the analyses: (1) the low-frequency power of the pressure signal was correlated with the high-frequency power as non-voiding contractions mostly occur at high pressures, (2) not all cell types were present in all experiments, and (3) the recording length complicated the estimation of information theoretic quantities (detailed in the next subsection). To overcome these limitations, we created surrogate cells (single cells or populations of similar cells) that reproduced the behavior of the main bladder neuron types, and drove them by idealised stimuli ('pressure signals'). A surrogate cell consisted of an 'intended firing' rate which was derived from the pressure signal (e.g., a low-pass filtered version of the pressure signal) that defined, together with an intended mean firing rate, the rate parameter of an inhomogeneous Poisson process to generate a spike train. See Table 4.2 for a list of the implemented fibre response types. We define a theoretical 'tonic' fibre whose intended firing rate perfectly matches the bladder pressure and a theoretical 'linear' fibre that rises linearly with time (coefficients a and b fit to data). The remaining three types of simulated cells match the response characteristics we found experimentally. The 'slow' fibres follow the low-pass filtered pressure at 0.0005 Hz, 'derivative' cells were driven by the pressure derivative, and 'phasic' responses were defined using a decay parameter τ in seconds that regulates how quickly the fibre adapts. From the spike times output by the inhomogeneous Poisson process, we computed the continuous firing rate just as we did in the real data by a non-causal triangular kernel of width 3 s.

Fibre type	response formula
Tonic	$r(t') = s(t')$
Linear	$r(t') = a + b \cdot t'$
Slow	$r(t') = s(t') * h_{LP}$
Derivative	$r(t') = \max(0, \frac{ds(t')}{dt})$
Phasic	$\frac{dr(t')}{dt} = \max(\frac{ds(t')}{dt}, 0) - \frac{1}{\tau} r(t')$

Table 4.2: Surrogate fibre responses in relation to a stimulus $s(t')$. The operation $*h_{HP/LP}$ indicates convolution with a high-pass or low-pass filter.

4.2.1.4 Information theoretic analysis

Information theory (Shannon, 1948; Cover and Thomas, 2005), originally developed for the study of communication channels in engineered systems, has proven to be a useful tool in neuroscience for quantifying the information carried by a single cell or a population of neurons about a variable of interest (Schultz et al., 2009; Panzeri et al., 1999; Panzeri and Schultz, 2001; Schultz et al., 2015; Schneidman et al., 2003). We here consider a common information theoretic quantity, the Shannon mutual information (MI), estimating (1) how much information each fibre carries about the pressure stimulus, and (2), how much benefit there is in combining the information from two different fibres or fibre types. In the continuous case, mutual information $I(X, Y)$ is computed between two variables X and Y of probability distributions $p_X(x)$ and $p_Y(y)$ and joint distribution $p_{(X,Y)}(x, y)$. In our case, X could for instance be the firing rate of a selected cell and Y could be the bladder pressure signal. $I(X, Y)$ then quantifies the amount of entropy of variable X that is lost when knowing what values Y assumes in all joint measurements of X and Y :

$$I(X, Y) = \int_Y \int_X p_{(X,Y)}(x, y) \log \left(\frac{p_{(X,Y)}(x, y)}{p_X(x) p_Y(y)} \right) dx dy, \quad (4.3)$$

In addition to the two-variable case, we can also quantify the joint mutual information that two variables X and Y carry together about a third variable of interest Z :

$$I(X, Y; Z) = I(X; Z) + I(Y; Z|X), \quad (4.4)$$

where for $I(Y; Z|X)$ we have to adapt Eq. 4.3 by replacing all distributions of X and Y by conditionals to Z and integrate over the distribution of Z . We can further combine the individual mutual information measures of both X and Y and their joint mutual information about Z to a quantity called ‘fractional redundancy’, \mathcal{R} , which can assume values between -1 and 1 and indicates how much less information the ensemble of X and Y contains about Z than the sum of the parts,

$$\mathcal{R}(X, Y; Z) = \frac{I(X; Z) + I(Y; Z) - I(X, Y; Z)}{I(X, Y; Z)}. \quad (4.5)$$

Note that negative values of redundancy imply synergistic interaction between variables. We compute the described information theoretic quantities from firing rate and pressure at a sampling rate of

1/s using the Kraskov mutual information estimator for continuous signals (Kraskov et al., 2004), implemented in the JIDT toolbox (Lizier, 2014) which we run from MATLAB (Mathworks, Natick, MA). The conditional mutual information needed for the joint MI (Eq. 4.4) was computed in the full joint space (Frenzel and Pompe, 2007; Vejmelka and Paluš, 2008) as implemented by the JIDT toolbox.

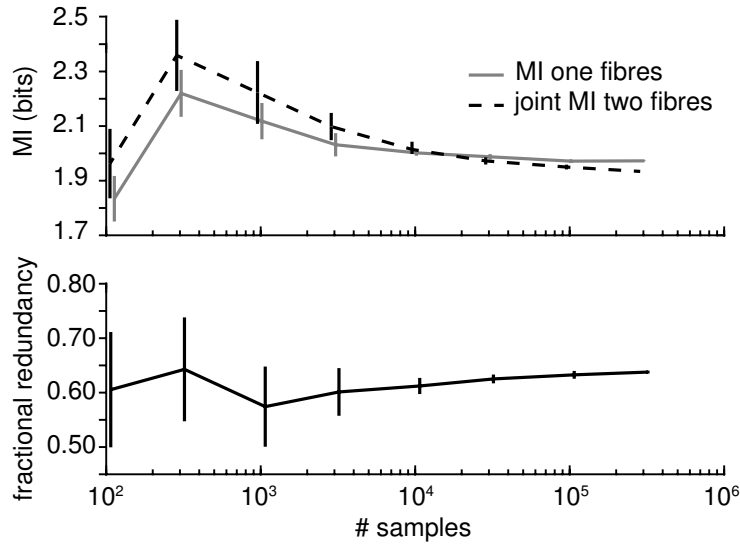


Figure 4.7: **Finite sampling bias results in mild overestimation of mutual information and joint mutual information, but a slight underestimation of redundancy.** Mutual information, joint mutual information and redundancy were computed from the firing rate of a simulated tonic fibre (pair) and an idealised pressure signal. Firing rate was set to 20/s for single fibres, and 10/s for each fibre in a pair; 5 repetitions for each signal length. See Sec. 4.2.1.3 and Fig. 4.10 for details of the simulated data.

As our trials were of limited length (1036 ± 399 samples), mutual information estimates were upwardly biased due to finite sampling effects, which are incompletely removed by the Kraskov estimator (Kraskov et al., 2004). This is illustrated in Fig. 4.7 for a single and a pair of simulated tonic fibre(s). At 1000 samples, mutual information of a single fibre is overestimated by approximately 7% and joint mutual information by approximately 14%, and redundancy is underestimated by 12%. From 10 000 samples, joint and single mutual information as well as the redundancy stabilize. Asymptotic behaviour was judged by visual inspection.

4.2.1.5 Decoding

So far we described the quantification of information that individual fibres and fibre combinations carry about pressure – on both real and surrogate data. Using the following approach, we made use of our refined understanding of the physiological encoding and designed an adapted decoder. When

estimating bladder pressure from nervous activity, we face two main areas of choice to be made. (1) The pre-processing of the neural signal: whether we sort cells or take some measure of activity per electrode, what cells we choose if sorted, how we compute the spike rate, and (2) the type of decoding algorithm we use: Optimal Linear Estimator (OLE), Kalman, etc. We focus here on the pre-processing based on the sorted cell responses and fix the decoding algorithm to an OLE for simplicity. For the optimal linear filter, the decoded pressure \hat{p}_t^{OLE} was obtained from the firing rates vector f_t and the regression coefficients β at a given time t :

$$\hat{p}_t^{OLE} = \beta^T \cdot f_t, \quad (4.6)$$

where β minimizes the mean-squared error E (N number of time-points):

$$E(p, \hat{p}) = \sum_{t=1}^N (p_t - \hat{p}_t)^2. \quad (4.7)$$

From our encoding results, we compare three signal variants to decode from in both estimation error and robustness against lost cells – a common problem due to electrode migration or cell death:

- all single sorted cells
- cells of each fibre type pooled (as in Fig. 4.6B)
- cells of each activity cluster pooled

For pooled signal variants, we normalised the firing rate of each cell by its mean to make sure their contributions added with equal weight. We tested the robustness of these different pre-processing variants to cell loss by training on all fibres, and removing a randomly chosen 20% of cells before testing. As a measure of decoding quality, we computed the normalised root mean squared error (NRMSE) between decoded pressure \hat{p} and true pressure p as in Eq. 4.8 with $p_{\min/\max}$ minimum and maximum pressure and N number of samples. All errors were averaged across 5 cross-validation folds within trials.

$$\text{NRMSE} = \frac{1}{p_{\min} - p_{\max}} \sqrt{\frac{\sum_{i=1}^N (p_i - \hat{p}_i)^2}{N}} \quad (4.8)$$

To compare decoding performances statistically, we conducted paired t -test across trials.

4.2.2 Results

We found 185 bladder-units within 1044 overall fibres across 22 trials in 8 animals by thresholding the Pearson correlation coefficient between firing rates and the pressure signals (see Sec. 4.2.1.2 for details). These 185 fibres serve as the basis of our subsequent analyses.

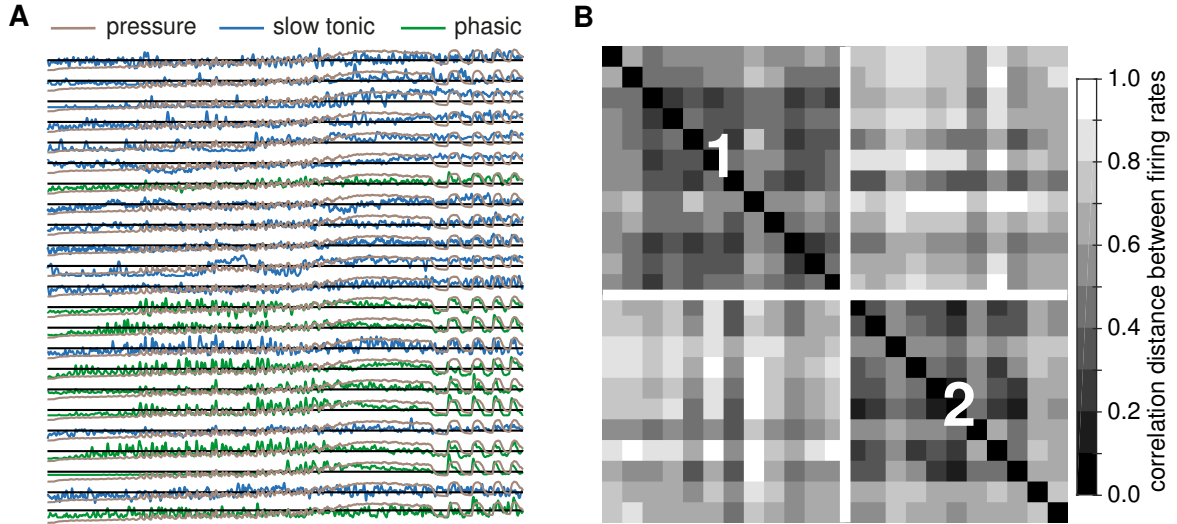


Figure 4.8: **Activity clusters per trial correspond to bladder neuron types; example trial E4T29.** **A** The time course of all normalised bladder unit firing rates along with the bladder pressure. **B** The correlation distance matrix shows the two main clusters. Overall, both clusters are quite homogeneous in their cell type content (see colors in (A)).

4.2.2.1 Groups of stereotypical bladder neuron types exist

As shown in Fig. 4.6B and described in Sec. 4.2.1.2, we first clustered cells globally by the correlation of their firing rates to the high-pass filtered pressure and the pressure derivative (‘correlation-features’). In this way, we distinguished 89 cells as ‘slow tonic’, 81 as ‘phasic’ and 15 as ‘derivative’. While ‘derivative’ cells were clearly separated from the other types in correlation-feature plane (Fig. 4.6B), ‘tonic’ and ‘phasic’ showed a more gradual transition. Some slow tonic fibres also responded to quick contractions to some extent and some phasic fibres did not completely decay to inactivity for stimulus plateau phases. In addition to these overlapping receptor properties, the stimulus signal did not separate phases of high low-frequency power and high high-frequency power well, as non-voiding contractions mostly occurred in the high-pressure regime. In many trials, this caused the firing rates of quick ‘phasic’ fibres to be correlated with the slow component of the pressure as well. We sought to overcome this limitation of the *in vivo* data with our surrogate data study. An

	Exp 1		Exp 2		Exp 3		Exp 4		Exp 5		Exp 6		Exp 6				Exp 8					
	T33	T57	T9	T11	T74	T100	T28	T29	T57	T58	T20	T24	T14	T16	T18	T19	T49	T50	T52	T67	T68	T72
slow tonic phasic derivative	3	1	7	3	1	7	6	14	1	1	2	3	5	2		4	5	5	5	1	6	7
	4	2	5	3	10	11	16	9		1	1		1	3	5			2	2	2	3	1
				2					6	6										1		

Table 4.3: **Summary of the identified bladder units across trials.** Numbers are fibre counts, TXX indicates experiment-specific trial numbers, among trials for other objectives in each experiment.

overview of the cell types in each trial is given in Table 4.3. Each trial was usually dominated by one or two fibre type(s).

		Fibre types contained in cluster		
		slow tonic	phasic	derivative
Dominant fibre type in cluster	slow tonic	74	15	0
	phasic	14	65	1
	derivative	1	1	14

Table 4.4: **Clustering by activity within trial often recovers the cell types obtained from clustering in correlation feature plane.** Rows show the dominant fibre type in each activity cluster, columns give the fibre type identities from correlation feature plane clustering.

The clustering described above required knowledge of the pressure signal in order to compute the correlation-features. As an alternative, we attempted to retrieve the cell types in an unsupervised way by grouping similarly firing cells within each trial to activity clusters. Because similar response characteristics should produce similar outputs given the same stimulus, the activity clusters should correspond to feature clusters (cell types) we observed across all trials. As Table 4.4 shows, activity clusters often reproduce cell types well. We here assigned a cell type label to each cluster from the dominant type. Fig. 4.8 shows an example of an activity clustered trial with a clean separation of fibre types. Table 4.S1 gives a more detailed overview of the relation between activity clusters and cell types in all trials.

The presence of imperfectly tuned fibres that respond to both static pressure and to quick pressure changes complicated a clean clustering into bladder neuron types, particularly a clean distinction of the types phasic and tonic. Also, slow tonic fibres could have low pairwise similarity due to noise from firing-rate estimation, complicating the activity clustering. We still often retrieved the same fibre groups by both global clustering across all trials based on correlation-features and by simply grouping

similarly firing fibres per trial. It was thus feasible to cluster cells online into different bladder neuron groups by their activity.

4.2.2.2 Encoding by groups of stereotypical bladder neurons is efficient and robust

We have shown that different bladder neuron types exist in the studied animals. In the following subsection, we aim to identify reasons for both the observed response diversity (different types) and the presence of multiple very similar bladder neurons (see Table 4.3).

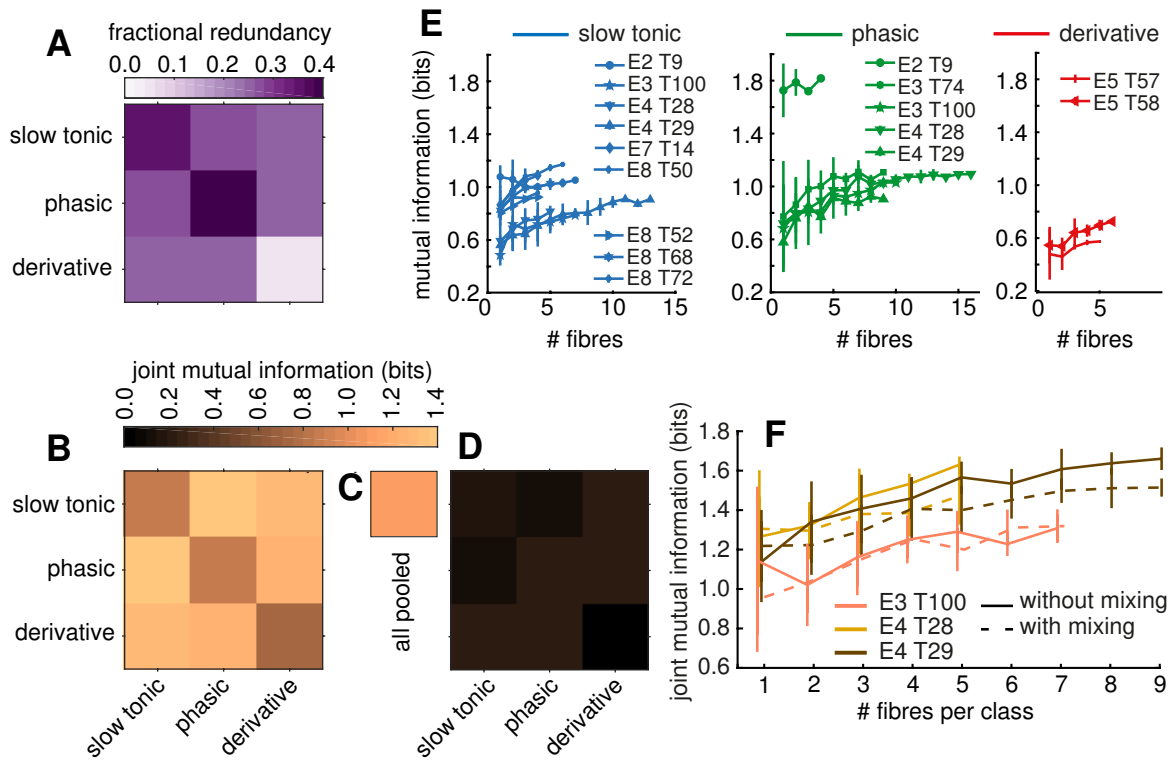


Figure 4.9: **Combining complementary fibre groups leads to high joint mutual information at a moderate redundancy. Real data.** **A** Fractional redundancy between average firing rates within fibre types. For on-diagonal entries, fibres were split into two equally large subpopulations of randomly chosen fibres of the same type five times between which the joint mutual information was computed and then averaged over repetitions; trials had to contain at least 4 fibres of the same type. **B** Mutual information between average firing rates within fibre type and pressure on the diagonal, averaged across trials. Joint mutual information between average firing rates of two different types and pressure in off-diagonal entries. **C** Mutual information of the average firing rate of all fibres and pressure, mean across trials. **D** Mean mutual information of single fibres across trials on the diagonal and joint mutual information of two fibres in the off-diagonal entries. **E** Mutual information between the average firing rate across an increasing number of fibres and pressure. **F** Joint mutual information between the mean firing rates of two growing pools of fibres; phasic and slow tonic. Pools either contain one fibre type (solid line) or are mixed (dashed line). Average firing rates computed from normalised firing rates.

Fibres of the same type were highly redundant, as indicated by the diagonal elements of Fig. 4.9A³.

³As single fibre responses were often too noisy to obtain meaningful redundancy estimates, we here computed it

A straightforward way of making use of this redundancy and quantifying the benefit of duplicating sensors is to pool these fibres into a single compound activity signal. Such pooling of similar sensors enhances the mutual information: the MI of the averaged firing rates of one fibre type on the diagonal of Fig. 4.9B is substantially higher (at least by a factor of 4, often more) than the average *single* fibre mutual information shown on the diagonal of Fig. 4.9C (see Table 4.S3 and Table 4.S4 for all MI values). As single units map bladder pressure (or an aspect of it such as the slow rise) imperfectly due to both their tuning (e.g., activation threshold) and the spiking nature of their output, pooling many similar cells increases the information content. The signal-to-noise ratio is enhanced through averaging many imperfect sensor outputs (Sterling and Laughlin, 2015). Fig. 4.9E further illustrates the benefit of averaging over multiple redundant cells: information rises with fibre count in almost every case.

Pooling redundant fibres increases information rate. Still, the average firing rate across all fibres of all types does not lead to the highest attainable mutual information between population activity and pressure. Even though the pooled rate of all fibres carries a higher mutual information (Fig. 4.9C, 1.082 ± 0.362 bits) than the average firing rate of each individual fibre type (on-diagonal in Fig. 4.9B, at most 0.886 ± 0.305), it is inferior to the joint mutual information of two different fibre types combined shown on the off-diagonal entries of Fig. 4.9B (at least 1.255 ± 0.410 bits; see Table 4.S3 for all MI values). This effect can be understood from the low fractional redundancy⁴ between types shown in the off-diagonal entries of Fig. 4.9A: the firing rates of different types are almost independent of each other (fractional redundancy approximately 25%, see Table 4.S2). It is therefore important for the transmitted information to keep the signals from different fibre types separate. To further illustrate that mutual information depends on preserving cell type-identity, Fig. 4.9F displays the evolution of joint mutual information between two fibre pools of increasing size while (1) only averaging within-type (solid line) and (2) mixing types to generate two inhomogeneous pools from which the average firing rate is computed.⁵ In the case of the cleanly distinguished fibre groups of Experiment 4 (see Fig. 4.8), the joint mutual information of the mixed populations is clearly inferior to the homogeneous populations. In Experiment 3, the difference between mixed and not-mixed is less pronounced

between within-type average firing rates.

⁴Derivative fibres are by themselves not very informative of the raw pressure signal and their within-type fractional redundancy becomes less meaningful. If we compute redundancy relative to the derivative of the pressure signal as shown in Fig. 4.S1, fractional redundancy also reaches high values for this fibre type.

⁵The shown example trials were chosen because they had at least 4 slow tonic and 4 phasic fibres.

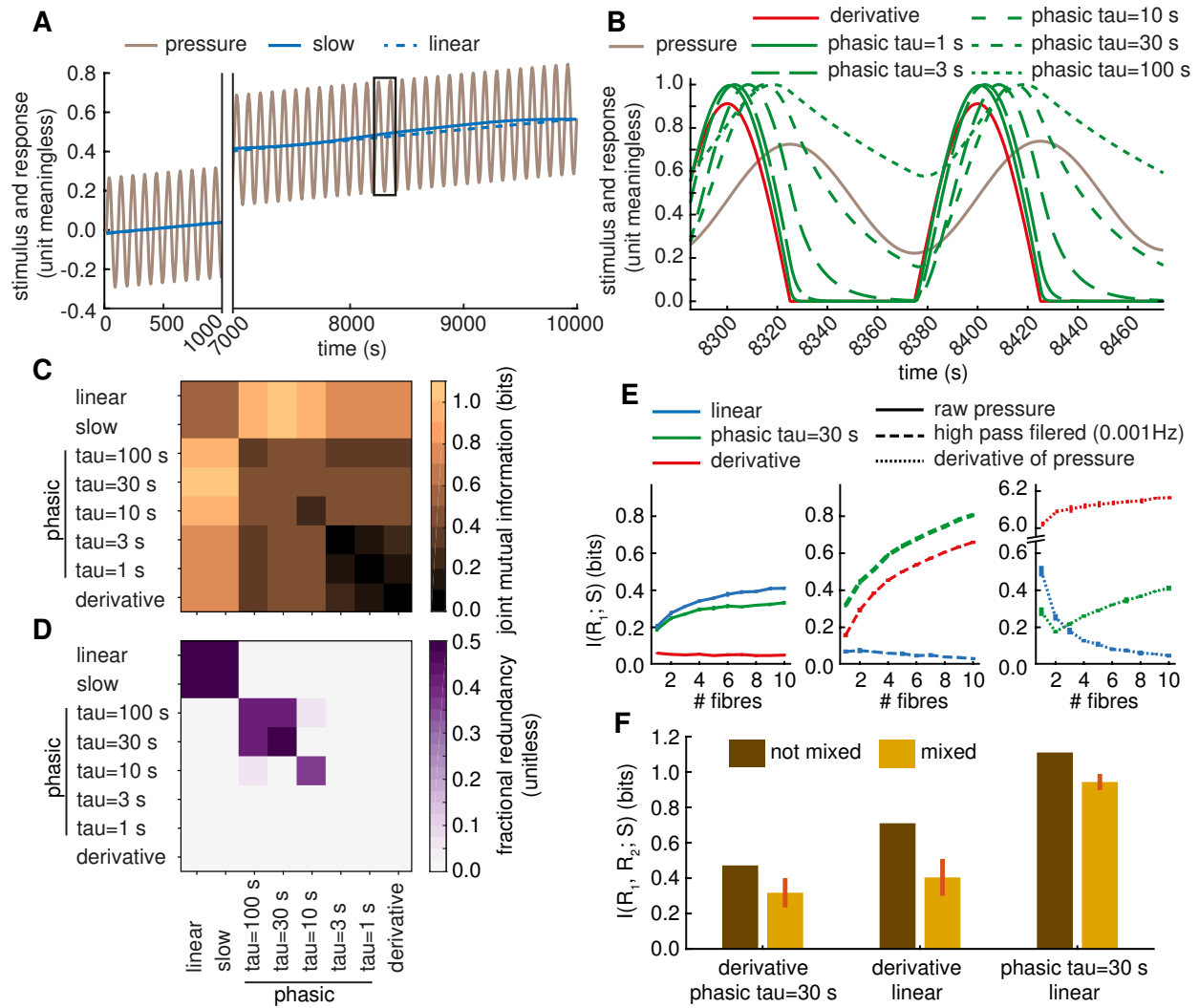


Figure 4.10: **Surrogate cells confirm the benefit of complementary fibres pools on information rate.**

A Simplified pressure time course used in the simulation study along with the idealised responses of ‘slow’ and ‘linear’ fibres. **B** Idealised responses of the fast fibre types. **C** Joint mutual information between single fibres of each type in (A) and (B) with firing rate 20/s. Each square is obtained as the mean over 10 repetitions of calculating the spike times from the inhomogeneous Poisson process, kernel-smoothing for firing rate estimation and computing the single repetition joint mutual information. For on-diagonal entries, the joint mutual information between two fibres of the same type and pressure was evaluated. **D** Fractional redundancy obtained through the same process as the joint mutual information shown in (C). **E** Mutual information between an average firing rate of a population of increasing size and the raw pressure, the high-pass filtered pressure, and the pressure derivative. Firing rate of each fibre 2/s. **F** Joint mutual information of two average firing rates across 10 fibres (firing rate 2/s each) and pressure; pools either homogeneous (one fibre type) or mixed 5 times.

because of the imperfect tuning of some fibres in that experiment (partly slow tonic and partly phasic at the same time). As we saw in the beginning of this subsection, averaging across *similar* (redundant) fibres reduces noise without signal loss. As we see now, averaging across multiple *dissimilar* (independent) fibres, on the other hand, washes out the messages of each homogeneous fibre group and destroys information. We therefore observe a coding in separate, near-independent groups.

In Fig. 4.10, we confirmed the benefit of different homogeneously tuned fibre pools in surrogate data (see Sec. 4.2.1.3). This additional simulation study enabled us to overcome the three main shortcomings of the *in vivo* data: (1) not all cell types were recorded in each trial, (2) the low- and high-frequency power of the pressure signal were correlated, and (3) the relatively short recording duration was likely to cause finite sampling biases in our estimates of information theoretic quantities. In simulation, we selected a simple idealised pressure time course consisting of a linear slope and a sinusoid of constant amplitude (period 100 s, see Fig. 4.10A). The different idealised responses are shown in Fig. 4.10A (slow) and B (fast). Making use of the increased degrees of freedom of a simulation, we implemented multiple phasic fibres with different decaying constants τ (see Table 4.2 for its meaning). After driving an inhomogeneous Poisson spiking process at mean firing rate 20/s with the idealised rates (shown in Fig. 4.10A and B) and kernel-smoothing the spikes to an estimated spike rate (see Sec. 4.2.1.3 for details), the heatmap of joint mutual information in Fig. 4.10C could be generated. Its values were similar to the mutual information from real data in Fig. 4.9B but it provides a more detailed picture. Both within the fast bladder neuron types on the lower right and the slow types on the upper left, the joint mutual information stayed low at about 0.5 bits. Within the fast group, the combination of derivative and phasic fibres with intermediate decay constants ($\tau=30$ s) reached slightly higher values as already seen in real data. Only the combination of slow and quick fibres achieved high information rates: slow tonic (and linear) and phasic fibres combined reached the highest mutual information (~ 1.1 bits). We further observed a match between the rate of decay in phasic fibres ($\tau=30$ s) and the dominant frequency (period $T=100$ s) in the pressure signal. When increasing the sinusoid frequency, smaller values of τ reached higher mutual information and vice versa (not shown). Fractional redundancy was high within the group of slow fibres and between phasic fibres of high and medium decay constants. As fibres became less relevant to the raw pressure signal (derivative and quickly-decaying phasic fibres), fractional redundancy decreased to about zero and the expected higher values became visible when computing redundancy towards the high-frequency component of the pressure signal (see Fig. 4.S2). Between the cleanly separated bladder neuron types of the simulated data, the off-diagonal fractional redundancies were all close to zero – fibres were truly independent. The positive effect of averaging on mutual information that we observed in real data (Fig. 4.9E) was confirmed in Fig. 4.10E where MI rises with increasing number of fibres to average over. When comparing the MI between the fibre types and different pressure variants in the

subplots of Fig. 4.10E, linear and phasic fibres are both informative of the raw pressure, derivative and phasic provide information about the quick components, and the fit between the intended firing rate and the pressure derivative causes an exceptionally high MI for derivative fibres and a much smaller relative benefit for added derivative fibres. In Fig. 4.10F we repeated the analysis of Fig. 4.9F with a fixed number of 10 selected fibres from each population at a firing rate of 2/s each. If we kept track of the fibre identities and only average within-type, the joint mutual information of the two fibre group mean firing rates was higher than when mixing the fibres randomly into two inhomogeneous groups – averaging between fibre types destroys information.

In summary, we observed a partly redundant (within-type) and partly independent (between-type) coding scheme that offers reliability and high SNR per channel by redundancy and a high information rate through complementary groups of bladder neurons.

4.2.2.3 A robust decoder based on stereotypical bladder neuron clusters

After identifying different recurring cell types by both global clustering in correlation-feature plane and by local activity clustering within trials, we demonstrated the functional significance of these groups for pressure encoding using information theory. In this last subsection we want to apply the encoding insights to the design of adapted decoding strategies to be used in next generation closed-loop bioelectronic medicines for bladder dysfunction.

Our information theoretic analysis showed that averaging within fibre type and keeping distinct types separate leads to a high information rate. A simple linear decoder was therefore trained on both single fibres and on the mean firing rates within fibre types or activity clusters (see Table 4.S1 for their relationship). Fig. 4.11 and Table 4.5 give an overview of the decoding error across trials. The bars display the 5-fold cross validated error within-trial when both training and testing on intact fibre populations. It can be seen that decoding from average firing rates (both fibre type mean and activity cluster mean) performs mildly (on average 9% and 12% higher error for fibre type and activity cluster means respectively) but significantly worse (p-values 0.00017 for fibre type and 0.0004 for activity cluster means in a paired *t*-test), than decoding from all single cell responses and that decoding from fibre type mean firing rates tends to be marginally more successful than from activity cluster means. We test the robustness of our proposed decoding scheme by removing 20% of the cells *after training*

and testing on a corrupt fibre set from which mean-responses were re-calculated. As can be seen in Fig. 4.11, the decoding error from single cells often became much larger after cell loss than when decoding from average responses, especially in cases like experiment 4 where many cells of each type allow for reliable cluster mean responses despite cell loss. The values in Table 4.5 confirm that the decoding error after cell loss from single cells was 18% higher than from subpopulation averages (p-values 0.00016 for fibre type and 0.00011 for activity cluster means): redundancy leads to reliability.

signal type	no cell loss	20% cell loss
single fibres	12.1 ± 3.4	17.6 ± 4.9
fibre type mean	13.2 ± 3.0	14.9 ± 3.6
activity cluster mean	13.6 ± 3.5	14.9 ± 3.7

Table 4.5: **Decoding from pooled fibre subpopulations is more robust.** Values are mean and standard deviation of NRMSE in percent across trials.

Clustering can have advantages for decoding beyond an increased robustness against cell loss. Grouping fibres periodically by their recorded activities may allow for a continuous identification of relevant cells *without knowledge of the pressure signal*. Similarly firing fibre groups are most likely driven by the same stimulus and if a subset of these similar fibres is already known to be bladder units, clustering offers an unsupervised way of identifying new relevant fibres on-line in the face of varying recording conditions caused by e.g., electrode migration.

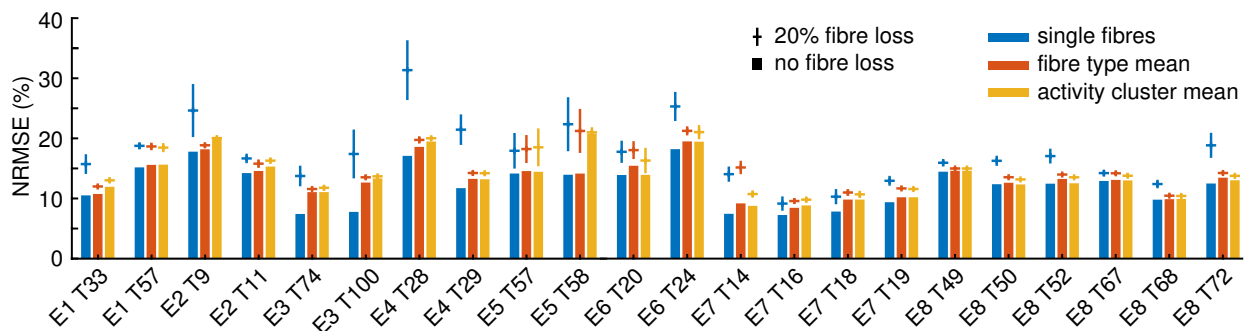


Figure 4.11: **Decoding from pooled fibre types and activity clusters is robust against cell loss.** Bars show the mean decoding test error (normalised by the maximum pressure) of a linear decoder in a 5-fold cross validation (CV) when training and testing on the complete fibre sets. Error bars and horizontal lines indicate the standard deviation and mean test error (again mean across 5-fold CV) across 10 repetitions of removing 20% of the cells between training and testing.

4.2.3 Discussion encoding and informed high-resolution decoder

To our knowledge, this is the first quantitative analysis of a population of peripheral sensory fibres. By applying tools from central neuroscience, information theory, to the periphery, we identified a beneficial interplay between different stereotypical response types. We have shown that stereotypical groups of bladder neuron types – slow tonic, phasic and derivative – implement a partly redundant, partly complementary encoding scheme for bladder pressure that achieves a reliable and effective information transmission. We clustered fibres globally across all trials from their correlations to differently filtered variants of the pressure signal and reproduced these types through unsupervised activity clustering within trials. In both real data and surrogate cell populations, we quantified the benefit of within-type redundancy (reliability, enhanced signal-to-noise ratio) and between-type tuning differences (maximisation of transmitted information by complementary channels) using information theory. Building on these encoding insights, we proposed an informed decoding scheme that builds on cluster (feature-based or activity-based) mean firing rates and thereby offers increased robustness at a moderate ($\sim 10\%$) accuracy reduction. Exploiting an understanding of the encoding for an informed decoder for physiological quantities from peripheral nerves is thus a novel approach with benefits for the estimation robustness. We hope our work will spark research towards next generation decoders for bioelectronic medicines.

One limitation of our study was the sparse sampling of fibres. Using microelectrode arrays, we could record from 6 to 125 cells in each trial – of which at most 23 were identified as bladder-units. Given the high number of cell bodies in the S1 and S2 DRG of cats ($\sim 12\,000$ (Chung and Coggeshall, 1984)) and bladder-units (~ 1000 (Jänig and Morrison, 1986; Applebaum et al., 1980; Uemura et al., 1975; de Groat, 1986)), we thus recorded from at most 2% of the overall bladder-unit population. This sparseness may well be the cause of the observed variability in the distribution of cell types across trials shown in Table 4.S1 and leaves uncertain whether cell types exist in consistent ratios across animals. The study is further limited by the pressure signal that drove the bladder neurons we were analysing. Firstly, the pressure did not contain much high frequency power, keeping us from conducting a sophisticated frequency-analysis or bladder neuron responsiveness mapping such as spike triggered averaging or coherence measures (Halliday and Rosenberg, 2000). Secondly, the non-stationary nature of the pressure signal and the limited reproducibility of the pressure signal across

trials prevented a principled error-analysis of our information theoretic measures (e.g., by bootstrapping). Lastly, the high-frequency events (contractions) usually took place at high stationary pressure. Therefore, the firing rates of fibres responding to high-frequency events (phasic and derivative) were usually high in correlation to the slow signal components simply by correlation of slow and fast stimulus components. This made it difficult to distinguish ‘purely phasic’ and mixed phasic and tonic bladder neurons. It has to be noted at this point that our clustering into three types of fibres is, to a certain extent, an oversimplification. As can be seen in Fig. 4.6B, tonic and phasic fibres do overlap in the correlation-feature space and this is at least partly due to a mixed bladder neuron tuning. It remains to be seen whether this overlap is an imprecision of the bladder neuron expression that induces noise or is in fact a feature of the transmission strategy that our analysis does not acknowledge. As we did not possess any information of fibre diameters, we could not link the different response types to different axon anatomies. It would be interesting to investigate whether, e.g., fibres that encode quick components were thicker (see Sec. 2.2). A limitation of the decoding scheme we proposed is its dependency on online spike sorting which in itself complicates the interface considerably. We did not observe any clustering of the cell types within the electrode arrays across experiments. Therefore, an unsorted ‘electrode-activity’ will not provide a clean separation of fibre types.

In addition to reliability and the benefits of averaging over imperfect sensors, other reasons for implementing multiple similar fibres are conceivable. If we look at the bladder and its feedback loop into the spinal cord as a control system, we observe that no quick control is required. The fastest events, single contractions, take place over the course of seconds to tens of seconds. The peripheral nervous system can thus afford a considerable lag between bladder pressure and the response by its higher control centers in the spinal cord at higher neural levels and can implement feedback by energetically cheap thin, slowly conducting fibres as it is observed (de Groat et al., 2015, 1981; Häbler et al., 1993; Evans, 1936). These thin fibres, however, do not fire at high frequencies, imposing a limit on the information rate per fibre (Sterling and Laughlin, 2015). The observed high number of thin similar fibres can therefore be viewed as the result of an energetic optimisation of the information channel that ensures a sufficient information rate at an affordable lag (Nakahira et al., 2015).

The different groups of bladder neurons we observed can be understood as reporting the two main components of the physiological pressure signal: the bladder (1) fills steadily at a very low rate of pressure change and (2) contracts ‘quickly’. It is not surprising that sensors for those two main signal

components exist in slow fibres on the one hand and fast phasic and derivative fibres on the other hand. This mapping of bladder neuron responsiveness to signal components has been reported in many studies on nervous sensory processing, for instance as receptive fields in the visual and auditory cortex (Freeman and Sherrington, 1907; Hubel and Wiesel, 1962).

Finally, many organ systems use an afferent encoding scheme based on stereotypical bladder neuron subpopulations, similar to our findings in the bladder. Phasic and tonic fibres have been reported in the colon (Blumberg et al., 1983; Jänig and Koltzenburg, 2017; Sengupta and Gebhart, 1994a), gall bladder (Foreman et al., 1986), the lung (slowly- and rapidly-adapting sensors) (Yu et al., 2017; Schelegle and Green, 2001; Coleridge and Coleridge, 2010; Kubin et al., 2006), similarly separate subpopulations were observed in muscle spindles (Brown et al., 1965; Koeze, 1973) and in the auditory system (Narins and Hillery, 1938). We hypothesise that the same benefits may have led the evolution of all these sensory populations towards an identical encoding scheme: complementary channels, each reliable due to within-type redundancy, independently encode different (quick and slow) aspects of the quantity of interest and together achieve a high information rate.

Acknowledgement

We thank Nikolas Barrera for spike sorting experiments 6 to 8.

4.2.4 Appendices

4.2.4.A Detailed analysis of the relation between activity clusters and cell types

In addition to the summary of the given in Table 4.4, Table 4.S1 gives a more detailed overview of the relationship between activity clusters and cell types (feature clusters) in all trials.

Exp 1			Exp 2			Exp 3			Exp 4			Exp 5			Exp 6		
T 33			T 9			T 74			T 28			T 57			T 24		
s	p	d	s	p	d	s	p	d	s	p	d	s	p	d	s	p	d
act. cluster 1	1		6	3	3	1			5	2	11	1	1		1		
act. cluster 2	2	4	1	2		2		10	1	14	3	8		6	2	1	1
act. cluster 3					1	2								1	4		
sum	3	4	1	2	7	5	3	3	2	1	10	7	11	6	16	14	9
Exp 7			Exp 8			Exp 8			Exp 8			Exp 8			Exp 8		
T 14			T 16			T 18			T 19			T 49			T 52		
s	p	d	s	p	d	s	p	d	s	p	d	s	p	d	s	p	d
act. cluster 1	2	2			5	4			5			5	1	5	1	4	1
act. cluster 2	3	1										1			1	2	3
act. cluster 3															1	1	
sum	5	1	2	3		5	4		5			5	2	5	2	6	3
Exp 7			Exp 8			Exp 8			Exp 8			Exp 8			Exp 8		
T 14			T 16			T 18			T 19			T 49			T 52		
s	p	d	s	p	d	s	p	d	s	p	d	s	p	d	s	p	d
act. cluster 1	2	2			5	4			5			5	1	5	1	4	1
act. cluster 2	3	1										1			1	2	3
act. cluster 3															1	1	
sum	5	1	2	3		5	4		5			5	2	5	2	6	3

Table 4.S1: **Unsupervised clustering by activity often yields near-homogeneous groups of one bladder neuron type.** Each trial is shown separately and the three columns per trial correspond to the three fibre types slow tonic (s), phasic (p), and derivative (d). In each row, fibres of the three activity clusters are counted. Ideally, each activity cluster would only contain one of the three fibre types. Numbers are fibre counts.

In some trials with multiple cell types, activity clusters were inhomogeneous: E2T9, E3T100, E8T72. Other diverse trials were more successful, with each cluster capturing one specific cell type: E1T57, E2T11, E4T28, E4T29, E8T67.

4.2.4.B Tables of mutual information and redundancy

The following tables give the numerical values for mutual information and fractional redundancy shown in Fig. 4.9A, B, and D.

	slow tonic	phasic	derivative
s	0.346 ± 0.152	0.268 ± 0.184	0.242 ± 0.149
p	0.268 ± 0.184	0.426 ± 0.118	0.243 ± 0.133
d	0.242 ± 0.149	0.243 ± 0.133	0.040 ± 0.057

Table 4.S2: Figure 4.9A. Fractional redundancy between within-type mean firing rates; mean across trials. All values in bits.

	slow tonic	phasic	derivative
s	0.886 ± 0.305	1.374 ± 0.375	1.281 ± 0.362
p	1.374 ± 0.375	0.865 ± 0.410	1.255 ± 0.410
d	1.281 ± 0.362	1.255 ± 0.410	0.709 ± 0.267

Table 4.S3: Figure 4.9B. Joint mutual information between within-type mean firing rates; mean across trials. All values in bits.

	slow tonic	phasic	derivative
s	0.182 ± 0.210	0.137 ± 0.177	0.209 ± 0.179
p	0.137 ± 0.177	0.214 ± 0.145	0.199 ± 0.147
d	0.209 ± 0.179	0.199 ± 0.147	0.036 ± 0.039

Table 4.S4: Figure 4.9D. Joint mutual information between single fibre firing rates, mean over all fibres of all trials for each type after MI calculation. All values in bits.

4.2.4.C Redundancy towards fast pressure components

Fractional redundancy of two firing rates only evaluates to meaningful values when computed in relation to a relevant signal with which at least one firing rate has a high mutual information. We therefore obtain very small fractional redundancies in relation to the raw pressure signal for very quick phasic and derivative fibres. Here, we repeat the redundancy computation in relation to only the quick components of the pressure.

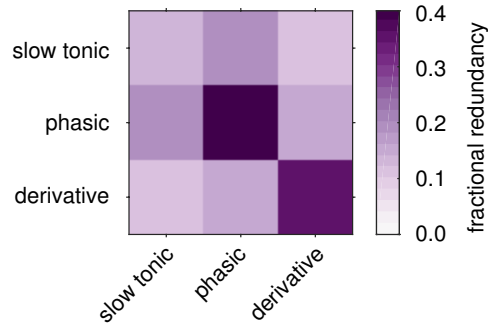


Figure 4.S1: **Derivative fibres only show their within-type redundancy with respect to the derivative of pressure. Real data.** Fractional redundancy of fibre type average firing rates and the derivative of pressure.

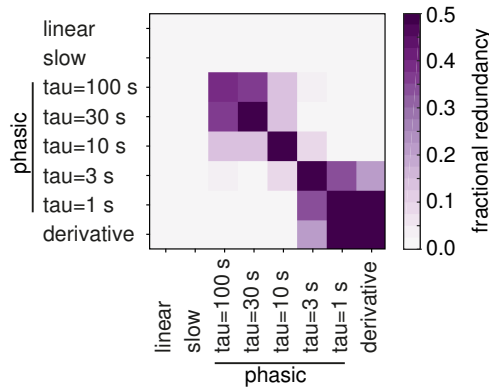


Figure 4.S2: **Fast fibres only show their mutual redundancy with respect to the high-pass filtered pressure. Surrogate data.** Fractional redundancy of simulated firing rates and the high-pass filtered pressure above 0.001 Hz.

4.3 Conclusion on decoding work

We have proposed two different decoders for different recording resolutions. For low-resolution hook electrode recordings, we mapped the individual nonlinear response characteristics of the monitored fibre populations in a piecewise linear function and could thereby train an optimal linear filter on the linearised activity. No nonlinear decoders (such as artificial neural networks and others as in previous works (Ross et al., 2018; Micera et al., 2001; Cavallaro et al., 2003)) were necessary. This simple real-time compatible decoder may find applications in bioelectronic medicines for the common cuff interface.

The more detailed recordings acquired by microelectrode arrays in the cat dorsal root ganglion let us conduct a principled investigation of the encoding of a physiological quantity by a population of peripheral fibres. We could, based on this analysis, propose a first informed decoder that presented obvious benefits such as an increased robustness against cell loss and an automatic re-calibration by

grouping fibres in an unsupervised hierarchical clustering. In an approximate comparison of the decoding errors, both the low-resolution hook electrode and the microelectrode array achieved about 10% NRMSE with slight advantages for the more precise interface. For this particular system, imprecise interfaces therefore seem sufficient. The informed decoding approach further required cells to be distinguished by spike sorting, an expensive and error-prone processing step that is not yet suited for real-time decoding in implanted devices.

We have focused on the pre-processing of the recorded activity and only considered simple linear filters (OLF for low-resolution and OLE for high-resolution recordings). Other decoders that include a state model have been demonstrated to perform better in the CNS (Koyama et al., 2010; Wu et al., 2005; Yu and Yu, 2017) and DRG (Ross et al., 2018) and performance gains can still be expected from the use of such more sophisticated methods that may be combined with our pre-processing methods.

Chapter 5

Feature-based time-series analyses

The quality of peripheral nerve recordings critically depends on the interface and one of the main tasks in algorithm development for bioelectronic medicines is to find appropriate pre-processing steps for each interface that extract informative summaries. An invasive electrode with a high, single-fibre resolution allows for a more sophisticated pre-processing (spike sorting), and an accordingly more precise, even biologically grounded decoding (see Ch. 4.2). Commercialised devices are, however, often equipped with mildly invasive recording techniques, predominantly cuff electrodes, that offer a sufficient long-term stability at the cost of a lower signal quality. Decoders in today’s bioelectronic medicines are therefore stuck with noisy compound action potentials as an input, compare our approach on low-resolution recordings in 4.1.

As already pointed out in the background section 2.5.2, the most common signal characterisation (pre-processing) for these a low-resolution recordings is a power or amplitude measure (possibly in a selected frequency band as in our decoder for low-resolution data, Ch. 4.1). It is obvious that by computing these coarse summaries, we discard much information about the waveform shape that might still be useful. We possibly miss differences in activated fibre distributions, fascicles, bursts, etc. that could still be recovered from shape of the continuous time series of noisy compound action potentials.

Against this background, we propose to characterise the continuous waveform of low-quality peripheral nerve recordings by general-purpose time-series features. Thanks to the particularly rich highly comparative time-series analysis (*hctsa*) feature library at our disposition (Fulcher et al., 2013;

Fulcher, 2017), we were able to analyse time series – and in particular low-resolution peripheral nerve recording – in a property space of unprecedented dimensions. We explored two different techniques. Both have a much more general applicability than our main scope of peripheral nerve recordings and extend to time series of various sources.

In the first section of this chapter Sec. 5.1, we present the first method. By transferring time series to a very high dimensional feature space and applying dimensionality reduction methods in this space, we detected the main varying firing characteristics in simulated peripheral nerve recordings generated in PyPNS (Ch. 3) in an unsupervised way. For each main characteristic, we proposed single features. The generated small feature subsets can be implemented efficiently and form an invaluable component in implanted bioelectronic medicines as they provide a new way to summarise noisy recordings acquired by the popular cuff electrode on-line in a few key firing characteristics (we demonstrate firing rate, myelination ratio, and burstiness). This method’s utility in uncovering low-dimensional structure is demonstrated on diverse additional synthetic datasets and a real-world example.

In the second part of this chapter, Sec. 5.2, we present a supervised selection pipeline to tailor low-dimensional feature-spaces to a given collection of classification problems. Applying this supervised method to the literature standard of time-series data mining problems, we present a canonical feature ensemble, *catch22*.

5.1 Inferring low-dimensional variation in time-series datasets

Modern science is characterised by the unprecedented scale of datasets, and the development and deployment of new statistical tools to analyse them. Time-series data – measurements of a system taken repeatedly through time – are exemplary of this trend, with massive, publicly available datasets driving progress in understanding dynamics of a range of real-world systems, from biomedical (e.g., neuroimaging data), financial (e.g., high-frequency trading data), social (e.g., communication across social networks), and astrophysical (e.g., NASA’s TESS mission (Ricker et al., 2016)). Bioelectronic medicines are not exempt from this trend of large-scale data collection and peripheral nerve recordings are being recorded in unprecedented volumes. For scientists that aim to distil interpretable understanding from these large, complex datasets, their hope is that this complexity will be some-

how reducible to some smaller number of core dimensions that capture important variation across the dataset. Such approaches to ‘dimensionality reduction’ have been routinely applied to sets of observations that are not time ordered (Hastie et al., 2009), but have eluded time-series datasets, where the temporal ordering of measurements is key.

In this work we present a new method for estimating the intrinsic dimensions underlying an empirical time-series dataset, as the core dynamical properties that capture variation across time series in the dataset. Our solution to this problem relies on a transformation of each time series from its measurement space, \mathbf{x} to an extracted high-dimensional feature space, \mathbf{f} , using the recently-developed highly comparative time-series analysis software, *hctsa*, that contains implementations of over 7000 time-series features derived from the interdisciplinary scientific time-series analysis literature (Fulcher et al., 2013). For example, elements of \mathbf{f} contain summaries of the properties of \mathbf{x} , its: autocorrelation function and Fourier power spectrum, distribution of values, temporal entropy/predictability, long-range scaling properties, and many others (Fulcher, 2017). Applying standard dimensionality-reduction algorithms in the extracted feature space meaningfully structures complex time-series datasets along interpretable reduced dimensions. We test the hypothesis that low-dimensional structure in these extracted feature matrices correspond to low-dimensional variation in the degrees of freedom of the generative time-series model which produced the dataset. We assess this hypothesis using a large and diverse range of 13 generative systems, from linear stochastic systems through to nonlinear deterministic chaotic systems, in each case generating a time-series dataset resulting from different degrees of parametric freedom (i.e., allowing a different number of parameters to vary freely). We show that feature-based dimensionality reduction can often recover the degrees of freedom in the generative model, and provide interpretable estimates of the underlying free parameters. As one demonstration, we apply our approach to a *Drosophila* movement phenotyping dataset and extract dimensions corresponding to sex differences and time-of-day variation across the movement time-series. For our main subject of peripheral nerve recordings, we analyse simulated data generated in our simulator PyPNS (varying firing rate, myelination ratio, and burstiness). For bioelectronic medicines, the selected estimators for the main firing characteristics can be efficiently implemented for on-line summarisation of peripheral nerve recordings and thus as a basis for a more accurate decoding and anomaly detection from cuff-electrodes in closed-loop bioelectronic medicines.

The method extends to time-series datasets from diverse sources and our results pave the way for

much-needed data-driven frameworks to bridge the gap between deep theoretical understanding of dynamics and the large-scale datasets that characterise the modern scientific landscape.

5.1.1 Methods

A simplifying overview of our approach is shown in Fig. 5.1.1. We basically apply dimensionality reduction to a high-dimensional feature space to uncover the underlying low-dimensional parametric variation within the data. The main technological advance lies in the feature library of which the utility is proven for diverse systems in this section. We give a much more detailed description of our methodology in the following.

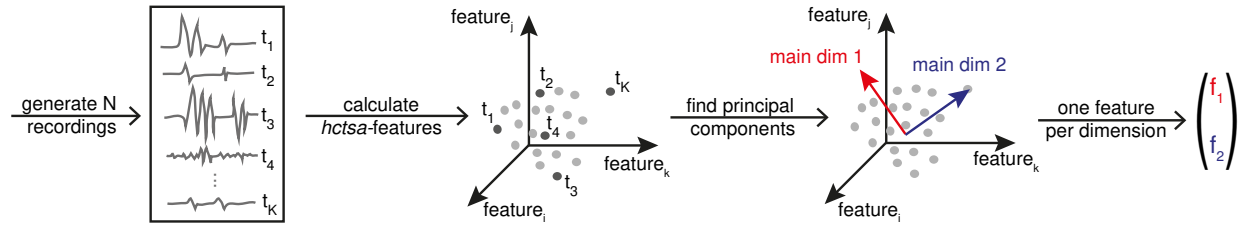


Figure 5.1.1: **Unsupervised selection of efficient estimators for the main varying signal characteristics.** Each of the N time series in a given dataset is transferred to a high-dimensional feature-vector using the *hctsa*-toolbox (here visualised as three-dimensional albeit having thousands of dimensions). In property space, we find the main directions of spread in the data caused by the dynamical properties that vary across single recordings. For each component, a single feature can be chosen that estimates one main characteristic.

5.1.1.1 Theory

We aim to detect meaningful low-dimensional structure in time-series datasets, $\mathcal{X} = \{\mathbf{x}_1 \dots \mathbf{x}_n\}$. A dataset contains many univariate time series, \mathbf{x}_i , each of which is a uniformly-sampled, time-ordered sequence of T_i measurements. We suppose that each dataset, \mathcal{X} , was produced from some time-series model, $\mathcal{M}(\Theta)$, controlled by a set of free parameters, $\Theta = \{\theta_1 \dots \theta_m\}$. The dynamical rules encoded in \mathcal{M} , and probability distributions over the random variables, Θ , determine a distribution over time series from which the time series in \mathcal{X} are sampled. Each \mathbf{x}_i corresponds to a parameter setting Θ_i of the generative model \mathcal{M} . Thus, understanding the range of dynamical properties in \mathcal{X} provides understanding of the properties of some underlying generative model, \mathcal{M} , and the parameters that control it.

In this work, we wish to infer basic properties of the parametric degrees of freedom, Θ , from patterns contained in the data sample, \mathcal{X} . We do this through a mapping from a time series, \mathbf{x} , to a set of p extracted real-valued features, $\mathbf{f} = \{f_1 \dots f_p\}$. Applying this mapping to all time series in a dataset, \mathcal{X} , represented as a time series \times time ($n \times T$) matrix, X , yields a time series \times feature ($n \times p$) matrix, F . The true model generates the ensemble \mathcal{X} from the $n \times m$ matrix of parameters. A key intuition is that the independent variation of each free parameter affects the properties of time series in a characteristic way. This common variation of time-series properties with the underlying parameter inducing dependencies between features that are sensitive to that property. Estimating feature–feature dependencies, through applying dimensionality-reduction techniques to F , thus provides a window into understanding the key parametric variation underlying a time-series dataset, \mathcal{X} . We emphasise that our method is not concerned with the dimensionality of the phase space of the dynamical system underlying; instead we are concerned with the *variation* in underlying parameters across a dataset, and how many numbers we need to measure to capture this dominant variation.

The problem, and our approach to solving it, is depicted schematically in Fig. 5.1.2. In Fig. 5.1.2A, we consider independent sampling from $d = 2$ parameters, $\Theta = \{\theta_1, \theta_2\}$, which yields an observed time-series dataset, \mathcal{X} . The variation in extracted features across the dataset, visible in the feature matrix, F , contains an imprint of the parametric degrees of freedom in the generative model (Fig. 5.1.2B). Specifically, features in F either vary with θ_1 , θ_2 , both θ_1 and θ_2 , or neither θ_1 nor θ_2 ; the interdependencies between features induced by θ_1 and θ_2 result in (possibly nonlinear) low-dimensional structure in F . Applying nonlinear dimensionality reduction to F , shown in Fig. 5.1.2D, reveals a saturation in variance explained at $d = 2$; the dimensions become estimators for the two parameters θ_1 and θ_2 .

This process is contrasted by a generative model with many more free parameters, shown in Fig. 5.1.2E, which can produce a much more diverse set of time series. In this case, features from the dataset vary with many underlying parameters, θ_i , yielding a high-dimensional F (Fig. 5.1.2F) that can be quantified using dimensionality reduction (Fig. 5.1.2H).

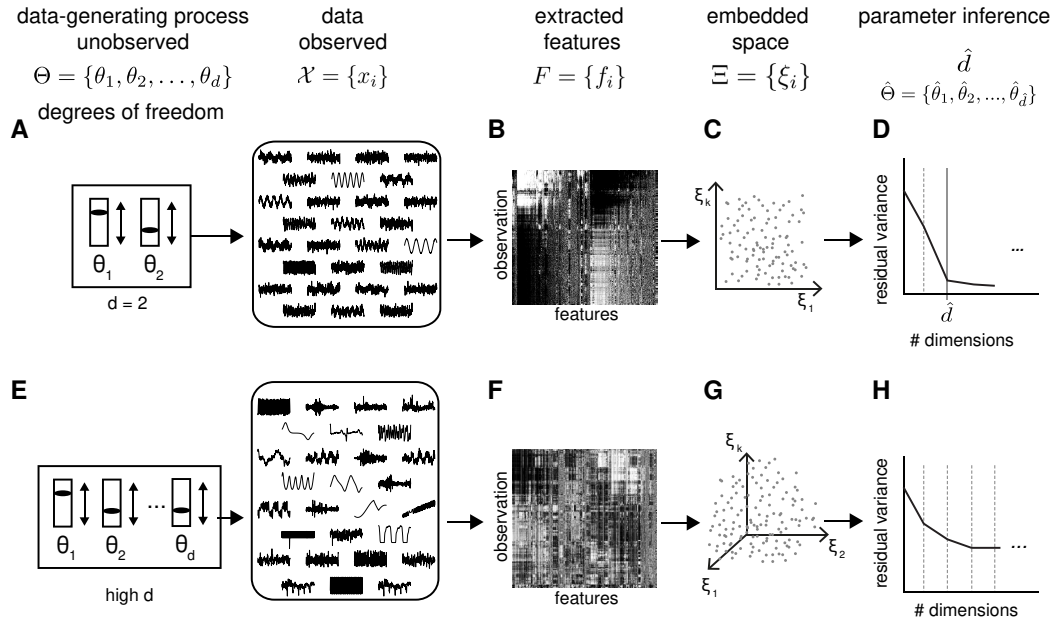


Figure 5.1.2: **Schematic of our approach.** We aim to infer the parametric dimensionality of the generative model underlying our time-series dataset. We imagine data being generated by a model with d free parameters $\Theta = \{\theta_1, \dots, \theta_d\}$. Because properties of the empirical dynamics vary together with underlying parameters, we hypothesise that low-dimensional parametric variation in the data generating process should manifest in a low-dimensional matrix of extracted features (if these features are sufficiently comprehensive). Applying nonlinear dimensionality-reduction to time-series feature matrices allows estimation of the dimensionality \hat{d} and estimators for each parameter $\hat{\theta}_1, \dots, \hat{\theta}_d$. This information can be used to structure the dataset in a natural space of inferred parametric variation. **A** In a dataset of low-dimensional parametric variation, clusters form in the feature-matrix (**B**) and a few dimensions in embedded space (**C**) capture most of the variance, so that residual variance falls to a low level (**D**). **E** In a high-dimensional system, no clear feature-clusters emerge (**F**), more embedded dimensions (more than the 3 we can visualise in **G**) are necessary to capture the variance (**H**).

5.1.1.2 Constructing a feature space

The key to tackling the problem shown in Fig. 5.1.2 is to have a sufficiently comprehensive set of features, \mathbf{f} , that are sufficiently sensitive to the types of changes to empirical dynamics observed in \mathcal{X} induced by the parameters Θ in any given model \mathcal{M} . While there is no perfect solution, progress can be made through a recent library made available for time-series feature extraction, *hctsa* (Fulcher, 2017), following research aimed at exploiting a wide scientific literature on time-series analysis to better understand complex systems (Fulcher et al., 2013; Fulcher and Jones, 2014; Fulcher, 2018). The *hctsa* feature library can be thought of as an agglomerate library of interdisciplinary scientific methods development, in the form of over 7700 time-series analysis features. This allows each empirical time series, \mathbf{x} , to be mapped to a real-valued feature-vector, \mathbf{f} . *hctsa* quantifies a wide range of time-series properties, including properties of the distribution of values, linear and nonlinear au-

to correlation structure, stationarity, summaries of basis-function decompositions (including Fourier and wavelet transforms), fits to various time-series models (e.g., autoregressive, state space, Gaussian Process, and hidden Markov models), measures from nonlinear time-series analysis (e.g., correlation-dimension estimates, nonlinear prediction errors, fractal scaling properties, etc.), and information theoretic complexity and entropy measures (e.g., Sample Entropy (Richman and Moorman, 2000)). Here we used *hctsa* v0.97 (available at <https://github.com/benfulcher/hctsa/tree/0.97>).

5.1.1.3 Normalisation and dimensionality reduction

After computing a feature matrix, F , we then normalised each column using a robust sigmoid transform (Fulcher et al., 2013). Features that were constant across the dataset or were inappropriate for the data were removed (these features are signified by special-valued outputs in *hctsa*, and include features that attempt to fit a positive-only distribution to non-positive data). These processes yield a reduced, normalised time-series feature matrix, \tilde{F} . To quantify redundancy in \tilde{F} that may be indicative of underlying parametric constraints, we find low-dimensional structure using PCA (to estimate linear structure) and Isomap (to estimate nonlinear structure) (Tenenbaum et al., 2000). Isomap estimates pairwise distances between data objects along a low-dimensional nonlinear manifold by creating a neighborhood graph (Tenenbaum et al., 2000). We set the number of neighbors to 7 (default).

We selected these two methods because PCA is a representative of the dimensionality reduction approach ‘matrix factorisation’: it projects the data linearly onto certain directions of the full, high-dimensional space to create a low-dimensional projection of high variance. PCA will encounter problems if the relation between dimensions in full space is non-linear. Imagine a line in 2D space that describes a spiral as shown in Fig. 5.1.3. The variance in of this point cloud along variable x is the same as in variable y and PCA would identify two equally relevant dimensions without achieving a meaningful simplification. Isomap, on the other hand, is a neighborhood-preserving dimensionality method. It is not concerned with global variance along certain dimensions but will create a neighbourhood graph by identifying the nearest neighbours of each point and computing their distances. Given this graph, it will iteratively calculate an embedding that preserves the distances within each neighbourhood with less dimensions. In our spiral example, it will identify a single curved dimension extending along the spiral.

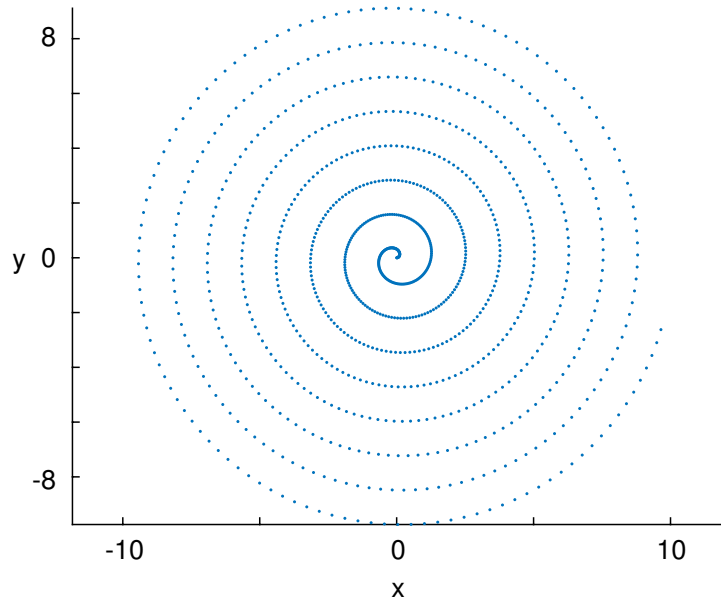


Figure 5.1.3: **Non-linear dimensionality reduction can disentangle complex point clouds.** If data points are ordered in a way that links axes in a non-linear manner, Isomap can uncover this relationship, PCA cannot.

Both methods yield a representation of the dataset in an estimated embedding space of a given dimension. PCA provides a direct measure of variance explained by each principal component, and a similar measure can be derived for Isomap as the residual variance. Residual variance, σ_{resid}^2 is computed as the unexplained variance $1 - \rho^2$, ρ Pearson correlation coefficient, between pairwise time-series distances in feature space \mathbf{d}_f and distances in embedded space \mathbf{d}_e :

$$\sigma_{\text{resid}}^2 = 1 - \rho(\mathbf{d}_f, \mathbf{d}_e)^2. \quad (5.1)$$

To estimate the number of dimensions required to capture the dominant sources of variance in the data, we inspected the residual variance as a function of the number of reduced dimensions, d .

5.1.1.4 Dimensionality estimation

We constructed a simple heuristic to estimate the saturation of residual variance, σ_{resid}^2 , and thus an estimate of the number of parametric freedoms in the generative model underlying the observed data. We first computed d_{sat} as the minimal d for which $\sigma_{\text{resid}}^2(d+1) - \sigma_{\text{resid}}^2(d) < 0.0025$. We then estimated the dimensionality, \hat{d} , as the minimal d for which $\sigma_{\text{resid}}^2(d) < \sigma_{\text{resid}}^2(d_{\text{sat}}) - 0.05$. Both heuristic thresholds (0.25% and 5%) were set manually from the decay characteristics of σ_{resid}^2 that

we observed across the studied simulated systems.

5.1.1.5 Evaluating the embedding

To measure how well the feature-based embedding space captures the parametric variation in the underlying model, we attempted to reconstruct each of the original parameters as a linear combination of the reduced dimensions. For each model parameter, we quantified this as the unexplained variance, $\chi = 1 - R^2$, between that parameter's variation across the dataset, and the best linear estimate of it computed from performing a multivariate linear regression using the first d estimated dimensions. For example, if a linear combination of first two estimated dimensions can well reproduce the underlying parametric variation of the model parameter, α , of a two-dimensional system, we would measure a low unexplained variance, χ_α . Since we might expect a nonlinear relationship between the parameter space and the embedding space Ξ we can under estimate the information that the embedding space gives about the parameter values.

5.1.1.6 Selecting efficiently implementable features

So far we have uncovered the construction of an informative embedding by dimensionality reduction in a high-dimensional feature space. Each dimension corresponds to a linear combination of thousands of features (PCA) or is an even more abstract virtual component for Isomap, both of which will depend on the computation of thousands of single features. To efficiently project new data onto the dimensions in embedded space, we approximate each of them by a single representative feature selected by maximum Pearson correlation to the component. In this way we devise our set of efficient estimators for the varying signal characteristics caused by changes in the underlying parameters.

5.1.1.7 Datasets

For our main subject of study, we generated surrogate peripheral nerve recordings in our simulator PyPNS (Ch. 3). Four simulated datasets were obtained from a nerve with a fixed length of 5 cm containing 500 active axons. For each of the four datasets, we generated snippets of length 400 ms, sampled at 20 kHz, across which two to three of the firing characteristics myelination ratio (0 - 2%),

firing rate (0.1 - 10 spikes/ axon/ second), and burstiness (0 - 100% of firing probability imbalance between two alternating intervals) varied.

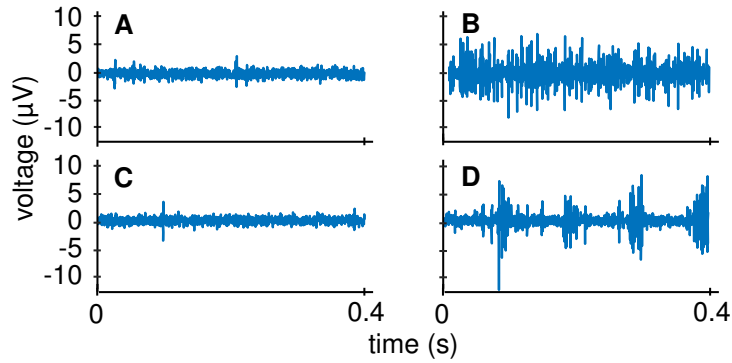


Figure 5.1.4: **Example simulated recording with varying characteristics firing rate and burstiness.** Data was generated in the peripheral nerve simulator PyPNS (Lubba et al., 2018). (a) Low rate, low burstiness, (b) high rate, low burstiness, (c) low rate, high burstiness, (d) high rate, high burstiness. At low rates, burstiness is not visible even for a human observer in (a) and (c).

To demonstrate the general utility of our methodology, we generated additional datasets from thirteen different dynamical models, \mathcal{M} , covering different classes of dynamics: *linear and nonlinear stochastic systems* (autoregressive process (Chatfield, 2013), noisy sinusoid with linear trend and mean shift, a noisy bimodal switch, a predator prey system (May, 1972), population growth (Verhulst, 1845)), a *deterministic oscillator* (van der Pol oscillator (van der Pol, 1926)), *deterministic low-dimensional chaotic maps* (stochastic sine map (Freitas et al., 2009), logistic map (May, 1976)) and flows (Lorenz (Lorenz, 1963) and Rössler attractors (Rössler, 1976)), a *high-dimensional chaotic flow* (the nonlinear time-delay Mackey-Glass equation (Mackey and Glass, 1977)), and a model of *self-affine* time series (Malamud and Turcotte, 1999). Details about all models and how they were simulated are in Sec. 5.1.11.B. This extensive library of simulated time-series datasets is made available along with the results of *hctsa* feature extraction at DOI 10.6084/m9.figshare.9912563. The time-series datasets were generated using the code in <https://github.com/benfulcher/TimeSeriesGeneration/>. Analysis code to generate the results is available at https://github.com/chlubba/HCTSA_dimRed_figures.

We generated a time-series dataset, \mathcal{X} , from a given model, \mathcal{M} , by independently sampling that system's free parameters. We first generated a set of one-dimensional datasets, $\mathcal{X}^{(1)}$, generated from sampling a single model parameter (from a uniform distribution) while fixing all other parameters. Similarly, we generated two-dimensional datasets from independently sampling two model parameters $\mathcal{X}^{(2)}$ (with all other parameters fixed), and three-dimensional datasets from independently sam-

pling three model parameters, $\mathcal{X}^{(3)}$. For all systems, uniform distributions from which parameters were sampled, and the value of each model parameter when it was kept fixed, are provided in Sec. 5.1.11.B. In total, we generated 4 peripheral nerve datasets containing 2200 time series (three $\mathcal{X}^{(2)}$ of 400 time series each; one $\mathcal{X}^{(3)}$ of 1000 time series) and 93 additional synthetic time-series datasets containing over 99 000 time series: 46 datasets of $\mathcal{X}^{(1)}$ (100 time series per dataset), 37 datasets of $\mathcal{X}^{(2)}$ (400 time series per dataset), and 10 datasets of $\mathcal{X}^{(3)}$ (8000 time series per dataset).

Example time series from a synthetic $\mathcal{X}^{(1)}$, $\mathcal{X}^{(2)}$, and $\mathcal{X}^{(3)}$ dataset is in Figs 5.1.5A, B, and C, respectively. One of the visually clearest examples of a $\mathcal{X}^{(1)}$ is in Figs 5.1.5A, where the time series are ordered by the randomly sampled parameter, T : the period of a sinusoid in the underlying time-series model. Generating a time-series dataset from independently sampling parameters r (growth rate) and K (carrying capacity) in the predator-prey model, $\mathcal{M}(r, K)$, yields the $\mathcal{X}^{(2)}$ dataset depicted in Fig. 5.1.5B. Despite the independent variation of K when time series are ordered by r (upper plot), a characteristic variation in waveform can be discerned. Ordering the time series by K reveals an independent variation in signal amplitude. We have selected this example for its visual clarity, but it is not typically the case for $\mathcal{X}^{(2)}$ datasets, for which the clear variation in the parameter of interest is obscured by the independent variation of the other parameter. As shown in Fig. 5.1.5C for the stochastic sine map model, $\mathcal{M}(\mu, q, b)$, independent variation in the other two parameters obscure predictable and interpretable variation in any single parameter. This is typical of the challenge in inferring the parametric variation underlying $\mathcal{X}^{(3)}$ datasets.

5.1.2 Results

We present results of applying and evaluating feature-based dimensionality reduction to infer the parametric variation underlying a given time-series dataset. We show that the *hctsa* feature library is sufficiently comprehensive to detect parametric variation in the wide range of systems studied here, detail how it works in a case study, demonstrate its utility for peripheral nerve recordings, and evaluate performance across all model systems. We then show the method's strong performance on an additional empirical dataset of fly movement time series, and finally investigate the robustness of the results to the characteristics of time-series datasets.

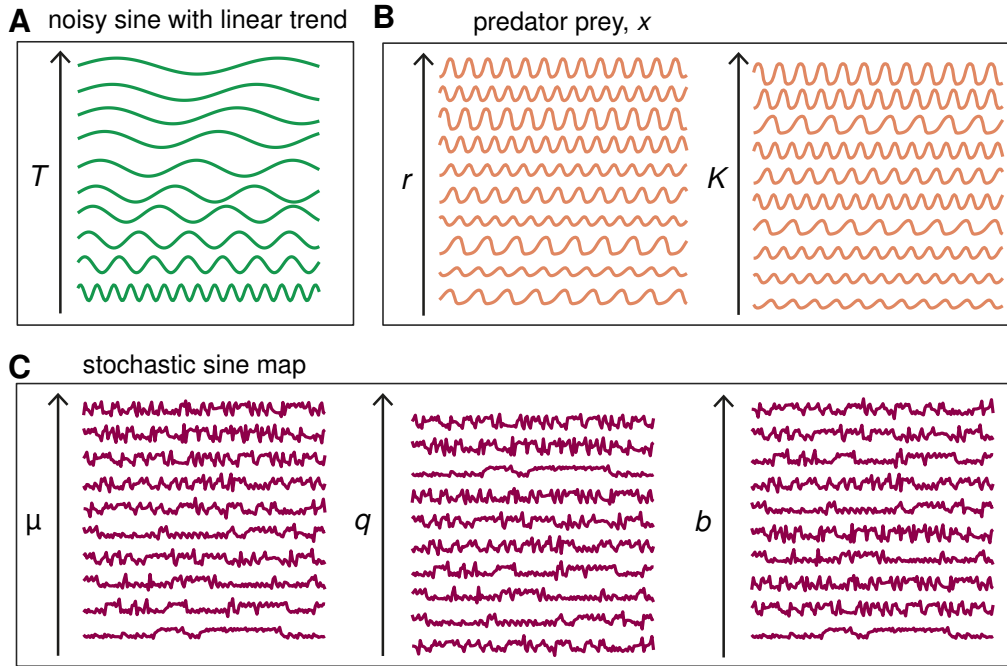


Figure 5.1.5: **Example time series generated from independently sampling from one, two, and three model parameters.** For three datasets, we plot segments (the first 150 samples) of 10 randomly selected time series, ordered by one of the model parameters used to generate the dataset. **A** Variation in period, T , of a sinusoid (from the ‘noisy trendy sinusoid’ model, fixing the noise level, $\eta = 0$, and trend, $m = 0$) yields a one-dimensional dataset, $\mathcal{X}^{(1)}$, of time series which we have ordered by T . The dataset exhibits a clear visual signature of the underlying one-dimensional parametric variation in T . **B** A two-dimensional dataset of time series, $\mathcal{X}^{(2)}$, generated from independently varying both r and K in the predator-prey model are ordered by the growth rate, r , and carrying capacity, K . **C** A three-dimensional time-series dataset, $\mathcal{X}^{(3)}$, generated by independently varying parameters μ , q , and b in the stochastic sine map. Because of independent variation in the other two parameters, ordering the time series by any one of the parameters reveals the challenge in estimating these three underlying dimensions of parametric variation.

5.1.2.1 Feature library assessment

The success of our approach requires a library of time-series summary statistics that is sufficiently comprehensive to contain multiple statistical estimators that are sensitive to each type of parametric variation in the wide range of time-series generative models analysed here. To assess the *hctsa* feature library (used here), we computed a measure of *hctsa* feature specificity to each parameter in each synthetic dataset. For any parameter there are ~ 7000 features it can covary with. We identify both the maximum correlation of each parameter to any feature and the level covariation of the top 5% of features with each parameter, ξ_{95} . High values of ξ_{95} indicate that there are sufficiently many *hctsa* features in the library that are sensitive to the parameter of interest (in the presence of confounding variation of at least one other parameter in the case of $\{\mathcal{X}^{(2)}\}$ and $\{\mathcal{X}^{(3)}\}$ datasets, cf. Fig. 5.1.5).

Distributions of ξ_{95} are plotted separately for one-, two-, and three-dimensional datasets in Fig. 5.1.6.

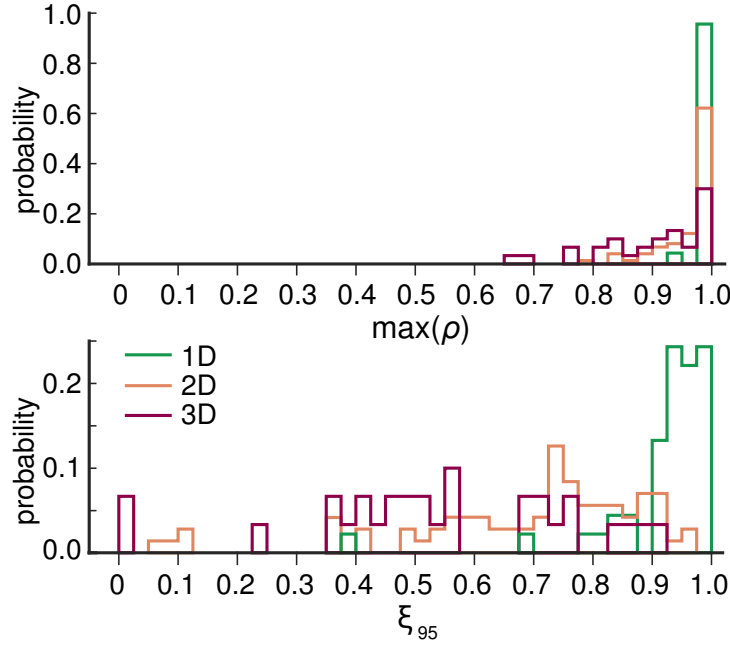


Figure 5.1.6: ***hctsa* is a comprehensive feature library, containing sufficiently many diverse features to capture the individual parametric variations across a wide range of time-series models.** We plot the distribution of $\max(\rho)$, the maximum correlation between the variation of a given parameter across a dataset, and that of each feature, and ξ_{95} , the 95th percentile of the distribution of correlations (high ξ_{95} indicate that *hctsa* contains many features that are sensitive to the parameter of interest). As more independent parametric variation is introduced (for two- and three-dimensional datasets), the fewer features have a high correlation with each parameter. Distributions are shown for: 46 one-parameter datasets, $\mathcal{X}^{(1)}$ (green), 74 parameters across 37 two-parameter datasets, $\mathcal{X}^{(2)}$ (orange), and 30 parameters across 10 three-parameter datasets, $\mathcal{X}^{(3)}$ (purple).

As expected, the difficulty in tracking a given parameter increases when there is more independent (confounding) variation: the median ξ_{95} across all 46 one-dimensional datasets is 0.94, dropping to 0.74 for 74 parameters across 37 two-dimensional datasets, and 0.53 for the 30 parameters across 10 three-dimensional datasets. High values of ξ_{95} measured in one-dimensional datasets demonstrates the presence of multiple features that are sensitive to the vast majority of time-series dynamics induced by parametric variation in the models analysed here. Note that each parameter of every system was well captured by some, if not by many, features at a correlation of at least 0.95 ($\mathcal{X}^{(1)}$), 0.79 ($\mathcal{X}^{(2)}$), and 0.66 ($\mathcal{X}^{(3)}$). This is impressive given the wide range of dynamics and parametric freedoms represented across our diverse set of time-series models. The scientific and creative breadth of the *hctsa* feature library underpins this result, with different parameters requiring different parts of the scientific literature to accurately track, from linear autoregressive modeling, stationarity, entropy, information theory, wavelet decompositions, derived graph theory statistics, and a range of novel features based on the physics of simulated particles driven by the time series (Fulcher et al., 2013). Two notable exceptions ($\xi_{95} < 0.7$) are for the mean-shift parameter s in the ‘noisy shifty sine’ model ($\xi_{95} = 0.38$) and

the linear trend parameter m in the ‘noisy trendy sine’ model ($\xi_{95} = 0.68$). In both cases *hctsa* contains many estimates of each parameter: s (e.g., the mean estimator has $r = 1.00$) and m (e.g., a measure of linear gradient across the time series has $r = 0.98$), but the relatively low values of ξ_{95} indicate that there are relatively few such features, which may prove a challenge for accumulating sufficient shared variance to be detected by the dimensionality reduction methods. We observed increased difficulty in estimating the same parameter in the two-dimensional case relative to the one-dimensional case when the new parameter dominates the effect on the empirical dynamics, obscuring the ability of individual features to disentangle the different parameters. An example is the noise-switch parameter q in the ‘stochastic sine map’ (which injects random noise at a given time step with probability q), and is well estimated by individual features when only q is varying ($\xi_{95} = 0.99$), but much less well when the intrinsic parameter of the sine map μ (which dominates the dynamics) is independently varying ($\xi_{95} = 0.50$). Overall, we found strong support for *hctsa* being a comprehensive interdisciplinary feature library for detecting diverse parametric variation across the broad range of dynamical models analysed in this work.

5.1.3 Case study 1: The Van der Pol Oscillator

Before examining the behavior of our method across all systems and on peripheral nerve recordings in specific, we first demonstrate it on the simple example of a two-parameter Van der Pol oscillator, $\mathcal{M}(c, k)$, defined by:

$$\ddot{x} - c(1 - x^2)\dot{x} + kx = 0, \quad (5.2)$$

yielding a $\mathcal{X}^{(2)}$ dataset of 400 time series by sampling $c \sim U(0.1, 5)$ and $k \sim U(0.1, 5)$. Sampled points are plotted in the (c, k) parameter space in Fig. 5.1.7A, with some example time series ordered by increasing c and k plotted along each axis. Without any knowledge of the generative model, $\mathcal{M}(c, k)$, or its parameters, we followed our method to reconstruct the underlying space of parametric variation in the dataset by applying dimensionality reduction to the extracted feature space (depicted in Fig. 5.1.2), yielding the two-dimensional Isomap reconstruction shown in Fig. 5.1.7B. In a purely data-driven way, the first two Isomap components structure the dataset in a way that clearly recapitulates the (*a priori* unknown) parametric variation of the underlying Van der Pol model used to generate the dataset. Both model parameters are well reconstructed as linear combinations of the two

Isomap dimensions, Isomap-1 and Isomap-2: $\chi_c = 0.09, \chi_k = 0.07$. Analysing the residual variance as a function of the number of Isomap dimensions, shown in Fig. 5.1.7C, we observe saturation at $\hat{d} = 2$, supporting the two-dimensional parametric variation of the underlying model. The unexplained variance in k, χ_k , drops with the first Isomap component (which therefore provides a data-driven estimate for k), and χ_c drops with the second Isomap component (which provides a data-driven estimate for c); both saturate at $\hat{d} = 2$, consistent with the two-parameter model used to generate the dataset (Fig. 5.1.7C). Consistent with k controlling oscillation frequency and c controlling the shape of the oscillation, Isomap-1 is highly correlated to time-series features derived from the power spectrum (that provide good empirical estimates of the oscillation frequency, $\sim k$) and Isomap-2 is highly correlated to features measuring smoothness/sharpness characteristics of the waveform (using momentum and wavelet-based features that provide good empirical estimates of c).

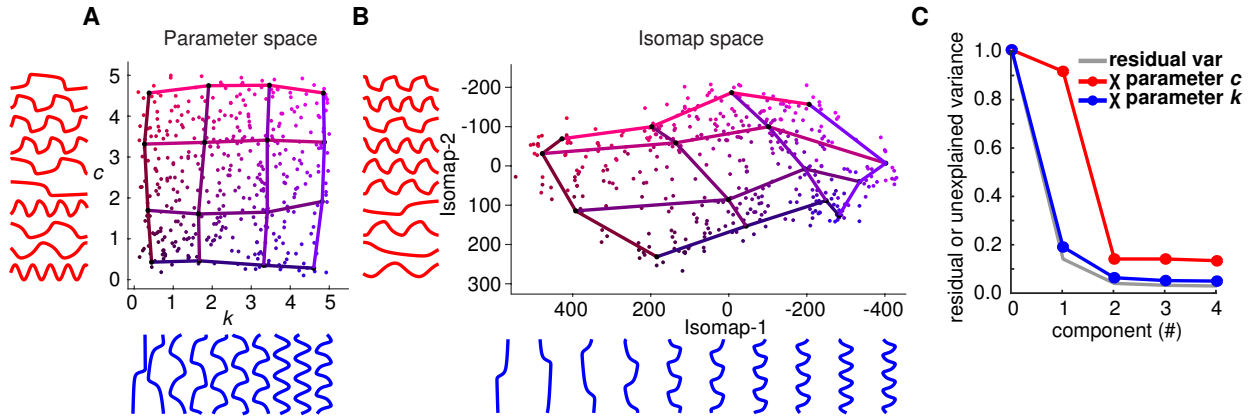


Figure 5.1.7: **Our method can infer a low-dimensional embedding of time-series properties that reconstructs the sampled parameter space of the time-series generative model for the Van der Pol oscillator.** Here we apply our method to the van der Pol oscillator: $\ddot{x} - c(1 - x^2)\dot{x} + kx = 0$, using x as the state variable of interest and independently sampling the two model parameters, c and k . **A** Sampled points in parameter space, generated by independently sampling $c \sim U(0.1, 5)$ and $k \sim U(0.1, 5)$. Simulating M at each point in parameter space specifies a time series. Points in the space are colored by their position in the space (from black \rightarrow blue along k and from black \rightarrow magenta along c). Some example time series are plotted along the horizontal and vertical axes, ordered by increasing c and k , respectively. Lines connect points in embedded space along which one parameter (in this case either c or k) was approximately constant. **B** Our unsupervised reconstruction of the parametric variation underlying variation across the dataset, by applying Isomap dimensionality reduction (Tenenbaum et al., 2000) to an extracted feature matrix (cf. Fig. 5.1.2). Points are colored according to their ground-truth parameter values, (c, k) , as in A, revealing a good reconstruction. **C** Unexplained variance as a function of the number of Isomap dimensions, reveals a saturation in explained variance at an estimated parametric dimensionality, $\hat{d} = 2$, corresponding to the true number of degrees of freedom in the generative model, $M(c, k)$.

This case study demonstrates how our feature-based dimensionality-reduction method, working only with an unlabeled time-series dataset, is able to: (i) structure the dataset in a low-dimensional embedding space that approximately reconstructs the parameter space sampled by the underlying generative

model, (ii) correctly estimates the two-dimensional parametric variation underlying the dynamical properties observed in the empirical dataset, and (iii) provides interpretable time-series estimators of those two dimensions, in terms of spectral features sensitive to oscillation frequency (which characterise Isomap-1, and the model parameter k), and features of waveform shape (which characterise Isomap-2, and the model parameter c).

These results, characterised by low residual variance in estimates of c ($\chi_c = 0.09$) and k ($\chi_k = 0.07$), are unique to applying dimensionality reduction in the space of extracted features (the time-series measurement space yields high unexplained variances $\chi_c = 0.97, \chi_k = 0.79$), and the good performance also owes to the comprehensiveness of the *hctsa* feature library (repeating the analysis using a reduced 22-feature library, *catch22*, failed to capture the subtle variation in waveform shape, $\chi_c > 0.9$). The feature space, not the dimensionality reduction method, was most crucial to these results (similar results were obtained with PCA).

5.1.4 Low-dimensional projections

Having characterised the performance of our method on an exemplar system, the van der Pol oscillator, and one example of our simulated peripheral nerve recordings (Sec. 5.1.5), we next examine selected low-dimensional projections of a range of different types of systems, shown in Fig. 5.1.8.

Feature-based dimensionality reduction of time-series datasets generated through varying a single parameter, $\mathcal{X}^{(1)}$, yielded meaningful and approximately one-dimensional structures in the extracted Isomap embedding space (Figs 5.1.8A1–A4). Examples are shown for datasets generated by: varying the powerlaw scaling exponent, $\alpha \sim U(-1, 3)$, in a dataset of self-affine time series (Fig. 5.1.8A1); varying the switch-rate, $\alpha \sim U(0, 1)$, in a bimodal switching model (Fig. 5.1.8A2); varying the parameter $a \sim U(0.15, 1.5)$ in the Mackey-Glass system (Mackey and Glass, 1977) (Fig. 5.1.8A3); and varying the shape parameter, $c \sim U(0.1, 5)$ of the Van der Pol oscillator (Sprott, 2003) (Fig. 5.1.8A4). In each case, the time series are automatically structured along an approximately one-dimensional manifold in the extracted Isomap embedding space, with the position along the curve approximately following the variation of the underlying parameter in the generative model. In each case, independent of the complexity of the generative model and the time series it produces, our data-driven method picks up the approximately one-dimensional variation in the underlying parametric variation.

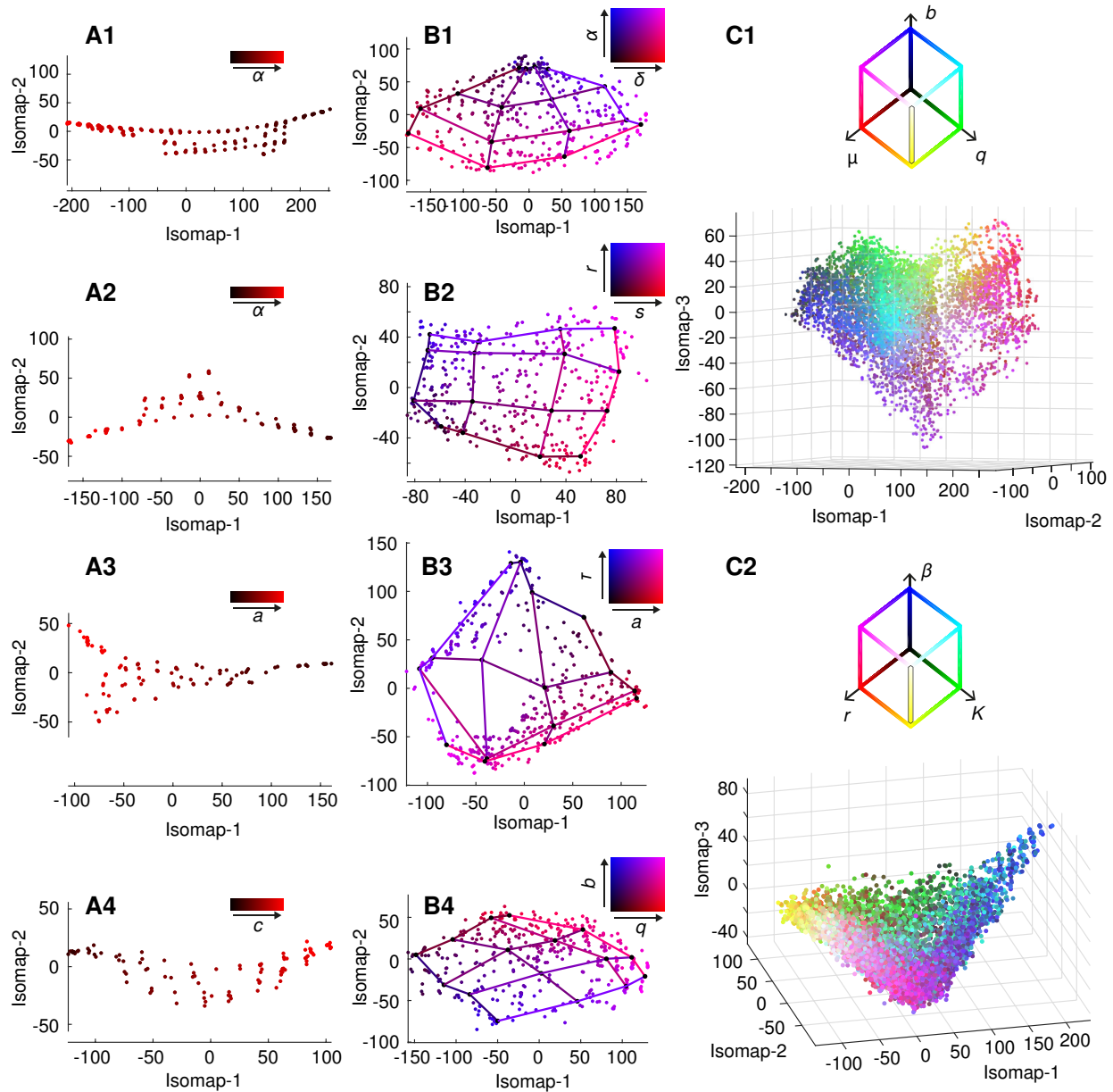


Figure 5.1.8: **Our library is sufficiently large and rich to allow automatic reconstruction of the underlying model parameter space from unlabeled empirical time-series datasets.** Examples of parameter reconstruction for selected systems with one free parameter, $\mathcal{X}^{(1)}$ (**A1–A4**), two free parameters, $\mathcal{X}^{(2)}$ (**B1–B4**), and three free parameters, $\mathcal{X}^{(3)}$ (**C1** and **C2**). **A1**: Self-affine (Malamud and Turcotte, 1999); **A2**: Bimodal (Fulcher, 2012), x , (α); **A3**: Mackey-Glass (Glass et al., 1988), (a); **A4**: Van der Pol (van der Pol, 1926), x , (c); **B1**: Bimodal (Fulcher, 2012), (δ, α); **B2**: Lorenz (Lorenz, 1963), y , (s, r); **B3**: Mackey-Glass (Glass et al., 1988), (a, τ); **B4**: Stochastic sine map Freitas et al. (2009), (q, b); **C1**: Stochastic sine map Freitas et al. (2009), (μ, q, b); **C2**: Population growth (Levins, 1969), (r, K, β). Each dot represents a time series in embedded space and is colored according to the true parameter values. For the two-dimensional parameter variations in panels **B1–B4**, grid lines indicate trajectories in the embedded space along which one parameter was approximately constant. Panels **C1** and **C2** display the 3D-space of the first three Isomap components. The color of time series points again indicates true parameter values, encoded by a three-dimensional color map.

When two parameters vary independently in generating $\mathcal{X}^{(2)}$ datasets, we typically find corresponding two-dimensional structure in the estimated low-dimensional feature-space embedding. Examples are

plotted for datasets generated by: varying the well separation $\delta \sim U(0, 6)$ and switch probability $\alpha \sim U(0, 1)$ in the bimodal switching model (Fig. 5.1.8B1); varying $s \sim U(8, 30)$ and $r \sim U(35, 60)$ of the Lorenz attractor (Fig. 5.1.8B2); varying $a \sim (0.15, 1.5)$ and $\tau \sim \{10, 11, \dots, 40\}$ in the Mackey-Glass system (Fig. 5.1.8B3); and varying the noise occurrence probability $q \sim U(0, 1)$ and amplitude $b \sim U(0, 3)$ in the stochastic sine map (Fig. 5.1.8B4). For each of these systems, the geometry of the underlying parameter space is approximately reconstructed in the extracted embedding. For the Lorenz attractor and stochastic sine map (Fig. 5.1.8B2 and B4), the reconstructed rectangular grid reflects the uniform sampling undertaken in parameter space. The bimodal switching system (Fig. 5.1.8B1) contracts towards low values of δ towards a point. This behavior reveals an important characteristic of the bimodal switching system, which draws data from one of two states, defined by two Gaussian distributions separated by a distance δ (see Eq. (5.7) in Appendix 5.1.11.B). As δ decreases the two states become less distinct, and in the limiting case, $\delta = 0$, both states are identical and variations in the switching probability, α , have no affect on the dynamics. This meaningful interplay between δ and α is clear in the geometry of the reconstructed embedding space, Fig. 5.1.8B1, which collapses to a point at low δ . Similar transition-like behavior in Mackey-Glass system with a (from a low- a chaotic regime to a high- a oscillatory regime), yields a meaningful distortion to the two-dimensional geometry of the sampled parameters, shown in Fig. 5.1.8B3.

When three parameters are independently sampled in generating $\mathcal{X}^{(3)}$ datasets, we found corresponding three-dimensional structure in the estimated low-dimensional feature-space embedding. Two selected examples are shown for simultaneously varying: the map parameter, $\mu \sim U(0.5, 4)$, noise probability, $q \sim U(0, 1)$, and noise amplitude, $b \sim U(0, 3)$, in the stochastic sine map (Fig. 5.1.8C1); and varying the growth rate, $r \sim U(0.1, 3)$, carrying capacity $K \sim U(0.5, 5)$, and noise amplitude $\beta \sim U(0.1, 10)$ in the population growth model (Fig. 5.1.8C2). In both cases, we reconstruct a meaningful three-dimensional embedding of the data that mirrors the three-dimensional space from which the underlying model parameters were sampled.

These results demonstrate the ability of our method to infer dynamical constraints as low-dimensional structure across a sufficiently rich feature set for selected one-, two-, and three-dimensional parameter spaces.

5.1.5 Case study 2: Simulated peripheral nerve recordings

Current non-invasive interfaces (cuff electrodes) used in bioelectronic medicines do not allow for the differentiation of single fibers. The resulting superposed activity of many axons in a nerve-bundle, compound action potentials (CAP), is often summarised by simple measures like amplitude of the rectified and integrated signal (Micera et al., 2001; Cavallaro et al., 2003) or the power (as square of amplitudes from a Fourier spectrum) in a certain frequency band (Ch. 4.1, (Lubba et al., 2017)). Many subtleties are known to exist in peripheral firing such as active fibre diameters, active fascicles and different rhythms (Malpas, 1998), many of which will be informative for decoding but are lost in these coarse summary measures. If we could identify some of those firing characteristics in a peripheral nerve recording and estimate them in each new observation, we might have a better starting point for decoding and to detect unusual activity.

We here apply our presented feature-based method to low-resolution peripheral nerve recordings generated in our simulator PyPNS to characterise the recordings by a few key measures. We want to uncover the three activity characteristics firing rate, myelination, and burstiness that varied in simulation just as we did for the parameters of our synthetic systems covered so far. Ideally, each of the two to three characteristics that varied in a given dataset would be recovered in one reduced component (we use PCA here) in feature-space each.

Similar to the Van der Pol oscillator, we demonstrate this correspondence between PCs and characteristics in a first example. Fig. 5.1.9 plots the time-series points for the varying characteristics firing rate and burstiness projected onto the first and second PC. As can be seen, firing rate is cleanly captured by the first component, burstiness by the second. At lower firing rates (to the left of the plots in Fig. 5.1.9), PC2 is less informative of burstiness, consistent with visual intuition from Fig. 5.1.4A and C (burstiness is harder to distinguish for low firing-rate).

As an overview over all our four PNS datasets, Fig. 5.1.10A shows the correlation between firing characteristics and each of the first components for datasets with noise-level -6dB (see Fig. 5.1.4 for an example recording). On the three $\mathcal{X}^{(2)}$ datasets with two varying characteristics, especially in the pairs (burstiness, myelination) and (firing rate, burstiness), each characteristic was recovered well by a single PC each. Per PC, one parameter had a correlation of at least 0.8, the second parameter less than 0.15. For the pair (myelination, firing rate), firing rate was not cleanly separated from myelination as

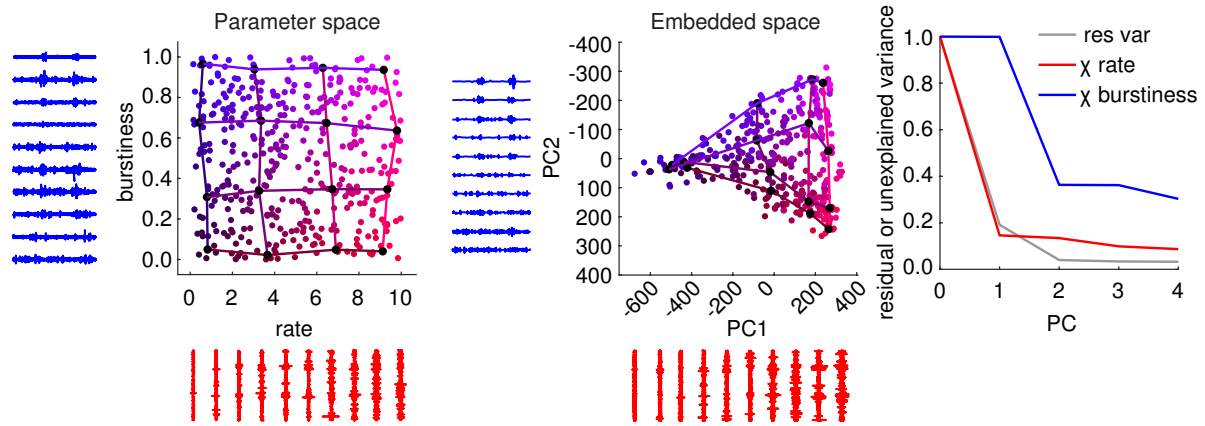


Figure 5.1.9: **Example for a successful unsupervised detection of the characteristics burstiness and firing rate in the first two principal components (PC).** When projecting the time series into the space of the first two principal components as obtained from PCA in our $\sim 7\,000$ -dimensional feature-space (here as axes in embedded space), each of the two main signal characteristics is captured in one dimension (coloring). Each dot is a time series. At low firing rates (low PC1, to the left of the embedding panel), burstiness cannot be detected anymore as was to be expected from Fig. 5.1.4.

noise partly shadowed action potentials from unmyelinated fibres. At three varying characteristics, burstiness and myelination were reasonably captured by the first and second PC (correlation > 0.6) but firing rate could not be cleanly separated anymore as no PC was the most correlated to this parameter. Across all datasets, PC1 captured between 60 and 90% of the variance, the PC2 5 to 25%, and PC3 1 to 5%.

The *hctsa* feature library is therefore suitable for peripheral nerve recordings. To further probe the method on our main study object, we conducted two more analyses on the robustness of the results. We first investigated how sensitive the results are towards reducing the number of features. To this end, we randomly selected subsets of the *hctsa* feature pool. A characteristics-dependent parameter reconstruction performance decline with modest losses from $\sim 1\,000$ features can be observed in Fig. 5.1.10C. We would therefore achieve the same results by pruning our feature set by a factor of about 7 and can therefore reduce computation time.

As it is a relevant problem in peripheral nerve recordings, we also tested the robustness of our method against noise by adding white Gaussian noise of different power to the signals. Such noise is to be expected due to the recording of very small potential changes and associated high gains by noisy amplifiers. Until a noise root-mean-square (RMS) power of half the signal RMS (-6dB), the characteristics set in our simulation were recovered well, see Fig. 5.1.10B. Myelination ratio was the most robust against noise as expected from the high action potential amplitudes from myelinated fibres,

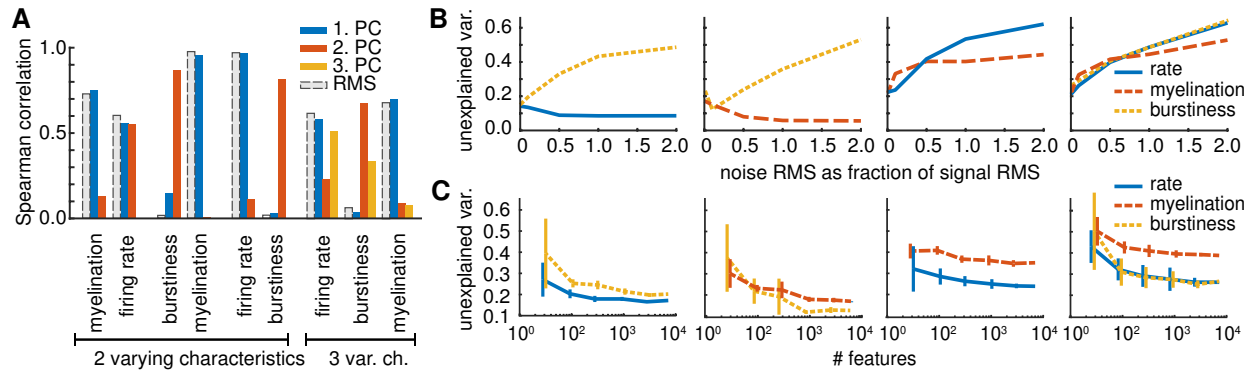


Figure 5.1.10: **Two varying characteristics are well recovered by PCA in feature space up to a noise-power of half the signal power (−6dB). The second and third principal component provide additional information compared to standard power-measures.** (a) Noise RMS was set to half the signal RMS, see Fig. 5.1.4 for example time series. Bars indicate the Spearman rank correlation between a single characteristic of a dataset and the classic measure RMS as well as the first principal components (PCs) obtained by dimensionality reduction. The feature RMS (grey bars with dashed outline) has similar correlations to parameters compared to the first PC. (b) Abscissa is the unexplained variance between the actual signal characteristics and the ones linearly regressed against the first dimensions. (c) When only considering a subset of all ~7 500 *hctsa*-features, characteristics recovery declines. Each number of features randomly sampled 10 times, SNR=0.1.

burstiness and firing rate could not be well detected at high noise levels.

So far we have shown that unsupervised dimensionality reduction in feature-space is a promising way of extracting meaningful low-dimensional variation in our simulated neural datasets. Even in the presence of noise and when reducing the number of features to reduce computation time. But can we interpret each dimension in terms of the signal properties that are being measured, and are they sensible given what we know is varying in the underlying system? To answer these questions, we rank single features by their Pearson correlation to the principal components – and therefore the varying characteristics in the data.

In general, the highest Pearson correlations between single features and principal components reached at least 0.8 and often 0.98 or better, meaning that we can find appropriate single features to represent each principle component. For the characteristic myelination ratio, features selected by our method typically evaluate extreme events, outliers, statistics on residuals in local fits. This makes sense as myelinated axons produce very strong peaks. Features corresponding to firing rate components often compute value distribution properties and autocorrelation measures that detect uncorrelated noise vs natural signals. Burstiness-features measure stationarity and predictability. We therefore automatically identify sensible features.

Finally we may ask what our low-dimensional representations add to the standard power-based features computed currently on peripheral nerve activity? For a brief comparison of our method to RMS as a feature, we added its Spearman rank correlations to the characteristics set in our simulation in Fig. 5.1.10A. Naturally, with a univariate power measure, no distinction between different firing characteristics is possible. Interestingly however, our first principal component behaves largely identical with RMS in terms of correlation to the data characteristics, meaning that this feature has very similar correlations to the parameters as did PC1. In the following PCs, more subtle dynamical properties such as burstiness and myelination were recovered. The estimators selected by our method thus cover all signal properties captured by state-of-the-art measures but importantly provide additional information about more subtle firing characteristics.

5.1.6 Performance across diverse synthetic time-series models

The above results demonstrate the success of our method across selected synthetic systems and for our simulated peripheral nerve recordings. It is thus a relevant technique for bioelectronic medicines as a data analysis and signal pre-processing step. We next aimed to understand the strengths and weaknesses of our method across the diverse library of dynamical systems and synthetic datasets we compared.

5.1.6.1 Dimensionality estimation

The first test involves empirical estimation of the parametric dimensionality of each system, \hat{d} . As described in Methods, we used a simple data-driven heuristic to estimate \hat{d} , based on the saturation of residual variance as a function of the number of dimensions. As shown in Fig. 5.1.11, the distribution of \hat{d} across all systems is mostly concentrated on the true parametric dimensionality of the system. However, it can also overestimate the dimensionality of one-dimensional systems, and underestimate the dimensionality of two- and three-dimensional systems.

Overestimation, $\hat{d} > d$, occurs when there are insufficiently many features in *hctsa* that are sensitive to the parametric variation represented in the system. An example is the one-dimensional variation of the mean, s , of a noisy sinusoid: as relatively few features in *hctsa* are mean-sensitive (17 features have

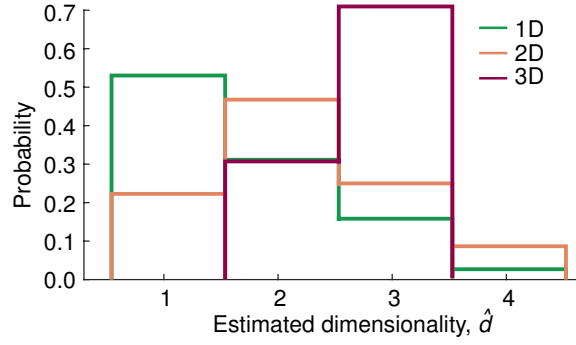


Figure 5.1.11: **The estimated dimensionality, \hat{d} , of the extracted feature matrix, F , mostly corresponds to the parametric dimensionality of the underlying generative time-series model.** Distributions of \hat{d} are shown for 93 datasets generated from varying a single parameter, $\chi^{(1)}$ (green), two independent parameters, $\chi^{(2)}$ (pink), and three independent parameters, $\chi^{(3)}$ (purple).

a strong correlation $r > 0.9$) such that noisy variation in the thousands of other features dominated the feature-space variance, leading to an overestimate, $\hat{d} = 4$, for this system. As a typical problem, only a small number of features in our library provide adequate estimators for a parameter of interest. We call these under-represented parameters ‘weak’. In some cases, both parameters of a 2D system were weak, e.g., Lorenz oscillator x and y (r, b). As neither r nor b drove many parameters ($\xi_{95} \leq 0.7$ for x and y), both were estimated as 4-d instead of 2-d. Underestimation, $\hat{d} < d$, occurred when the sampled variation in one parameter dominated the variation in time-series dynamics relative to the other sampled parameter(s). This gives the appearance of low-dimensionality, as variation in the additional parameters resulted in relatively small changes to the empirical dynamics. This occurred for the ‘noisy shifty sine’ model with two-dimensional variation in the mean-shift, s , and noise level, η . As outlined above, our feature library contains relatively few estimators of s compared to η , resulting in a dominating effect of η which shadows the relatively subtle variations in s .

5.1.6.2 Parameter reconstruction

We next investigated how successfully the model parameters could be reconstructed as linear combinations of the low-dimensional data-driven embedding dimensions. As explained in Methods, this was assessed on the basis of the unexplained variance, χ_α , of a given parameter, α , of the optimal linear combination of d dimensions (for a d -dimensional system). Distributions of χ are shown for every parameter in every system in Fig. 5.1.12. As expected, the ability to linearly reconstruct the variation of a given parameter, χ , is highly correlated to the representation of that parameter in the feature space, quantified as the 95th percentile of the distribution of univariate correlations, ξ_{95} (Fig. 5.1.S1,

Pearson correlation $\chi^{(1)}$ 0.72, $\chi^{(2)}$ 0.82, $\chi^{(3)}$ 0.80). Thus, when there are more feature-based estimators of a parameter, that parameter will drive more variance in the *hctsa* feature library, and thus make a greater contribution to the estimated low-dimensional embedding. Results for parameter reconstruction thus follow the results for ξ_{95} above. Even in cases for which such an exercise may seem impossible (e.g., inferring the map parameter μ , noise amplitude b , and noise probability q from a stochastic sine map dataset, depicted in Fig. 5.1.5), our data-driven three-dimensional embedding linearly captures variation in μ ($\chi_\mu = 0.18$) and b ($\chi_b = 0.22$), and contains some information about q ($\chi_q = 0.63$).

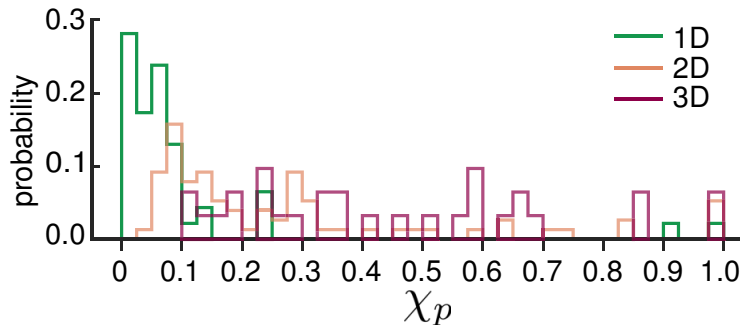


Figure 5.1.12: **Our library is of sufficient size and diversity to allow us to successfully recover the parameter values for 1-d and 2-d systems. Three-dimensional parametric variation had mixed outcomes.** We plot the distribution of χ , the unexplained variance $1 - R^2$, between linearly estimated parameters \hat{p} from the first d embedded components and true parameters p . Distributions are shown for: 46 one-parameter datasets, $\chi^{(1)}$ (green), 74 parameters across 37 two-parameter datasets, $\chi^{(2)}$ (orange), and 30 parameters across 10 three-parameter datasets, $\chi^{(3)}$ (purple).

Taken together with the low-dimensional projection results presented above, we find that leveraging a diverse scientific literature on time-series analysis using *hctsa* allows time-series datasets to be embedded into a space that best captures the parametric variation of the underlying model across it. The construction of the feature space (including what features are included) is crucial to the quantification of ‘dynamical variation’, and in effectively weighting the relative importance of different types of dynamical variation. For example, dynamical variation for which there are more estimators in *hctsa* is more highly weighted than types of dynamical variation for which there are relatively few estimators. Parameters for which there are relatively few estimators in *hctsa* (like trivial variation of mean-shifts) can thus be neglected, and the range over which a parameter is varied in the underlying model also affects the amount of dynamical variance that it contributes to shaping across the empirical dataset.

5.1.7 What characteristics of data are suitable

Our method performs best in 1-d and 2-d cases where parameters cause a smooth change in dynamics that is captured by enough features.

There exist several conditions for which we encounter difficulties in both dimensionality estimation and parameter reconstruction. As a typical problem, only a small number of features in our library provide adequate estimators for a parameter of interest ('weak' parameters). The classic example designed to demonstrate this effect is the 'noisy shifty sine', in which only a few features evaluate a constant offset, s ($\chi_s = 1.00$). A similar case is the carrying capacity K of 'population growth' ($\chi_K = 0.23$). Weak parameters can appear in pairs: in the system Lorenz $x(r, b)$, not many features correlate with either r or b ($\xi_{95}^r = 0.56$, $\xi_{95}^b = 0.70$), causing a low reconstruction performance ($\chi_r = 0.74$, $\chi_b = 0.32$) and an overestimated dimensionality ($\hat{d} = 4$). At multiple varying parameters, an imbalance in number of responsive feature between parameters causes problems. If one parameter drives a much larger share of features, this variation can shadow less influential ones. This effect can be observed in 'noisy trendy sine' (T, η) where the noise controlled by η is captured by many features ($\hat{d} = 2$, $\xi_{95}^\eta = 0.92$, $\xi_{95}^T = 0.36$, $\chi_T = 0.45$, $\chi_\eta = 0.10$), similarly the parameter combination (η, m) of the same system ($\hat{d} = 2$, $\xi_{95}^\eta = 0.90$, $\xi_{95}^m = 0.08$, $\chi_m = 1.00$, $\chi_\eta = 0.08$).

In embedded space Ξ , time series with similar dynamics – as judged by the *hctsa* feature ensemble – are positioned nearby one another. If a parameter causes abrupt changes in dynamics or no changes, the resulting jumps or plateau-phases in dynamics along the uniformly sampled parameter space will become apparent in embedded space as gaps or accumulations of similar time series. A 1-d example is stochastic sine map (A) that passes through several bifurcations with increasing A -values to produce very different dynamics (periodic or chaotic) depending on the exact A -value ($\hat{d} = 2$, $\chi_A = 0.90$, $\xi_{95} = 0.85$). Still, the second embedding component recovers A well ($\chi_A = 0.11$). Similarly, the dynamics of Mackey-Glass (a, r) in Fig. 5.1.8B3 do not change smoothly with r , leaving an accumulation and a gap ($\hat{d} = 2$, $\xi_{95}^a = 0.78$, $\xi_{95}^r = 0.85$, $\chi_a = 0.26$, $\chi_r = 0.11$).

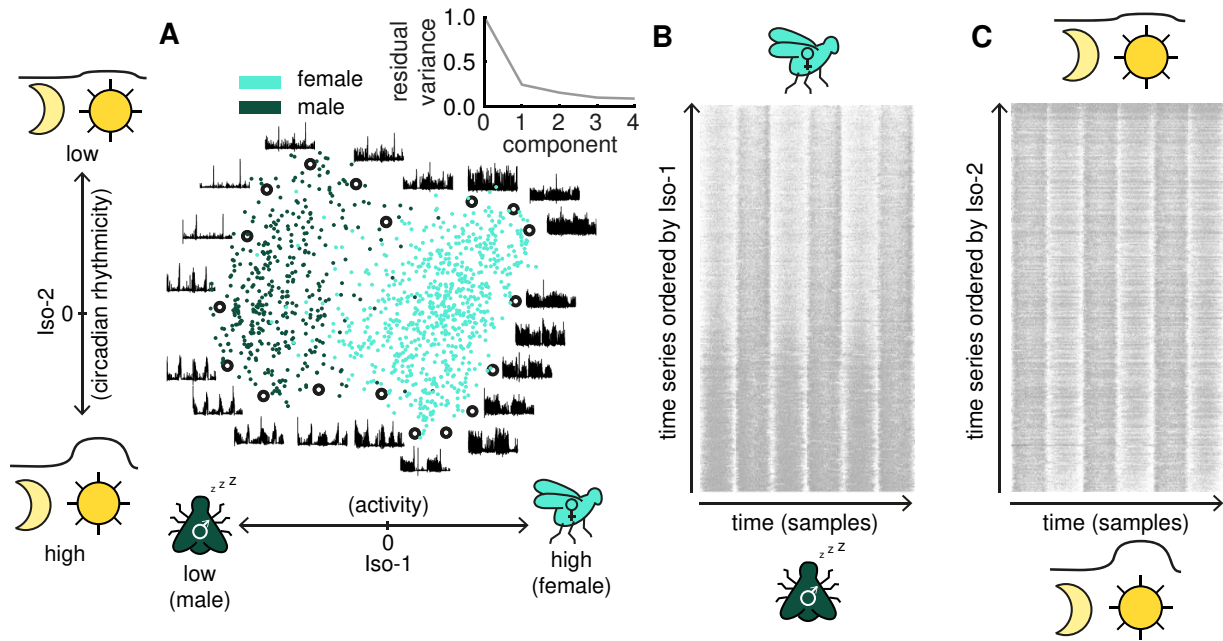


Figure 5.1.13: **Our data-driven method constructs a meaningful low-dimensional embedding space for a movement speed dataset of 1143 flies, organising the files by activity level and circadian rhythmicity.** **A** The Isomap embedding of the time-series dataset, where 12 h time-series segments have been annotated to selected time series. **B** Raster plot of all time series ordered by Isomap component 1, revealing a clear variation in activity profiles of flies with Iso-1. White means high velocity, dark low velocity. Time series were cut to the first 18 h to be of equal length. **C** Raster plot of all time series ordered by Isomap component 2, revealing a variation of circadian rhythmicity of activity with Iso-2.

5.1.8 Case Study 3: Empirical fly data

The synthetic datasets analysed above allowed us to demonstrate the success of our method in reproducing the known parametric variation underlying an empirical dataset. To further assess the performance of feature-based dimensionality reduction to automatically uncover the main sources of dynamical variation underlying real-world datasets, we analysed a *Drosophila melanogaster* movement dataset. It has to be noted here that this type of data does not relate to our original scope of study, peripheral nerve recordings. We still keep it here as a case study to demonstrate the applicability of our more general time series analysis method to experimental data and to show that it can indeed act as a data-driven discovery engine to uncover dominant temporal dynamics. The dataset contains time-series measurements of the movement speed of 1143 flies (408 male, 735 female) confined to an approximately one-dimensional tube and measured over the course of at least 12 h (all >18 h except 4 cases) (during which 3 h dark and 3 h light phases alternated successively). Taking average speeds over non-overlapping 10 s windows yielded a dataset of 1143 time series, each containing a variable number of samples, ranging from 4359–8640 (mean = 8595).

The first two Isomap components had an unexplained variance of 15%, yielding a two-dimensional projection of the dataset shown in Fig. 5.1.13A, where each fly's time series have been colored by sex. We first notice that the first inferred dimension, Iso-1, clearly separates the male and female flies. Ordering all flies along this dimension and plotting their activity time series with color, shown in Fig. 5.1.13B (and visible from the annotations in Fig. 5.1.13A), reveals a sensible ordering of flies along the Iso-1 dimension according to the distribution of activity across time, with low-activity (mostly male) flies exhibiting large bursts of activity with an approximately 3 h period, and high-activity (mostly female) flies exhibiting more consistent activity levels across the full recording. Consistent with this visual intuition, time-series features in *hctsa* that correlate most strongly with Iso-1 were mostly related to the entropy of the movement-speed distribution (including `EN_DistributionEntropy_hist_fd_0`, $r_{\text{Iso1}} = 0.97$). The second Isomap dimension, Iso-2, revealed a more subtle dynamical variation, visible most clearly from the raster plot where flies have been ordered by Iso-2, shown in Fig. 5.1.13C. This plot shows that Iso-2 organises flies on the strength of their circadian (day-night) rhythmicity of activity with the imposed 3 h light-dark cycle. Consistent with this, time-series features in *hctsa* that are most strongly correlated with Iso-2 were related to measures of stationarity (e.g., `StatAvl250`, $r_{\text{Iso1}} = 0.81$) and automutual information on longer timescales (e.g., `IN_AutoMutualInfoStats_40_kraskov1_4_ami40`, $r_{\text{Iso1}} = 0.81$).

To summarise, we found that our data-driven method was able to embed a large and complex dataset of biological time series into a two-dimensional space. Each axis of this space corresponds to a meaningful and biologically interpretable property of the movement-speed dynamics that captures inter-fly variation across the dataset. The performance was specific to the large *hctsa* feature space; alternative smaller feature-sets did not give the same qualitative performance. Using the *catch22* feature set, only the variation in activity (Iso-1) could be retrieved, no rhythmicity; male and female flies were not separated cleanly.

5.1.9 Robustness and Sensitivity

Having demonstrated an ability to embed complex time-series datasets into meaningful low-dimensional spaces that capture the key sources of dynamical variability across the dataset, we now perform tests to further assess the method's strengths and limitations, including its applicability to time-series

datasets of different characteristics (e.g., length, size, signal-to-noise, etc.) on the synthetic datasets as we already did to a certain extent for our case study on simulated peripheral nerve recordings (see Sec. 5.1.5).

We first compare four key parameters of the methodology in their unexplained variance, χ , of each parameter for each synthetic dataset. In each case, shown in Fig. 5.1.14, the two alternatives are compared as the difference in χ between the method we present and an alternative choice; higher values indicate better performance of the method we present.

As a first sanity check it is impossible to obtain a meaningful embedding without computing features from the raw ordered time-series measurements. When computing Isomap in the 5000-dimensional (number of samples per time series) measurement space, the reconstruction fails for all 1D, 2D, and 3D systems, with a mean unexplained variance of at least 0.8 (Fig. 5.1.14A). Only cases where parameters caused clear changes in the overall time series shape could be recovered in measurement space. Examples are the slope, m , in ‘noisy trendy sine’ or the mean shift, s , in ‘noisy shifty sine’.

The ability of our method to detect diverse types of dynamical variation across time-series datasets therefore requires a comprehensive feature library, as in *hctsa*. When we compare to a reduced set of 22 features, *catch22* (that provide similar classification performance across time-series classification tasks; Ch. 5.2, (Lubba et al., 2019)) the average unexplained variance increases by 110% (1D), 73% (2D), and 27% (3D), as shown in Fig. 5.1.14B.

While the *hctsa* feature ensemble is critical for a good performance, the dimensionality reduction method is not. We find a stronger performance in reconstructing the underlying parameters using Isomap relative to PCA (Fig. 5.1.14C). However, PCA performs only slightly worse (50% higher unexplained variance for one-dimensional systems, but only 8% for two-dimensional, 7.5% for three-dimensional systems).

5.1.9.1 Number of features required

We have seen that the success of our method hinges on the comprehensive feature library provided by the *hctsa* toolbox. A subset of 22 proven general purpose features could not achieve a comparable parameter reconstruction (Fig. 5.1.14B). Computing 7 000 features on every new dataset is, however, a

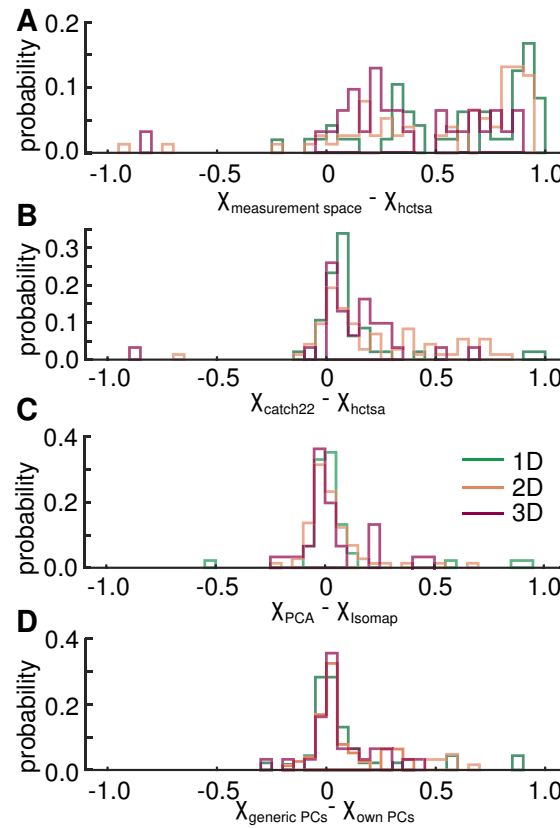


Figure 5.1.14: **Our method is not highly dependent on the dimensionality reduction method, but on the feature library.** **A** Difference in unexplained variance of parameter reconstruction χ when applying Isomap to either the raw 5000 samples of each time series or the feature-based representation using *hctsa*. The positive values indicate that the feature-based representation is clearly superior. **B** Difference in performance χ between Isomap on either 22 selected features (*catch22*) or the full *hctsa* feature set. **C** Again, difference in χ , now between the linear PCA and the nonlinear Isomap. Positive values indicate that Isomap was more successful. **D** Difference in χ between PCA score from either the PCs of the dataset at hand or from a generic, diverse time-series set. Positive values indicate that performance is better using the dataset's own PCs.

substantial computational burden. We therefore investigated at what number of features the parameter reconstruction saturates. By randomly sampling an increasing number of features from the *hctsa* library, we found a performance plateau at only about 300, similar to the 1000 found for peripheral nerve recordings in Fig. 5.1.15A. The full wealth of *hctsa*'s features is often not needed for this library of models.

5.1.9.2 Number of time series required

Not only computation time is a constraint in applying our method to new real-world data but, more importantly, data availability. Not every investigator will be in possession of 1000 real-world time series as we were in our case study (Fig. 5.1.13) – but do we really need that many to successfully

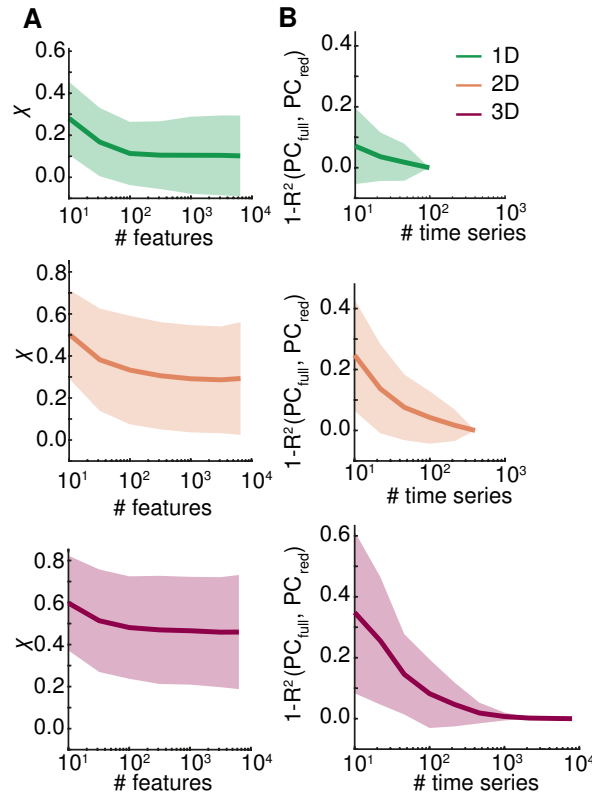


Figure 5.1.15: **The dimensionality reduction requires about 300 features and 1000 time series.** **A** Unexplained variance of parameter reconstruction using a randomly sampled subset of features (10 repetitions), error surface indicates standard deviation across mean errors across repetitions. A saturation at about 300 features can be observed for all system dimensionalities. **B** As the unexplained variance of parameter reconstruction is difficult to estimate with few time series (always low), we demonstrate the saturation of dimensionality reduction outcomes with number of time series for PCA and compare the scores of all time series with the PCs of a reduced time-series set. Saturation is only clearly visible at about 1000 time series for 3-d systems.

identify the relevant dynamics? Using the well-known parameter reconstruction error of Isomap, χ , Sec 5.1.1.5, was not possible in this analysis because a decreasing number of time series prevents us to compute a meaningful correlation between time-series Isomap-scores. Instead, we compute the pairwise unexplained variance between principal components of PCA of (1) the full time-series set and (2) randomly sampled reduced sets in Fig. 5.1.15B. These correlations only visibly saturate for the 3-d systems at about 1000 time series. The 1-d and 2-d cases were limited at 100 and 400 time series, respectively, and do not shown a clear plateau phase. In 1-d, the PCs' unexplained variance start at remarkably low values, however; 2-d PCs had unexplained variances below 0.1 at 100 time series as well. The number of time series therefore becomes increasingly important for higher-dimensional parameter variations but still saturates at about a thousand. Lower dimensional systems do not depend on the availability of large datasets.

It might surprise that the number of time series is often not crucial for performance. Let us consider PCA for a simpler, more intuitive understanding. Each PC bundles the features that were jointly driven by a certain parameter as one projection direction. So how can PCA pick out the relevant projection directions in a 7000 dimensional space by only considering 50 time series? The explanation lies in the biased nature of our feature library. Within the *hctsa* ensemble, there exist large feature families which are algorithmically similar (e.g., autocorrelation at different lags). Members of such families will, even if given a non-constrained dataset (as shown in schematic Fig. 5.1.2E), form similarly behaving feature-clusters, and therefore projection directions within PCA. These default PCs, even though dataset-independent, often capture generically useful classes of variation. The predominance of a certain feature type in *hctsa* toolbox often reflects its importance in the time-series analysis literature, and therefore its utility. In fact, Fig. 5.1.14D demonstrates that ‘generic’ PCs, computed on a dataset of diverse empirical time series (Fulcher, 2017), often perform almost as well as the the principle components obtained from the dataset itself.

5.1.9.3 Influence of number of samples, sampling rate, and signal-to-noise ratio

Our entire analysis was based on 5000-sample time series at a sampling rate suited to the system at hand. What time series properties does our method require? In a single case study system, van der Pol, x , we varied (1) number of samples, (2) sampling rate, and (3) signal-to-noise ratio (SNR) through added Gaussian white noise. As can be seen in from the difference between Fig. 5.1.16A and B for parameters c (dampening) and k (frequency), the results were very specific to the time-series dynamics at hand. The more subtle parameter c (Fig. 5.1.16A) required long time series of high signal-to-noise ratio (Fig. 5.1.16A1-A3). Parameter k on the other hand, causing a more obvious variation in oscillation frequency, could be well reconstructed, even for only 100 time steps, as long as the signal-to-noise ratio was high (Fig. 5.1.16B1-B3). Low SNR could sometimes be compensated by long time series (cyan in Fig. 5.1.16B2), high SNR was the most crucial factor for success (Fig. 5.1.16B3). The dependence of our method success on these additional parameters will vary from dataset to dataset. Presumably more subtle dynamics will require longer time series and a higher signal-to-noise ratio as the parameter c in this case study.

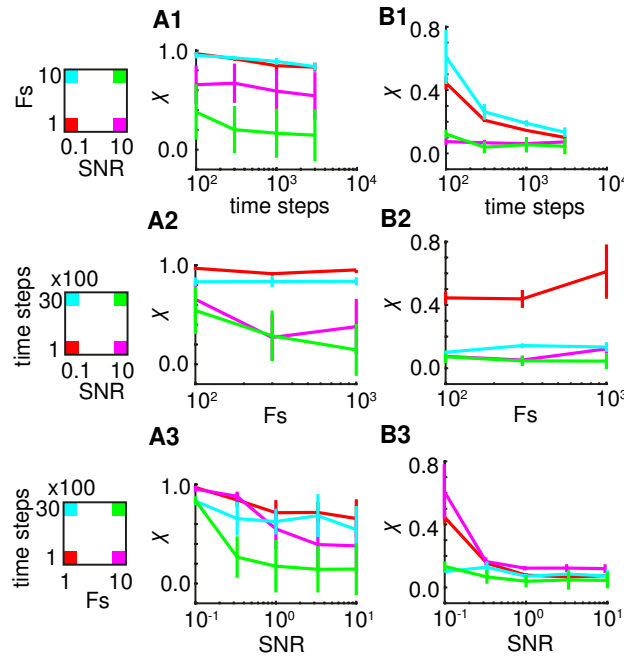


Figure 5.1.16: **Case study of parameter reconstruction robustness against shortening of time series and decreasing signal-to-noise ratio. Van der Pol x.** **A** Parameter c. **B** Parameter k. Error bars across 10 repetition with 300 time series randomly sampled from 400.

5.1.10 Discussion

We have in this work shown that dimensionality reduction in a high-dimensional feature space covering decades of interdisciplinary time-series analysis can be used to discover and estimate sources of free variation in constrained time-series datasets. We tested our method on a range of various synthetic datasets generated by different types of generative models. On this data, we showed that the parameters governing the low-dimensional variation can be reliably estimated for a broad range of one- and two-parameter systems. We further successfully applied the method to simulated peripheral nerve recordings and to a real-world dataset of *Drosophila melanogaster* fly movement patterns.

Note that such results could not be obtained by analysing the time series in the measurement space. In measurement space, (i) longer recordings increase the dimensionality of each time series, (ii) differences in phase affect ability to estimate low-dimensional manifolds, and (iii) nonlinear or chaotic dynamics often lead to very different waveform shapes for the same parameter settings. Using our feature-based approach, however, here we are able to identify the underlying variation for time series independent of length and phase by the dynamical properties of the recordings. We are able to extract meaningful embeddings for time-series datasets in terms of their *properties* rather than simply their values. If the real source of variation underlying a time-series dataset is unknown, this method can

be use to (1) detect dominant variation in time-series dynamics and (2) extract a set of features that correspond to each type of dynamics. Feature interpretation could help a time-series analyst understand what time-series properties are important in explaining most of the variation in a dataset. Our framework therefore allows one to understand both how many free parameters are required, and what sorts of dynamical properties they control. It may form the basis to linking a theoretical understanding of time-series models with the empirical practice of collecting and analysing time series.

In our field of peripheral nerve decoding algorithms, low-resolution cuff recordings have been characterised by simple amplitude- or power-based measures in the past. We here demonstrate the feasibility of our feature-based analysis approach to (1) automatically detect important firing characteristics in the continuous recorded waveform and (2) provide simple feature-based estimators for each. Our method is successful on simulated peripheral nerve recordings in which two independent peripheral firing characteristics could be recovered cleanly in most cases. The method provides a low-dimensional representation of the neural time-series data in meaningful dynamical properties that is more informative than the state-of-the-art characterisation by simple power measures (RMS). Applied to different data, the method will automatically select features that reflect the interface technology used, the nerve targeted, and the firing patterns recorded – it will therefore adapt to any new recording setup. The selected single estimators for important dynamical properties of peripheral firing can be implemented efficiently for the use in next generation bioelectronic medicines devices and the method may find application in related BMI tasks as well.

5.1.11 Appendix

5.1.11.A Feature library

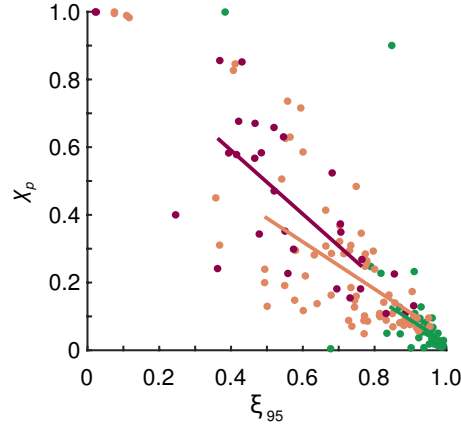


Figure 5.1.S1: **The more features a parameter drives, the better it is recovered by our method.** Scatter of feasibility ξ (as in Fig. 5.1.6) vs reconstruction performance χ (as in Fig. 5.1.12. Correlations 0.72 (1-d), 0.82 (2-d), 0.80 (3-d).).

5.1.11.B Time-series Datasets

Noisy Trendy Sine This simple time-series system generates a sinusoid with period T , with a linear trend of gradient m and additive noise of standard deviation η . Time series, x_t , are generated according to the following model:

$$x_t = \sin(2\pi t/T) + mt/N + \eta n_t, \quad (5.3)$$

for a period T , gradient m , and noise standard deviation η , and $n_t \sim \mathcal{N}(0, 1)$. In generating datasets, we varied T , m , and η as in the table below:

Parameter	Values
T	$U(10, 100)$, or 30.
m	$U(-5, 5)$, or 0.
η	$U(0, 3)$, or 0.

Noisy Shifty Sine This model generates a noisy sinusoid with a constant mean offset:

$$x_t = \sin(2\pi t/T) + \beta + \eta n_t, \quad (5.4)$$

for period T , mean offset β , and noise standard deviation η , and $n_t \sim \mathcal{N}(0, 1)$.

Parameter	Values
T	$U(10, 100)$ or 30.
β	$U(-5, 5)$ or 0.
η	$U(0, 3)$ or 0.

Autoregressive (AR) process We generated data from an autoregressive process (Chatfield, 2013) with amplitude α , memory τ , and a constant Gaussian noise term η .

$$x_t = \alpha \frac{1}{\tau} \sum_{i=1}^{\tau} x_{t-i} + \eta_t, \quad (5.5)$$

where $\eta_t \sim \mathcal{N}(0, 1)$.

Parameter	Values
α	$U(0.8, 0.999)$ or 0.9.
τ	$\{2, 3, 4, 5, 6, 7, 8, 9, 10\}$ or 2.

Bimodal switching model This two-state model samples from one of two Gaussian distributions, each with a different mean (Fulcher, 2012). At each time point, there is a probability of switching between the two states:

$$x_t = n_t + v_t \delta \quad (5.6)$$

$$v_t = Y_t(\alpha) v_{t-1} + (1 - Y_t(\alpha))(1 - v_{t-1}). \quad (5.7)$$

for a time series x_t , underlying state variable v_t , $n_t \sim \mathcal{N}(0, 1)$. State switching is controlled by the Bernoulli random variable, Y_t , which takes a value of 1 with probability α , and a value of 0 with probability $1 - \alpha$.

Parameter	Values
δ	$U(0, 6)$ or 3.
α	$U(0, 1)$ or 0.5.

Population growth A growing population with a limited carrying capacity and a variable growth rate (Levins, 1969), stochastic through an additive noise term.

$$\dot{x} = rx(K - x) + x\eta_\beta \quad (5.8)$$

Parameters are the maximum population size K , a growth rate r , and the amplitude of a uniform noise term η_β between 0 and β .

Parameter	Values
r	(0.1, 3) or 3
K	(0.5, 5) or 5
β	(0.1, 10) or 0.1

Stochastic sine map The stochastic sine map model was introduced by Freitas et al. (2009) and is defined as:

$$x_{t+1} = \mu \sin(x_t) + Y_t(q)\eta_t(b), \quad (5.9)$$

for a sinusoidal amplitude μ , a Bernoulli random variable Y ($Y = 0$ with probability q , and $Y = 1$ with probability $1 - q$), and an identically and independently distributed random variable η_t which has a uniform distribution between $-b$ and b .

Parameter	Values
μ	$U(0.5, 4)$ or 2.4.
q	$U(0, 1)$ or 0.5.
b	$U(0, 3)$ or 1.

All following flows (Van der Pol, Lorenz, Mackey-Glass) were simulated in Matlab using the ordinary differential equation solver ode45. Each system was then evaluated on an even time grid of an appropriate frequency for each system (listed below). In all cases, the first 500 samples were removed to minimise the dependence on initial conditions.

van der Pol Oscillator A deterministic, nonlinear flow with negative dampening for low amplitudes of x and positive dampening for high values that approaches a limit cycle (van der Pol, 1926; Sprott, 2003). The parameter c controls the degree of dampening (positive or negative) and k regulates frequency. The sampling rate was set to to 1/6 Hz.

$$\ddot{x} - c(1 - x^2)\dot{x} + kx = 0 \quad (5.10)$$

Parameter	Values
c	$U(0.1, 5)$ or 1.
k	$U(0.1, 5)$ or 1.

Rössler Oscillator A three-dimensional chaotic flow proposed by Rössler (1976) (Sprott, 2003). It is one of the simplest chaotic flows with a single quadratic nonlinearity (zx). The sampling rate was set to to 1/5 Hz.

$$\dot{x} = -y - z \quad (5.11)$$

$$\dot{y} = x + ay \quad (5.12)$$

$$\dot{z} = b + z(x - c) \quad (5.13)$$

Parameter	Values
a	$(0.1, 0.3)$ or 0.2
b	$(0.01, 2)$ or 0.2
c	$(4.5, 20)$ or 5.7

Lorenz Attractor A three-dimensional chaotic flow discovered by Lorenz (1963) (Sprott, 2003) while studying atmospheric convection. Sampling rate set to 1/5 Hz.

$$\dot{x} = s(y - x) \quad (5.14)$$

$$\dot{y} = x(r - z) - y \quad (5.15)$$

$$\dot{z} = xy - bz. \quad (5.16)$$

Mackey-Glass system A delay differential equation that implements a high-dimensional chaotic flow (Mackey and Glass, 1977; Glass et al., 1988). As initial conditions (x values) for the whole

Parameter	Values
s	$U(8, 30)$ or 10.
r	$U(35, 60)$ or 35.
b	$U(1, 2.8)$ or 2.6667.

duration τ are required to define a state, the phase space dimension of this system approaches infinity for a diminishing time step size.

$$\frac{dx(t)}{dt} = \frac{ax(t - \tau)}{1 + x(t - \tau)^{10}} - 0.1x(t) \quad (5.17)$$

Parameter	Values
a	$U(0.15, 1.5)$ or 1.
τ	$\{10, 11, \dots, 39, 40\}$ or 17.

Logistic Map This very simple, one-dimensional chaotic map has become a famous example after May used it in his demonstration of complex behavior produced by very simple systems (May, 1976; Sprott, 2003). For values of the single parameter A below 3.449..., x describes a logistic growth but becomes an oscillator of increasing period for higher A s until 3.570..., where a chaotic behavior onsets. For the value range we select, both periodic and aperiodic (chaotic) oscillations occur.

$$x_t = Ax_t(1 - x_t), \quad (5.18)$$

for the parameter A . In generating the Logistic Map dataset, we sampled $A \sim U(3.5, 4)$.

Predator-prey system A stochastic map that models the populations of a predator and a prey species that interact (May, 1972; Hoppensteadt, 2006).

$$x_t = x_{t-1} \exp[r(1 - x_{t-1}/K)] - \alpha y_{t-1} \quad (5.19)$$

$$y_t = x_{t-1}[1 - \exp(-\alpha y_{t-1})] \quad (5.20)$$

Parameter	Values
r	(0.3, 1) or 0.5
K	(0.7, 1.2) or 1
α	5

Self-affine Time series with an powerlaw characteristic in the power spectrum with scaling exponent α . The time series are generated by an inverse Fourier transform (IFFT) from the desired powerlaw spectrum with random phase (Fox, 1987) using Matlab.

Parameter	Values
α	(-1, 3)

5.2 Condensed feature-spaces – *catch22*

In the last section we described a method to uncover low-dimensional parametric variation in time-series datasets and selected single features for each in an unsupervised way. We here propose an alternative, supervised method, that works with labelled classification tasks to select small feature subsets with high classification performance.

The number of time-series analysis methods that have been devised to convert a complex time-series data stream into an interpretable set of real numbers is vast, with contributions from a diverse range of disciplinary applications. Some examples include standard deviation, the position of peaks in the Fourier power spectrum, temporal entropy, and many thousands of others (Fulcher, 2018; Fulcher et al., 2013). From among this wide range of possible features, selecting a set of features that successfully captures the dynamics relevant to the problem at hand has typically been done manually without quantitative comparison across a variety of potential candidates (Timmer et al., 1993; Nanopoulos et al., 2001; Mörchen, 2003; Wang et al., 2006; Bagnall et al., 2012). However, subjective feature selection leaves uncertain whether a different feature set may have optimal performance on a task at hand. Addressing this shortcoming, recent methods have been introduced that take a systematic, data-driven approach involving large-scale comparisons across thousands of time-series features (Fulcher et al., 2013; Fulcher and Jones, 2017).

This ‘highly-comparative’ approach involves comparison across a comprehensive collection of thousands of diverse time-series features and has recently been operationalised as the *hctsa* (highly com-

parative time-series analysis) toolbox (Fulcher et al., 2013; Fulcher and Jones, 2017, 2014). *hctsa* has been used for data-driven selection of features that capture the informative properties in a given dataset in applications ranging from classifying Parkinsonian speech signals (Fulcher et al., 2013) to identifying correlates of mouse-brain dynamics in the structural connectome (Sethi et al., 2017). These applications have demonstrated how automatically constructed feature-based representations of time series can, despite vast dimensionality reduction, yield competitive classifiers that can be applied to new data efficiently (Fulcher and Jones, 2014). Perhaps most importantly, the selected features provide interpretable understanding of the differences between classes, and therefore a path towards a deeper understanding of the underlying dynamical mechanisms at play.

Selecting a subset of features from thousands of candidate features is computationally expensive, making the highly-comparative approach unfeasible for some real-world applications, especially those involving large training datasets (Bandara et al., 2017; Shekar et al., 2018; Bason et al., 2017). Furthermore, the *hctsa* feature library requires a Matlab license to run, limiting its widespread adoption. Many more real-world applications of time-series analysis could be tackled using a feature-based approach if a reduced, efficient subset of features, that capture the diversity of analysis approaches contained in *hctsa*, was developed.

In this study we develop a data-driven pipeline to distill reduced subsets of the most useful and complementary features for classification from thousands of initial candidates, such as those in the *hctsa* toolbox. Our approach involves scoring the performance of each feature independently according to its classification accuracy across a calibration set of 93 time-series classification problems (Bagnall et al., 2017b). We show that the performance of an initial (filtered) pool of 4791 features from *hctsa* (mean class-balanced accuracy across all tasks: 77.2%) can be well summarised by a smaller set of just 22 features (mean accuracy: 71.7%). We denote this high-performing subset of time-series features as *catch22* (22 CAnonical Time-series CHaracteristics). The *catch22* feature set: (1) computes quickly (~ 0.5 second/ 10 000 samples, roughly a thousand times faster than the full *hctsa* feature set in Matlab) and empirically scales almost linearly, $O(N^{1.16})$; (2) provides a low-dimensional summary of time series into a concise set of interpretable characteristics that are useful for classification of diverse real-world time-series; and (3) is implemented in C with wrappers for python, R, and Matlab, facilitating fast time-series clustering and classification. We envisage *catch22* expanding the set of problems – including scientific, industrial, financial, and medical applications – that can be tackled

using a common feature-based language of canonical time-series properties.

Given a suitable collection of peripheral nerve datasets, e.g., annotated recordings from different nerves, different active fibre types, firing patterns, etc., the same pipeline could be used to generate reduced feature-spaces for this kind of data. We did not have a suitable collection of datasets at our disposal and one future task could be to collect such data to feed into our supervised feature-selection pipeline.

5.2.1 Methods

We here describe the datasets we evaluate features on and the selection pipeline to generate a reduced feature subset.

5.2.1.1 Data

To select a reduced set of useful features, we need to define a measure of usefulness. Here we use a diverse calibration set of time-series classification tasks from the UEA/UCR (University of East Anglia and University of California, Riverside) Time-Series Classification Repository (Bagnall et al., 2017a). The number of time series per dataset ranges from 28 (‘ECGMeditation’) to 33 274 (‘ElectricalDevices’) adding up to a total of 147 198 time series. Individual time series range in length from 24 samples (‘ItalyPowerDemand’) to 3750 samples (‘HeartbeatBIDMC’), and datasets contain between 2 classes (e.g., ‘BeetleFly’) and 60 classes (‘ShapesAll’). For 85 of the 93 datasets, unbalanced classification accuracies were provided for different shape-based classifiers such as dynamic time warping (DTW) (Berndt and Clifford, 1994) nearest neighbor, as well as for hybrid approaches such as COTE (Bagnall et al., 2016). All unbalanced accuracies, a^{ub} , were computed using the fixed training-test split provided by the UCR repository, as the proportion of class predictions that matched the actual class labels:

$$a^{\text{ub}}(y, \hat{y}) = \frac{1}{n_{\text{TS}}} \sum_{l=1}^{n_{\text{TS}}} \mathbb{1}(\hat{y}_l = y_l), \quad (5.21)$$

where y_l is the actual class, \hat{y}_l is the predicted class, n_{TS} is the total number of time series in the dataset, and $\mathbb{1}$ is the indicator function.

5.2.1.2 Time-series features

Our aim is to obtain a data-driven subset of the most useful time-series features by comparing across as diverse a set of time-series analysis algorithms as possible. An ideal starting point for such an exercise is the comprehensive library of over 7500 features provided in the *hctsa* toolbox (Fulcher et al., 2013; Fulcher and Jones, 2017). Features were calculated in Matlab 2017a (a product of The MathWorks, Natick, MA) using *hctsa* v0.97. For each dataset, each feature was linearly rescaled to the unit interval.

We performed an initial filtering of all 7658 *hctsa* features based on their characteristics and general applicability. Because the vast majority of time series in the UCR/UEA repository are z -score normalised¹, we first removed the 766 features that are sensitive to the mean and variance of the distribution of values in a time series based on keywords assigned through previous work (Fulcher et al., 2013), resulting in a set of 6892 features. We note that on specific tasks with non-normalised data, features of the raw value distribution (such as mean, standard deviation, and higher moments) can lead to significant performance gains and that for some applications, this initial preselection is undesirable (Dau et al., 2018). Given a suitable collection of datasets in which the raw value distributions contain information about class differences, our pipeline can easily skip this preselection. We next excluded the features that frequently outputted special values, which indicate that an algorithm is not suitable for the input data, or that it did not evaluate successfully. Algorithms that produced special-valued outputs on at least one time series in more than 80% of our datasets were excluded: a total of 2101 features (across datasets, minimum: 655, maximum: 3427, mean: 1327), leaving a remaining set of 4791 features. This relatively high number of features lost during preselection reflects our strict exclusion criterion for requiring real-valued outputs across a diverse range of input data, and the restricted applicability of many algorithms (e.g., that require a minimum length of input data, require positive-valued data, or cannot deal with data repeated identical values). For example, the datasets with the most special-valued features are ‘ElectricDevices’ (3427 special-valued features), which contains 96-sample time series with many repeated values (e.g., some time series contain just 10 unique values), and ‘ItalyPowerDemand’ (2678 special-valued features), which consists of very short (24-sample) time series. The 4791 features that survived the preselection gave real-valued out-

¹With the notable exception of four unnormalised datasets: ‘AALTDChallenge’, ‘ElectricDeviceOn’, ‘ECGMeditation’, ‘HeartbeatBIDMC’.

puts on at least 90% of the time series of all datasets, and 90% of them succeeded on at least 99% of time series.

5.2.1.3 Performance-based selection

In contrast to typical feature-selection algorithms, which search for combinations of features that perform well together (and might therefore include features that have low individual performance), our procedure involves a pre-filtration to identify features that individually possess discriminatory power across a diverse range of real-world data, before subsequently identifying those that exhibit complementary behavior. To this end we used the pipeline depicted in Fig. 5.2.1, which evaluates the univariate classification performance of each feature on each task, combines feature-scores across tasks, and then selects a reduced set of the most useful features across a two-step filtering process which involves: (1) *performance filtering*: select features that perform best across all tasks, and (2) *redundancy minimisation*: reduce redundancy between features. The method is general and is easily extendable to different sets of classification tasks, or to different initial pools of features. All analysis was performed in Python 2.7 using `scikit-learn` and code to reproduce all of our analyses is accessible on GitHub (https://github.com/chlubba/op_importance).

5.2.1.4 Quantifying feature performance

Our pipeline (Fig. 5.2.1) requires a method to score the performance of individual features across classification tasks. We scored each feature by its ability to distinguish the labeled classes in each of our $M = 93$ classification tasks and then computed a combined performance score for that feature across all tasks. Classification was performed using a decision tree with stratified cross validation with N_{CV} folds. The number of folds, N_{CV} , was chosen separately for each task according to:

$$N_{CV} = \min \left\{ 10, \max \left[2, \min_{k=1}^{N_c} \left(\sum_{l=1}^{N_{TS}} \mathbb{1}(y_l = k) \right) \right] \right\}, \quad (5.22)$$

where N_{TS} is the number of time series, N_c is the number of classes, and y_l is the class-label of the l th time series.

For feature i ($i = 1, \dots, 4791$) on classification task j ($j = 1, \dots, M$), we computed the mean class-

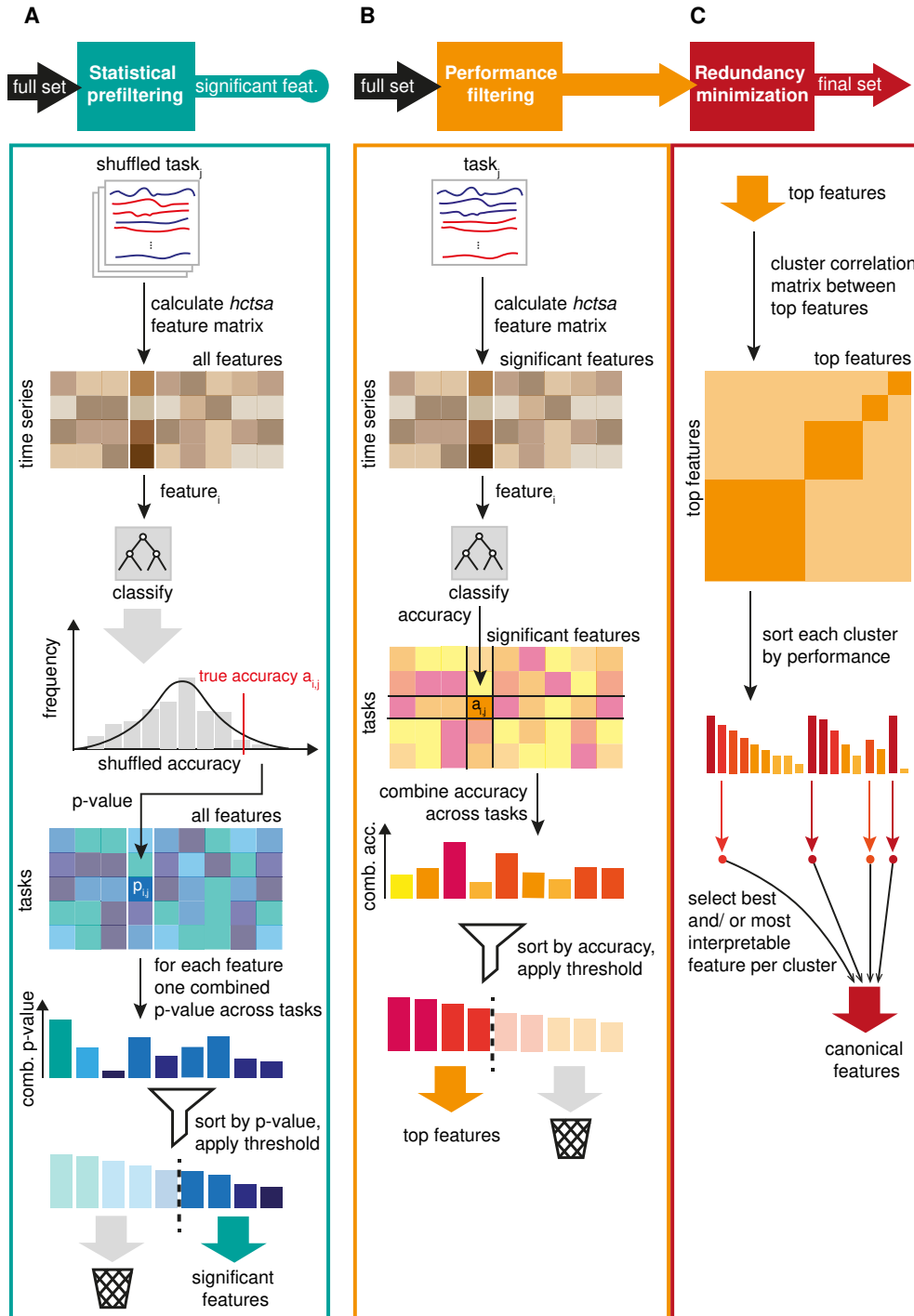


Figure 5.2.1: **Given a set of classification tasks, our pipeline selects a reduced set of high-performing features while minimising inter-feature redundancy.** **A Statistical prefiltering:** We identified features with performance consistent with that of random number generators. To this end, we derived null accuracy distributions for each feature on each task by classifying repeatedly on shuffled class labels. *P*-values from those null distributions were combined across datasets to identify features with performance consistent with random-number generators. **B Performance filtering:** We selected an intermediate set of top features by ranking and thresholding the combined accuracy over all datasets. **C Redundancy minimisation:** Top performing features were clustered into groups with similar performance across tasks to minimise redundancy between the final set of canonical features. We selected a single representative feature per cluster to yield a canonical feature set.

balanced classification accuracy across folds $a_{i,j}$ as a performance score.

$$a_{i,j}(y, \hat{y}, w) = \frac{1}{\sum_{l=1}^{N_{TS}} w_l} \sum_{l=1}^{N_{TS}} \mathbb{1}(\hat{y}_l = y_l) w_l, \quad (5.23)$$

where the weights for each time series w_l compensate for imbalances in the number of samples per class, $w_l = 1 / \sum_{m=1}^{N_{TS}} \mathbb{1}(y_m = y_l)$. To combine scores across tasks, we computed a normalised accuracy of the j th task by dividing raw feature accuracies, $a_{i,j}$, by the mean accuracy across all features on that task, \bar{a}_j , as follows:

$$a_{i,j}^n = \frac{a_{i,j}}{\bar{a}_j}. \quad (5.24)$$

This allowed us to quantify the performance of each feature on a given task relative to the performances of other features in our library.

Finally, the combined feature-accuracy-score across all tasks, $a_i^{n,c}$, was calculated as the mean over normalised accuracies, $a_{i,j}^n$, on our $M = 93$ tasks:

$$a_i^{n,c} = \frac{1}{M} \sum_{j=1}^M a_{i,j}^n. \quad (5.25)$$

5.2.1.5 Statistical prefiltering

Given the size and diversity of features in *hctsa*, we first wanted to determine whether some features exhibited performance consistent with chance on this set of classification tasks. To estimate a p -value for each feature on each classification task, we generated null accuracy distributions, $a_{i,j}^s$ (superscript s indicating ‘shuffled’), using a permutation-based procedure that involved repeated classification on randomly shuffled class labels, shown in Fig. 5.2.1A. The computational expense of estimating $\sim 440,000$ p -values using permutation testing, one for each of the 4791 features on each of the 93 problems, scales linearly with the number of repetitions. To limit computation time to within reasonable bounds, we fitted a Gaussian approximation, estimated from 1000 null samples for each feature-task combination, $a_{i,j}^s$, and used it to estimate p -values to a resolution beyond the limits of traditional permutation testing with this many null samples (i.e., 0.001). From visual inspection, the distributions were mostly unimodal and approximately normally distributed and, as expected, had higher variance on datasets with fewer time series.

The p -values for a given feature across all classification tasks were combined using Fisher’s method (Fisher, 1925) and corrected for multiple hypothesis testing across features using the Holm-Bonferroni method (Holm, 1979) at a significance level of 0.05.

5.2.1.6 Selecting a canonical set of features

From the features that performed significantly better than chance, we selected a subset of β high-performing features by ranking them by their combined normalised accuracy $a^{n,c}$ (Fig. 5.2.1B), comparing values in the range $100 \leq \beta \leq 1000$. As shown in Fig. 5.2.1C, we then aimed to reduce the redundancy in these top-performing features, defining redundancy in terms of patterns of performance across classification tasks. To achieve this, we used hierarchical clustering on the Pearson correlation distance, $d_{ij} = 1 - r_{ij}$ between the M -dimensional performance vectors of normalised accuracies a^n of features i and j . Clustering was performed using complete linkage at a threshold $\gamma = 0.2$ to form clusters of similarly performing features, that are all inter-correlated by $r_{ij} > 1 - \gamma$ (for all i, j in the cluster). We then selected a single feature to represent each cluster, comparing two different methods: (i) the feature with the highest normalised accuracy combined across tasks, and (ii) manual selection of representative features to favour interpretability (while also taking into account computational efficiency and classification performance).

5.2.1.7 Overall classification performance

To evaluate the classification performance of different feature sets, and compare our feature-based classification to alternative time-series classification methods, we used two different accuracy measures. Comparisons between different sets of *hctsa*-features were based on the mean class-balanced accuracy across M tasks and N_{CV} cross-validation folds:

$$a_{\text{tot}} = \frac{1}{M} \sum_{j=1}^M \frac{1}{N_{CV,j}} \sum_{k=1}^{N_{CV,j}} a_{j,k}. \quad (5.26)$$

When comparing our feature sets to existing methods we used the mean unbalanced classification accuracy across tasks as in Eq. (5.21) on the given train-test split to match the metric used for the

accuracies supplied with the UEA/UCR repository:

$$a_{\text{tot}}^{\text{ub}} = \frac{1}{N_{\text{tasks}}} \sum_{j=1}^{N_{\text{tasks}}} a_j^{\text{ub}}. \quad (5.27)$$

5.2.1.8 Execution times and scaling

One of the merits of a small canonical feature set for time-series characterisation is that it is quick to compute. To compare the execution time of different feature sets, we used a benchmark set of 40 time series from different sources, including simulated dynamical systems, financial data, medical recordings, meteorology, astrophysics, and bird sounds (see Sec. 5.2.4.A for a complete list). To estimate how features scale with time-series length, we generated multiple versions for each of our 40 reference time series of different lengths from 50 to 10 000 samples. Lengths were adapted by either removing points after a certain sample count or by up-sampling of the whole time series to the desired length. Execution times were obtained on a 2.2 GHz Intel Core i7, using single-threaded execution (although we note that feature calculation can be parallelised straightforwardly).

5.2.1.9 Selecting the two most informative features from a small subset

For the purpose of quickly analysing a dataset visually in feature space, it can be helpful to identify the two features that, taken together, are the most informative to distinguish between time-series classes of the selected dataset. To this end, we used sequential forward selection (Whitney, 1971; Fulcher and Jones, 2014) that first selects a single feature which achieves the best mean class-balanced accuracy across cross-validation folds and then iterates over the remaining features to select the one that, combined with the first feature, reaches the best accuracy.

5.2.2 Results

We present results of using our pipeline to obtain a canonical set of 22 time-series features from an initial pool of 4791 candidates. We name our set *catch22* (22 CAnonical Time-series CHaracteristics), which approximates the classification performance of the initial feature pool to 90% and computes in less than 0.5 s on 10 000 samples.

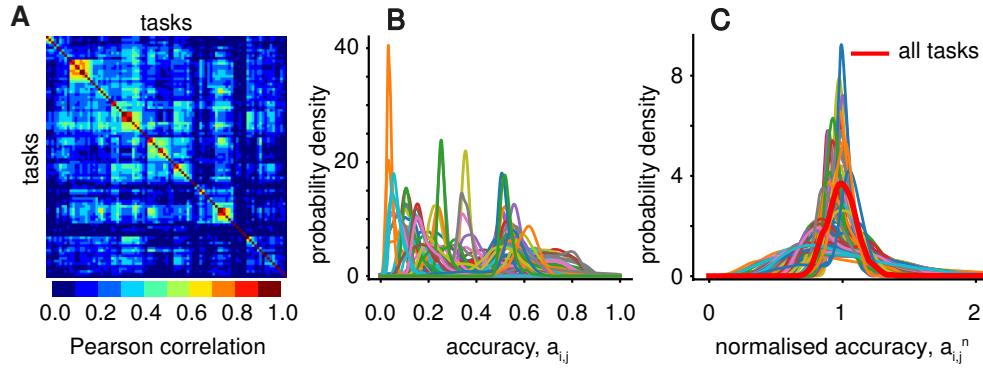


Figure 5.2.2: **Normalisation of feature accuracies allows comparison of performance scores across a diverse set of 93 classification tasks.** **A** A 93×93 matrix of Pearson correlation coefficients between the 4791-dimensional accuracy vectors of pairs of tasks, reordered according to hierarchical linkage clustering. **B** Each line shows the smoothed distribution over feature-accuracies on one classification task. Differences in task difficulty are reflected by a wide range of accuracies. **C** The accuracies plotted in **B** were normalised by the mean accuracy of each task, as in Eq. (5.24). The red line shows the distribution of normalised and combined accuracies across all tasks, Eq. (5.25).

5.2.2.1 Performance diversity across classification tasks

We first analyse the 93 classification tasks, which are highly diverse in their properties (see Sec. 5.2.1.1) and difficulty, as shown in Fig. 5.2.2. We characterised the similarity of two tasks in terms of the types of features that perform well on them, as the Pearson correlation coefficient between accuracies of all features, shown in Fig 5.2.2A. The figure reveals a diversity of performance signatures across tasks: for some groups of tasks, similar types of features contribute to successful classification, whereas very different types of features are required for other tasks. The 93 tasks also vary markedly in their difficulty, as judged by the distribution of accuracies, $a_{i,j}$, across tasks, shown in Fig. 5.2.2B. We normalised feature accuracies across tasks by dividing them by the mean accuracy of the task at hand, Eq. (5.24), yielding normalised accuracies, $a_{i,j}^n$, that were comparable across tasks, shown in Fig. 5.2.2C. Note that this normalised accuracy scores features relative to all other features on a given task. The red line in Fig. 5.2.2C shows the distribution of the mean normalised accuracies across tasks $a_i^{n,c}$, Eq. (5.25).

5.2.2.2 Features with performance consistent with chance

To detect whether some features in *hctsa* exhibit a combined performance across classification tasks that is consistent with the performance of a random-number generator, we used a permutation-testing based procedure (described in Sec. 5.2.1.5). At a significance level $p < 0.05$, 145 of the 4791 features

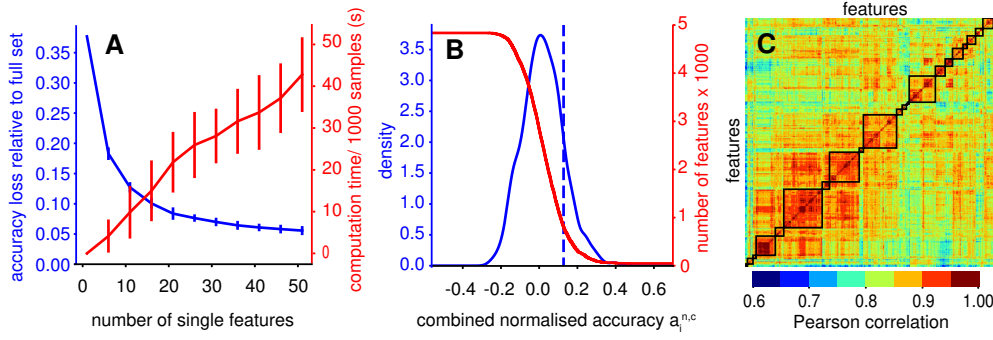


Figure 5.2.3: The mean classification performance of the full feature set can be well approximated (to within 10%) by as few as 20 features. **A** While computation time is observed to rise linearly with increasing number of single selected features, the relative difference in accuracy to the full set of 4791 features starts to saturate at around 20 features. The performance of our final set of features is not highly sensitive to the size of our intermediate set of top-performing features, β . Error bars signify standard deviation over both relative loss in accuracy and computation time for different numbers of top features ($\beta = 100, 200, \dots, 1000$), which were clustered to obtain single features (see Methods Sec. 5.2.1.6). **B** We select the number of top features from a relative threshold on the combined normalised accuracy across tasks shown as a dashed blue vertical line, yielding a set of 710 high-performing features. **C** High-performing features were clustered on performance-correlation distances using hierarchical complete linkage clustering, using a distance threshold γ of 0.2, yielding 22 clusters.

(or 3%) exhibited chance-level performance. These 145 features were mostly related to quantifying complex dynamics in longer time series, such as nonlinear time-series analysis methods, long-range automutual information; properties that are not meaningful for the short, shape-based time-series patterns that dominate the UEA/UCR database.

5.2.2.3 Top-performing features

As a second step in our pipeline, we ranked features by their combined accuracy across tasks and then selected a subset of β best performers. How important is the choice of β ?

Fig. 5.2.3A shows how the relative difference in classification accuracy between full and reduced set $(a_{tot,full} - a_{tot,subset})/a_{tot,full}$ (blue line) and computation time (red line) evolve when increasing the number of clusters (1 to 50) into which the top performing features are grouped. The relative classification accuracy difference saturated at under 10% for between 20 and 30 selected features showing that this modest number of estimators covers most of diversity of the full set. Error bars signify the standard deviation over accuracies and computation times when starting from different numbers of top performers $\beta = 100, 200, 300, \dots, 1000$. Their tightness demonstrates that the accuracy of the final feature subset was not highly sensitive to the value of β . Computation time is more

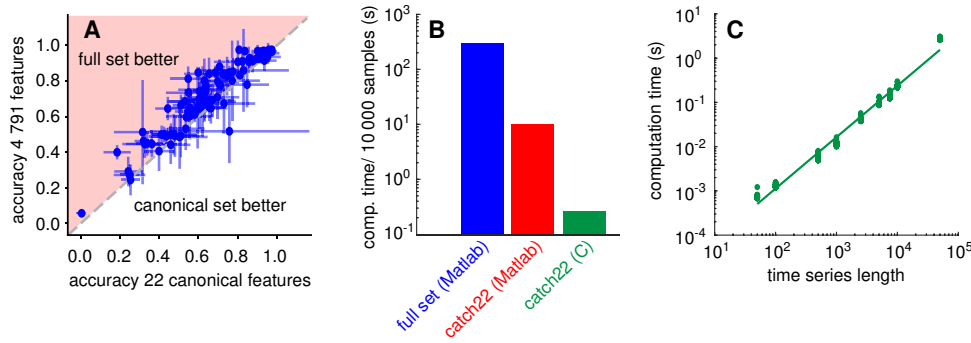


Figure 5.2.4: **The *catch22* set of 22 features approximates the classification performance of all 4791 features despite a dramatic reduction in computation time.** **A** Each point represents one dataset in its balanced accuracy based on the *catch22* feature set (*x*-axis) and the full set of 4791 features (*y*-axis). Error bars signify standard deviation across cross-validation folds. *catch22* performs only a relative 7.5% worse than the full set of 4791 features: 71.7% vs 77.2% mean class-balanced accuracy across tasks a^{tot} as defined in Eq. (5.26). **B** Bars represents average over serial computation times for each of our 40 reference time series at a length of 10 000 samples using the full set of 4791 features, *catch22* in Matlab and *catch22* in C. From full set in Matlab to *catch22* in C, computation time decreases from ~300 seconds to less than 0.5 s. **C** Each dot shows computation time for one of the 40 reference time series adjusted to different lengths for the C-implemented *catch22* set. The linear fit in the logarithmic plot reveals an almost linear scaling, with a scaling exponent of 1.16. See Sec. 5.2.1.8 for a description of the data.

variable. To obtain a reduced set of high-performing features, we used a threshold on the combined normalised accuracy $a^{n,c}$ of one standard deviation above the mean, $a_{\text{th}} = \overline{a^{n,c}} + \sigma_{a^{n,c}}$, shown in Fig. 5.2.3B, yielding a set of 710 features.

5.2.2.4 A canonical feature set, *catch22*

We reduced inter-feature redundancy in *hctsa* (Fulcher et al., 2013), by applying hierarchical complete linkage clustering based on the correlation distances between performance vectors of the set of 710 high-performing features, as shown in Fig. 5.2.3C. Clustering at a distance threshold $\gamma = 0.2$ (see Sec. 5.2.1.6) yielded 22 clusters of similarly-performing features, where the correlation of performance vectors between all pairs of features within each cluster was greater than 0.8. Different values of γ correspond to different penalties for redundancy; e.g., higher values ($\gamma > 0.4$) group all features into a single cluster, whereas low values would form many more clusters and increase the size and complexity of computing the resulting canonical feature set. We found $\gamma = 0.2$ to represent a good compromise that yields a resulting set of 22 clusters that matches the saturation of performance observed between 20–30 features (Fig. 5.2.3A).

We next aimed to capture the behavior of each of the 22 clusters as a single feature with the most

representative behavior of its cluster. We first achieved this automatically: selecting the feature with the highest combined normalised accuracy $a^{n,c}$ from each cluster. When classifying our tasks with this set of 22 best estimators, it reached an overall class-balanced accuracy over folds and tasks a^{tot} , Eq. (5.27), of $\sim 70\%$, compared to $\sim 77\%$ using the full set. However, it is desirable for our 22 features to be as fast and easily interpretable as possible. For 6 of the 22 clusters, the top-performing feature was relatively complicated to compute and only offered a relatively small improvement in performance relative to simpler features with similar performance in the same cluster. In these cases, we manually selected a simpler and more interpretable feature, yielding a final canonical set of 22 features which we call *catch22* (CAnonical Time-series CHaracteristics). The 22 features that make up *catch22* are described in Tab. 5.2.1. The *catch22* features reflect the diverse and interdisciplinary literature of time-series analysis methods that have been developed to date (Fulcher et al., 2013), simultaneously probing different types of structure in the data, including properties of the distribution of values in the time series, its linear and nonlinear autocorrelation, predictability, scaling of fluctuations, and others.

htcsa feature name	Description
<i>Distribution</i>	
DN_HistogramMode_5	Mode of z -scored distribution (5-bin histogram)
DN_HistogramMode_10	Mode of z -scored distribution (10-bin histogram)
<i>Simple temporal statistics</i>	
SB_BinaryStats_mean_longstretch1	Longest period of consecutive values above the mean
DN_OutlierInclude_p_001_mdrmd	Time intervals between successive extreme events above the mean
DN_OutlierInclude_n_001_mdrmd	Time intervals between successive extreme events below the mean
<i>Linear autocorrelation</i>	
CO_flecac	First $1/e$ crossing of autocorrelation function
CO_FirstMin_ac	First minimum of autocorrelation function
SP_Summaries_welch_rect_area_5_1	Total power in lowest fifth of frequencies in the Fourier power spectrum
SP_Summaries_welch_rect_centroid	Centroid of the Fourier power spectrum
FC_LocalSimple_mean3_stderr	Mean error from a rolling 3-sample mean forecasting
<i>nonlinear autocorrelation</i>	
CO_trev_1_num	Time-reversibility statistic, $\langle (x_{t+1} - x_t)^3 \rangle_t$
CO_HistogramAMI_even_2_5	Automutual information, $m = 2, \tau = 5$
IN_AutoMutualInfoStats_40_gaussian_fmni	First minimum of the automutual information function
<i>Successive differences</i>	
MD_hrv_classic_pnn40	Proportion of successive differences exceeding 0.04σ (Mietus, 2002)
SB_BinaryStats_diff_longstretch0	Longest period of successive incremental decreases
SB_MotifThree_quantile_hh	Shannon entropy of two successive letters in equiprobable 3-letter symbolisation
FC_LocalSimple_mean1_ttauresrat	Change in correlation length after iterative differencing
CO_Embed2_Dist_tau_d_expfit_meandiff	Exponential fit to successive distances in 2-d embedding space
<i>Fluctuation Analysis</i>	
SC_FluctAnal_2_dfa_50_1_2_logi_prop_r1	Proportion of slower timescale fluctuations that scale with DFA (50% sampling)
SC_FluctAnal_2_rsrangefit_50_1_logi_prop_r1	Proportion of slower timescale fluctuations that scale with linearly rescaled range fits
<i>Others</i>	
SB_TransitionMatrix_3ac_sumdiagcov	Trace of covariance of transition matrix between symbols in 3-letter alphabet
PD_PeriodicityWang_th0_01	Periodicity measure of (Wang et al., 2007)

Table 5.2.1: **The catch22 feature set spans a diverse range of time-series characteristics representative of the diversity of interdisciplinary methods for time-series analysis.** Features in *catch22* capture time-series properties of the distribution of values in the time series, linear and nonlinear temporal autocorrelation properties, scaling of fluctuations, and others.

Using the diverse canonical *catch22* feature set, the mean class-balanced accuracy across all datasets, a^{tot} , of *catch22* was $\sim 72\%$, a small reduction relative to the $\sim 77\%$ achieved when computing all 4791 features and very similar to the $\sim 70\%$ of the 22 highest-ranked features in each cluster. See Fig. 5.2.4A for a dataset-by-dataset scatter. The change in mean accuracy across folds and tasks, a^{tot} , from using the 22 features of *catch22* instead of all 4791 features depends on the properties of a given dataset, but there was an average reduction in class-balanced accuracy (mean across folds) of 7.5% relative to the full set accuracy (77.2% full vs 71.7% canonical, 7.5 percentage points). For some difficult problems, the increased computational expense of the full set of 4791 features yields a large boost in classification accuracy (accuracy of *catch22* lower by a relative difference of 37% for the dataset ‘EthanolLevel’; 50.2% full vs 31.8% *catch22*). The reduced set gave better mean performance in only a small number of cases: e.g., for ‘ECGMeditation’ with 60% full vs 81.2% *catch22*; given that this dataset contained just 28 time series and had a high standard deviation in accuracies of the full set between folds (35.3%), the performance might not be significantly increased.

How does the performance of the data-driven features, *catch22*, compare to other small feature sets proposed in the literature? One popular collection of features is the manually-curated *tsfeatures* package (Hyndman et al., 2019) of which certain features were used for forecasting (Bandara et al., 2017), anomaly detection (Hyndman et al., 2016), and clustering (Williams, 2014). While not being explicitly optimised for classification and clustering, its widespread adoption demonstrates its versatility in characterising time series and makes it an interesting candidate to compare with *catch22*. We classified all datasets based on the 16 features of *tsfeatures* (version 1.0.0) listed in Tab. 5.2.2. Reassuringly, the class-balanced accuracies of both feature sets were very similar across the generic UCR/UAE datasets, with a Pearson correlation coefficient $r = 0.93$ (Fig. 5.2.5). The mean accuracy across tasks and folds, a^{tot} , was slightly higher for *catch22* (71.7%) than *tsfeatures* (69.4%). Our pipeline is general, and can select informative subsets of features for any collection of problems; e.g., for a more complex set of time-series classification tasks, our pipeline may yield estimators of more distinctive and complex dynamics.

frequency	nperiods	seasonal_period	trend
spike	linearity	curvature	e_acf1
e_acf10	entropy	x_acf1	x_acf10
diff1_acf1	diff1_acf10	diff2_acf1	diff2_acf10

Table 5.2.2: The 16 features of *tsfeatures* used for classification.

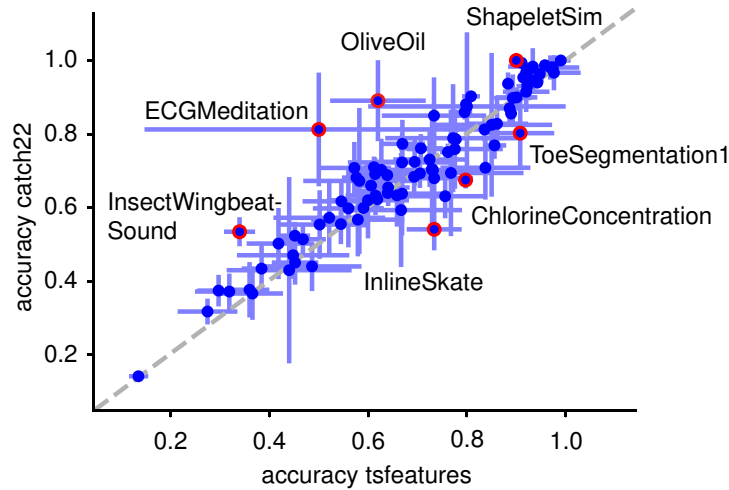


Figure 5.2.5: **Our automatically selected *catch22* feature set performs as well as the standard feature set for simple time series contained in the *tsfeatures* package.** Class-balanced accuracy is shown for *tsfeatures* and *catch22*, error bars indicate standard deviation across folds. A gray dashed equality line is annotated, and particular datasets with the greatest differences in accuracy are highlighted as red circles and labeled.

How diverse are the features in *catch22*? Fig. 5.2.6 displays the class-balanced accuracies of each of the *catch22* features (rows) on each task (columns), z-normalised by task. Some groups of tasks recruit the same types of features for classification (reflected by groups of columns with similar patterns). Patterns across rows capture the characteristic performance signature of each feature, and are visually very different, reflecting the diversity of features that make up *catch22*. This diversity is key to being able to probe the different types of temporal structure required to capture specific differences between labeled classes in different time-series classification tasks in the UCR/UAE repository. Feature-performances often fit the known dynamics in the data, e.g., for the two datasets ‘FordA’ and ‘FordB’ in which manual inspection reveals class differences in the low frequency content, the most successful feature is ‘CO_FirstMin_ac’ which finds the first minimum in the autocorrelation function. In some datasets, high performance can be attained using just a single feature, e.g., in ‘ChlorineConcentration’ (‘SB_motifThree_quantile.hh’, 52.3% vs 67.5% class-balanced mean accuracy over folds *a* for *catch22* vs all features) and ‘TwoPatterns’ (‘CO_trev_1.num’, 73.4% vs 88.1%).

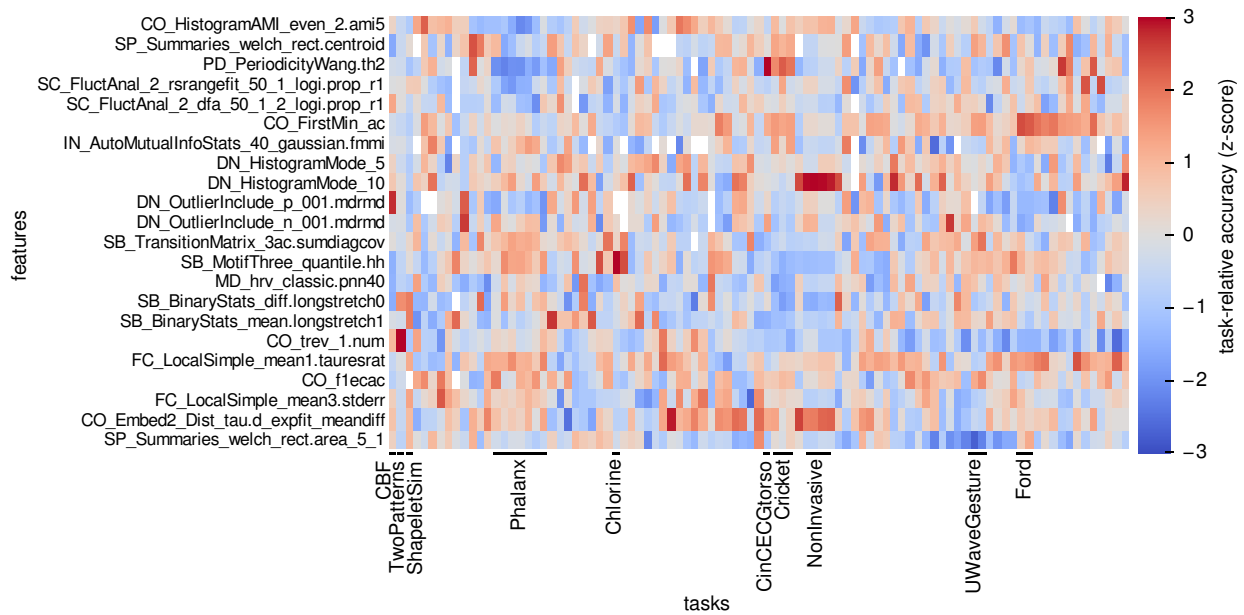


Figure 5.2.6: **The canonical features in *catch22* are sufficiently diverse to enable high performance across diverse classification tasks.** The matrix shows class-balanced accuracies, z -scored per task (column), truncated at ± 3 , and was reordered by hierarchical linkage clustering based on correlation distance in both columns (93 classification tasks) and rows (22 features). Similar columns are visible for datasets of the same type. The *catch22* features each show strengths and weaknesses, and their diversity allows them to complement each other across a range of tasks.

5.2.2.5 Computation time and complexity

The classification performance using all 4791 features is well approximated by the 22 features in *catch22*, but how much computational effort does it save? To maximise the acceleration in execution time and make our condensed subset accessible from all major ecosystems used by the data-mining community, we implemented all *catch22* features in C and wrapped them for R, Python and Matlab. All code is accesible on GitHub <https://github.com/chlubba/catch22>. Using this C-implementation, the *catch22* feature set can be computed sequentially on all 93 datasets of the UEA/UCR repository in less than 15 minutes on an Intel Core i7. On average, the features for each dataset were calculated within 9.4 s, the slowest being ‘StarLightCurves’ with 97 s due to its many (9236) relatively long (1024 samples) time series. The 27 quickest datasets stayed below 1 s in computation time; the three quickest, ‘BirdChicken’, ‘Coffee’, and ‘BeetleFly’ took less than 0.25 s.

While time series contained in the UEA/UCR repository are usually short, with an average length of 500 samples, real-world recordings can be substantially longer. Therefore, to understand how the computation times of our feature set scale with time-series lengths above those available in the UEA/UCR repository, we used a set of 40 reference time series from diverse sources (described in

Sec. 5.2.1.8) to evaluate execution times of all *hctsa*- and the *catch22*-features for longer time series. Fig. 5.2.4B shows execution times of different feature sets as a mean over our 40 reference time series at length 10 000. The Matlab implementation of *catch22* accelerates computation time by a factor of ~ 30 compared to the full set of 4791 from ~ 300 s to ~ 10 s. The C-implementation of *catch22* again reduces execution time by a factor of approximately 30 compared to the Matlab implementation to ~ 0.3 s at 10 000 samples, signifying an approximately 1000-fold acceleration compared to the full *hctsa* feature set in Matlab. The C-version of *catch22* exhibits near-linear computational complexity, $O(N^{1.16})$, as shown in Fig. 5.2.4C. Features varied markedly in their execution time, ranging from (C-implemented) DN_HistogramMode_10 (< 0.1 ms for our 10 000-sample reference series) to PD_PeriodicityWang_th0_01 (79 ms), with the latter representing approximately one third of the total computation time for *catch22*. A further acceleration by a factor of 3 could be achieved through parallelisation, limited by the slowest feature PD_PeriodicityWang_th0_01 which takes up one third of the overall computation time.

5.2.2.6 Performance comparison

Compared to conventional shape-based time-series classifiers, that use distinguishing patterns in the time domain as the basis for classification (Fulcher and Jones, 2014; Fulcher, 2018), feature-based representations can reduce high-dimensional time series down to a compact and interpretable set of important numbers, constituting a dramatic reduction in dimensionality. While this computationally efficient representation of potentially long and complex streams of data is appealing, important information may be lost in the process, resulting in poorer performance than alternative methods that learn classification rules on the full time-series object. To investigate this, we compared the classification performance of *catch22* (using a decision tree classifier as for every classification, see Sec. 5.2.1.4) to that of 36 other classifiers (accuracies obtained from the UEA/UCR repository (Bagnall et al., 2017a)) including shape-based approaches like Euclidean or DTW nearest neighbor, ensembles of different elastic distance metrics (Lines and Bagnall, 2015), interval methods, shapelets (Ye and Keogh, 2009), dictionary based classifiers, or complex transformation ensemble classifiers that combine multiple time-series representations (COTE) (Bagnall et al., 2016). All comparisons are based on (class unbalanced) classification accuracies $a_{\text{tot}}^{\text{ub}}$ on a fixed train-test split obtained from UCR/UEA classification repository. As shown in Fig. 5.2.7A, most datasets exhibit similar performance between the

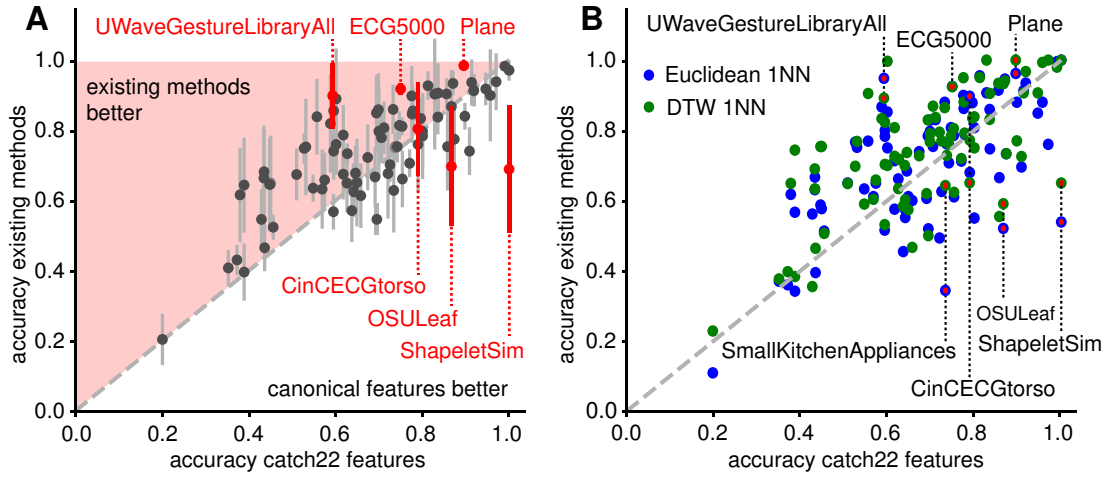


Figure 5.2.7: **Despite massive dimensionality reduction to 22 features, the *catch22* representation often achieves similar or better performance on time-series classification tasks.** **A** Classification accuracy is plotted from using the feature-based *catch22* representation versus the performance of a range of existing methods across the 93 tasks in the UEA/UCR repository. Each dot represents the mean accuracy of alternative classifiers on a given dataset; error bars show the standard deviation over the 36 considered other methods containing simple full sequence shape-based approaches, over ensembles, shapelets, intervals, to complex transformation ensembles. An equality gray-dashed line is plotted, and regions in which *catch22* or other methods perform better are labeled. **B** The two purely shape-based classifiers, Euclidean (blue circles) and DTW (green circles) 1 nearest-neighbor, are compared against *catch22* features and a classification tree. All accuracies are unbalanced, as Eq. (5.21), and evaluated on the fixed train-test split provided in the UEA/UCR repository.

alternative methods and *catch22*, with a majority of datasets exhibiting better performance using existing algorithms than *catch22*. However, despite drastic dimensionality reduction, our feature-based approach outperforms the existing methods on a range of datasets, some of which are labeled in Fig. 5.2.7A. To better understand the strengths and weaknesses of our low-dimensional feature-based representation of time series, we compared it directly to two of the most well-studied and purely shape-based time-series classification methods: Euclidean-1NN and DTW-1NN (‘DTW-R1-1NN’ in the UEA/UCR repository), as shown in Fig. 5.2.7B. There is an overall high correlation in performance across datasets, with a range of average performance (unbalanced classification rate on the given train-test partition $a_{\text{tot}}^{\text{ub}}$): *catch22* (69%), Euclidean 1-NN (71%), and DTW 1-NN (74%). The most interesting datasets are those for which one of the two approaches (shape-based or feature-based) markedly outperforms the other, as in these cases there is a clear advantage to tailoring your classification method to the structure of the data (Fulcher, 2018); selected examples are annotated in Fig. 5.2.7B). We next investigate the characteristics of time-series datasets that make them better suited to different classification approaches.

5.2.2.7 Case studies: feature- vs shape-based representations

There is no single representation that is best for all time-series datasets, but rather, the optimal representation depends on the structure of the dataset and the questions being asked of it (Fulcher, 2018). In this section we characterise the properties of selected datasets that show a strong preference for either feature-based or shape-based classification, as highlighted in Fig. 5.2.7.

One striking example, is that of ‘ShapeletSim’, where the two labeled classes are much more accurately distinguished using the *catch22* feature-based representation (unbalanced accuracy a^{ub} of 100%) than by all but two existing methods (BOSS (Schäfer, 2015) and Fast Shapelets (Rakthanmanon and Keogh, 2013)) with a mean and standard deviation over all other classifiers of $69.0 \pm 18.7\%$ (DTW-1NN 65%, Euc-1NN 53.9%). To understand the discrepancy, we visualised the data in the time-domain, as shown in Fig. 5.2.8A (upper), where one example time series and the mean in each class are plotted, revealing no consistent time-domain shape across the 100 instances of each class. However, the two classes of time series are clearly distinguished by their frequency content, as shown in the corresponding Welch power spectra in Fig. 5.2.8A (lower). The features in *catch22* capture the temporal autocorrelation properties of each time series in various ways, facilitating an efficient representation to successfully capture class differences in ‘ShapeletSim’; these differences cannot be captured straightforwardly from the time series’ shape. In general, datasets without reliable shape differences between classes pose problems for time-domain distance metrics; consequently, the *catch22* feature-based representation often yields superior classification performance. Examples are ‘USOLeaf’ (86.7 *catch22* vs $69.5 \pm 13.3\%$ others; DTW-1NN 59.1%, Euc-1NN 52.1%), and ‘Small-KitchenAppliances’ (73.3% vs $63.3 \pm 12.1\%$; DTW-1NN 64.3%, Euc-1NN 34.4%).

An example of a dataset that is well-suited to shape-based classification is the seven-class ‘Plane’ dataset, shown in Fig. 5.2.8B. Apart from a minority of anomalous instances in e.g., the ‘Harrier’ class, each class has a subtle but robust shape, and these shapes are phase-aligned, allowing shape-based classifiers to accurately capture class differences. Despite being visually well-suited to shape-based classification, *catch22* captures the class differences with only a small reduction in accuracy a^{ub} (89.5%) compared to the shape-based classifiers ($99.2 \pm 1.4\%$ over all given classifiers; DTW-1NN 100%, Euc-1NN 96.1%), demonstrating that feature-based representations can be versatile in capturing differences in time-series shape, despite a substantial reduction in dimensionality.

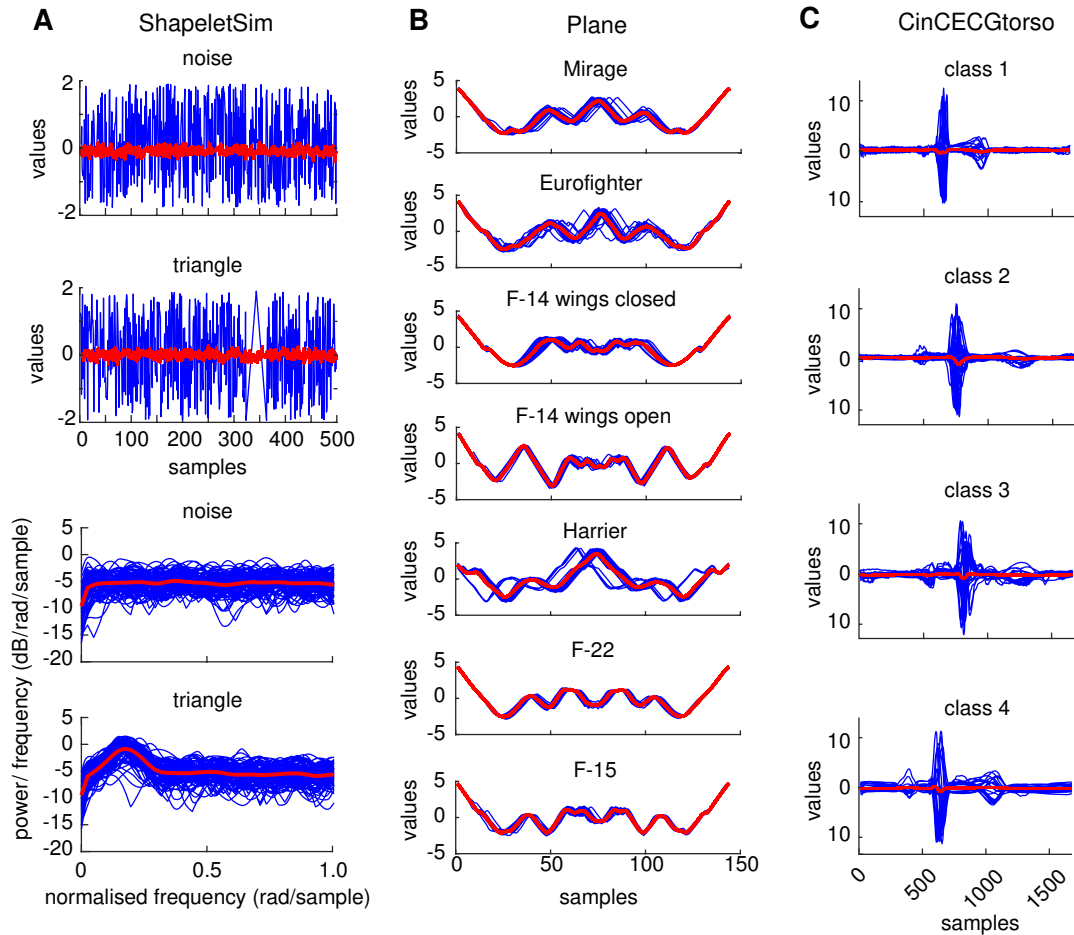


Figure 5.2.8: **Differences in the frequency domain are better picked up by features; subtle differences in shape are better detected by shape-based methods.** Each subplot represents a class, blue lines show individual time series, red lines show an average over all time series in one class. **A** In the time domain (upper two plots), we show one example time series of the ‘ShapeletSim’ dataset (blue) and the average across all time series (red) for each class. The lower two plots display the Welch spectra of all time series individually in blue and the average over single time-series spectra in red. The mean spectra of the two classes differ visibly while there is no reliable difference in the time domain. **B** The individual (blue) and averaged (red) time series of the dataset ‘Plane’ should favor shape-based comparisons because of the highly reliable and aligned shapes in each class. **C** For the dataset ‘CincECGtorso’, all four classes can be well distinguished by their temporal offsets.

As a final example we consider the four classes of the ‘CinCECGtorso’ dataset, which are similarly accurately classified by our *catch22* feature-based method (78.9%) and the average existing classifier ($81.3 \pm 13.3\%$). Interestingly, when comparing selected shape-based classifiers in Fig. 5.2.7, Euclidean-1NN (89.7%) outperforms the more complex DTW-1NN (65.1%). This difference in performance is due to the subtle differences in shape (particularly temporal offset of the deviation from zero) between the four classes, as shown in Fig. 5.2.8B. Simple time-domain distance metrics like Euclidean-1NN will capture these important differences well, whereas elastic distance measures like DTW shadow the informative temporal offsets. Converting to our feature-based representation discards most of the phase-information but still leads to a high classification accuracy.

5.2.2.8 Informative features provide understanding

Concise, low-dimensional summaries of time series, that exploit decades of interdisciplinary methods development for time-series analysis, are perhaps most important for scientists because they provide a means to understand class differences. Often a researcher will favor a method that provides interpretable understanding that can be used to motivate new solutions to a problem, even if it involves a small drop in classification accuracy relative to an opaque, black-box method. To demonstrate the ability of *catch22* to provide understanding into class difference, we projected all datasets into a two-dimensional feature space determined using sequential forward selection (Whitney, 1971) as described in Sec. 5.2.1.9. Two examples are shown in Fig. 5.2.9. In the dataset ‘ShapeletSim’ (Fig. 5.2.9A), the simple feature, `SB.BinaryStats.diff_longstretch0`, clearly distinguishes the two classes. This simple measure quantifies the length of the longest continued descending increments in the data which enables a perfect separation of the two classes because time series of the ‘triangle’ class vary on a slower timescale than ‘noise’ time series.

In the most accurate two-dimensional feature space for the 7-class ‘Plane’ dataset, shown in Fig. 5.2.9B, each class occupies a distinctive part of the space. The first feature, `FC.LocalSimple_mean3_stderr` captures variability in residuals for local 3-sample mean predictions of the next datapoint applied to through time, while the second feature, `SP.Summaries.welch_rect_area_5_1`, captures the proportion of low-frequency power in the time series. We discover, e.g., that time series of ‘F-14 wings open’ are less predictable from a 3-sample running mean than other planes, and that time series of

‘Harrier’ planes exhibit a greater proportion of low-frequency power than other types of planes. Thus, in cases when both shape-based and feature-based methods exhibit comparable performance (unbalanced accuracies a^{ub} on given split: 89.5% by *catch22* vs 99.1% mean over other classifiers), the ability to understand class differences can be a major advantage of the feature-based approach.

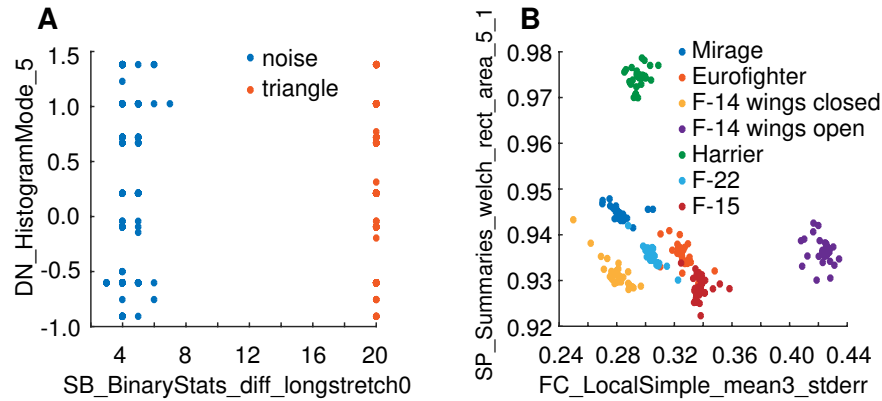


Figure 5.2.9: **Class differences can be interpreted using feature-based representations of time series.** We plot a projection of time series into an informative two-dimensional feature space (estimated from *catch22* using sequential forward selection, see Sec. 5.2.1.9), where each time series is a point in the space and colored by its class label. Plots are shown for two datasets: **A** ‘ShapeletSim’, and **B** ‘Plane’; in both cases, all labeled classes are clearly distinguished in the space. In ‘ShapeletSim’, `SB_BinaryStats_diff_longstretch0`, which calculates the length of the longest run of consecutive decreases in the time series. The two features selected for the ‘Plane’ dataset are the local predictability measure, `FC_LocalSimple_mean3_stderr`, and the low-frequency power estimate, `SP_Summaries_welch_rect_area_5_1`.

5.2.3 Discussion

Feature-based representations of time-series can distill complex time-varying dynamical patterns into a small set of interpretable characteristics that can be used to represent the data for applications like classification and clustering. Most importantly, features connect the data analyst to deeper theory, allowing interpretation of the properties of the data that facilitate successful performance. While large feature libraries have helped to overcome the limitations of manual, subjective curation of time-series features, they are inefficient and computationally expensive. Overcoming this limitation, here we introduce a methodology to generate small, canonical subsets of features that each display high classification performance across a given ensemble of tasks, and exhibit complementary performance characteristics with each other. We apply the method to a set of 93 classification tasks from the UCR/UAE repository, showing how a large library of 4791 features can be reduced to a canonical subset of just 22 features, *catch22*, which displays similar classification accuracy as the full set (rel-

ative reduction of 7.5% on average, 77.2% vs 71.7%), computes quickly (<0.5 s/10 000 samples), scales approximately linearly with time-series length ($O(N^{1.16})$), and allows the investigator to learn and understand what types of dynamical properties distinguish the labeled classes of their dataset. Compared to shape-based methods like dynamic time warping (DTW), *catch22* gives comparable, and often superior classification performance, despite substantial dimensionality reduction. Using case studies, we explain why some datasets are better suited to shape-based classification (e.g., there are characteristic aligned shapes within each class), while others are better suited to feature-based classification (e.g., where classes do not have a characteristic, temporally aligned shape, but have characteristic dynamical properties that are encapsulated in one or more time-series features).

While some applications may be able to justify the computational expense of searching across a large feature library such as *hctsa* (Fulcher and Jones, 2014, 2017), the availability of an efficient, reduced set of features, as *catch22*, will make the advantages of feature-based time-series classification and clustering more widely accessible. As an example application *catch22* is being used in the self-organising time-series database for data-driven interdisciplinary collaboration *CompEngine* to assess the similarity of recordings (Fulcher et al., 2019). Unlike the Matlab-based *hctsa*, *catch22* does not require a commercial license to run, computes efficiently, and scales approximately linearly with time-series length in the cases we tested. This makes it straightforwardly applicable to much longer time series than are typically considered in the time-series classification literature, e.g., for a 10 000-sample time series, *catch22* computes in 0.5 s. As well as being suitable for long recordings, feature-based representations do not require all time series to be the same length (unlike conventional shape-based classifiers), opening up the feature-based approach to new types of datasets – and indeed new types of analyses. Even though *catch22* is selected here based on classification performance, the availability and ease of computing *catch22* opens up applications to areas including feature-based time-series modeling, forecasting, anomaly detection, motif discovery, and others. To facilitate its adoption, we provide an efficient C-implementation of *catch22*, with wrappers for Matlab, Python, and R.

We have shown that the most useful representation of a time series varies widely across datasets, with some problems better suited to feature-based classification, and others better suited to shape-based classification. The 22 features selected here are tailored to the properties of the UCR/UEA datasets (which are typically short and phase-aligned), but the method we present here is general and could be used to generate reduced feature sets tailored to any application domain of interest that allows indi-

vidual features to be assigned performance scores. For example, given a different set of classification datasets where key class differences are the result of subtle variations in dynamical properties in long streams of time-series data, we would obtain a canonical set that might include features of long-range automutual information or measures the nonlinear time-series analysis literature: very different features to the relatively simple measures contained in *catch22*. As new time-series datasets are added to the UCR/UEA repository, that better capture the diversity of time-series data studied across industry and science, our feature reduction method could be rerun to extract new canonical feature sets that reflect the types of time-series properties that are important to measure in the new data. Note that hybrid methods such as COTE (Bagnall et al., 2016), which are not limited to a single time-series representation but can adapt to the problem at hand, consistently outperform both the shape-based existing classifiers and our features at the price of a much higher computational effort. Given its computational efficiency, *catch22* could be incorporated straightforwardly in these ensemble-based frameworks of multiple representations. Here we excluded features that are sensitive to the location and spread of the data distribution, to ensure a fair comparison to shape-based methods which use normalised data; but for many real-world applications these could be highly relevant and should therefore be retained to allow improvements in classification accuracy. Our selection pipeline is agnostic to the classification task collection used and can in principle be generalised beyond classification tasks to different time-series analyses as well. Here we score the performance of each feature on a given task as the classification accuracy, but this metric could be adapted to allow application to regression problems (correlation of a feature with the exogenous target variable), forecasting problems (prediction error), and clustering problems (separation of known clusters). The proposed method has the advantage of identifying individually informative estimators and transparently grouping features into similarly performing clusters for enhanced interpretability. Still, other approaches for selecting feature subsets exist, such as sequential forward selection or LASSO, and it would be interesting to compare the results of alternative pipelines building on these existing selection techniques with our results in future work.

In conclusion, here we present *catch22*, a concise, accessible feature-based summary of an interdisciplinary time-series analysis literature for use in time-series classification tasks. We hope that the ability to readily leverage feature-based representations of time series – and to generate new reduced feature sets tailored to specific domain problems – will aid diverse applications involving time series

including feature-based characterisation of peripheral nerve recordings.

5.2.4 Appendix

5.2.4.A Time series for computation time evaluation

A selection of 40 time series was obtained from the dataset ‘1000 Empirical Time series’ (Fulcher, 2017).

ID	name	keywords
1	NS_beta.L10000.a1_b3.2.dat	synthetic,noise,beta
25	ST_M5a.N10000.a-0.01_b-0.6_c0_d0.x0.1.2.dat	synthetic,stochastic,SDE,M5
53	SY_rwalk.L10000.20.dat	synthetic,randomwalk
75	FL_ddp.L300.N5000.IC.0.1.0.1.y.dat	synthetic,dynsys,ddp
106	FL_lorenz.L250.N10000.IC.0.-0.01_9.1.y.dat	synthetic,dynsys,chaos,lorenz
125	FL_shawvdp.L300.N5000.IC.1.3.0.1.x.dat	synthetic,dynsys,shawvdp
158	MP_burgers.L300.IC.-0.2.0.1.x.dat	synthetic,map,burgers
175	MP_chirikov.L300.IC.0.2.6.y.dat	synthetic,map,chirikov
211	MP_henon.L1000.a1.4.b0.3.IC.0.0.9.dat	synthetic,map,henon
225	MP_holmes cubic.L300.IC.1.7.0.y.dat	synthetic,map,holmes cubic
263	MP_lorenz3d.L300.IC.0.51.0.5.-1.x.dat	synthetic,map,chaos,lorenz3d
275	MP_pinchers.L5000.s2.1c.0.55.dat	synthetic,map,pinchers
316	MP_spence.L5000.x0.0.27.dat	synthetic,map,spence
325	MP_tent.L5000.A1.88.dat	synthetic,map,tent,chaos
369	SY_MA.L500.p8.7.dat	synthetic,MA,MA8
375	SY_MIX.p0.3.L5000.5.dat	synthetic,MIXP,MIX0.3
421	FI_yahoo.HL_KLSE.dat	finance,yahoo,opening
425	FI_yahoo.HL_z28.SPMIB.dat	finance,yahoo,opening
474	FL_dbscroll.L1000.N5000.IC.0.01.0.01.0.z.dat	synthetic,dynsys,chaos,dbscroll
475	FL_dbscroll.L200.N10000.IC.0.01.0.01.0.z.dat	synthetic,dynsys,chaos,dbscroll
525	FL_moorespiegel.L250.N1000.IC.0.1.0.0.x.dat	synthetic,dynsys, chaos,moorespiegel
526	FL_moorespiegel.L250.N5000.IC.0.1.0.0.x.dat	synthetic,dynsys, chaos,moorespiegel
575	FL_simpqcf.L1000.N10000.IC.-0.9.0.0.5.z.dat	synthetic,dynsys,chaos,simpqcf
579	FL_simpqcf.L2000.N1000.IC.-0.9.0.0.5.z.dat	synthetic,dynsys,chaos,simpqcf
625	MP_Lozi.iii.dat	synthetic,map,chaos,lozi
631	MP_freitas_nlma.L500.a-3.92.b-3.1526.1.dat	synthetic,map,nonlinear,freita
675	TR_arge030.rf.dat	treerings
684	AS.s2.2.f4_b8.I8800.58925.dat	sound,animalsounds
725	FI_yahoo.Op.IFL.L.LOGR.dat	finance,logr
737	lch_recflow.dat	meteorology,riverflow, reconstructed,UK
775	SF_E.5.dat	SantaFe,astronomy
789	SPIDR_hpidsmp.F15_meas.dat	space,hpidsmp
825	SPIDR_meanDelay_ACE.hrly.dat	space,magneticfield
842	SPIDR_vostok.L6600.Sep2002.vostok.dat	space,vostok
875	t.osaka.rf.dat	meteorology,temperature
894	MD_chfdb_chf07_seg039.SNIP.9574-17073.dat	medical,physionet,ecg,chfdb,snip
925	MD_tremordb_g12ren.dat	medical,tremor,physionet,lowamp, dbson,medon,gpi
947	MUS_Tetra-Sync.1364s.F0.02.b8.dat	sound,music,downed
976	MD_nsrdnb_nsr19088_seg007.SNIP.5659-15658.dat	medical,physionet,ecg,nsrdnb,snip
1000	MD_mghdb_mgh79_PAP.SNIP.9047-15146.dat	medical,physionet,mghdb, snip,pulmonaryarterialpressure

Table 5.2.S1: 40 empirical time series selected for evaluating the computation times of features.

5.2.4.B Manually replaced features

Table 5.2.S2 lists the best five features of each cluster in which a feature has been manually exchanged. The full list of 710 features grouped by cluster can be accessed as a supplementary file.

<i>hctsa</i> feature name	z-scored combined accuracy
Cluster 3	
EX_MovingThreshold_01_01_meankickf	1.44
PH_Walker_prop_01_res_ac1	1.39
SP_Summaries_welch_rect_area_5.1	1.18
PH_Walker_prop_11_w_std	1.17
IN_AutoMutualInfoStats_40_gaussian_pextrema	1.13
Cluster 6	
MF_arfit_1_8_sbc_meanA	2.57
FC_LocalSimple_mean3_stderr	2.26
FC_LocalSimple_mean4_stderr	2.25
NL_embed_PCA_1_10_std	2.19
NL_embed_PCA_1_10_perc_1	2.17
Cluster 10	
SB_TransitionMatrix_2ac_sumdiagcov	2.51
SB_TransitionMatrix_2ac_T3	2.25
SB_TransitionMatrix_2ac_onddiag	2.18
SB_TransitionMatrix_2ac_T1	2.07
SB_BinaryStats_mean_longstretch1	2.05
Cluster 17	
SB_TransitionMatrix_3ac_maxeigcov	2.65
SB_TransitionMatrix_3ac_stdeigcov	2.56
SB_TransitionMatrix_3ac_stdeig	2.53
SB_TransitionMatrix_5ac_stdeigcov	2.53
SB_TransitionMatrix_3ac_sumdiagcov	2.46
Cluster 18	
SB_TransitionMatrix_41_onddiag	1.83
SB_TransitionMatrix_51_onddiag	1.80
EN_SampEn_5_03_sampen1	1.54
CO_HistogramAMI_quantiles_10_1	1.51
MD_hrv_classic_pnn40	1.50
Cluster 19	
PH_Walker_prop_01_sw_propcross	1.99
IN_AutoMutualInfoStats_40_gaussian_fmml	1.92
SB_TransitionMatrix_31_onddiag	1.52
PH_Walker_prop_01_sw_taudiff	1.47
CO_Embed2_Basic_1_updiag01	1.40

Table 5.2.S2: The five best features of each cluster with manual replacement. The feature in bold was used instead of the top feature.

5.3 Conclusion on feature-based time-series analyses

Thanks to the availability of a feature set of unprecedented diversity, we had the chance to develop two feature-selection methods. We first proposed a novel framework that identifies the low-dimensional main varying dynamics in a dataset. We achieve this functionality by transferring time series to a high-

dimensional feature space and applying dimensionality reduction methods to the time-series points in feature space. For each main varyin dynamic, we proposed single estimators.

For our core area of bioelectronic medicines, this unsupervised method proved useful on simulated data in automatically detecting different firing characteristics. The identified features can perform an on-line characterisation of low-resolution cuff recordings in implanted devices that goes beyond the usual power-measures and does not require expensive signal conditioning. We thus propose a novel pre-processing approach that automatically extracts informative features and adapts to the recording technique, the nerve, and the relevant firing characteristics for a signal-to-noise ratio not yet well harvested by existing methods. For the future, we might augment the feature-set by features that will be developed specifically for peripheral nerve signal processing.

In a second contribution to feature-based time-series analysis, we developed a supervised selection pipeline to automatically tailor feature sets of high discriminative power to collections of datasets. Applying this method to a literature standard collection of classification problems, we devised a canonical feature set, *catch22*, that executes quickly and is informative of diverse time series dynamics.

Chapter 6

Conclusion

6.1 Summary of thesis achievements

In terms of the core topic of this PhD – peripheral nerve decoding – we provided three immediately relevant contributions. First, a simple real-time compatible decoder for low-resolution recordings as obtained by the common cuff electrode. By mapping and linearising the non-linear relation between bladder pressure and power of the recorded population activity within a selected frequency band, we enabled the use of a linear decoder (optimal linear filter) and avoided more complex models such as artificial neural networks. This simple step reduces computational complexity of the decoding and allows for an efficient bladder pressure estimation for the commonly used cuff interface. Second, we investigated the encoding principles by which the ‘spine listens to the bladder’ by applying information theory, a powerful analysis tool from the analysis of the central nervous system, to a population of bladder afferents. We exploited the observed population code to construct a first informed decoder that is accurate, robust against cell loss, and even offers rudimentary means of automatic re-calibration, demonstrating the advantages of an informed approach. Third, we leveraged decades of time-series analysis literature to automatically detect the main varying firing characteristics of a peripheral nerve in a high-dimensional feature space and identified single relevant features that can be implemented efficiently and be used to summarise low-resolution activity as recorded by a cuff in an implanted device by a few key dynamical properties.

In addition to these core achievements that directly translate into progress towards next generation

bioelectronic medicines, we presented a few supporting methodological advances. First, we implemented an easy-to-use Python-based peripheral nerve simulator, PyPNS, that we used to generate artificial recordings to test our feature-based analysis method. The model is the first ready-to-use hybrid peripheral nerve simulator that unites compartmentalised axon models and extracellular field models. It enables a quick generation of surrogate data but also integrates means of intra- and extracellular stimulation and spontaneous activity generation. Innovative features are the automatically placed tortuous axons and the efficient integration of pre-computed potential distributions from finite element methods software. Second, our feature-based analysis method that uncovers low-dimensional parametric variation in an unsupervised way from many recordings and that we applied to peripheral nerve recordings is not limited to this type of data. Because of the generically useful nature of the features, it can be applied to a wide variety of time-series generating systems. We demonstrated its universal utility on many different synthetic systems and an additional real-world example. It is thus a general-purpose ‘discovery engine’ for low-dimensional variation and for the identification of single estimators for each variation dimension. As a third and last additional achievement, we developed a flexible pipeline to distill small feature-sets of high performance for a collection of classification tasks. We selected a canonical set of features by applying this pipeline to a literature-standard set of time-series classification problems, *catch22*, which is generically useful and fast, and signifies the first feature-set selected by highly-comparative time-series analysis as a surrogate of the much larger feature library *hctsa*.

Comparing with our original objectives (cf. Ch. 1), we thus firstly achieved the development of a publicly available, easy-to-use peripheral nerve simulator that we indeed used in our algorithm development (Sec. 3). We secondly proposed specific decoding algorithms – one simple and suited to low-resolution interfaces (Sec. 4.1) and one biologically informed for high-resolution interfaces (Sec. 4.2). In our exploration of different applications of feature-based time-series analysis, we showed that the features included in the *hctsa*-toolbox are suited to peripheral nerve recordings and can in fact close a gap in pre-processing methods for low-resolution peripheral nerve recordings where the currently used coarse power or amplitude measures discard informative structure (Sec. 5.1).

6.2 Future Work

The feature-based characterisation of peripheral nerve recordings is promising, but needs to be tested on real data and prove its reliability and usefulness for peripheral nerve recordings.

Provided a suitable long chronic recording, it can be cut into short snippets and fed into our dimensionality reduction in feature space (Sec. 5.1). We might then see firing characteristics of the recordings recovered as second or third component that are informative for bioelectronic medicines.

The feature selection pipeline we presented in Sec. 5.2 could be better connected to our core topic by applying it to annotated peripheral nerve recordings. We might then select similar features to the ones obtained in the unsupervised manner above. We might also find generically useful ones that can be informative on diverse peripheral nerve recordings. Given a subset of ~ 20 of such features, we might see what dynamical properties are the best for characterising peripheral nerve recordings. Researchers may then be guided to a deeper understanding of important signal characteristics in PNS recordings and engineers may be guided towards conceiving specialised features specifically for PNS firing characterisation.

In order to use the features for decoding, it can then be attempted to feed the feature outputs into a continuous decoder or even a categorical classifier that classifies the recorded nerve's state. It may prove that characterising the nerve's activity, without explicitly decoding the organs' physiological state, is sufficient to select on stimulation/ block or even for finely modulating the nerve.

When we have devised the most relevant features for peripheral nerve recordings, these need to be implemented efficiently for bioelectronic medicines. Energy efficiency is crucial in order not to deplete the battery of the device. Hardware implementations like specialised digital signal processing (DSP) processors or field programmable gate arrays (FPGAs) should therefore be investigated for the efficient implementation of core features.

Given all these steps, future bioelectronic medicines devices might then be able to characterise a nerve's state – and perhaps an associated organ state – just from a low-resolution recording by computing a few efficiently implemented features.

Naturally, the selection selection pipeline we devised for our *catch22* feature set can be applied to

all sorts of other labelled time-series datasets and can generate other generic feature sets that probe for dynamical properties relevant to e.g., long and more complex time series than included in the UEA/UCR classification problems. The *catch22* feature set reflects the class differences of the used UEA/UCR classification task library that mainly contains short, aligned, normalised time series suitable for a shape-based comparison. The feature set is not sensitive to mean shifts and spread in the data because the datasets it was selected on were normalised. It cannot be expected to yield good classification performance on longer and more complex time series where other features from the *hctsa* collection would be more suitable. We look forward to researchers re-running the pipeline and automatically curating feature sets to their specific domain.

In our feature-based time-series analyses, the unsupervised discovery of low-dimensional variation (Sec. 5.1) signifies a proof-of-concept that can still be developed much further. As one major drawback, we did not correct for existing feature-feature dependencies in our library and our results are still highly shaped by the imbalanced representations of certain feature classes. By incorporating knowledge of the interactions to be expected between features without constraints of the data, the method can be expected to perform better in cases where the dynamical variation caused by parametric drive is not well represented in the feature set. These feature-feature dependencies can be identified on truly unconstrained data from diverse sources where any correlation between two features across time series has to be caused by algorithmic similarity, not by similarity of the time series. Given such diverse data, we can then compute the correlation, mutual information or another measure of similarity between all feature pairs and either remove redundant features or compensate for their redundancy by an adapted dimensionality reduction method.

In terms of decoding, our first simple decoder (Sec. 4.1) has the beauty of removing non-linearities in a first step and therefore being able to apply a linear temporal filter to the linearised relation between an independent, observed variable and a dependent, estimated variable. We look forward to the application of this concept to other peripheral nerve decoding tasks on afferent and/ or efferent nerves. The mapping of the non-linear relation can be improved by replacing the piece-wise linear fit with another function adapted to the non-linearity in question. This may in our case improve the decoding of low bladder pressure ranges. We applied our decoder to a univariate recording of the nerve's activity by a hook electrode. The decoding approach (linearisation + linear filtering) is easily applicable to higher dimensional recordings, e.g., by microelectrode arrays. The non-linear steady-state response

characteristic of each electrode or sorted unit can be mapped in the same way and a linear filter can be trained on the linearised responses.

Based on the second dataset at our disposition, our work on encoding in the periphery is a first step towards a functional characterisation of peripheral sensory populations. The work we carried out was limited by the properties of the data as no controlled repetitions with the same pressure time courses per trial were available, the spikes were not sorted across trials and the pressure time course was not designed to separate different aspects of the pressure signal such as high constant pressures and high varying pressure amplitudes. It would be very helpful to repeat experiments while actively controlling the bladder pressure and/ or record at isobaric and/ or isovolumetric conditions. Only then, the complete characterisation of the bladder neuron response characteristics can be achieved.

No principled analysis has yet been conducted on the encoding of e.g., temperature sensors, baroreceptors, muscle spindles, etc., and it would be very interesting to compare these in terms of their encoding strategies. Often, similar single cell responses have been reported. Perhaps we will find a recurring encoding scheme across these different monitoring systems of the body. Based on this understanding we might be able to design better interventions (stimulation or block) and adapted decoders to accelerate the progress of bioelectronic medicines which can then more quickly conquer new organ systems. A detailed investigation of these populations (using destructive invasive interfaces available today) would thus prepare the field of bioelectronics medicines for the future interfaces of high resolution at acceptable long-term stability that will become available with advances in materials research.

A refined understanding of the encoding can in particular be used by informed decoders. We demonstrated this in our example bladder system. In the informed decoding approach we proposed, a simple averaging across stereotypical, redundant bladder neurons was able to significantly increase the robustness against cell loss of our decoder. This idea of an informed decoder can easily be extended to more advanced ideas. We hope our simple approach will spark research towards specialised decoding algorithms that e.g., automatically detect redundancy in the sensory population and optimise the trade-off between accuracy loss and robustness gains. The grouping of cells can also be straightforwardly combined with our ideas on linearising the non-linear steady-state relationship. The response of a stereotypical subpopulation of fibres and could thus first be linearised and then used by a sub-

sequent decoder, together with the linearised responses of other subpopulations. The demonstration of the advantages of the informed decoder we constructed was hampered by the lack of controlled repetitions and cell sorting across trials. We hope that new experiments will be conducted that allow the more accurate, quantitative analysis of the merits of informed decoders.

Our simulation, PyPNS, is a simple, accessible way of generating generic surrogate peripheral nerve recordings. To further accelerate the simulation, parallelisation of axon simulations should be integrated. It is also imaginable that action potentials (AP) which are out of reach of the recording and/or stimulation electrodes, could be simulated in an abstracted way without simulating all channels. Instead, the AP position could be moved along the axon at the respective conduction velocity. Only when entering the relevant regions of the nerve in proximity to the electrodes, the whole axon simulation including the action of ion channels, could be launched.

The axon trajectories we devised in our simulation went beyond the classical perfectly straight directions. In PyPNS, axons can have a curvy, tortuous trajectory that is automatically generated and can be fit to imaged data. One simplification in the axon placing algorithm was the lack of fascicles. It would be interesting to define groups of axons that move through the nerve while keeping close together, perhaps guided by a common randomly placed guide trajectory.

One limitation of PyPNS is the lack of accurate C-fibre models for mammalian axons. Literature has usually resorted to the classical Hodgkin-Huxley-model (HH) with slight parameter adjustments (most notably temperature) as we did, too. One obvious inaccuracy resulting from this inappropriate model is the low conduction velocity. We hope that future research will finally characterise the ion-channels of the C-fibres in mammals and then lead to a new standard that can replace the currently used HH-model.

Our simulation further simplified the geometry of the extracellular tissue to enable the efficient import of pre-computed FEM results. For more complex trajectories, it would be necessary to compute a transfer function between every axon segment current and every electrode potential. To simplify this for the investigator, PyPNS could integrate an FEM module itself and pre-compute these transfer functions once in order to be able to compute signals from arbitrary firing patterns for a given nerve geometry.

For our topic of bioelectronic medicines it would further be interesting to include a closed-loop simu-

lation of a peripheral nerve that includes both a recording and a stimulation site on the same simulated nerve to model closed-loop control *in silico*.

Bibliography

- D Adrian, D W Bronk, G Phillips, and E D Adrian. Discharges in mammalian sympathetic nerves. *The Journal of Physiology*, 74(2):115–133, 1932. ISSN 14697793. doi: 10.1113/jphysiol.1932.sp002832. URL <http://www.ncbi.nlm.nih.gov/pubmed/16994262><http://www.ncbi.nlm.nih.gov/pmc/articles/PMC1394445/pdf/jphysiol01646-0003.pdf>.
- E D Adrian and Y Zotterman. The impulses produced by sensory nerveendings. Part II. The response of a single endorgan. *The Journal of Physiology*, 61(2):151–171, 1926. ISSN 14697793. doi: 10.1113/jphysiol.1926.sp002281.
- A Agudelo-Toro and A Neef. Computationally efficient simulation of electrical activity at cell membranes interacting with self-generated and externally imposed electric fields. *Journal of Neural Engineering*, 10(2):1–19, 2013. ISSN 1741-2560. doi: 10.1088/1741-2560/10/2/026019. URL <http://stacks.iop.org/1741-2552/10/i=2/a=026019?key=crossref.43022dd560627da27c4437e3798baf31>.
- N Ahmadi, T G Constandinou, and C S Bouganis. Decoding hand kinematics from local field potentials using Long Short-Term Memory (LSTM) network. *International IEEE/EMBS Conference on Neural Engineering, NER*, 2019-March:415–419, 2019. ISSN 19483554. doi: 10.1109/NER.2019.8717045.
- A Al Qasem, F Smith, and S Clifford. Adherence to medication among chronic patients in Middle Eastern countries: review of studies. *Eastern Mediterranean Health Journal*, 17(04):356–363, 2011. ISSN 10203397. doi: 10.26719/2011.17.4.356.
- H E Anderson, A K Fontaine, J H Caldwell, and R F Weir. Imaging of electrical activity in small diameter fibers of the murine peripheral nerve with virally-delivered GCaMP6f. *Scientific Reports*,

- 8(1):2–10, 2018. ISSN 20452322. doi: 10.1038/s41598-018-21528-1. URL <http://dx.doi.org/10.1038/s41598-018-21528-1>.
- U Andersson and K J Tracey. Reflex principles of immunological homeostasis. *Annual Review of Immunology*, 30(1):313–335, 2012. ISSN 0732-0582. doi: 10.1146/annurev-immunol-020711-075015. URL <http://www.annualreviews.org/doi/10.1146/annurev-immunol-020711-075015>.
- C M Apovian, S N Shah, B M Wolfe, S Ikramuddin, C J Miller, K S Tweden, C J Billington, and S A Shikora. Two-year outcomes of vagal nerve blocking (vBloc) for the treatment of obesity in the ReCharge trial. *Obesity Surgery*, 27(1):169–176, 2017. ISSN 17080428. doi: 10.1007/s11695-016-2325-7. URL <http://dx.doi.org/10.1007/s11695-016-2325-7>.
- A E Applebaum, W H Vance, and R E Coggeshall. Segmental localization of sensory cells that innervate the bladder. *Journal of Comparative Neurology*, 192(2):203–209, 1980. ISSN 10969861. doi: 10.1002/cne.901920202.
- K Aristovich, M Donegá, C Blochet, J Avery, S Hannan, D J Chew, and D Holder. Imaging fast neural traffic at fascicular level with electrical impedance tomography: proof of principle in rat sciatic nerve. *Journal of Neural Engineering*, 15(5), 2018. ISSN 17412552. doi: 10.1088/1741-2552/aad78e.
- M Aström, J J Lemaire, and K Wardell. Influence of heterogeneous and anisotropic tissue conductivity on electric field distribution in deep brain stimulation. *Medical and Biological Engineering and Computing*, 50(1):23–32, 2012. ISSN 01400118. doi: 10.1007/s11517-011-0842-z.
- A Bagnall, L M Davis, J Hills, and J Lines. Transformation based ensembles for time series classification. In *Proceedings of the 2012 SIAM International conference on data mining*, pages 307–318, 2012. ISBN 978-1-61197-232-0.
- A Bagnall, J Lines, J Hills, and A Bostrom. Time-series classification with COTE: The collective of transformation-based ensembles. *2016 IEEE 32nd International Conference on Data Engineering, ICDE 2016*, 27(9):1548–1549, 2016. ISSN 10414347. doi: 10.1109/ICDE.2016.7498418.
- A Bagnall, J Lines, A Bostrom, J Large, and E Keogh. The great time series classification bake off: a

- review and experimental evaluation of recent algorithmic advances. *Data Mining and Knowledge Discovery*, 31(3):606–660, 2017a. ISSN 1573756X. doi: 10.1007/s10618-016-0483-9.
- A Bagnall, J Lines, W Vickers, and E Keogh. The UEA & UCR Time Series Classification Repository, 2017b. URL <http://www.timeseriesclassification.com/>.
- E Bahns, U Ernsberger, W Jänig, and A Nelke. Functional characteristics of lumbar visceral afferent fibres from the urinary bladder and the urethra in the cat. *Pflügers Archiv European Journal of Physiology*, 407(5):510–518, 1986. ISSN 00316768. doi: 10.1007/BF00657509.
- E Bahns, U Halsband, and W Jänig. Responses of sacral visceral afferents from the lower urinary tract, colon and anus to mechanical stimulation. *Pflügers Archiv European Journal of Physiology*, 410(3):296–303, 1987. ISSN 00316768. doi: 10.1007/BF00580280.
- K Bandara, C Bergmeir, and S Smyl. Forecasting across time series databases using long short-term memory networks on groups of similar series: a clustering approach. *arXiv*, 2017. ISSN 13578170. doi: 10.1002/pdi.718. URL <http://arxiv.org/abs/1710.03222>.
- N Barber, J Parsons, S Clifford, R Darracott, and R Horne. Patients’ problems with new medication for chronic conditions. *Quality and Safety in Health Care*, 13(3):172–175, 2004. ISSN 14753898. doi: 10.1136/qshc.2003.005926.
- A L Barker, D E Brown, and W N Martin. Bayesian estimation and the Kalman filter. *Computers & Mathematics with Applications*, 30(10):55–77, 1995. ISSN 08981221. doi: 10.1016/0898-1221(95)00156-S. URL <http://linkinghub.elsevier.com/retrieve/pii/S089812219500156S>.
- R P J Barretto, S Gillis-Smith, J Chandrashekar, D A Yarmolinsky, M J Schnitzer, N J P Ryba, and C S Zuker. The neural representation of taste quality at the periphery. *Nature*, 517(7534):373–376, 2015. ISSN 14764687. doi: 10.1038/nature13873. URL <http://dx.doi.org/10.1038/nature13873>.
- A I Basbaum. Peripheral mechanisms of sensitization and hyperalgesia. In T H Stanley, M A Ashburn, and P G Fine, editors, *Anesthesiology and Pain Management*, pages 31–37. Springer Netherlands, Dordrecht, 1991. ISBN 978-94-011-3318-0. doi: 10.1007/978-94-011-3318-0_{_}2. URL https://doi.org/10.1007/978-94-011-3318-0_2.

- T Bayes. An essay towards solving a problem in the doctrine of chances. *Philosophical transactions of the Royal Society of London*, 53:370–418, 1763. doi: 10.1016/B978-044450871-3/50096-6.
- C Bédard and A Destexhe. Macroscopic models of local field potentials and the apparent 1/f noise in brain activity. *Biophysical Journal*, 96(7):2589–2603, 2009. ISSN 00063495. doi: 10.1016/j.bpj.2008.12.3951.
- A L Benabid, S Chabardes, J Mitrofanis, and P Pollak. Deep brain stimulation of the subthalamic nucleus for the treatment of Parkinsons disease. *The Lancet Neurology*, 8(1):67–81, 2009.
- D Berndt and J Clifford. Using dynamic time warping to find patterns in time series. In *Workshop on Knowledge Knowledge Discovery in Databases*, volume 398, pages 359–370, 1994. ISBN 0-929280-73-3.
- C H Berthold and M Rydmark. Electron microscopic serial section analysis of nodes of Ranvier in lumbosacral spinal roots of the cat: Ultrastructural organization of nodal compartments in fibres of different sizes. *Journal of Neurocytology*, 12(3):475–505, 1983. ISSN 03004864. doi: 10.1007/BF01159386.
- H R Berthoud and W L Neuhuber. Functional and chemical anatomy of the afferent vagal system. *Autonomic Neuroscience: Basic and Clinical*, 85(1-3):1–17, 2000. ISSN 15660702. doi: 10.1016/S1566-0702(00)00215-0.
- A Biazon, C Pielli, M Rossi, A Zanella, D Zordan, M Kelly, and M Zorzi. EC-CENTRIC: An energy- and context-centric perspective on IoT systems and protocol design. *IEEE Access*, 5:6894–6908, 2017. ISSN 21693536. doi: 10.1109/ACCESS.2017.2692522.
- R Biran, D C Martin, and P A Tresco. Neuronal cell loss accompanies the brain tissue response to chronically implanted silicon microelectrode arrays. *Experimental Neurology*, 195(1):115–126, 2005. ISSN 00144886. doi: 10.1016/j.expneurol.2005.04.020.
- R I Birks. Regulation by patterned preganglionic neural activity of transmitter stores in a sympathetic ganglion. *Journal of Physiology*, 280:559–572, 1978. ISSN 00223751.
- K Birmingham, V Gradinaru, P Anikeeva, W M Grill, V Pikov, B McLaughlin, P Pasricha, D Weber, K Ludwig, and K Famm. Bioelectronic medicines: a research roadmap. *Nature Reviews Drug*

- Discovery*, 13(6):399–400, 2014. ISSN 1474-1776. doi: 10.1038/nrd4351. URL <http://www.nature.com/doifinder/10.1038/nrd4351>.
- I Birnieks and R M Vickery. Spike timing matters in novel neuronal code involved in vibrotactile frequency perception. *Current Biology*, 27(10):1485–1490, 2017. ISSN 09609822. doi: 10.1016/j.cub.2017.04.011. URL <http://dx.doi.org/10.1016/j.cub.2017.04.011>.
- H Blumberg, P Haupt, W Jänig, and W Kohler. Encoding of visceral noxious stimuli in the discharge patterns of visceral afferent fibres from the colon. *Pflügers Archiv European Journal of Physiology*, 398(1):33–40, 1983. ISSN 00316768. doi: 10.1007/BF00584710.
- H Bokil, N Laaris, K Blinder, M Ennis, and A Keller. Ephaptic interactions in the mammalian olfactory system. *The Journal of Neuroscience*, 21(20):1–5, 2001. ISSN 1529-2401. doi: 20015719[pil]. URL <http://www.ncbi.nlm.nih.gov/pubmed/11588203>.
- T Boretius, J Badia, A Pascual-Font, M Schuettler, X Navarro, K Yoshida, and T Stieglitz. A transverse intrafascicular multichannel electrode (TIME) to interface with the peripheral nerve. *Biosensors and Bioelectronics*, 26(1):62–69, 2010. ISSN 09565663. doi: 10.1016/j.bios.2010.05.010. URL <http://dx.doi.org/10.1016/j.bios.2010.05.010>.
- L V Borovikova, S Ivanova, M Zhang, H Yang, G I Botchkina, L R Watkins, H Wang, N Abumrad, J W Eaton, and K J Tracey. Vagus nerve stimulation attenuates the systemic inflammatory response to endotoxin. *Nature*, 405(6785):458–462, 2000. ISSN 0028-0836. doi: 10.1038/35013070.
- C A Bossetti, M J Birdno, and W M Grill. Validity of the quasi-static approximation for neural stimulation. *Journal of Neural Engineering*, 5:44–53, 2008. doi: 10.1088/1741-2560/5/1/005.
- C Bouton. Neural decoding and applications in bioelectronic medicine. *Bioelectronic Medicine*, 2(1):20–24, 2015. doi: 10.15424/bioelectronmed.2014.00012.
- C Bouton. Cracking the neural code, treating paralysis and the future of bioelectronic medicine. *Journal of Internal Medicine*, 282(1):37–45, 2017. ISSN 13652796. doi: 10.1111/joim.12610.
- B R Bowman and R C Erickson. Acute and chronic implantation of coiled wire intraneural electrodes during cyclical electrical stimulation. *Annals of Biomedical Engineering*, 13(1):75–93, 1985. ISSN 00906964. doi: 10.1007/BF02371251.

- A Brockwell, A Rojas, and R Kass. Recursive Bayesian decoding of motor cortical signals by particle filtering. *Journal of Neurophysiology*, 91:1899–1907, 2004. ISSN 0022-3077. doi: 10.1152/jn.00438.2003.
- D R Brown, L V Brown, A Patwardhan, and D C Randall. Sympathetic activity and blood pressure are tightly coupled at 0.4 Hz in conscious rats. *American Journal of Physiology*, 267(5 Pt 2):1378–84, 11 1994. ISSN 0002-9513. URL <http://www.ncbi.nlm.nih.gov/pubmed/7977868>.
- M C Brown, A Crowe, and P B C Matthews. Observations on the fusimotor fibres of the tibialis posterior muscle of the cat. *The Journal of Physiology*, 177(1):140–159, 1965. ISSN 14697793. doi: 10.1113/jphysiol.1965.sp007582.
- K N Browning and R A Travagli. Central nervous system control of gastrointestinal motility and secretion and modulation of gastrointestinal functions. *Comprehensive Physiology*, 4(4):1339–1368, 2014. ISSN 20404603. doi: 10.1002/cphy.c130055.
- T M Bruns, R A Gaunt, and D J Weber. Estimating bladder pressure from sacral dorsal root ganglia recordings. *IEEE EMBS Conference on Neural Engineering*, pages 4239–4242, 2011a. ISSN 1557170X. doi: 10.1109/IEMBS.2011.6091052.
- T M Bruns, T A Gaunt, and D J Weber. Afferent activity from the sacral dorsal root ganglia. *Journal of Neural Engineering*, 8(5):1–17, 2011b. doi: 10.1088/1741-2560/8/5/056010.Multielectrode.
- T M Bruns, D J Weber, and R A Gaunt. Microstimulation of afferents in the sacral dorsal root ganglia can evoke reflex bladder activity. *Neuourology and Urodynamics*, 34:65–71, 2015. ISSN 03262383. doi: 10.1002/nau.
- A P Cameron, L P Wallner, D G Tate, A V Sarma, G M Rodriguez, and J Q Clemens. Bladder management after spinal cord injury in the United States 1972 to 2005. *Journal of Urology*, 184(1):213–217, 2010. ISSN 00225347. doi: 10.1016/j.juro.2010.03.008.
- D R Cantrell, S Inayat, A Taflove, R S Ruoff, and J B Troy. Incorporation of the electrode-electrolyte interface into finite-element models of metal microelectrodes. *Journal of Neural Engineering*, 5(1):54–67, 2008. ISSN 1741-2560. doi: 10.1088/1741-2560/5/1/006. URL <http://www.ncbi.nlm.nih.gov/pubmed/18310811>.

- H Cao, U Tata, V Landge, A L Li, Y B Peng, and J C Chiao. A wireless bladder volume monitoring system using a flexible capacitance-based sensor. *2013 IEEE Topical Conference on Biomedical Wireless Technologies, Networks, and Sensing Systems*, pages 34–36, 2013. doi: 10.1109/BioWireleSS.2013.6613666.
- M Capogrosso, N Wenger, S Raspopovic, P Musienko, J Beauparlant, L Bassi Luciani, G Courtine, and S Micera. A computational model for epidural electrical stimulation of spinal sensorimotor circuits. *Journal of Neuroscience*, 33(49):19326–19340, 2013. ISSN 0270-6474. doi: 10.1523/JNEUROSCI.1688-13.2013. URL <http://www.jneurosci.org/cgi/doi/10.1523/JNEUROSCI.1688-13.2013>.
- A S Caravaca, T Tsaava, L Goldman, H Silverman, G Riggott, S S Chavan, C Bouton, K J Tracey, R Desimone, E S Boyden, H S Sohal, and P S Olofsson. A novel flexible cuff-like microelectrode for dual purpose, acute and chronic electrical interfacing with the mouse cervical vagus nerve. *Journal of Neural Engineering*, 14(6), 2017. ISSN 17412552. doi: 10.1088/1741-2552/aa7a42.
- D Carnevale, M Perrotta, F Pallante, V Fardella, R Iacobucci, S Fardella, L Carnevale, R Carnevale, M De Lucia, G Cifelli, and G Lembo. A cholinergic-sympathetic pathway primes immunity in hypertension and mediates brain-to-spleen communication. *Nature Communications*, 7:1–13, 2016. ISSN 20411723. doi: 10.1038/ncomms13035. URL <http://dx.doi.org/10.1038/ncomms13035>.
- N Carta. *Acquisition systems and decoding algorithms of peripheral neural signals for prosthetic applications*. PhD thesis, University of Cagliari, 2013.
- E Cavallaro, S Micera, P Dario, W Jensen, and T Sinkjær. On the intersubject generalization ability in extracting kinematic information from afferent nervous signals. *IEEE Transactions on Biomedical Engineering*, 50(9):1063–1073, 2003. ISSN 00189294. doi: 10.1109/TBME.2003.816075.
- M B Chancellor and E J Chartier-Kastler. Principles of Sacral Nerve Stimulation (SNS) for the treatment of bladder and urethral sphincter dysfunctions. *Neuromodulation*, 3(1):16–26, 2000. ISSN 1094-7159. doi: 10.1046/j.1525-1403.2000.00015.x.
- H S Chang, K Staras, J E Smith, and M P Gilbey. Sympathetic neuronal oscillators are capable of

- dynamic synchronization. *The Journal of neuroscience : the official journal of the Society for Neuroscience*, 19(8):3183–3197, 1999. ISSN 0270-6474.
- R B Chang, D E Strohlic, E K Williams, B D Umans, and S D Liberles. Vagal sensory neuron subtypes that differentially control breathing. *Cell*, 161(3):622–633, 2015. ISSN 10974172. doi: 10.1016/j.cell.2015.03.022. URL <http://dx.doi.org/10.1016/j.cell.2015.03.022>.
- C Chatfield. *The analysis of time series: theory and practice*. Springer, 2013.
- Z Chen. An overview of bayesian methods for neural spike train analysis. *Computational Intelligence and Neuroscience*, 2013, 2013. ISSN 16875265. doi: 10.1155/2013/251905.
- C A Chestek, V Gilja, P Nuyujukian, J D Foster, J M Fan, M T Kaufman, M M Churchland, Z Rivera-Alvidrez, J P Cunningham, S I Ryu, and K V Shenoy. Long-term stability of neural prosthetic control signals from silicon cortical arrays in rhesus macaque motor cortex. *Journal of Neural Engineering*, 8(4), 2011. ISSN 17412560. doi: 10.1088/1741-2560/8/4/045005.
- D J Chew, L Zhu, E Delivopoulos, I R Minev, K M Musick, C A Mosse, M Craggs, N Donaldson, S P Lacour, S B McMahon, and J W Fawcett. A microchannel neuroprosthesis for bladder control after spinal cord injury in rat. *Science Translational Medicine*, 5(210):155–210, 2013. ISSN 1946-6234. doi: 10.1126/scitranslmed.3007186. URL <http://stm.sciencemag.org/cgi/doi/10.1126/scitranslmed.3007186>.
- M B Christensen, H A C Wark, and D T Hutchinson. A histological analysis of human median and ulnar nerves following implantation of Utah slanted electrode arrays. *Biomaterials*, 77:235–242, 2016. ISSN 18785905. doi: 10.1016/j.biomaterials.2015.11.012. URL <http://dx.doi.org/10.1016/j.biomaterials.2015.11.012>.
- B P Christie, D M Tat, Z T Irwin, V Gilja, P Nuyujukian, J D Foster, S I Ryu, K V Shenoy, D E Thompson, and C A Chestek. Comparison of spike sorting and thresholding of voltage waveforms for intracortical brain-machine interface performance. *Journal of Neural Engineering*, 12(1), 2015. ISSN 17412552. doi: 10.1088/1741-2560/12/1/016009.
- B P Christie, M Freeberg, W D Memberg, G J C Pinault, H A Hoyer, D J Tyler, and R J Triolo. "Long-term stability of stimulating spiral nerve cuff electrodes on human peripheral nerves".

- Journal of NeuroEngineering and Rehabilitation*, 14(1):1–12, 2017. ISSN 17430003. doi: 10.1186/s12984-017-0285-3.
- K Chung and R E Coggeshall. The ratio of dorsal root ganglion cells to dorsal root axons in sacral segments of the cat. *The Journal of Comparative Neurology*, 225(1):24–30, 1984.
- L Citi, J Carpaneto, K Yoshida, K P Hoffmann, K P Koch, Paolo Dario, and S Micera. On the use of wavelet denoising and spike sorting techniques to process electroneurographic signals recorded using intraneural electrodes. *Journal of Neuroscience Methods*, 172(2):294–302, 2008. ISSN 01650270. doi: 10.1016/j.jneumeth.2008.04.025.
- N Clerc and J P Niel. Inhibition of peripheral fast synaptic inputs to celiac ganglion neurons by splanchnic preganglionic fibers in the cat. *Brain Research Bulletin*, 31(5):627–630, 1993. ISSN 03619230. doi: 10.1016/0361-9230(93)90132-U.
- J Cohen, J L Vincent, N K J Adhikari, F R Machado, D C Angus, T Calandra, K Jatton, S Giulieri, J Delaloye, S Opal, K Tracey, T van der Poll, and E Pelfrene. Sepsis: A roadmap for future research. *The Lancet Infectious Diseases*, 15(5):581–614, 2015. ISSN 15882780. doi: 10.1007/s10967-015-4001-0. URL [http://dx.doi.org/10.1016/S1473-3099\(15\)70112-X](http://dx.doi.org/10.1016/S1473-3099(15)70112-X).
- H M Coleridge and J C G Coleridge. Reflexes evoked from tracheobronchial tree and lungs. *Comprehensive Physiology*, 2010. doi: 10.1002/cphy.cp030212.
- J L Collinger, B Wodlinger, J E Downey, W Wang, E C Tyler-Kabara, D J Weber, A J C McMorland, M Velliste, M L Boninger, and A B Schwartz. High-performance neuroprosthetic control by an individual with tetraplegia. *The Lancet*, 381(9866):557–564, 2013. ISSN 01406736. doi: 10.1016/S0140-6736(12)61816-9. URL <http://linkinghub.elsevier.com/retrieve/pii/S0140673612618169>.
- B A Conway, D M Halliday, S F Farmer, U Shahani, P Maas, A I Weir, and J R Rosenberg. Synchronization between motor cortex and spinal motoneuronal pool during the performance of a maintained motor task in man. *The Journal of Physiology*, 489(3):917–924, 1995. ISSN 14697793. doi: 10.1113/jphysiol.1995.sp021104.
- S C Cork, A Eftekhari, K B Mirza, C Zuliani, K Nikolic, J V Gardiner, S R Bloom, and C Toumazou.

- Extracellular pH monitoring for use in closed-loop vagus nerve stimulation. *Journal of Neural Engineering*, 15(1), 2018. ISSN 17412552. doi: 10.1088/1741-2552/aa8239.
- T M Cover and J A Thomas. *Elements of Information Theory*. Wiley, 2005. ISBN 9780471241959. doi: 10.1002/047174882X.
- M Cracchiolo, J F Sacramento, A Mazzoni, A Panarese, J Carpaneto, S V Conde, and S Micera. Decoding neural metabolic markers from the carotid sinus nerve in a type 2 diabetes model. *IEEE Transactions on Neural Systems and Rehabilitation Engineering*, 27(10):1–1, 2019. ISSN 1534-4320. doi: 10.1109/tnsre.2019.2942398.
- G D Cramer and S A Darby. *Clinical Anatomy of the Spine, Spinal Cord, and ANS*. Mosby, 2013. ISBN 9780323079549. doi: 10.1016/C2009-0-42801-0.
- R Cueva-Rolón, E J Muñoz-Marínez, R Delgado-Lezama, and J G Raya. The cat pudendal nerve: afferent fibers responding to mechanical stimulation of the perineal skin, the vagina or the uterine cervix. *Brain Research*, 655:1–6, 1994.
- H Damon, X Barth, S Roman, and F Mion. Sacral nerve stimulation for fecal incontinence improves symptoms, quality of life and patients’ satisfaction: Results of a monocentric series of 119 patients. *International Journal of Colorectal Disease*, 28(2):227–233, 2013. ISSN 01791958. doi: 10.1007/s00384-012-1558-8.
- Z C Danziger and W M Grill. Dynamics of the sensory response to urethral flow over multiple time scales in rat. *The Journal of Physiology*, 593(15):2251–3371, 2015. ISSN 00223751. doi: 10.1113/JP270911.This.
- H A Dau, A Bagnall, K Kamgar, C M Yeh, and Y Zhu. UCR time series archive 2018. *arXiv*, 2018.
- W C de Groat. Spinal cord projections and neuropeptides in visceral afferent neurons. In F Cervero and J F B Morrison, editors, *Progress in Brain Research*, volume 67, pages 165–187. Elsevier Science Publishers B.V. (Biomedical Division), 1986. URL http://www.ncbi.nlm.nih.gov/entrez/query.fcgi?db=pubmed&cmd=Retrieve&dopt=AbstractPlus&list_uids=3823470%5Cnpapers://f0c76c90-5375-47b0-9b04-48b6fd877a16/Paper/p559.

- W C de Groat. Integrative control of the lower urinary tract: Preclinical perspective. *British Journal of Pharmacology*, 147(SUPPL. 2):25–40, 2006. ISSN 00071188. doi: 10.1038/sj.bjp.0706604.
- W C de Groat and N Yoshimura. Changes in afferent activity after spinal cord injury. *Neuourology and Urodynamics*, 29(1):63–76, 2010. ISSN 07332467. doi: 10.1002/nau.20761.
- W C de Groat, I Nadelhaft, R J Milne, A M Booth, C Morgan, and K Thor. Organization of the sacral parasympathetic reflex pathways to the urinary bladder and large intestine. *Journal of the Autonomic Nervous System*, 3(2-4):135–160, 1981. ISSN 01651838. doi: 10.1016/0165-1838(81)90059-X.
- W C de Groat, D Griffiths, and N Yoshimura. Neural control of the lower urinary tract. *Comprehensive Physiology*, 5(1):327–396, 2015. doi: 10.1002/cphy.c130056.Neural.
- S A Deuchars. How sympathetic are your spinal cord circuits? *Experimental Physiology*, 100(4):365–371, 2015.
- R A DiCaprio, C P Billimoria, and B C Ludwar. Information rate and spike-timing precision of proprioceptive afferents. *Journal of Neurophysiology*, 98(3):1706–1717, 2007. ISSN 00223077. doi: 10.1152/jn.00176.2007.
- A Diedrich, W Charoensuk, R J Brychta, Andrew C Ertl, and R Shiavi. Analysis of raw microneurographic recordings based on wavelet de-noising technique and classification algorithm: Wavelet analysis in microneurography. *IEEE Transactions on Biomedical Engineering*, 50(1):41–50, 2003. ISSN 00189294. doi: 10.1109/TBME.2002.807323.
- A C Diokno, B M Brock, M B Brown, and A R Herzog. Prevalence of urinary incontinence and other urological symptoms in the noninstitutionalized elderly. *The Journal of Urology*, 136(5):1022–5, 1986. ISSN 0022-5347. doi: 10.1016/S0022-5347(17)45194-9. URL <http://www.ncbi.nlm.nih.gov/pubmed/3490584>.
- H H Donaldson. On the temperature-sense. *Mind Association*, 10(39):399–416, 1885.
- D L Donoho. De-noising by soft thresholding. *IEEE transactions on information theory*, 43(1):613–627, 1995. ISSN 0902-4506. doi: 10.1111/ejh.12375. URL <http://www.ncbi.nlm.nih.gov/pubmed/24960424>.

- P K Dorward, S L Burke, W Jänig, and J Cassell. Reflex responses to baroreceptor, chemoreceptor and nociceptor inputs in single renal sympathetic neurones in the rabbit and the effects of anaesthesia on them. *Journal of the Autonomic Nervous System*, 18(1):39–54, 1987. ISSN 01651838. doi: 10.1016/0165-1838(87)90133-0.
- J W Downie, J A Champion, and D M Nance. A quantitative analysis of the afferent and extrinsic efferent innervation of specific regions of the bladder and urethra in the cat. *Brain Research Bulletin*, 12(6):735–740, 1984. ISSN 03619230. doi: 10.1016/0361-9230(84)90154-0.
- S A Engel, D E Rumelhart, B A Wandell, A T Lee, G H Glover, E J Chichilnisky, and M N Shadlen. fMRI of human visual cortex. *Nature*, 369(June):525, 1994.
- B D Evans and K Nikolic. From bytes to insights with modelling as a service a new paradigm for computational modelling illustrated with PyRhO. *Proceedings - 2016 IEEE Biomedical Circuits and Systems Conference, BioCAS 2016*, pages 316–319, 2016. doi: 10.1109/BioCAS.2016.7833795.
- J P Evans. Observations on the nerves of supply to the bladder and urethra of the cat, with a study of their action potentials. *The Journal of Physiology*, 86(4):396–414, 1936. ISSN 0022-3751. URL <http://www.ncbi.nlm.nih.gov/pubmed/16994767><http://www.ncbi.nlm.nih.gov/pubmedcentral.nih.gov/articlerender.fcgi?artid=PMC1394687>.
- A A Faisal, S B Laughlin, and J A White. How reliable is the connectivity in cortical neural networks? *2002 International Joint Conference on Neural Networks*, 2(February):1661–1666, 2002. doi: 10.1109/IJCNN.2002.1007767.
- C Faloutsos, M Ranganathan, and Y Manolopoulos. Fast subsequence matching in time-series databases. In *SIGMOD '94 Proceedings of the 1994 ACM SIGMOD international conference on management of data*, pages 419–429, 1994.
- J Feher. *Quantitative Human Physiology*. Academic Press, 2012. ISBN 9780123821638. doi: 10.1016/B978-0-12-382163-8.00030-X. URL <http://www.sciencedirect.com/science/article/pii/B978012382163800030X>.
- R A Fisher. *Statistical Methods for Research Workers*. Kalpaz Publications, 1925. ISBN 978-1614271666. doi: 52,281-302.

- R D Flint, E W Lindberg, L R Jordan, L E Miller, and M W Slutzky. Accurate decoding of reaching movements from field potentials in the absence of spikes. *Journal of Neural Engineering*, 9(4):1–22, 2012. doi: 10.1088/1741-2560/9/4/046006.Accurate.
- A K Fontaine, E A Gibson, J H Caldwell, and R F Weir. Optical read-out of neural activity in mammalian peripheral axons: Calcium signaling at nodes of Ranvier. *Scientific Reports*, 7(1):1–11, 2017. ISSN 20452322. doi: 10.1038/s41598-017-03541-y. URL <http://dx.doi.org/10.1038/s41598-017-03541-y>.
- R D Foreman, R W Blair, and W S Ammons. Neural Mechanisms of cardiac pain. In F Cervero and J F B Morrison, editors, *Progress in Brain Research*, Vol. 67, pages 227–243. Elsevier Science Publishers B.V. (Biomedical Division), 1986.
- C G Fox. An inverse fourier transform algorithm for generating random signals of a specified spectral form. *Computers and Geosciences*, 13(4):369–374, 1987. ISSN 00983004. doi: 10.1016/0098-3004(87)90009-4.
- M Frank. An analysis of hamster afferent taste nerve response functions. *Journal of General Physiology*, 61(5):588–618, 1973. ISSN 15407748. doi: 10.1085/jgp.61.5.588.
- F N Freeman and S Sherrington. The integrative action of the nervous system. *The Journal of Philosophy, Psychology and Scientific Methods*, 1907. ISSN 01609335. doi: 10.2307/2010953.
- U S Freitas, C Letellier, and L A Aguirre. Failure in distinguishing colored noise from chaos using the noise titration technique. *Phys Rev E Stat Nonlin Soft Matter Phys*, 79(3):2–5, 2009. doi: 10.1103/PhysRevE.79.035201.
- A S French, U Höger, S I Sekizawa, and P H Torkkeli. Frequency response functions and information capacities of paired spider mechanoreceptor neurons. *Biological Cybernetics*, 85(4):293–300, 2001. ISSN 03401200. doi: 10.1007/s004220100260.
- S Frenzel and B Pompe. Partial mutual information for coupling analysis of multivariate time series. *Physical Review Letters*, 99(20):1–4, 2007. ISSN 00319007. doi: 10.1103/PhysRevLett.99.204101.
- B D Fulcher. *Highly Comparative Time-Series Analysis*. PhD thesis, University of Oxford, 2012.

B D Fulcher. 1000 empirical time series, 2017.

B D Fulcher. Feature-based time-series analysis. In G Dong and H Liu, editors, *Feature Engineering for Machine Learning and Data Analytics*, chapter 4, pages 87–116. CRC Press, 2018.

B D Fulcher and N S Jones. Highly comparative feature-based time-series classification. *IEEE Transactions on Knowledge and Data Engineering*, 26(12):3026–3037, 2014. ISSN 10414347. doi: 10.1109/TKDE.2014.2316504.

B D Fulcher and N S Jones. hctsa: A computational framework for automated time-series phenotyping using massive feature extraction. *Cell Systems*, 5(5):527–531, 2017. ISSN 24054720. doi: 10.1016/j.cels.2017.10.001.

B D Fulcher, M A Little, and N S Jones. Highly comparative time-series analysis: the empirical structure of time series and their methods. *Journal of the Royal Society Interface*, 10(83):20130048, 2013. ISSN 1742-5662. doi: 10.1098/rsif.2013.0048.

B D Fulcher, C H Lubba, S S Sethi, and N S Jones. CompEngine: a self-organizing, living library of time-series data. (*in submission*), 2019.

J B Furness. Enteric Nervous System, 2007. URL http://www.scholarpedia.org/article/Enteric_nervous_system.

C Gabriel, R W Lau, and C Gabriel. The dielectric properties of biological tissues: III. Parameteric models for the dielectric spectrum of tissues. *Physics in Medicine and Biology*, 41:2271–2293, 1996. ISSN 0031-9155. doi: 10.1088/0031-9155/41/11/003.

M Gallio, T A Ofstad, L J Macpherson, J W Wang, and C S Zuker. The coding of temperature in the Drosophila brain. *Cell*, 144(4):614–624, 2011. ISSN 00928674. doi: 10.1016/j.cell.2011.01.028. URL <http://dx.doi.org/10.1016/j.cell.2011.01.028>.

J P Gassler and J D Bisognano. Baroreflex activation therapy in hypertension. *Journal of Human Hypertension*, 28(8):469–74, 2014. ISSN 1476-5527. doi: 10.1038/jhh.2013.139. URL <http://www.ncbi.nlm.nih.gov/pubmed/24477209>.

- L Gautron, J K Elmquist, and K W Williams. Neural control of energy balance: Translating circuits to therapies. *Cell*, 161(1):133–145, 2015. ISSN 10974172. doi: 10.1016/j.cell.2015.02.023. URL <http://dx.doi.org/10.1016/j.cell.2015.02.023>.
- R Gayet and M Guillaumie. Transmission by the vagus nerves controlling secretion of insulin. *Compte rendu des seances de la societe de biologie*, 112:1194–1197, 1933.
- M S George, H E Ward, P T Ninan, M Pollack, Z Nahas, B Anderson, S Kose, R H Howland, W K Goodman, and J C Ballenger. A pilot study of vagus nerve stimulation (VNS) for treatment-resistant anxiety disorders. *Brain Stimulation*, 1(2):112–121, 2008. ISSN 1935861X. doi: 10.1016/j.brs.2008.02.001.
- A P Georgopoulos, A B Schwartz, R E Kettner, and A B Schwartz. Neuronal population coding of movement direction. *Science*, 233(March):1416–1419, 1986. ISSN 0036-8075. doi: 10.1126/science.3749885. URL <http://dx.doi.org/10.1126/science.3749885><http://www.ncbi.nlm.nih.gov/pubmed/10479708><http://www.ncbi.nlm.nih.gov/pubmed/3749885>.
- A A Gharibans, B L Smarr, D C Kunkel, L J Kriegsfeld, H M Mousa, and T P Coleman. Artifact rejection methodology enables continuous, noninvasive measurement of gastric myoelectric activity in ambulatory subjects. *Scientific Reports*, 8(1):1–12, 2018. ISSN 20452322. doi: 10.1038/s41598-018-23302-9. URL <http://dx.doi.org/10.1038/s41598-018-23302-9>.
- M P Gilbey. Multiple Oscillators, Dynamic Synchronization and Sympathetic Control. *Experimental Biology 2000 Symposium on Differential Control of Sympathetic Outflow*, 6(April 2000):115–119, 2001. URL <http://eprints.ucl.ac.uk/9606/>.
- M P Gilbey. Sympathetic rhythms and nervous integration. *Clinical and Experimental Pharmacology and Physiology*, 34(4):356–361, 2007. ISSN 03051870. doi: 10.1111/j.1440-1681.2007.04587.x.
- W F Gillis, C A Lissandrello, J Shen, B W Pearre, A Mertiri, F Deku, S Cogan, B J Holinski, D J Chew, A E White, T M Otchy, and T J Gardner. Carbon fiber on polyimide ultra-microelectrodes. *Journal of Neural Engineering*, 15(1), 2018. ISSN 17412552. doi: 10.1088/1741-2552/aa8c88.
- L Glass, M C Mackey, and P F Zweifel. *From Clocks to Chaos: The Rhythms of Life*. Princeton University Press, 1988. doi: 10.1063/1.2811091.

- M Gola, J P Niel, R Bessone, and R Fayolle. Single-channel and whole-cell recordings from non-dissociated sympathetic neurones in rabbit coeliac ganglia. *Journal of Neuroscience Methods*, 43 (1):13–22, 1992. ISSN 01650270. doi: 10.1016/0165-0270(92)90062-I.
- E V Goodall, L M Kosterman, J Holsheimer, and J J Struijk. Modeling study of activation and propagation delays during stimulation of peripheral nerve fibers with a tripolar cuff electrode. *IEEE Transactions on Neural Systems and Rehabilitation Engineering*, 3(3):272 – 282, 1995.
- M C Gosselin, E Neufeld, H Moser, E Huber, S Farcito, L Gerber, M Jedensjo, I Hilber, F Di Genaro, B Lloyd, E Cherubini, D Szczerba, W Kainz, and N Kuster. Development of a new generation of high-resolution anatomical models for medical device evaluation: The Virtual Population 3.0. *Physics in Medicine and Biology*, 59(18):5287–5303, 2014. ISSN 13616560. doi: 10.1088/0031-9155/59/18/5287.
- T Goto, R Hatanaka, T Ogawa, A Sumiyoshi, J Riera, and R Kawashima. An evaluation of the conductivity profile in the somatosensory barrel cortex of Wistar rats. *Journal of Neurophysiology*, 104(6):3388–3412, 2010. ISSN 0022-3077. doi: 10.1152/jn.00122.2010. URL <http://jn.physiology.org/cgi/doi/10.1152/jn.00122.2010>.
- Y Grinberg, M A Schiefer, D J Tyler, and K J Gustafson. Fascicular perineurium thickness, size, and position affect model prediction of neural excitation. *IEEE Transactions on Neural Systems and Rehabilitation Engineering*, 16(6):572–581, 2008. doi: 10.1109/TNSRE.2008.2010348.Fascicular.
- D Guiraud, D Andreu, S Bonnet, G Carrault, P Couderc, A Hagege, C Henry, A Hernandez, N Karam, Rolle Le V, P Mabo, P Maciejasz, C H Malbert, E Marijon, S Maubert, C Picq, O Rossel, and J L Bonnet. Vagus nerve stimulation: state of the art of stimulation and recording strategies to address autonomic function neuromodulation\4611. *J. Neural Eng*, 13(4):41002, 2016. doi: 10.1088/1741-2560/13/4/041002[doi]. URL <http://www.ncbi.nlm.nih.gov/pubmed/27351347>.
- H J Häbler, W Jänig, and M Koltzenburg. Myelinated primary afferent of the sacral spinal cord resopnding to slow filling and distension of the cat urinary bladder. *Journal of Physiology*, 463: 449–460, 1993.
- D. M. Halliday and J. R. Rosenberg. On the application, estimation and interpretation of coher-

- ence and pooled coherence. *Journal of Neuroscience Methods*, 100(1-2):173–174, 2000. ISSN 01650270. doi: 10.1016/S0165-0270(00)00267-3.
- R M Hallock and P M Di Lorenzo. Temporal coding in the gustatory system. *Neuroscience and Biobehavioral Reviews*, 30(8):1145–1160, 2006. ISSN 01497634. doi: 10.1016/j.neubiorev.2006.07.005.
- G Haldnes, T Mäki-Marttunen, D Keller, K H Pettersen, O A Andreassen, and G T Einevoll. Effect of ionic diffusion on extracellular potentials in neural tissue. *PLoS Computational Biology*, 12(11):1–38, 2016. ISSN 15537358. doi: 10.1371/journal.pcbi.1005193.
- M S Hämäläinen, R Hari, R J Ilmoniemi, J Knuutila, and O V Lounasmaa. Magnetoencephalography - theory, instrumentation, and applications to noninvasive studies of the working human brain. *Reviews of Modern Physics*, 65(2):413–505, 1993. ISSN 00346861. doi: 10.1103/RevModPhys.65.413.
- N Hammer, S Löffler, Y O Cakmak, B Ondruschka, U Planitzer, M Schultz, D Winkler, and D Weise. Cervical vagus nerve morphometry and vascularity in the context of nerve stimulation - A cadaveric study. *Scientific Reports*, 8(1):1–9, 2018. ISSN 20452322. doi: 10.1038/s41598-018-26135-8.
- J E Hardebo. Influence of impulse pattern on noradrenaline release from sympathetic nerves in cerebral and some peripheral vessels. *Acta Physiologica Scandinavica*, 144(3):333–9, 3 1992. ISSN 0001-6772. doi: 10.1111/j.1748-1716.1992.tb09302.x. URL <http://www.ncbi.nlm.nih.gov/pubmed/1585816>.
- T Hastie, R Tibshirani, and J Friedman. The Elements of Statistical Learning. *Elements*, 1:337–387, 2009. ISSN 03436993. doi: 10.1007/b94608. URL <http://www.springerlink.com/index/10.1007/b94608>.
- M L Hines and N T Carnevale. The NEURON simulation environment. *Neural Computation*, 9(6):1179–1209, 1997. ISSN 0899-7667. doi: 10.1162/neco.1997.9.6.1179.
- M L Hines, A P Davison, and E Muller. NEURON and Python. *Frontiers in Neuroinformatics*, 3(1), 2009. ISSN 1662-5196. doi: 10.3389/neuro.11.001.2009.

- L R Hochberg, M D Serruya, G M Friebs, J A Mukand, M Saleh, A H Caplan, A Branner, D Chen, R D Penn, and J P Donoghue. Neuronal ensemble control of prosthetic devices by a human with tetraplegia. *Nature*, 442(7099):164–171, 2006. ISSN 0028-0836. doi: 10.1038/nature04970. URL <http://www.nature.com/doifinder/10.1038/nature04970>.
- A L Hodgkin and A F Huxley. A quantitative description of membrane current and its application to conduction and excitation in nerves. *Journal of Physiology*, 117:500–544, 1952. ISSN 0022-3751. doi: 10.1016/S0092-8240(05)80004-7.
- S Holm. A simple sequentially rejective multiple test procedure. *Scandinavian Journal of Statistics*, 6:65–70, 1979. ISSN 03036898. doi: 10.2307/4615733.
- G R Holt and C Koch. Electrical interactions via the extracellular potential near cell bodies. *Journal of Computational Neuroscience*, 6(2):169–184, 1999. ISSN 09295313. doi: 10.1023/A:1008832702585.
- F Hoppensteadt. Predator-prey model. *Scholarpedia*, 1(10):1563, 2006.
- T Hosman, M Vilela, D Milstein, J N Kelemen, D M Brandman, L R Hochberg, and J D Simeral. BCI decoder performance comparison of an LSTM recurrent neural network and a Kalman filter in retrospective simulation. *International IEEE/EMBS Conference on Neural Engineering, NER*, pages 1066–1071, 2019. ISSN 19483554. doi: 10.1109/NER.2019.8717140.
- D H Hubel and T N Wiesel. Receptive fields, binocular interaction and functional architecture in the cat’s visual cortex. *The Journal of Physiology*, 160(1):106–154, 1962. ISSN 14697793. doi: 10.1113/jphysiol.1962.sp006837.
- R J Hyndman, E Wang, and N Laptev. Large-scale unusual time series detection. *Proceedings - 15th IEEE International Conference on Data Mining Workshop, ICDMW 2015*, pages 1616–1619, 2016. ISSN 2375-9259. doi: 10.1109/ICDMW.2015.104.
- R J Hyndman, E Wang, Y Kang, T Talagala, and S B Taieb. tsfeatures: Time Series Feature Extraction, 2019. URL <https://github.com/robjhyndman/tsfeatures>.
- B Y A Iggo. Tension receptors in the stomach and the urinary bladder. *Journal of Physiology*, 128: 593–607, 1955.

- J S R Jang and C T Sun. Neuro-fuzzy modeling and control. *Proceedings of the IEEE*, 83(3):378–406, 1995. ISSN 00189219. doi: 10.1109/5.364486.
- W Jänig. Pre- and postganglionic vasoconstrictor neurons: differentiation, types, and discharge properties. *Annual Review of Physiology*, 50(57):525–39, 1988. ISSN 0066-4278. doi: 10.1146/annurev.ph.50.030188.002521. URL <http://www.ncbi.nlm.nih.gov/pubmed/3288104>.
- W Jänig. *The Integrative Action of the Autonomic Nervous System - Neurobiology of Homeostasis*. Cambridge University Press, 2006. ISBN 9780521845182.
- W Jänig and M Koltzenburg. Receptive properties of sacral primary afferent neurons supplying the colon. *Journal of Neurophysiology*, 65(5):1067–1077, 2017. ISSN 0022-3077. doi: 10.1152/jn.1991.65.5.1067.
- W Jänig and H Kümmel. Functional discrimination of postganglionic neurones to the cat's hind-paw with respect to the skin potentials recorded from the hairless skin. *Pflügers Archiv European Journal of Physiology*, 371(3):217–225, 1977. ISSN 00316768. doi: 10.1007/BF00586261.
- W Jänig and J F B Morrison. Functional properties of spinal visceral afferents supplying abdominal and pelvic organs, with special emphasis on visceral nociception. In F Cervero and J F B Morrison, editors, *Progress in Brain Research*, Vol. 67, pages 87–113. Elsevier Science Publishers B.V. (Biomedical Division), 1986.
- B J Janssen, S C Malpas, S L Burke, and G A Head. Frequency-dependent modulation of renal blood flow by renal nerve activity in conscious rabbits. *American Journal of Physiology - Regulatory, Integrative and Comparative Physiology*, 273(2), 1997. URL <http://ajpregu.physiology.org/content/273/2/R597>.
- S Jezernik, W M Grill, and T Sinkjaer. Detection and inhibition of hyperreflexialike bladder contractions in the cat by sacral nerve root recording and electrical stimulation. *Neurourology and Urodynamics: Official Journal of the International Continence Society*, 20(2):215–230, 2001.
- R S Johansson and I Birznieks. First spikes in ensembles of human tactile afferents code complex spatial fingertip events. *Nature Neuroscience*, 7(2):170–177, 2004. ISSN 10976256. doi: 10.1038/nn1177.

- D A Johnson and D Purves. Post-natal reduction of neural unit size in the rabbit ciliary ganglion. *Journal of Physiology*, 318:143–159, 1981. ISSN 14697793. doi: 10.1113/jphysiol.1981.sp013855. URL <http://www.ncbi.nlm.nih.gov/pubmed/7320886>.
- L A Jones and A M Smith. Tactile sensory system: Encoding from the periphery to the cortex. *Wiley Interdisciplinary Reviews: Systems Biology and Medicine*, 6(3):279–287, 2014. ISSN 1939005X. doi: 10.1002/wsbm.1267.
- C Julien. The enigma of Mayer waves: Facts and models. *Cardiovascular Research*, 70(1):12–21, 2006. ISSN 00086363. doi: 10.1016/j.cardiores.2005.11.008.
- R E Kalman and R S Bucy. New results in linear filtering and prediction theory. *Journal of Basic Engineering*, 83(1):95–108, 1961. ISSN 1528901X. doi: 10.1115/1.3658902.
- R Karam, D Bourbeau, S Majerus, I Makovey, H B Goldman, M S Damaser, and Swarup Bhunia. Real-time classification of bladder events for effective diagnosis and treatment of urinary incontinence. *IEEE Transactions on Biomedical Engineering*, 63(4):721–729, 2016. ISSN 15582531. doi: 10.1109/TBME.2015.2469604.
- P R Kennedy, R A Bakay, M M Moore, K Adams, and J Goldwithe. Direct control of a computer from the human central nervous system. *IEEE transactions on rehabilitation engineering : a publication of the IEEE Engineering in Medicine and Biology Society*, 8(2):198–202, 2000. ISSN 1063-6528. doi: 10.1109/86.847815.
- A R Kent and W M Grill. Model-based analysis and design of nerve cuff electrodes for restoring bladder function by selective stimulation of the pudendal nerve. *Journal of Neural Engineering*, 10(3), 2013. ISSN 17412560. doi: 10.1088/1741-2560/10/3/036010.
- A Khurram, S E Ross, Z J Sperry, A Ouyang, C Stephan, A A Jiman, and T M Bruns. Chronic monitoring of lower urinary tract activity via a sacral dorsal root ganglia interface. *Journal of Neural Engineering*, 14(3):215–225, 2017. ISSN 1527-5418. doi: 10.1097/NCN.0b013e3181a91b58. Exploring.
- B Klevmark. Natural pressure-volume curves and conventional cystometry. *Scandinavian Journal of Urology and Nephrology*, 33(201):1–4, 2002. ISSN 0036-5599. doi: 10.1080/003655999750169358.

- T H Koeze. Muscle spindle afferent studies in the baboon. *Journal of Physiology*, 229:297–317, 1973.
- F A Koopman, S S Chavan, S Miljko, S Grazio, S Sokolovic, P R Schuurman, A D Mehta, Y A Levine, M Faltys, R Zitnik, K J Tracey, and P P Tak. Vagus nerve stimulation inhibits cytokine production and attenuates disease severity in rheumatoid arthritis. *Proceedings of the National Academy of Sciences of the United States of America*, 113(29):8284–9, 2016. ISSN 1091-6490. doi: 10.1073/pnas.1605635113. URL <http://www.pnas.org/lookup/doi/10.1073/pnas.1605635113><http://www.ncbi.nlm.nih.gov/pubmed/27382171><http://www.pubmedcentral.nih.gov/articlerender.fcgi?artid=PMC4961187>.
- K Kostarelos, M Vincent, C Hebert, and J A Garrido. Graphene in the design and engineering of next-generation neural interfaces, 2017. ISSN 15214095.
- N H Kostick. *Novel carbon-nanotube based neural interface for chronic recording of glossopharyngeal nerve activity*. PhD thesis, Case Western Reserve University, 2018. URL https://etd.ohiolink.edu/!etd.send_file?accession=case1517920588275806&disposition=inline.
- S Koyama, S M Chase, A S Whitford, M Velliste, A B Schwartz, and R E Kass. Comparison of brain-computer interface decoding algorithms in open-loop and closed-loop control. *Journal of Computational Neuroscience*, 29(1-2):73–87, 2010. ISSN 0929-5313. doi: 10.1007/s10827-009-0196-9. URL <http://link.springer.com/10.1007/s10827-009-0196-9>.
- A Kraskov, H Stögbauer, and P Grassberger. Estimating mutual information. *Physical Review E*, 69(6 2):1–16, 2004. ISSN 15393755. doi: 10.1103/PhysRevE.69.066138.
- A Kraskov, H Stögbauer, R G Andrzejak, and P Grassberger. A hierarchical clustering based on mutual information maximization. *Europhysics Letters*, 70(2):1–11, 2005. ISSN 15224880. doi: 10.1109/ICIP.2007.4378945.
- G Krzysztow, A Bugajski, M Kurnik-Lucka, and P G Thor. Electrical vagus nerve stimulation decreases food consumption and weight gain in rats fed a high-fat diet. *Journal of Physiology and Pharmacology*, 62(6):637–646, 2011. ISSN 1899-1505. URL <http://www.ncbi.nlm.nih.gov/pubmed/22314566>.

- L Kubin, G F Alheid, E J Zuperku, and D R McCrimmon. Central pathways of pulmonary and lower airway vagal afferents. *Journal of Applied Physiology*, 101(2):618–627, 2006. ISSN 8750-7587. doi: 10.1152/japplphysiol.00252.2006. URL <http://www.physiology.org/doi/10.1152/japplphysiol.00252.2006>.
- L LaFleur and P Yager. Biomaterials Science. In B D Ratner, A S Hoffman, F J Schoen, and J E Lemons, editors, *Applications of Biomaterials*, chapter Medical bi, pages 996–1006. Academic Press, 2013.
- J N Langley. *The Autonomic Nervous System. Part I*. Cambridge: W. Heffer, 1921.
- G Lanzani. Materials for bioelectronics: Organic electronics meets biology. *Nature Materials*, 13(8): 775–776, 2014. ISSN 14764660. doi: 10.1038/nmat4021. URL <http://dx.doi.org/10.1038/nmat4021>.
- S M Lawrence, G S Dhillon, W Jensen, K Yoshida, and K W Horch. Acute peripheral nerve recording characteristics of of polymer-based longitudinal intrafascicular electrodes. *Rehabilitation*, 12(3): 345–348, 2004.
- S Lee, W Y X Peh, J Wang, F Yang, J S Ho, N V Thakor, S C Yen, and C Lee. Toward Bioelectronic Medicine - Neuromodulation of Small Peripheral Nerves Using Flexible Neural Clip. *Advanced Science*, 4(11), 2017a. ISSN 21983844. doi: 10.1002/advs.201700149.
- S Lee, S Sheshadri, Z Xiang, I Delgado-Martinez, N Xue, T Sun, N V Thakor, S C Yen, and C Lee. Selective stimulation and neural recording on peripheral nerves using flexible split ring electrodes. *Sensors and Actuators, B: Chemical*, 242:1165–1170, 2017b. ISSN 09254005. doi: 10.1016/j.snb.2016.09.127. URL <http://dx.doi.org/10.1016/j.snb.2016.09.127>.
- R Levins. The effect of random variations of different types on population growth. *Proceedings of the National Academy of Sciences of the United States of America*, 62(4):1061–1065, 1969. ISSN 00278424. doi: 10.1073/pnas.62.4.1061.
- M S Lewicki. A review of methods for spike sorting: the detection and classification of neural action potentials. *Network*, 9(4):R53–R78, 1998. ISSN 0954-898X. doi: 10.1088/0954-898X/9/4/001.

- M J Lewis, A L Short, and K E Lewis. Autonomic nervous system control of the cardiovascular and respiratory systems in asthma. *Respiratory Medicine*, 100(10):1688–1705, 2006. ISSN 09546111. doi: 10.1016/j.rmed.2006.01.019.
- Z Li, J E O’Doherty, T L Hanson, M A Lebedev, C S Henriquez, and M A L Nicolelis. Unscented Kalman filter for brain-machine interfaces. *PLoS ONE*, 4(7):e6243, 2009. ISSN 1932-6203. doi: 10.1371/journal.pone.0006243. URL <http://dx.plos.org/10.1371/journal.pone.0006243>.
- J W Lichtman. The reorganization of synaptic connexions in the rat submandibular ganglion during post-natal development. *Journal of Physiology*, 273(1):155–177, 1977. ISSN 0022-3751. doi: 10.1113/jphysiol.1977.sp012087.
- H Lindén, E Hagen, S Leski, E S Norheim, K H Pettersen, and G T Einevoll. LFPy: a tool for biophysical simulation of extracellular potentials generated by detailed model neurons. *Frontiers in Neuroinformatics*, 7(41), 2014. ISSN 1662-5196. doi: 10.3389/fninf.2013.00041. URL <http://journal.frontiersin.org/article/10.3389/fninf.2013.00041/abstract>.
- J Lines and A Bagnall. Time series classification with ensembles of elastic distance measures. *Data Mining and Knowledge Discovery*, 29(3):565–592, 2015. ISSN 13845810. doi: 10.1007/s10618-014-0361-2.
- C A Lissandrello, W F Gillis, J Shen, B W Pearre, F Vitale, M Pasquali, B J Holinski, D J Chew, A E White, and T J Gardner. A micro-scale printable nanoclip for electrical stimulation and recording in small nerves. *Journal of Neural Engineering*, 14(3), 2017. ISSN 17412552. doi: 10.1088/1741-2552/aa5a5b.
- J T Lizier. JIDT: An information-theoretic toolkit for studying the dynamics of complex systems. *Frontiers in Robotics and AI*, 1(December):1–20, 2014. ISSN 2296-9144. doi: 10.3389/frobt.2014.00011. URL <http://arxiv.org/abs/1408.3270><http://dx.doi.org/10.3389/frobt.2014.00011>.
- S Löffler, K Melican, K P R Nilsson, and A Richter-Dahlfors. Organic bioelectronics in medicine. *Journal of Internal Medicine*, pages 1–13, 2017. ISSN 13652796. doi: 10.1111/joim.12595.

- T E Lohmeier and J E Hall. Device-based neuromodulation for resistant hypertension therapy. *Circulation Research*, 124(7):1071–1093, 2019. ISSN 15244571. doi: 10.1161/CIRCRESAHA.118.313221.
- E N Lorenz. Deterministic nonperiodic flow. *Journal of the atmospheric sciences*, 20(2):130–141, 1963. ISSN 0022-4928. doi: 10.1201/9780203734636.
- S Luan, I Williams, K Nikolic, and T G Constandinou. Neuromodulation: Present and emerging methods. *Frontiers in Neuroengineering*, 7(JUL):1–9, 2014. ISSN 16626443. doi: 10.3389/fneng.2014.00027.
- C H Lubba, E Mitrani, J Hokanson, W M Grill, and S R Schultz. Real-time decoding of bladder pressure from pelvic nerve activity. *IEEE EMBS Conference on Neural Engineering*, 1:617–620, 2017.
- C H Lubba, Y Le Guen, S Jarvis, N S Jones, S C Cork, A Eftekhari, and S R Schultz. PyPNS: Multiscale simulation of a peripheral nerve in Python. *Neuroinformatics*, 17(1):63–81, 2018. ISSN 15392791. doi: 10.1007/s12021-018-9383-z. URL <https://doi.org/10.1007/s12021-018-9383-z>.
- C H Lubba, S S Sethi, P Knaute, S R Schultz, B D Fulcher, and N S Jones. catch22: CAnonical Time-series CHaracteristics: Selected through highly comparative time-series analysis. *Data Mining and Knowledge Discovery*, 33(6):1821–1852, 2019. ISSN 1573756X. doi: 10.1007/s10618-019-00647-x. URL <https://doi.org/10.1007/s10618-019-00647-x>.
- Q Ma. Labeled lines meet and talk: Population coding of somatic sensations. *Journal of Clinical Investigation*, 120(11):3773–3778, 2010. ISSN 00219738. doi: 10.1172/JCI43426.
- V G Macefield, B G Wallin, and A B Vallbo. The discharge behaviour of single vasoconstrictor motoneurons in human muscle nerves. *The Journal of Physiology*, 481(1994):799–809, 1994. ISSN 0022-3751. doi: 10.1113/jphysiol.1994.sp020482. URL <http://www.pubmedcentral.nih.gov/articlerender.fcgi?artid=1155919&tool=pmcentrez&rendertype=abstract>.
- V G Macefield, B Rundqvist, Y B Sverrisdottir, B G Wallin, and M Elam. Firing properties of single muscle vasoconstrictor neurons in the sympathoexcitation associated with congestive heart failure [In Process Citation]. *Circulation*, 100(16):1708–1713, 1999.

- M C Mackey and L Glass. Oscillation and chaos in physiological control systems. *Science*, 197 (4300):287–289, 1977.
- S J A Majerus, P C Fletter, E K Ferry, H Zhu, K Gustafson, and M S Damaser. Suburothelial bladder contraction detection with implanted pressure sensor. *PLoS ONE*, 12(1):1–16, 2017. ISSN 19326203. doi: 10.1371/journal.pone.0168375.
- B D Malamud and D L Turcotte. Self-Affine Time Series: I. Generation and Analyses. *Advances in Geophysics*, 40:1–90, 1999. ISSN 00652687. doi: 10.1016/S0065-2687(08)60293-9.
- A Malhotra. Hypoglossal-nerve stimulation for obstructive sleep apnea. *The New England Journal of Medicine*, 370(2):170–171, 2014. ISSN 15378276. doi: 10.1016/j.dcn.2011.01.002.The.
- J Malmivuo and R Plonsey. *Bioelectromagnetism: Principles and applications of bioelectric and biomagnetic Fields*. Oxford university press, 1995. ISBN 9780199847839. doi: 10.1093/acprof:oso/9780195058239.001.0001.
- S C Malpas. The rhythmicity of sympathetic nerve activity. *Progress in Neurobiology*, 56(1):65–96, 1998. ISSN 0301-0082.
- M D Mann. Chapter 12: Peripheral Nerves, 2019. URL <http://michaeldmann.net/mann12.html>.
- M O Martel, P H Finan, A J Dolman, R R Edwards, A D Wasan, and N Robert. Self-reports of medication side effects and pain-related activity interference in patients with chronic pain: a longitudinal cohort study. *Pain*, 156(6):1092–1100, 2015. doi: 10.1097/j.pain.000000000000154.Self-reports.
- O G Martinsen, S Grimmes, and H P Schwan. Interface phenomena and dielectric properties of biological tissue. In P Somasundaran, editor, *Encyclopedia of Surface and Colloid Science*, pages 2643–2652. CRC Press, 3 edition, 2002.
- R M May. Limit cycles in predator-prey communities. *Science*, 177(4052):900–902, 1972.
- R M May. Simple mathematical models with very complicated dynamics. *Nature*, 261(1): 459, 1976. URL <https://www-nature-com.accesdistant.sorbonne-universite.fr/articles/261459a0.pdf>.

- R M McAllen and S C Malpas. Sympathetic burst activity: characteristics and significance. *Clinical and Experimental Pharmacology and Physiology*, 24(11):791–799, 1997. ISSN 0305-1870. doi: 10.1111/j.1440-1681.1997.tb02693.x.
- G A McCallum, X Sui, C Qiu, J Marmerstein, Y Zheng, T E Eggers, C Hu, L Dai, and D M Durand. Chronic interfacing with the autonomic nervous system using carbon nanotube (CNT) yarn electrodes. *Scientific Reports*, 7(1):1–14, 2017. ISSN 20452322. doi: 10.1038/s41598-017-10639-w. URL <http://dx.doi.org/10.1038/s41598-017-10639-w>.
- L K McCorry. Physiology of the autonomic nervous system. *Acta Anaesthesiologica Scandinavica*, 8(4):17–20, 1964. ISSN 13996576. doi: 10.1111/j.1399-6576.1964.tb00252.x.
- L M McCracken, J Hoskins, and C Eccleston. Concerns about medication and medication use in chronic pain. *Journal of Pain*, 7(10):726–734, 2006. ISSN 15265900. doi: 10.1016/j.jpain.2006.02.014.
- C C McIntyre, A G Richardson, and W M Grill. Modeling the excitability of mammalian nerve fibers: Influence of afterpotentials on the recovery cycle. *Journal of Neurophysiology*, 87(2):995–1006, 2002. ISSN 0022-3077. doi: 10.1152/jn.00353.2001.
- T G McNaughton and K W Horch. Action potential classification with dual channel intrafascicular electrodes. *IEEE transactions on bio-medical engineering*, 41(7):609–616, 1994. ISSN 0018-9294. doi: 10.1109/10.301727.
- D R McNeal. Analysis of a model for excitation of myelinated nerve. *IEEE Transactions on Biomedical Engineering*, 23(4):329–337, 1976.
- R L Meckler and L C Weaver. Characteristics of ongoing and reflex discharge of single splenic and renal sympathetic postganglionic fibres in cats. *Journal of Physiology*, 396(1):139–153, 1988.
- P Mehrotra. Biosensors and their applications - A review, 5 2016. ISSN 22124268.
- A Mendez and M Sawan. A custom signal processor based neuroprosthesis intended to recover urinary bladder functions. *Proceedings - IEEE International Symposium on Circuits and Systems*, pages 1608–1611, 2014. ISSN 02714310. doi: 10.1109/ISCAS.2014.6865458.

- A Mendez, M Sawan, T Minagawa, and J J Wyndaele. Estimation of bladder volume from afferent neural activity. *IEEE Transactions on Neural Systems and Rehabilitation Engineering*, 21(5):704–715, 2013. ISSN 15344320. doi: 10.1109/TNSRE.2013.2266899.
- J Meregnani, D Clarençon, M Vivier, A Peinnequin, C Mouret, V Sinniger, C Picq, A Job, F Canini, M Jacquier-Sarlin, and B Bonaz. Anti-inflammatory effect of vagus nerve stimulation in a rat model of inflammatory bowel disease. *Autonomic Neuroscience : Basic & Clinical*, 160(1-2):82–89, 2011. ISSN 1872-7484. doi: 10.1016/j.autneu.2010.10.007.
- B Metcalfe, D Chew, C Clarke, N Donaldson, and J Taylor. Fibre-selective discrimination of physiological ENG using velocity selective recording: report on pilot rat experiments. *Annual International Conference of the IEEE Engineering in Medicine and Biology Society*, pages 2645–2648, 2014. ISSN 1557170X. doi: 10.1109/EMBC.2014.6944166.
- S Micera, W Jensen, F Sepulveda, R R Riso, and T Sinkjær. Neuro-fuzzy extraction of angular information from muscle afferents for ankle control during standing in paraplegic subjects: An animal model. *IEEE Transactions on Biomedical Engineering*, 48(7):787–794, 2001. ISSN 00189294. doi: 10.1109/10.930903.
- S Micera, L Citi, J Rigosa, J Carpaneto, S Raspopovic, G Di Pino, L Rossini, K Yoshida, L Denaro, P Dario, and P M Rossini. Decoding information from neural signals recorded using intraneural electrodes: Toward the development of a neurocontrolled hand prosthesis. *Proceedings of the IEEE*, 98(3):407–417, 2010. ISSN 00189219. doi: 10.1109/JPROC.2009.2038726.
- J E Mietus. The pNNx files: re-examining a widely used heart rate variability measure. *Heart*, 88(4):378–380, 2002. ISSN 00070769. doi: 10.1136/heart.88.4.378.
- A H Milby, C H Halpern, and G H Baltuch. Vagus nerve stimulation for epilepsy. *Drug and Therapeutics Bulletin*, 48(4):42–45, 2010. ISSN 0012-6543. doi: 10.1136/dtb.2010.02.0015.
- I Milsom, K S Coyne, S Nicholson, M Kvasz, C I Chen, and A J Wein. Global prevalence and economic burden of urgency urinary incontinence: A systematic review. *European Urology*, 65(1):79–95, 1 2014. ISSN 03022838. doi: 10.1016/j.eururo.2013.08.031.
- Y-S Moon, K-Y Whang, and W-K Loh. Duality-based subsequence matching in time-series databases.

- Proceedings 17th International Conference on Data Engineering*, pages 263–272, 2001. ISSN 1063-6382. doi: 10.1109/ICDE.2001.914837.
- F Mörchen. Time series feature extraction for data mining using DWT and DFT. *Technical Report*, 33, 2003.
- J F Morrison. The physiological mechanisms involved in bladder emptying. *Scandinavian Journal of Urology and Nephrology Supplementary*, 184:15–18, 1997.
- G Nagel, D Ollig, M Fuhrmann, S Kateriya, A Maria, E Bamberg, P Hegemann, G Nagelt, D Ollig, M Fuhrmann, S Kateriya, A M Musti, E Bamberg, and P Hegemann. Channelrhodopsin-1 : A light-gated proton channel in green algae. *Science*, 296(5577):2395–2398, 2002.
- Y Nakahira. *Connecting the speed-accuracy trade-offs in sensorimotor control and neurophysiology reveals diversity sweet spots in layered control architectures*. PhD thesis, Caltech, 2019.
- Y Nakahira, N Matni, and J C Doyle. Hard limits on robust control over delayed and quantized communication channels with applications to sensorimotor control. In *Conference on Decision and Control (CDC)*, pages 7522–7529, 2015. ISBN 9781479978854.
- Y Nakahira, Q Liu, T J Sejnowski, and J C Doyle. Fitts’ Law for speed-accuracy trade-off is a diversity sweet spot in sensorimotor control. *arXiv*, pages 1–17, 2019. URL <http://arxiv.org/abs/1906.00905>.
- A Nanopoulos, R J Alcock, and Y Manolopoulos. Feature-based classification of time-series data. *International Journal of Computer Research*, 10(3), 2001.
- P M Narins and C M Hillery. Frequency coding in the inner ear of anuran amphibians. In *HEARING Physiological Bases and Psychophysics*, pages 70–76. Springer, 1938. doi: 10.1007/978-3-642-69257-4_{ }11.
- A I Nascimento, F M Mar, and M M Sousa. The intriguing nature of dorsal root ganglion neurons: Linking structure with polarity and function. *Progress in Neurobiology*, 168(December 2017):86–103, 2018. ISSN 18735118. doi: 10.1016/j.pneurobio.2018.05.002. URL <https://doi.org/10.1016/j.pneurobio.2018.05.002>.

- X Navarro, T B Krueger, N Lago, S Micera, T Stieglitz, and P Dario. A critical review of interfaces with the peripheral nervous system for the control of neuroprostheses and hybrid bionic systems. *J Peripher Nerv Syst*, 10:229–258, 2005. ISSN 1085-9489. doi: 10.1111/j.1085-9489.2005.10303.x.
- A M Neishabouri and A Faisal. The metabolic efficiency of myelinated vs unmyelinated axons. *BMC Neuroscience*, 12(Suppl 1):P100, 2011. ISSN 1471-2202. doi: 10.1186/1471-2202-12-S1-P100. URL <http://www.biomedcentral.com/1471-2202/12/S1/P100>.
- M A Neishabouri. *Engineering Design Principles of Neural Fibres*. PhD thesis, Imperial College London, 2014.
- C Nicholson and J A Freeman. Theory of current source-density analysis and determination of conductivity tensor for anuran cerebellum. *Journal of Neurophysiology*, 38(2):356–368, 1975. ISSN 0022-3077. doi: 10.1121/1.3569737.
- I Ninomiya, T Akiyama, and N Nishiura. Mechanism of cardiac-related synchronized cardiac sympathetic nerve activity in awake cats. *American Journal of Physiology*, 259(3 Pt 2):499–506, 1990. ISSN 00029513. URL <http://ajpregu.physiology.org/content/259/3/R499><http://www.ncbi.nlm.nih.gov/pubmed/2396708><http://ajpregu.physiology.org/content/259/3/R499.full.pdf>.
- V W Nitti. The prevalence of urinary incontinence. *Reviews in Urology*, 3(Suppl. 1):S2 – S6, 2001. ISSN 14730804. doi: 10.1080/13697137.2018.1543263.
- J E O’Doherty, M A Lebedev, P J Ifft, K Z Zhuang, S Shokur, H Bleuler, and M A L Nicolelis. Active tactile exploration using a brain-machine-brain interface. *Nature*, 479(7372):228–231, 2011. ISSN 0028-0836. doi: 10.1038/nature10489. URL <http://www.nature.com/doifinder/10.1038/nature10489>.
- Y Ootsuka, T Xu, and N Terui. The spinally mediated 10-Hz rhythm in the sympathetic nerve activity of cats. *Journal of the Autonomic Nervous System*, 54(2):89–103, 1995. ISSN 01651838. doi: 10.1016/0165-1838(94)00194-O.
- J S Ordóñez, V Píkov, H Wiggins, C Patten, T Stieglitz, J Rickert, and M Schuettler. Cuff electrodes for very small diameter nerves – prototyping and first recordings in vivo. *Annual International*

- Conference of the IEEE Engineering in Medicine and Biology Society*, pages 6846–6849, 2014. ISSN 1557170X. doi: 10.1109/EMBC.2014.6945201.
- Z Ouyang, Z J Sperry, N D Barrera, and T M Bruns. Real-time bladder pressure estimation for closed-loop control in a detrusor overactivity model. *IEEE Transactions on Neural Systems and Rehabilitation Engineering*, 27(6):1209–1216, 2019. ISSN 1534-4320. doi: 10.1109/TNSRE.2019.2912374. URL <https://ieeexplore.ieee.org/document/8695082/>.
- S Panzeri and S R Schultz. A unified approach to the study of temporal, correlational, and rate coding. *Neural Computation*, 13:1311–1349, 2001.
- S Panzeri, S R Schultz, A Treves, and E T Rolls. Correlations and the encoding of information in the nervous system. *Proceedings of the Royal Society of London. Series B: Biological Sciences*, 266(1423):1001–1012, 1999.
- Y A Patel, A Willsie, I P Clements, R Aguilar, S Rajaraman, and R J Butera. Microneedle cuff electrodes for extrafascicular peripheral nerve interfacing. *Proceedings of the Annual International Conference of the IEEE Engineering in Medicine and Biology Society, EMBS*, 2016-Octob:1741–1744, 2016. ISSN 1557170X. doi: 10.1109/EMBC.2016.7591053.
- W Y X Peh, M N Raczkowska, Y Teh, M Alam, N V Thakor, and S C Yen. Closed-loop stimulation of the pelvic nerve for optimal micturition. *Journal of Neural Engineering*, 15(6), 2018. ISSN 17412552. doi: 10.1088/1741-2552/aadee9.
- J A Perge, K Koch, R Miller, P Sterling, and V Balasubramanian. How the optic nerve allocates space, energy capacity, and information. *J Neurosci*, 29(24):7917–7928, 2009. ISSN 1529-2401. doi: 10.1523/JNEUROSCI.5200-08.2009.How.
- J A Perge, J E Niven, E Mugnaini, V Balasubramanian, and P Sterling. Why do axons differ in caliber? *The Journal of Neuroscience*, 32(2):626–638, 2012. ISSN 0270-6474. doi: 10.1523/JNEUROSCI.4254-11.2012. URL <http://www.pubmedcentral.nih.gov/articlerender.fcgi?artid=3571697&tool=pmcentrez&rendertype=abstract%5Cnhttp://dx.doi.org/10.1523/?JNEUROSCI.4254-11.2012>.
- E Perra, A Rapeaux, and K Nikolic. The crucial role of nerve depolarisation in high frequency conduction block in mammalian nerves: Simulation study. *Proceedings of the Annual International*

- Conference of the IEEE Engineering in Medicine and Biology Society, EMBS*, 2018-July:2214–2217, 2018. ISSN 1557170X. doi: 10.1109/EMBC.2018.8512759.
- C Pfaffmann. The afferent code for sensory quality. *American Psychologist*, 14(5):226–232, 1959. ISSN 0003-066X. doi: 10.1037/h0049324.
- D T T Plachta, J Sonnenfeld, O Cota, and T Stieglitz. A virtual workbench for peripheral electrode design. *Automatisierungstechnische Verfahren für die Medizin*, 17(286):62–63, 2012.
- D T T Plachta, M Gierthmuehlen, O Cota, N Espinosa, F Boeser, T C Herrera, T Stieglitz, and J Zentner. Blood pressure control with selective vagal nerve stimulation and minimal side effects. *Journal of Neural Engineering*, 11(3):036011, 2014. ISSN 1741-2552. doi: 10.1088/1741-2560/11/3/036011. URL <http://www.ncbi.nlm.nih.gov/pubmed/24809832>.
- J Pods. A comparison of computational models for the extracellular potential of neurons. *Journal of Integrative Neuroscience*, 16(1):19–32, 2017. ISSN 1757448X. doi: 10.3233/JIN-170009.
- J Pods, J Schönke, and P Bastian. Electrodifusion models of neurons and extracellular space using the Poisson-Nernst-Planck equations numerical simulation of the intra- and extracellular potential for an axon model. *Biophysical Journal*, 105(1):242–254, 2013. ISSN 00063495. doi: 10.1016/j.bpj.2013.05.041.
- S Poliak and E Peles. The local differentiation of myelinated axons at nodes of Ranvier. *Nature Reviews Neuroscience*, 4(12):968–980, 2003. ISSN 1471-003X. doi: 10.1038/nrn1253.
- J C Prechtl and T L Powley. The fiber composition of the abdominal vagus of the rat. *Anatomy and Embryology*, 181(2):101–115, 1990. ISSN 03402061. doi: 10.1007/BF00198950.
- D Purves, E Rubin, W D Snider, and J Lichtman. Relation of animal size to convergence, divergence, and neuronal number in peripheral sympathetic pathways. *The Journal of Neuroscience*, 6(1):158–63, 1986. ISSN 0270-6474. URL <http://www.ncbi.nlm.nih.gov/pubmed/3944617>.
- T Rakthanmanon and E Keogh. Fast shapelets: a scalable algorithm for discovering time series shapelets. *Proceedings of the 2013 SIAM International Conference on Data Mining*, pages 668–676, 2013. ISSN 1063-4266. doi: 10.1137/1.9781611972832.74. URL <http://epubs.siam.org/doi/abs/10.1137/1.9781611972832.74>.

- A Rapeaux, K Nikolic, I Williams, A Eftekhari, and T G Constandinou. Fiber size-selective stimulation using action potential filtering for a peripheral nerve interface: A simulation study. *Proceedings of the Annual International Conference of the IEEE Engineering in Medicine and Biology Society, EMBS*, 2015-Novem:3411–3414, 2015. ISSN 1557170X. doi: 10.1109/EMBC.2015.7319125.
- S Raspopovic, M Capogrosso, and S Micera. A computational model for the stimulation of rat sciatic nerve using a transverse intrafascicular multichannel electrode. *IEEE Transactions on Neural Systems and Rehabilitation Engineering*, 19(4):333–344, 2011. ISSN 15344320. doi: 10.1109/TNSRE.2011.2151878.
- S Raspopovic, M Capogrosso, J Badia, X Navarro, and S Micera. Experimental validation of a hybrid computational model for selective stimulation using transverse intrafascicular multichannel electrodes. *IEEE Transactions on Neural Systems and Rehabilitation Engineering*, 20(3):395–404, 2012. ISSN 15344320. doi: 10.1109/TNSRE.2012.2189021.
- H G Rey, C Pedreira, and R Quiñan Quiroga. Past, present and future of spike sorting techniques. *Brain Research Bulletin*, 119:106–117, 2015. ISSN 18732747. doi: 10.1016/j.brainresbull.2015.04.007. URL <http://dx.doi.org/10.1016/j.brainresbull.2015.04.007>.
- J S Richman and J R Moorman. Physiological time-series analysis using approximate entropy and sample entropy maturity in premature infants. *American Journal of Physiology Heart and Circulatory Physiology*, 278(6):H2039–H2049, 2000.
- G R Ricker, R Vanderspek, J Winn, S Seager, Z Berta-Thompson, A Levine, J Villaseñor, D Latham, D Charbonneau, M Holman, J Johnson, D Sasselov, A Szentgyorgyi, G Torres, G Bakos, T Brown, J Christensen-Dalsgaard, H Kjeldsen, M Clampin, S Rinehart, D Deming, J Doty, E Dunham, S Ida, N Kawai, B Sato, J Jenkins, J Lissauer, G Jernigan, L Kaltenegger, G Laughlin, D Lin, P McCullough, N Narita, J Pepper, K Stassun, and S Udry. The Transiting Exoplanet Survey Satellite. *Journal of Astronomical Telescopes, Instruments, and Systems*, 1(1):014003–1, 2016. ISSN 1996756X. doi: 10.1117/12.2232071.
- E H Rijnbeek, N Eleveld, and W Olthuis. Update on peripheral nerve electrodes for closed-loop neuroprosthetics. *Frontiers in Neuroscience*, 12(May):1–9, 2018. ISSN 1662453X. doi: 10.3389/fnins.2018.00350.

- J V Ringwood and S C Malpas. Slow oscillations in blood pressure via a nonlinear feedback model. *American journal of physiology. Regulatory, integrative and comparative physiology*, 280(4):1105–15, 2001. ISSN 0363-6119. doi: citeulike-article-id:2195425. URL <http://ajpregu.physiology.org/content/280/4/R1105.abstract>.
- F J Rodríguez, D Ceballos, M Schüttler, A Valero, E Valderrama, T Stieglitz, and X Navarro. Polyimide cuff electrodes for peripheral nerve stimulation. *Journal of Neuroscience Methods*, 98(2):105–118, 2000. ISSN 01650270. doi: 10.1016/S0165-0270(00)00192-8.
- E Romero, J F Denef, J Delbeke, A Robert, and C Veraart. Neural morphological effects of long-term implantation of the self-sizing spiral cuff nerve electrode. *Medical and Biological Engineering and Computing*, 39(1):90–100, 2001. ISSN 01400118. doi: 10.1007/BF02345271.
- J Röper and J R Schwarz. Heterogeneous distribution of fast and slow potassium channels in myelinated rat nerve fibres. *The Journal of Physiology*, 416(1989):93–110, 1989. ISSN 0022-3751. URL <http://www.pubmedcentral.nih.gov/articlerender.fcgi?artid=1189205&tool=pmcentrez&rendertype=abstract>.
- B Rosin, M Slovik, R Mitelman, M Rivlin-Etzion, S N Haber, Z Israel, E Vaadia, and H Bergman. Closed-loop deep brain stimulation is superior in ameliorating parkinsonism. *Neuron*, 72(2):370–384, 2011. ISSN 08966273. doi: 10.1016/j.neuron.2011.08.023. URL <http://dx.doi.org/10.1016/j.neuron.2011.08.023>.
- S E Ross, Z J Sperry, C M Mahar, and T M Bruns. Hysteretic behavior of bladder afferent neurons in response to changes in bladder pressure. *BMC Neuroscience*, 17(1):1–12, 2016. ISSN 14712202. doi: 10.1186/s12868-016-0292-5.
- S E Ross, Z Ouyang, S Rajagopalan, and T M Bruns. Evaluation of decoding algorithms for estimating bladder pressure from dorsal root ganglia neural recordings. *Annals of Biomedical Engineering*, 46(2):233–246, 2018. ISSN 15739686. doi: 10.1007/s10439-017-1966-6.
- O E Rössler. An equation for continuous chaos. *Physics Letters A*, 57(5):397–398, 1976. ISSN 03759601. doi: 10.1016/0375-9601(76)90101-8.
- L Rousselet, V Le Rolle, D Ojeda, D Guiraud, A Hagège, A Bel, J L Bonnet, P Mabo, G Carrault, and A I Hernández. Influence of vagus nerve stimulation parameters on chronotropism and inotropism

- in heart failure. *36th Annual International Conference of the IEEE Engineering in Medicine and Biology Society*, 36:526–529, 2014. doi: 10.1109/EMBC.2014.6943644.
- H P Saal, X Wang, and S J Bensmaia. Importance of spike timing in touch: an analogy with hearing? *Current Opinion in Neurobiology*, 40:142–149, 2016. ISSN 18736882. doi: 10.1016/j.conb.2016.07.013. URL <http://dx.doi.org/10.1016/j.conb.2016.07.013>.
- J F Sacramento, D J Chew, B F Melo, M Donegá, W Dopson, M P Guarino, A Robinson, J Prieto-Lloret, S Patel, B J Holinski, N Ramnarain, V Pikov, K Famm, and S V Conde. Bioelectronic modulation of carotid sinus nerve activity in the rat: a potential therapeutic approach for type 2 diabetes. *Diabetologia*, 61(3):700–710, 2018. ISSN 14320428. doi: 10.1007/s00125-017-4533-7.
- E Salinas and L F Abbott. Vector reconstruction from firing rates. *Journal of Computational Neuroscience*, 1(1-2):89–107, 1994. ISSN 09295313. doi: 10.1007/BF00962720.
- C Y Saylam, E Ozgiray, M Orhan, S Cagli, and M Zileli. Neuroanatomy of cervical sympathetic trunk: A cadaveric study. *Clinical Anatomy*, 22(3):324–330, 2009. ISSN 08973806. doi: 10.1002/ca.20764.
- P Schäfer. The BOSS is concerned with time series classification in the presence of noise. *Data Mining and Knowledge Discovery*, 29(6):1505–1530, 2015. ISSN 13845810. doi: 10.1007/s10618-014-0377-7. URL <http://dx.doi.org/10.1007/s10618-014-0377-7>.
- E S Schelegle and J F Green. An overview of the anatomy and physiology of slowly adapting pulmonary stretch receptors. *Respiration Physiology*, 125(1-2):17–31, 2001. ISSN 00345687. doi: 10.1016/S0034-5687(00)00202-4.
- H Schmalbruch. Fiber composition of the rat sciatic nerve. *The Anatomical record*, 215(1):71–81, 1986. ISSN 0003-276X. doi: 10.1002/ar.1092150111. URL <http://www.ncbi.nlm.nih.gov/pubmed/3706794>.
- E Schneidman, W Berry, and M J Bialek. Synergy, Redundancy, and Independence in population codes. *Journal of Neuroscience*, 23(37):11539–11553, 2003. ISSN 1529-2401. doi: 10.1523/JNEUROSCI.23-37-11539.2003.

- S R Schultz, K Kitamura, A Post-Uiterweer, J Krupic, and M Hausser. Spatial pattern coding of sensory information by climbing fiber-evoked calcium signals in networks of neighboring cerebellar purkinje cells. *Journal of Neuroscience*, 29(25):8005–8015, 2009. ISSN 0270-6474. doi: 10.1523/jneurosci.4919-08.2009.
- S R Schultz, R A A Ince, and S Panzeri. Applications of information theory to analysis of neural data. In *Encyclopedia of Computational Neuroscience*, pages 199–203. Springer, 2015. ISBN 9781461473206. doi: 10.4249/scholarpedia.1286. URL http://www.scholarpedia.org/article/Encyclopedia_of_computational_neuroscience.
- A R Schwartz, M L Bennett, P L Smith, W De Backer, J Hedner, A Boudewyns, P Van De Heyning, H Ejnell, W Hochban, L Knaack, T Podszus, T Penzel, J H Peter, G S Goding, D J Erickson, R Testerman, F Ottenhoff, and D W Eisele. Therapeutic electrical stimulation of the hypoglossal nerve in obstructive sleep apnea. *Archives of Otolaryngology - Head and Neck Surgery*, 127(10): 1216–1223, 2001. ISSN 08864470. doi: 10.1001/archotol.127.10.1216.
- K Scott. The sweet and the bitter of mammalian taste. *Current Opinion in Neurobiology*, 14(4): 423–427, 2004. ISSN 09594388. doi: 10.1016/j.conb.2004.06.003.
- A D Sdrulla, Q Xu, S Q He, V Tiwari, F Yang, C Zhang, B Shu, R Shechter, S N Raja, Y Wang, X Dong, and Y Guan. Electrical stimulation of low-threshold afferent fibers induces a prolonged synaptic depression in lamina II dorsal horn neurons to high-threshold afferent inputs in mice. *Pain*, 156(6):1008–1017, 2015. ISSN 18726623. doi: 10.1097/01.j.pain.0000460353.15460.a3.
- P Sembulingam. *Essentials of Medical Physiology*. Jaypee Brothers Medical Publishers, 2012. doi: 10.5005/jp/books/11696.
- J N Sengupta and G F Gebhart. Characterization of mechanosensitive pelvic nerve afferent fibers innervating the colon of the rat. *Journal of Neurophysiology*, 71(6):2046–2060, 1994a. ISSN 0022-3077. doi: 10.1152/jn.1994.71.6.2046.
- J N Sengupta and G F Gebhart. Mechanosensitive properties of pelvic nerve afferent fibers innervating the urinary bladder of the rat. *Journal of Neurophysiology*, 72(5):2420–2430, 1994b. ISSN 0022-3077. doi: 10.1152/jn.1994.72.5.2420.

- D Seo, R M Neely, K Shen, U Singhal, E Alon, J M Rabaey, J M Carmena, and M M Maharbiz. Wireless recording in the peripheral nervous system with ultrasonic neural dust. *Neuron*, 91(3): 529–539, 2016. ISSN 10974199. doi: 10.1016/j.neuron.2016.06.034. URL <http://dx.doi.org/10.1016/j.neuron.2016.06.034>.
- M Serruya, M Fellows, L Paninski, J Donoghue, and N Hatsopoulos. Robustness of neuroprosthetic decoding algorithms. *Biological Cybernetics*, 88(3):219–228, 2003. ISSN 0340-1200. doi: 10.1007/s00422-002-0374-6. URL <http://link.springer.com/10.1007/s00422-002-0374-6>.
- M D Serruya, N G Hatsopoulos, L Paninski, M R Fellows, and J P Donoghue. Instant neural control of a movement signal. *Nature*, 416(6877):141–142, 2002. ISSN 0028-0836. doi: 10.1038/416141a.
- S S Sethi, V Zerbi, N Wenderoth, A Fornito, and B D Fulcher. Structural connectome topology relates to regional BOLD signal dynamics in the mouse brain. *Chaos*, 27(4), 2017. ISSN 10541500. doi: 10.1063/1.4979281.
- C Sevcencu and J J Struijk. Neural markers and implantable bioelectronic systems for the treatment of hypertension. *Bioelectronics in Medicine*, 1(2):139–150, 2018. ISSN 2059-1500. doi: 10.2217/bem-2017-0014.
- C Sevcencu, T N Nielsen, and J J Struijk. An intraneural electrode for bioelectronic medicines for treatment of hypertension. *Neuromodulation*, 21(8):777–786, 2018. ISSN 15251403. doi: 10.1111/ner.12758.
- C E Shannon. A mathematical theory of communication. *The Bell System Technical Journal*, 27(July 1928):379–423, 1948.
- Z Sheikh, P J Brooks, O Barzilay, N Fine, and M Glogauer. Macrophages, foreign body giant cells and their response to implantable biomaterials. *Materials*, 8(9):5671–5701, 2015. ISSN 19961944. doi: 10.3390/ma8095269.
- A K Shekar, M Pappik, P Iglesias Sánchez, and E Müller. Selection of relevant and non-redundant multivariate ordinal patterns for time series classification. In Larisa Soldatova, Joaquin Vanschoren, George Papadopoulos, and Michelangelo Ceci, editors, *Discovery Science*, pages 224–240, Cham, 2018. Springer International Publishing. ISBN 978-3-030-01771-2.

- T Shimizu, M Hayashi, A Kawata, T Mizutani, K Watabe, and S Matsubara. A morphometric study of the vagus nerve in amyotrophic lateral sclerosis with circulatory collapse. *Amyotrophic Lateral Sclerosis*, 12(5):356–62, 2011. ISSN 1471-180X. doi: 10.3109/17482968.2011.566342. URL <http://www.ncbi.nlm.nih.gov/pubmed/21434813>.
- W B Shingleton and D R Bodner. The development of urologic complications in relationship to bladder pressure in spinal cord injured patients. *The Journal of the American Paraplegia Society*, 16(1):14–17, 1993. ISSN 01952307. doi: 10.1080/01952307.1993.11735878.
- M Sjogren, P Hellstrom, M Jonsson, M Runnerstam, H Silander, and E Ben-Menachem. Cognition-enhancing effect of vagus nerve stimulation in patients with alzheimer’s disease: A pilot study. *Journal of Clinical Psychiatry*, 63:972–980, 1997.
- A G Smith. Electromyography and neuromuscular disorders clinical-electrophysiologic correlations. *Neurology*, 67(7):1317–1317, 2006.
- N Snaidero and M Simons. Myelination at a glance. *Journal of cell science*, 127(Pt 14):2999–3004, 2014. ISSN 1477-9137. doi: 10.1242/jcs.151043. URL <http://www.ncbi.nlm.nih.gov/pubmed/25024457>.
- B S Spearman, V H Desai, S Mobini, M D McDermott, J B Graham, K J Otto, J W Judy, and C E Schmidt. Tissue-engineered peripheral nerve interfaces. *Advanced Functional Materials*, 28(12):1–18, 2018. ISSN 16163028. doi: 10.1002/adfm.201701713.
- Z J Sperry, K Na, S S Parizi, H J Chiel, J Seymour, E Yoon, and T M Bruns. Flexible microelectrode array for interfacing with the surface of neural ganglia. *Journal of Neural Engineering*, 15(3):036027, 2018. ISSN 17412552. doi: 10.1088/1741-2552/aab55f.
- J C Sprott. *Chaos and time-series analysis*. Oxford university press, 2003.
- K H Srivastava, C M Holmes, M Vellema, A R Pack, C P H Elemans, and I Nemenman. Motor control by precisely timed spike patterns. *Proceedings of the National Academy of Sciences*, 114(5):1171–1176, 2017. ISSN 1098-6596. doi: 10.1101/056010. URL <http://biorxiv.org/content/early/2016/05/31/056010.abstract>.

- S D Stavisky, J C Kao, P Nuyujukian, S I Ryu, and K V Shenoy. A high performing brain-machine interface driven by low-frequency local field potentials alone and together with spikes. *Journal of Neural Engineering*, 12(3), 2015. ISSN 17412552. doi: 10.1088/1741-2560/12/3/036009.
- R B Stein, D Charles, L Davis, J Jhamandas, A Mannard, and T R Nichols. Principles underlying new methods for chronic neural recording. *Canadian Journal of Neurological Sciences / Journal Canadien des Sciences Neurologiques*, 2(3):235–244, 1975. ISSN 20570155. doi: 10.1017/S0317167100020333.
- R B Stein, T R Nichols, J Jhamandas, L Davis, and D Charles. Stable long-term recordings from cat peripheral nerves. *Brain Research*, 128(1):21–38, 1977. ISSN 00068993. doi: 10.1016/0006-8993(77)90233-5.
- P Sterling. Homeostasis vs allostasis implications for brain function and mental disorders. *JAMA Psychiatry*, 71(10):1192–1193, 2014. doi: 10.1001/jamapsychiatry.2014.1043.Conflict.
- P Sterling and S Laughlin. *Principles of Neural Design*. MIT Press, 2015. ISBN 9780262327312. URL <http://www.scopus.com/inward/record.url?eid=2-s2.0-84952028199&partnerID=tZ0tx3y1>.
- T Stieglitz, H Beutel, and J U Meyer. A flexible, light-weight multichannel sieve electrode with integrated cables for interfacing regenerating peripheral nerves. *Sensors and Actuators, A: Physical*, 60(1-3):240–243, 1997. ISSN 09244247. doi: 10.1016/S0924-4247(97)01494-5.
- C Stöllberger, W Lutz, and J Finsterer. Heat-related side-effects of neurological and non-neurological medication may increase heatwave fatalities. *European Journal of Neurology*, 16(7):879–882, 2009. ISSN 13515101. doi: 10.1111/j.1468-1331.2009.02581.x.
- P J Strollo, R J Soose, J T Maurer, N de Vries, J Cornelius, O Froymovich, R D Hanson, T A Padhya, D L Steward, M B Gillespie, B T Woodson, P H Van de Heyning, M G Goetting, O M Vanderveken, N Feldman, L Knaack, and K P Strohl. Upper-airway stimulation for obstructive sleep apnea. *The New England Journal of Medicine*, 370(2):139–49, 2014. ISSN 1533-4406. doi: 10.1056/NEJMoal308659. URL <http://www.ncbi.nlm.nih.gov/pubmed/24401051>.
- J J Struijk. The extracellular potential of a myelinated nerve fiber in an unbounded medium and in

- nerve cuff models. *Biophysical Journal*, 72(6):2457–2469, 1997. ISSN 00063495. doi: 10.1016/S0006-3495(97)78890-8. URL [http://dx.doi.org/10.1016/S0006-3495\(97\)78890-8](http://dx.doi.org/10.1016/S0006-3495(97)78890-8).
- J J Struijk, M Thomsen, J O Larsen, and T Sinkjaer. Cuff electrodes for long-term recording of natural sensory information. *IEEE Engineering in Medicine and Biology Magazine*, 18(3):91–98, 1999. ISSN 07395175. doi: 10.1109/51.765194.
- E Sundman and P S Olofsson. Neural control of the immune system. *Advances in Physiology Education*, 38(2):135–139, 2015. ISSN 15221229. doi: 10.1152/advan.00094.2013.
- D Sundt, N Gamper, and D B Jaffe. Spike propagation through the dorsal root ganglia in an unmyelinated sensory neuron: a modeling study. *Journal of neurophysiology*, 114(6):3140–53, 2015. ISSN 1522-1598. doi: 10.1152/jn.00226.2015. URL <http://jn.physiology.org/lookup/doi/10.1152/jn.00226.2015> <http://www.ncbi.nlm.nih.gov/pubmed/26334005> <http://www.pubmedcentral.nih.gov/articlerender.fcgi?artid=PMC4686302>.
- M D Tarler and J T Mortimer. Selective and independent activation of four motor fascicles using a four contact nerve-cuff electrode. *IEEE Transactions on Neural Systems and Rehabilitation Engineering*, 12(2):251–257, 2004. ISSN 15344320. doi: 10.1109/TNSRE.2004.828415.
- I Tarotin, K Y Aristovich, and D S Holder. Simulation of impedance changes with a FEM model of a myelinated nerve fibre. *Journal of Neural Engineering*, 2019. ISSN 1741-2560. doi: 10.1088/1741-2552/ab2d1c.
- J Taylor, B Metcalfe, C Clarke, D Chew, T Nielsen, and N Donaldson. A summary of current and new methods in velocity selective recording (VSR) of electroneurogram (ENG). *Proceedings of IEEE Computer Society Annual Symposium on VLSI, ISVLSI*, pages 221–226, 2015. ISSN 21593477. doi: 10.1109/ISVLSI.2015.34.
- J B Tenenbaum, V de Silva, and J C Langford. A global geometric framework for nonlinear dimensionality reduction. *Science (New York, N.Y.)*, 290(5500):2319–23, 2000. ISSN 0036-8075. doi: 10.1126/science.290.5500.2319. URL <http://www.ncbi.nlm.nih.gov/pubmed/11125149>.
- S Thrun. Probabilistic robotics. *Communications of the ACM*, 45(3):1999–2000, 2002. ISSN 00010782. doi: 10.1145/504729.504754.

- R Tibshirani. Regression shrinkage and selection via the lasso. *Journal of the Royal Statistical Society*, 58(1):267–288, 1996.
- J Timmer, C Gantert, G Deuschl, and J Honerkamp. Characteristics of hand tremor time series. *Biological Cybernetics*, 70(1):75–80, 1993. ISSN 03401200. doi: 10.1007/BF00202568.
- J K Todd. Afferent impulses in the pudendal nerves of the cat. *Quarterly Journal of Experimental Physiology and Cognate Medical Sciences: Translation and Integration*, 49(3):258–267, 1964.
- B H Tracey, P Krastev, Z Han, and M Williams. Computational modeling of peripheral nerve stimulation. In *Annual International Conference of the IEEE Engineering in Medicine and Biology Society*, pages 6777–6780, 2009. ISBN 9781424432967. doi: 10.1109/IEMBS.2009.5332515.
- F Tuisku and C Hildebrand. Nodes of Ranvier and myelin sheath dimensions along exceptionally thin myelinated vertebrate PNS axons. *Journal of Neurocytology*, 21(11):796–806, 1992. ISSN 03004864. doi: 10.1007/BF01237905.
- A Tveito, K H Jæger, G T Lines, L Paszkowski, J Sundnes, A G Edwards, T Mäki-Marttunen, G Halnes, and G T Einevoll. An evaluation of the accuracy of classical models for computing the membrane potential and extracellular potential for neurons. *Frontiers in Computational Neuroscience*, 11(27):1–18, 2017. ISSN 1662-5188. doi: 10.3389/fncom.2017.00027. URL <http://journal.frontiersin.org/article/10.3389/fncom.2017.00027/full>.
- E Uemura, T F Fletcher, and W E Bradley. Distribution of lumbar and sacral afferent axons in submucosa of cat urinary bladder. *The Anatomical Record*, 183(4):579–587, 1975. ISSN 10970185. doi: 10.1002/ar.1091830408.
- B van der Pol. On relaxation-oscillations. *Philosophical Magazine and Journal of Science*, 2(11): 978–992, 1926. ISSN 1941-5982. doi: 10.1080/14786442608564127.
- B P Van Wunnik, B Govaert, R Leong, F H Nieman, and C G Baeten. Patient experience and satisfaction with sacral neuromodulation: Results of a single-center sample survey. *Diseases of the Colon and Rectum*, 54(1):95–100, 2011. ISSN 00123706. doi: 10.1007/DCR.0b013e3181f46810. URL <http://dx.doi.org/10.1016/j.juro.2010.09.090>.

- M Vejmelka and M Paluš. Inferring the directionality of coupling with conditional mutual information. *Physical Review E - Statistical, Nonlinear, and Soft Matter Physics*, 77(2):1–12, 2008. ISSN 15393755. doi: 10.1103/PhysRevE.77.026214.
- P H Veltink, B K Van Veen, J J Struijk, J Holsheimer, and H B K Boom. A modeling study of nerve fascicle stimulation. *IEEE Transactions on Biomedical Engineering*, 36(7):683–692, 1989. ISSN 15582531. doi: 10.1109/10.32100.
- P F Verhulst. La loi d'accroissement de la population. *Nouv. Mem. Acad. Roy. Soc. Belle-lett. Bruxelles*, 18(1):1–38, 1845.
- M Vlachos, G Kollios, and D Gunopulos. Discovering similar multidimensional trajectories. In *Data Mining and Knowledge Discovery*, page 673, 2002. ISBN 978-3-319-23519-6. doi: 10.1007/978-3-319-23519-6_1401-2.
- D B Vodušek. Anatomy and neurocontrol of the pelvic floor. *Digestion*, 69(2):87–92, 2004. ISSN 00122823. doi: 10.1159/000077874.
- B G Wallin, D Burke, and S Gandevia. Coupling between variations in strength and baroreflex latency of sympathetic discharges in human muscle nerves. *The Journal of physiology*, 474(2):331–8, 1994. ISSN 0022-3751. doi: 10.1113/jphysiol.1994.sp020025. URL <http://www.ncbi.nlm.nih.gov/pubmed/8006818>
<http://www.pubmedcentral.nih.gov/articlerender.fcgi?artid=PMC1160321>.
- E Waltz. Erratum: A spark at the periphery. *Nature Biotechnology*, 34(12):1292–1292, 2016. ISSN 1087-0156. doi: 10.1038/nbt1216-1292b.
- F B Wang, M C Holst, and T L Powley. The ratio of pre- to postganglionic neurons and related issues in the autonomic nervous system. *Brain Research Reviews*, 21(1):93–115, 1995. ISSN 01650173. doi: 10.1016/0165-0173(95)00006-O.
- X Wang, K Smith, and R Hyndman. Characteristic-based clustering for time series data. *Data Mining and Knowledge Discovery*, 13(3):335–364, 2006. ISSN 13845810. doi: 10.1007/s10618-005-0039-x.

- X Wang, A Wirth, and L Wang. Structure-based statistical features and multivariate time series clustering. *Proceedings - IEEE International Conference on Data Mining, ICDM*, pages 351–360, 2007. ISSN 15504786. doi: 10.1109/ICDM.2007.103.
- W K Ward. A review of the foreign-body response to subcutaneously-implanted devices: The role of Macrophages and cytokines in biofouling and fibrosis. *Journal of Diabetes Science and Technology*, 2(5):768–777, 2008. ISSN 19322968. doi: 10.1177/193229680800200504.
- T Watanabe, D A Rivas, and M B Chancellor. Urodynamics of spinal cord injury. *Urologic Clinics*, 23(3):459–73, 1996. ISSN 0094-0143. URL <http://www.ncbi.nlm.nih.gov/pubmed/8701559>.
- S G Waxman. Determinants of conduction velocity in myelinated nerve fibers. *Muscle & nerve*, 3(2):141–150, 1980. ISSN 0148-639X. doi: 10.1002/mus.880030207.
- D J Weber, R B Stein, D G Everaert, and A Prochazka. Limb-state feedback from ensembles of simultaneously recorded dorsal root ganglion neurons. *Journal of Neural Engineering*, 4(3):S168–S180, 2007. ISSN 17412560. doi: 10.1088/1741-2560/4/3/S04.
- B J Wenzel, W M Grill, J W Boggs, and K J Gustafson. Detecting the onset of hyper-reflexive bladder contractions from pudendal nerve electrical activity. *IEEE EMBS Conference on Neural Engineering*, 6(3):4213–4216, 2004. ISSN 1557-170X. doi: 10.1109/IEMBS.2004.1404175.
- B J Wenzel, J W Boggs, K J Gustafson, and W M Grill. Closed loop electrical control of urinary continence. *Journal of Urology*, 175(4):1559–1563, 2006. ISSN 00225347. doi: 10.1016/S0022-5347(05)00657-9.
- J Wessberg, C R Stambaugh, J D Kralik, P D Beck, M Laubach, J K Chapin, J Kim, S J Biggs, M A Srinivasan, and M A Nicolelis. Real-time prediction of hand trajectory by ensembles of cortical neurons in primates. *Nature*, 408(6810):361–365, 2000. ISSN 0028-0836. doi: 10.1038/35042582.
- what-when-how.com. Diseases of the Peripheral Nervous System Part 1. URL <http://what-when-how.com/acp-medicine/diseases-of-the-peripheral-nervous-system-part-1/>.
- B C Wheeler and W J Heetderks. A comparison of techniques for classification of multiple neural

- signals. *IEEE transactions on bio-medical engineering*, 29(12):752–759, 1982. ISSN 0018-9294. doi: 10.1109/TBME.1982.324870.
- T L Wheeler, W de Groat, K Eisner, A Emmanuel, J French, W Grill, M J Kennelly, A Krassioukov, B Gallo Santacruz, F Biering-Sørensen, and N Kleitman. Translating promising strategies for bowel and bladder management in spinal cord injury. *Experimental Neurology*, 306(March):169–176, 2018. ISSN 10902430. doi: 10.1016/j.expneurol.2018.05.006. URL <https://doi.org/10.1016/j.expneurol.2018.05.006>.
- A W Whitney. A direct method of nonparametric measurement selection. *IEEE Transactions on Computers*, 20(September):1100–1103, 1971.
- J Williams. Clustering household electricity use profiles. In *MLSDA '13 Proceedings of Workshop on Machine Learning for Sensory Data Analysis*, pages 19–26, 2014. ISBN 9781450325134. doi: 10.1145/2542652.2542656.
- I H Witten, E Frank, and J Geller. *Data Mining: Practical Machine Learning Tools and Techniques with Java Implementations*, volume 31. *Acm Sigmod Record*, 2002. doi: 10.1145/507338.507355.
- J D Wood. Enteric nervous system: reflexes, pattern generators and motility. *Current Opinion in Gastroenterology*, 24(2):149–58, 2008. ISSN 1531-7056. doi: 10.1097/MOG.0b013e3282f56125. URL <http://www.ncbi.nlm.nih.gov/pubmed/18301264>.
- B T Woodson, K P Strohl, R J Soose, M B Gillespie, J T Maurer, N de Vries, T A Padhya, M S Badr, H S Lin, O M Vanderveken, S Mickelson, and P J Strollo. Upper airway stimulation for obstructive sleep apnea: 5-year outcomes. *Otolaryngology - Head and Neck Surgery (United States)*, 159(1):194–202, 2018. ISSN 10976817. doi: 10.1177/0194599818762383.
- W Wu, Y Gao, E Bienenstock, J P Donoghue, M J Black, E Biemenstock, J P Donoghue, and M J Black. Bayesian population decoding of motor cortical activity using a Kalman filter. *Neural computation*, 18(1):80–118, 2005.
- S Wurth, M Capogrosso, S Raspopovic, J Gandar, G Federici, N Kinany, A Cutrone, A Piersigilli, N Pavlova, R Guiet, G Taverni, J Rigosa, P Shkorbatova, X Navarro, Q Barraud, G Courtine, and S Micera. Long-term usability and bio-integration of polyimide-based intra-neural stimulating

- electrodes. *Biomaterials*, 122:114–129, 2017. ISSN 18785905. doi: 10.1016/j.biomaterials.2017.01.014. URL <http://dx.doi.org/10.1016/j.biomaterials.2017.01.014>.
- J J Wyndaele. The management of neurogenic lower urinary tract dysfunction after spinal cord injury. *Nature Reviews Urology*, 13(12):705–714, 12 2016. ISSN 17594820. doi: 10.1038/nrurol.2016.206.
- N Xue, T Sun, W M Tsang, I Delgado-Martinez, S H Lee, S Sheshadri, Z Xiang, S Merugu, Y Gu, S C Yen, and N V Thakor. Polymeric C-shaped cuff electrode for recording of peripheral nerve signal. *Sensors and Actuators, B: Chemical*, 210:640–648, 2015. ISSN 09254005. doi: 10.1016/j.snb.2015.01.006. URL <http://dx.doi.org/10.1016/j.snb.2015.01.006>.
- D Yan, T M Bruns, Y Wu, L L Zimmerman, C Stephan, A P Cameron, E Yoon, and J P Seymour. Ultra-compliant carbon nanotube stretchable direct bladder interface. *bioRxiv*, 1900477:580902, 2019a. doi: 10.1101/580902. URL <https://www.biorxiv.org/content/10.1101/580902v2>.
- D Yan, A Jiman, D Ratze, S Huang, S Parizi, E Welle, Z Ouyang, P Patel, M J Kushner, C Chestek, T M Bruns, E Yoon, and J Seymour. Microneedle penetrating array with axon-sized dimensions for cuff-less Pperipheral nerve interfacing. In *International IEEE/EMBS Conference on Neural Engineering, NER*, pages 827–830. IEEE, 2019b. ISBN 9781538679210. doi: 10.1109/NER.2019.8717097.
- L Ye and E Keogh. Time series shapelets. *Proceedings of the 15th ACM SIGKDD international conference on Knowledge discovery and data mining - KDD '09*, page 947, 2009. doi: 10.1145/1557019.1557122.
- J Yin, F Ji, P Gharibani, and J D Chen. Vagal nerve stimulation for glycemic control in a rodent model of Type 2 Diabetes. *Obesity Surgery*, 29(9):2869–2877, 2019. ISSN 17080428. doi: 10.1007/s11695-019-03901-9.
- A Yousefi, A K Gillespie, J A Guidera, M Karlsson, L Frank, and U Eden. Efficient decoding of multi-dimensional signals from population spiking activity using a Gaussian mixture particle filter. In *IEEE Transactions on Biomedical Engineering*, pages 1–12. IEEE, 2019. doi: 10.1109/tbme.2019.2906640.

- J Yu, H D Schultz, J Goodman, J C Coleridge, H M Coleridge, and B Davis. Pulmonary rapidly adapting receptors reflexly increase airway secretion in dogs. *Journal of Applied Physiology*, 67(2):682–687, 2017. ISSN 8750-7587. doi: 10.1152/jappl.1989.67.2.682.
- L Yu and Y Yu. Energy-efficient neural information processing in individual neurons and neuronal networks. *Journal of Neuroscience Research*, 2017. ISSN 0360-4012. doi: 10.1002/jnr.24131. URL <http://doi.wiley.com/10.1002/jnr.24131>.
- T P Zanos, H A Silverman, T Levy, T Tsaava, E Battinelli, P W Lorraine, J M Ashe, S S Chavan, K J Tracey, and C E Bouton. Identification of cytokine-specific sensory neural signals by decoding murine vagus nerve activity. *Proceedings of the National Academy of Sciences*, 115(21):E4843–E4852, 2018. ISSN 0027-8424. doi: 10.1073/pnas.1719083115.
- M Zhang, M A Schwemmer, J E Ting, C E Majstorovic, D A Friedenberg, M A Bockbrader, W Jerry Mysiw, A R Rezai, N V Annetta, C E Bouton, H S Bresler, and G Sharma. Extracting wavelet based neural features from human intracortical recordings for neuroprosthetics applications. *Bioelectronic Medicine*, 4(1):1–14, 2018. ISSN 2332-8886. doi: 10.1186/s42234-018-0011-x.
- J Zhuang, W Truccolo, C Vargas-Irwin, and J P Donoghue. Decoding 3-D reach and grasp kinematics from high-frequency local field potentials in primate primary motor cortex. *IEEE Transactions on Biomedical Engineering*, 57(7):1774–1784, 2010. doi: 10.1016/j.cortex.2009.08.003.Predictive.

This document contains 388 references.